IntechOpen

Mass Transfer

Advancement in Process Modelling

Edited by Marek Solecki

MASS TRANSFER - ADVANCEMENT IN PROCESS MODELLING

Edited by **Marek Solecki**

Mass Transfer - Advancement in Process Modelling
http://dx.doi.org/10.5772/59640
Edited by Marek Solecki

Contributors

Sandile Motsa, Rafał Rakoczy, Abdelraheem Mahmoud Aly, Mitsuteru Asai, Ahlem Arfaoui, Badie I. Morsi, Omar M. Basha, Amira Abdelrasoul, Huu Doan, Ali Lohi, Chil-Hung Cheng, Maria Angelica Barros, Roberto Parreiras Tavares, Marek Solecki, Monika Solecka, Pen-Chi Chiang, Shu-Yuan Pan, Leôncio Diógenes Tavares Câmara

© The Editor(s) and the Author(s) 2015
The moral rights of the and the author(s) have been asserted.
All rights to the book as a whole are reserved by INTECH. The book as a whole (compilation) cannot be reproduced, distributed or used for commercial or non-commercial purposes without INTECH’s written permission.
Enquiries concerning the use of the book should be directed to INTECH rights and permissions department (permissions@intechopen.com).
Violations are liable to prosecution under the governing Copyright Law.

Individual chapters of this publication are distributed under the terms of the Creative Commons Attribution 3.0 Unported License which permits commercial use, distribution and reproduction of the individual chapters, provided the original author(s) and source publication are appropriately acknowledged. If so indicated, certain images may not be included under the Creative Commons license. In such cases users will need to obtain permission from the license holder to reproduce the material. More details and guidelines concerning content reuse and adaptation can be foundat http://www.intechopen.com/copyright-policy.html.

Notice

Statements and opinions expressed in the chapters are these of the individual contributors and not necessarily those of the editors or publisher. No responsibility is accepted for the accuracy of information contained in the published chapters. The publisher assumes no responsibility for any damage or injury to persons or property arising out of the use of any materials, instructions, methods or ideas contained in the book.

First published in Croatia, 2015 by INTECH d.o.o.
eBook (PDF) Published by IN TECH d.o.o.
Place and year of publication of eBook (PDF): Rijeka, 2019.
IntechOpen is the global imprint of IN TECH d.o.o.
Printed in Croatia

Legal deposit, Croatia: National and University Library in Zagreb

Additional hard and PDF copies can be obtained from orders@intechopen.com

Mass Transfer - Advancement in Process Modelling
Edited by Marek Solecki

p. cm.

ISBN 978-953-51-2192-3

eBook (PDF) ISBN 978-953-51-6394-7

Meet the editor

Marek Solecki received an M.Sc. degree in the Faculty of Mechanical Engineering of the Lodz University of Technology. He was granted his Ph.D. and D.Sc. from the Faculty of Process and Environmental Engineering at the Lodz University of Technology. Since 1998, Dr. Solecki has been working as an assistant professor in the Department of Process Equipment of the Lodz University of Technology. His academic interests include dynamic processes and process equipment. He is the author and co-author of over 100 reviewed papers published in international science journals and peer-reviewed proceedings, co-inventor of five patents, and author of one monograph and chapters published in three books. Dr. Solecki is a member of the European Federation of Biotechnology and the Polish Society of Mechanical Engineers and Technicians.

Contents

Preface

Mass transfer is the basis for the occurrence of many phenomena: physical, chemical, biological, as well as many others from related disciplines and areas of human activity. The transfer of different particle matter sets based on specific transport principles is described by analogous laws, congruent models, and similar relations. Research results obtained from mass transfer have a wide interdisciplinary application and, as a consequence, they have a great impact on the progress. The effects of intensive research carried out in selected directions are often applied spectacularly to other areas. Therefore, the creation of a platform for exchange of observation, experience, and achievements in various fields in the area of mass transfer contributes to the development and dissemination of knowledge and improves processes and technical means to carry them out.

This book is aimed at presenting the most recent achievements of mass transfer theory and methods by stages of modelling different processes. Development of knowledge occurs cyclically, generally reaching successive stages: observation, hypothesis, experiment, and formulation of theory. Searching for appropriate mathematical description must be preceded by a critical assessment of the present state and definition of demand for a new solution. Built models require validation. Such research stages from various academic disciplines are described in further chapters of this book. I hope that they will trigger further interactions between different fields of science. The book contains a wide variety of issues related to advancements in modelling mass transfer. I would like to thank all the authors for their contribution to facilitate the understanding of complex problems and issues. The book is dedicated to those in the chemical, biotechnological, pharmaceutical, and nanotechnology industries as well as to students of natural sciences, technical, environmental and to employees in companies which manufacture machines for the above-mentioned industries. This work can also be a useful source for researchers and engineers dealing with mass transfer and related issues.

Dr. Marek Solecki
Department of Process Equipment
Lodz University of Technology, Lodz, Poland

Chapter 1

On the New Bivariate Local Linearisation Method for Solving Coupled Partial Differential Equations in Some Applications of Unsteady Fluid Flows with Heat and Mass Transfer

Sandile Motsa

Additional information is available at the end of the chapter

http://dx.doi.org/10.5772/60444

Abstract

This work presents a new numerical approach for solving unsteady two-dimensional boundary layer flow with heat and mass transfer. The flow model is described in terms of a highly coupled and nonlinear system of partial differential equations that models the problem of unsteady mixed convection flow over a vertical cone due to impulsive motion. The proposed method of solution uses a local linearisation approach to decouple the original system of PDEs to form a sequence of equations that can be solved in a computationally efficient manner. Approximate functions defined in terms of bivariate Lagrange interpolation polynomials are used with spectral collocation to approximate the solutions of the decoupled linearised equations. To test the accuracy and to validate the results of the proposed method, numerical error analysis and convergence tests are conducted. The present results are also compared with results from published literature for some special cases. The proposed algorithm is shown to be very accurate, convergent and very effective in generating numerical results in a computationally efficient manner.

On the New Bivariate Local Linearisation Method for Solving Coupled Partial Differential Equations in Some Applications of Unsteady Fluid Flows with Heat and Mass Transfer

Keywords: Unsteady boundary layer flow, heat and mass transfer, bivariate spectral collocation, impulsive flow

1. Introduction

In this investigation we revisit the problem of unsteady mixed convection flow over a vertical cone due to impulsive motion that was previously discussed in Singh and Roy [7]. In the flow model, the external stream is impulsively set into motion and the surface temperature is suddenly changed from its ambient temperature. The resulting constitutive equations describing the flow properties are a system of highly coupled non-linear partial differential equations (PDEs) which cannot be solved exactly. In [7], the solution of the PDEs system was approximated numerically using implicit finite differences after linearising using the quasi-linearisation (QLM) technique of Bellman and Kalaba [1]. The QLM simplifies the solution process by simply reducing the original PDEs to a linearised form which, nevertheless, is coupled. In view of the coupled nature of the QLM iteration scheme, matrices of very large dimensions are obtained when using any numerical method is used for discretization. For systems of coupled equations, the method proposed by [3] was used in [7] to decouple the governing equations. There is generally a large overhead in computing resources when performing computational tasks on large matrix systems. To avoid dealing with large matrix systems, relaxation methods can be used. However, the disadvantage of relaxation methods is that they convergence much slower than quasi-linearisation schemes which are known to converge quadratically.

A linearisation method, termed the local linearisation method (LLM), was recently introduced in [4] as an efficient method for solving coupled systems of non-linear ordinary differential equations that model boundary layer equations. This method was extended to a PDE system in [5] where the Chebyshev spectral collocation method [2, 8] was used for discretization in one independent variable and finite differences was used for discretization in the second independent variable of the PDE. In this study, we present a new approach that seeks to improve on the original LLM approach of [5] by eliminating the need for using finite differences for discretizing in one of the independent variables and, instead, apply spectral collocation independently in all independent variables of the PDE system. Finite differences require very fine grids (with a large number of grid points) to give more accurate solutions. In contrast, spectral methods are computationally less expensive, converge faster and are more accurate than finite difference methods particularly for problems with smooth solutions. The collocation method applied in this work uses bivariate Lagrange interpolation polynomials as basis functions. The proposed method converges fast and gives very accurate results which are obtained in a computationally efficient manner. The accuracy is established through residual and solution error analysis. Further validation of present results in established by comparing with existing results from literature.

2. Governing equations

The model under consideration is that of an unsteady mixed convection flow over a vertical cone that is impulsively set into motion to cause unsteadiness in the flow (see [6, 7]). It is assumed that buoyancy forces are present due to temperature and concentration variation of the fluid flow. The governing boundary layer momentum, energy and concentration equations were reduced to dimensionless form in [7] using transformations that were initially proposed in Williams and Rhyne [9] to give,

$$\begin{gathered}\frac{\partial^3 f}{\partial \eta^3}+\frac{\eta}{2}(1-\xi)\frac{\partial^2 f}{\partial \eta^2}+f\frac{\partial^2 f}{\partial \eta^2}\left[\xi\left(\frac{m+3}{6}\right)-(1-\xi)\left(\frac{m-3}{6}\right)\log(1-\xi)\right]+\frac{m}{3}\xi\left[1-\left(\frac{\partial f}{\partial \eta}\right)^2\right]\\ \lambda\xi(\theta+N\phi)=\xi(1-\xi)\frac{\partial^2 f}{\partial \eta \partial \xi}+\frac{\xi}{3}(m-3)(1-\xi)\log(1-\xi)\left[\frac{\partial^2 f}{\partial \eta^2}\frac{\partial f}{\partial \xi}-\frac{\partial f}{\partial \eta}\frac{\partial^2 f}{\partial \eta \partial \xi}\right],\end{gathered} \tag{1}$$

$$\begin{gathered}\frac{\partial^2 \theta}{\partial \eta^2}+\frac{\eta}{2}Pr(1-\xi)\frac{\partial \theta}{\partial \eta}+Prf\frac{\partial \theta}{\partial \eta}\left[\xi\left(\frac{m+3}{6}\right)-(1-\xi)\left(\frac{m-3}{6}\right)\log(1-\xi)\right]-Pr\left(\frac{2m-3}{3}\right)\xi\theta\frac{\partial f}{\partial \eta}\\ =\xi(1-\xi)Pr\frac{\partial \theta}{\partial \xi}+Pr(1-\xi)\log(1-\xi)\xi\left(\frac{m-3}{3}\right)\left[\frac{\partial \theta}{\partial \eta}\frac{\partial f}{\partial \xi}-\frac{\partial f}{\partial \eta}\frac{\partial \theta}{\partial \xi}\right],\end{gathered} \tag{2}$$

$$\begin{gathered}\frac{\partial^2 \phi}{\partial \eta^2}+\frac{\eta}{2}Sc(1-\xi)\frac{\partial \phi}{\partial \eta}+Scf\frac{\partial \phi}{\partial \eta}\left[\xi\left(\frac{m+3}{6}\right)-(1-\xi)\left(\frac{m-3}{6}\right)\log(1-\xi)\right]-Sc\left(\frac{2m-3}{3}\right)\xi\phi\frac{\partial f}{\partial \eta}\\ =\xi(1-\xi)Sc\frac{\partial \phi}{\partial \xi}+Sc(1-\xi)\log(1-\xi)\xi\left(\frac{m-3}{3}\right)\left[\frac{\partial \phi}{\partial \eta}\frac{\partial f}{\partial \xi}-\frac{\partial f}{\partial \eta}\frac{\partial \phi}{\partial \xi}\right],\end{gathered} \tag{3}$$

where Pr is the Prandtl number, Sc is the Schmidt number, f is the dimensionless stream function, θ and ϕ are the dimensionless temperature and concentration, $N=\lambda/\lambda^*$ is the ratio of the thermal (λ) and concentration λ^* buoyancy parameter.

The boundary conditions are

$$\begin{gathered}f(0,\xi)=0,\quad \frac{\partial f(0,\xi)}{\partial \eta}=0,\quad \theta(0,\xi)=1,\quad \phi(0,\xi)=1,\\ \frac{\partial f(\infty,\xi)}{\partial \eta}=1,\quad \theta(\infty,\xi)=0,\quad \phi(\infty,\xi)=0.\end{gathered} \tag{4}$$

Other quantities of physical interest include the local skin friction coefficient, Nusselt number and Sherwood numbers which are given, in dimensionless forms as,

$$Re_L^{1/2}C_f=2\xi^{-1/2}f''(0,\xi), \tag{5}$$

$$Re_L^{-1/2}Nu=-\xi^{-1/2}\theta'(0,\xi), \tag{6}$$

$$Re_L^{-1/2}Sh = -\xi^{-1/2}\phi'(0,\xi). \tag{7}$$

3. Derivation of solution method

The derivation of the solution method is described for a general system of non-linear PDEs in this section. Consider a system of 3 coupled PDEs in $f(\eta,\xi)$, $\theta(\eta,\xi)$ and $\phi(\eta,\xi)$

$$\Omega_k\left[F,T,H\right] = 0, \quad for \;\; k = 1,2,3, \tag{8}$$

where Ω_1, Ω_2 and Ω_3 are non-linear operators that represent the non-linear PDEs (1), (2) and (3), respectively and F,T,H are defined as

$$\begin{aligned}
F &= \left\{ f, \frac{\partial f}{\partial \eta}, \frac{\partial^2 f}{\partial \eta^2}, \frac{\partial^3 f}{\partial \eta^3}, \frac{\partial^2 f}{\partial \xi \partial \eta} \right\}, \\
T &= \left\{ \theta, \frac{\partial \theta}{\partial \eta}, \frac{\partial^2 \theta}{\partial \eta^2}, \frac{\partial \theta}{\partial \xi} \right\}, \\
H &= \left\{ \phi, \frac{\partial \phi}{\partial \eta}, \frac{\partial^2 \phi}{\partial \eta^2}, \frac{\partial \phi}{\partial \xi} \right\}.
\end{aligned}$$

Equation (8) can be simplified and decoupled by using the following algorithm called local linearisation method (LLM):

LLM Algorithm

1. Solve for F in 1st equation assuming that T and H are known from previous iteration. ↣ F_{r+1}.
2. With F_{r+1} now known, solve for T in 2nd equation, assuming that H is known from previous iteration. ↣ T_{r+1}.
3. Solve for H in 3rd equation ↣ H_{r+1}.

The LLM algorithm was recently reported in [4] as an efficient method for solving coupled system of non-linear ordinary differential equations that model boundary layer equations. The method was later extended to partial differential equations in [5]. Applying the algorithm in equations (8) gives

$$F \cdot \nabla_f \Omega_1\left[F_r,T_r,H_r\right] = F_r \cdot \nabla_f \Omega_1\left[F_r,T_r,H_r\right] - \Omega_1\left[F_r,T_r,H_r\right], \tag{9}$$

$$T\cdot\nabla_{\theta}\Omega_2\left[F_{r+1},T_r,H_r\right]=T_r\cdot\nabla_{\theta}\Omega_2\left[F_{r+1},T_r,H_r\right]-\Omega_2\left[F_{r+1},T_r,H_r\right], \tag{10}$$

$$H\cdot\nabla_{\phi}\Omega_3\left[F_{r+1},T_{r+1},H_r\right]=H_r\cdot\nabla_{\phi}\Omega_3\left[F_{r+1},T_{r+1},H_r\right]-\Omega_3\left[F_{r+1},T_{r+1},H_r\right]. \tag{11}$$

The above equation forms a system of three decoupled linear PDEs that are to be solved iteratively for $f(\eta,\xi)$, $\theta(\eta,\xi)$ and $\phi(\eta,\xi)$, where ∇ is a vector of partial derivatives defined as

$$\begin{aligned}
\nabla &= \left\{\nabla_f,\nabla_\theta,\nabla_\phi\right\},\\
\nabla_f &= \left\{\frac{\partial}{\partial f},\frac{\partial}{\partial f'},\frac{\partial}{\partial f''},\frac{\partial}{\partial f'''},\frac{\partial}{\partial f'_\xi}\right\},\\
\nabla_\theta &= \left\{\frac{\partial}{\partial \theta},\frac{\partial}{\partial \theta'},\frac{\partial}{\partial \theta''},\frac{\partial}{\partial \theta_\xi}\right\},\\
\nabla_\phi &= \left\{\frac{\partial}{\partial \phi},\frac{\partial}{\partial \phi'},\frac{\partial}{\partial \phi''},\frac{\partial}{\partial \phi_\xi}\right\}.
\end{aligned}$$

Applying the LLM iteration scheme (9) - (11) on the governing non-linear PDE system (1) - (3) gives

$$f_{r+1}'''+a_{1,r}\left(\eta,\xi\right)f_{r+1}''+a_{2,r}\left(\eta,\xi\right)f_{r+1}'+a_{3,r}\left(\eta,\xi\right)f_{r+1}+a_{4,r}\left(\eta,\xi\right)\frac{\partial f_{r+1}'}{\partial\xi}=R_{1,r}\left(\eta,\xi\right), \tag{12}$$

$$\theta_{r+1}''+b_{1,r}\left(\eta,\xi\right)\theta_{r+1}'+b_{2,r}\left(\eta,\xi\right)\theta_{r+1}+b_{3,r}\left(\eta,\xi\right)\frac{\partial\theta_{r+1}}{\partial\xi}=R_{2,r}\left(\eta,\xi\right), \tag{13}$$

$$\phi_{r+1}''+c_{1,r}\left(\eta,\xi\right)\phi_{r+1}'+c_{2,r}\left(\eta,\xi\right)\phi_{r+1}+c_{3,r}\left(\eta,\xi\right)\frac{\partial\phi_{r+1}}{\partial\xi}=R_{3,r}\left(\eta,\xi\right), \tag{14}$$

where the primes denote partial differentiation with respect to η and the coefficients $a_{i,r}$,$b_{i,r}$ and $c_{i,r}$ $(i=1,2,3,4)$ are known coefficients whose quantities are known from the previous iteration level r. The definition of the coefficients is given in the Appendix.

The boundary conditions are given by

$$f_{r+1}\left(0,\xi\right)=0,\quad f'_{r+1}\left(0,\xi\right)=0,\quad \theta_{r+1}\left(0,\xi\right)=1,\quad \phi_{r+1}\left(0,\xi\right)=1, \tag{15}$$

$$f'_{r+1}\left(\infty,\xi\right)=1,\quad \theta_{r+1}\left(\infty,\xi\right)=0,\quad \phi_{r+1}\left(\infty,\xi\right)=0. \tag{16}$$

Starting from given initial approximations, denoted by $f_0(\eta,\xi),\theta_0(\eta,\xi)$ and $\phi_0(\eta,\xi)$, equations (12) – (14) are solved iteratively for $r=1,2,\ldots$, until approximate solutions that are consistent to within a certain tolerance level are obtained.

To solve the linearised equations (12) – (16), an approximate solution defined in terms of bivariate Lagrange interpolation polynomials in sought. For example, the approximate solution for $f(\eta,\xi)$ takes the form

$$f(\eta,\xi)\approx\sum_{m=0}^{N_x}\sum_{j=0}^{N_t}f(\tau_m,\zeta_j)L_m(\tau)L_j(\zeta), \tag{17}$$

where the functions $L_m(\tau)$ and $L_j(\zeta)$ are the well-known characteristic Lagrange cardinal polynomials. The function (17) interpolates $f(\eta,\xi)$ at the collocation points (known as Chebyshev-Gauss-Lobatto) defined by

$$\tau_i=\cos\left(\frac{\pi i}{N_x}\right),\quad \zeta_j=\cos\left(\frac{\pi j}{N_t}\right),\quad i=0,1,\ldots,N_x;\ j=0,1,\ldots,N_t. \tag{18}$$

The choice of collocation points (18) makes it possible for the Chebyshev spectral collocation method to be used as a solution procedure. The Chebyshev collocation method requires that the domain of the problem be transformed to $[-1,1]\times[-1,1]$. Accordingly, linear transformations have been used to transform $\eta\in[0,\eta_\infty]$ and $\xi\in[0,L_t]$ to $\tau\in[-1,1]$ and $\zeta\in[-1,1]$, respectively. Here η_∞ is a finite value that is introduced to facilitate the application of the numerical method at infinity and L_t is the largest value of ξ.

Substituting equation (17) in equation (12)-(14) and making use of the derivatives formulas for Lagrange functions at Gauss-Lobatto points given in [2, 8], results in

$$A_iF_{r+1,i}+a_{4,i}\sum_{j=0}^{N_t}d_{i,j}DF_{r+1,j}+a_{5,i}\sum_{j=0}^{N_t}d_{i,j}F_{r+1,j}=R_{1,i}, \tag{19}$$

$$B_i\mathrm{Q}_{r+1,i}+b_{3,i}\sum_{j=0}^{N_t}d_{i,j}\mathrm{Q}_{r+1,j}=R_{2,i}, \tag{20}$$

$$C_i\mathrm{F}_{r+1,i}+c_{3,i}\sum_{j=0}^{N_t}d_{i,j}\mathrm{F}_{r+1,j}=R_{3,i}, \tag{21}$$

where $d_{i,j}$ $(i,j=0,1,\ldots,N_t)$ are entries of the standard Chebyshev differentiation matrix $d=[d_{i,j}]$ of size $(N_t+1)\times(N_t+1)$ (see, for example [2, 8]), $D2\eta_e)[D_{r,s}]$ $(r,s=0,1,2,\ldots,N_x)$ with $[D_{r,s}]$ being an $(N_x+1)\times(N_x+1)$ Chebyshev derivative matrix. The vectors and matrices are defined as

$$
\begin{aligned}
&F_{r+1,i} = [f_{r+1,i}(\tau_0), f_{r+1,i}(\tau_1), \ldots, f_{r+1,i}(\tau_{N_x})]^T,\\
&\mathrm{Q}_{r+1,i} = [\theta_{r+1,i}(\tau_0), \theta_{r+1,i}(\tau_1), \ldots, \theta_{r+1,i}(\tau_{N_x})]^T,\\
&\mathrm{F}_{r+1,i} = [\phi_{r+1,i}(\tau_0), \phi_{r+1,i}(\tau_1), \ldots, \phi_{r+1,i}(\tau_{N_x})]^T,\\
&A_i = D^3 + a_{1,i}D^2 + a_{2,i}D + a_{3,i},\\
&B_i = D^2 + b_{1,i}D + b_{2,i},\\
&C_i = D^2 + c_{1,i}D + c_{2,i},
\end{aligned}
$$

$a_{m,r}(\xi_i)(m=1,2,3,4,5)$ is the diagonal matrix of the vector $[a_{m,r}(\tau_0), a_{m,r}(\tau_1), \ldots, a_{m,r}(\tau_{N_x})]^T$. The matrices $b_{1,i}, b_{2,i}, c_{1,i}, c_{2,i}$ are also diagonal matrices corresponding to $b_{1,r}, b_{2,r}, c_{1,r}, c_{2,r}$ evaluated at collocation points. Additionally, $R_{1,i}$, $R_{2,i}$ and $R_{3,i}$ are $(N_x+1)\times 1$ vectors corresponding to $R_{1,r}$, $R_{2,r}$ and $R_{3,r}$, respectively, evaluated at the collocation points.

After imposing the boundary conditions for $i=0,1,\ldots,N_t$, equation (20) can be written as the following matrix equation:

$$
\begin{bmatrix} A_{0,0} & A_{0,1} & \cdots & A_{0,N_t} \\ A_{1,0} & A_{1,1} & \cdots & A_{1,N_t} \\ \vdots & \vdots & \ddots & \vdots \\ A_{N_t,0} & A_{N_t,1} & \cdots & A_{N_t,N_t} \end{bmatrix}
\begin{bmatrix} F_{r+1,0} \\ F_{r+1,1} \\ \vdots \\ F_{r+1,N_t} \end{bmatrix}
=
\begin{bmatrix} R_{1,0} \\ R_{1,1} \\ \vdots \\ R_{1,N_t} \end{bmatrix}, \tag{22}
$$

where

$$
\begin{aligned}
&A_{i,j} = A_i + a_{4,i}d_{i,i}D + a_{5,i}d_{i,i}I,\\
&A_{i,j} = a_{4,i}d_{i,i}D + a_{5,i}d_{i,i}I, \quad when\; i \neq j,
\end{aligned}
$$

where I is an $(N_x+1)\times(N_x+1)$ identity matrix.

Applying the same approach to (20) and (21) gives

$$
\begin{bmatrix} B_{0,0} & B_{0,1} & \cdots & B_{0,N_t} \\ B_{1,0} & B_{1,1} & \cdots & B_{1,N_t} \\ \vdots & \vdots & \ddots & \vdots \\ B_{N_t,0} & B_{N_t,1} & \cdots & B_{N_t,N_t} \end{bmatrix}
\begin{bmatrix} \mathrm{Q}_{r+1,0} \\ \mathrm{Q}_{r+1,1} \\ \vdots \\ \mathrm{Q}_{r+1,N_t} \end{bmatrix}
=
\begin{bmatrix} R_{2,0} \\ R_{2,1} \\ \vdots \\ R_{2,N_t} \end{bmatrix}, \tag{23}
$$

$$
\begin{bmatrix} C_{0,0} & C_{0,1} & \cdots & C_{0,N_t} \\ C_{1,0} & C_{1,1} & \cdots & C_{1,N_t} \\ \vdots & \vdots & \ddots & \vdots \\ C_{N_t,0} & C_{N_t,1} & \cdots & C_{N_t,N_t} \end{bmatrix}
\begin{bmatrix} \mathrm{F}_{r+1,0} \\ \mathrm{F}_{r+1,1} \\ \vdots \\ \mathrm{F}_{r+1,N_t-1} \end{bmatrix}
=
\begin{bmatrix} R_{3,0} \\ R_{3,1} \\ \vdots \\ R_{3,N_t} \end{bmatrix}, \tag{24}
$$

where

$$\begin{aligned}
B_{i,j} &= B_i + b_{3,i} d_{i,i} I, \\
B_{i,j} &= b_{3,i} d_{i,j} I, \quad when\ i \neq j, \\
C_{i,j} &= C_i + c_{3,i} d_{i,i} I, \\
C_{i,j} &= c_{3,i} d_{i,j} I, \quad when\ i \neq j,
\end{aligned}$$

Starting from a given initial guess, the approximate solutions for $f(\eta,\xi)$, $\theta(\eta,\xi)$ and $\phi(\eta,\xi)$ are obtained by iteratively solving the matrix equations (22), (23) and (24), in turn, for $r=0,1,2,\ldots$. Convergence to the expected solution can be affirmed by considering the norm of the difference between successive iterations. If this quantity is less than a given tolerance level, the algorithm is assumed to have converged. The following error norms are defined for the difference between values of successive iterations,

$$E_f = \max_{0 \le i \le N_t} \left\| F_{r+1,i} - F_{r,i} \right\|_\infty, \quad E_\theta = \max_{0 \le i \le N_t} \left\| \mathrm{Q}_{r+1,i} - \mathrm{Q}_{r,i} \right\|_\infty, \quad E_\phi = \max_{0 \le i \le N_t} \left\| \mathtt{F}_{r+1,i} - \mathtt{F}_{r,i} \right\|_\infty. \tag{25}$$

4. Results and discussion

The local linearisation method (LLM) described by equations (12) - (14 was used to generate approximate numerical solutions for the governing systems of equations (1) - (3). The linearised equations were subsequently solved using the bivariate spectral collocation method as described in the previous section. The whole solution process is termed bivariate spectral local linearisation method (BSLLM). In this section, we present the results of the numerical computations for the various flow profiles. The BSLLM results are compared with published results from literature. In computing the numerical results presented in this paper, $N_x=60$ and $N_t=15$ collocation points in the η and ξ domain, respectively, were found to be sufficient to give accurate and consistent results. The minimum number of iterations required to give consistent results to within a tolerance level of 10^{-7} were determined using equation (25).

The effects of buoyancy parameter (λ) and Prandtl number (Pr) on velocity and temperature profiles are shown in Figs. 1 and 2, respectively for when $N=0.5$, $Sc=0.94$ at $\xi=0.5$. It can be seen from the figures that the results from the present work match those reported in [7] exactly. We remark that in [7], the quasi-linearisation approach was used with implicit finite differences as a solution method. Details of the analysis of the effects of various governing parameters on the governing equations (1) – (3) can be found in [7] and have not been repeated here.

Figs. 3, 4 and 5 show the effect of buoyancy ratio N on the velocity, temperature and concentration profiles, respectively, when $Pr=0.7$, $Sc=0.94$ and $\lambda=5$ at $\xi=0.5$. The graphs are qualitatively similar to those reported in [7]. These figures are a qualitative validation of the numerical results generated using the proposed BSLLM.

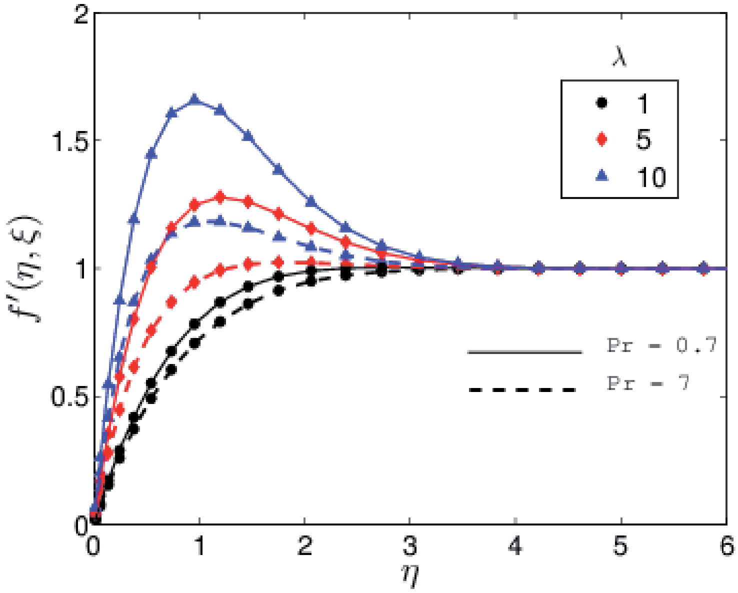

Figure 1. Effect of λ and Pr on the velocity profile $f^{'}(\eta,\xi)$

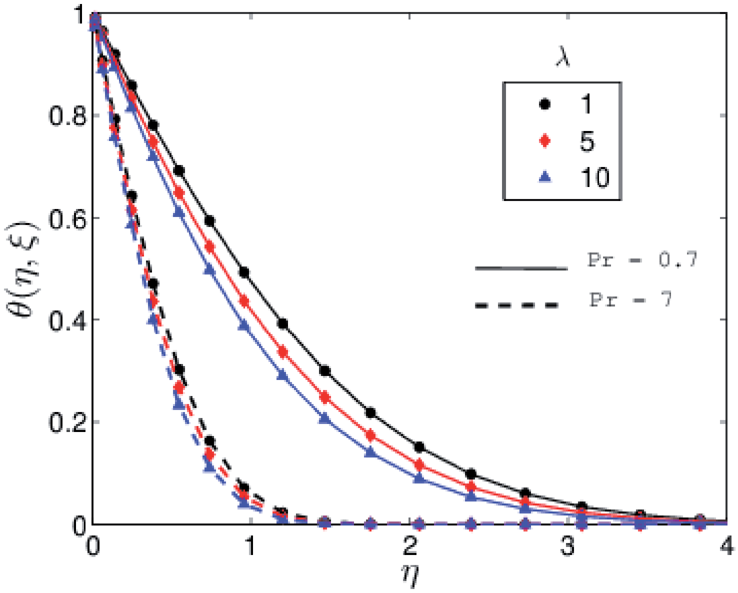

Figure 2. Effect of λ and Pr on the temperature profile $\theta(\eta,\xi)$

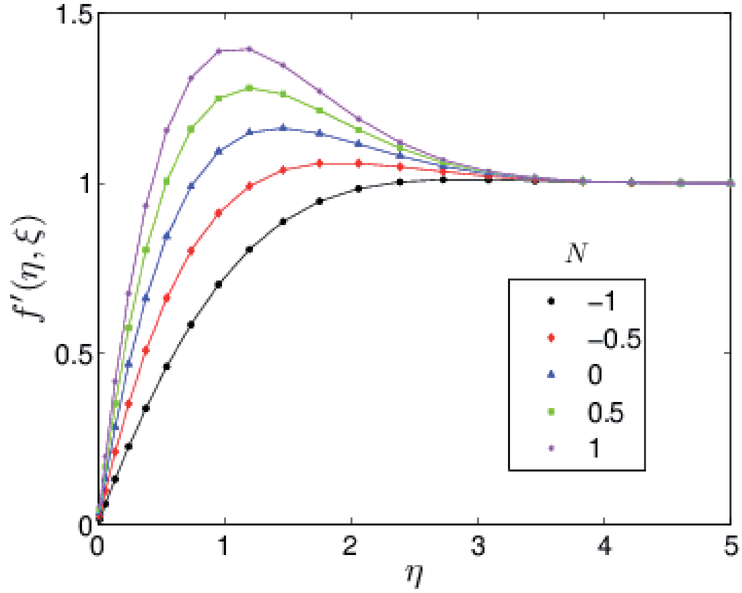

Figure 3. Effect of N velocity profile $f^{'}(\eta,\xi)$

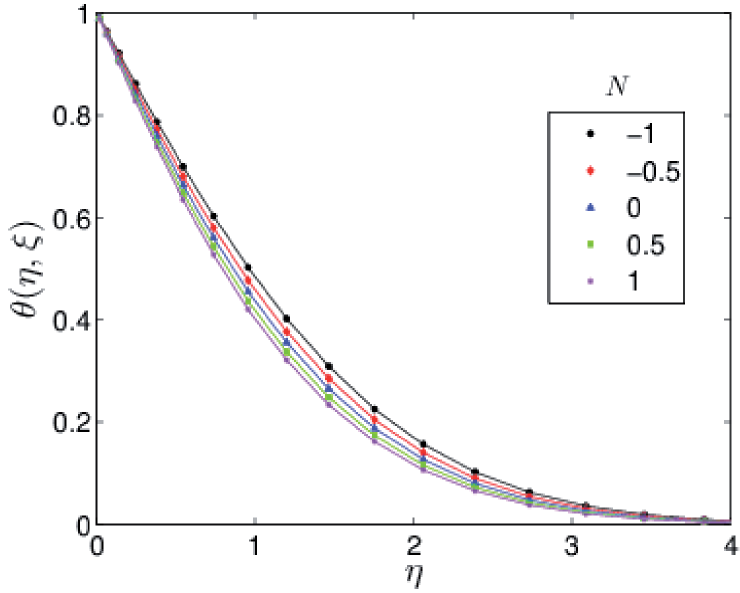

Figure 4. Effect of N on the temperature profile $\theta(\eta,\xi)$

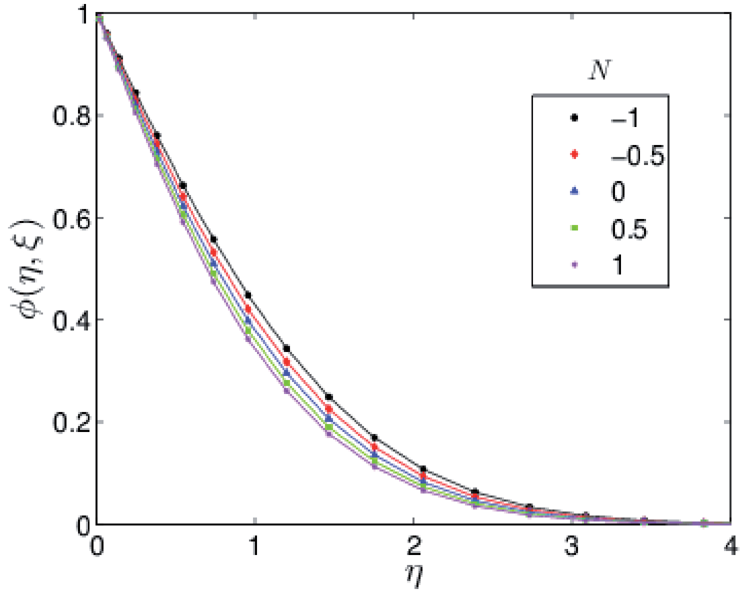

Figure 5. Effect of N concentration profile $\phi(\eta,\xi)$

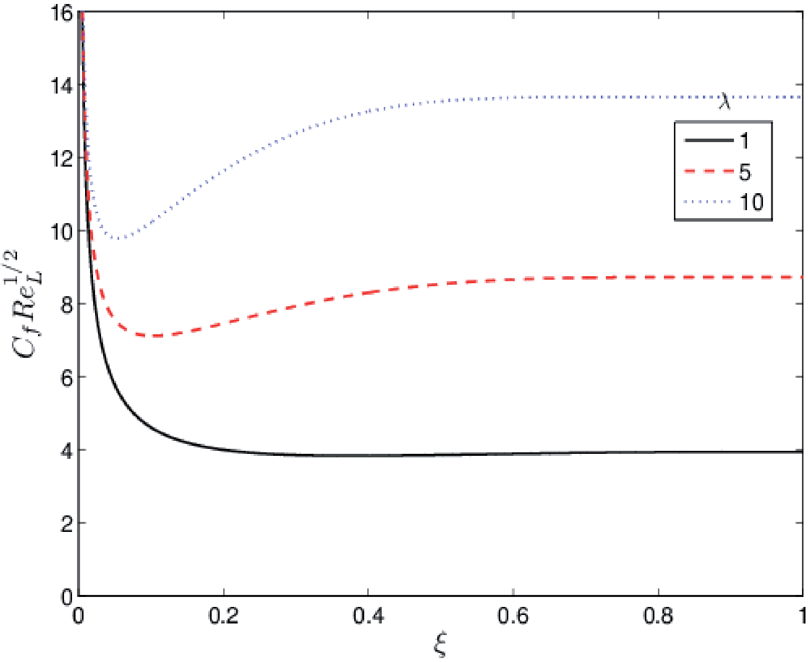

Figure 6. Effect of λ on the skin friction coefficient $C_f\, Re_L^1$

The effect of λ on the skin friction coefficient is shown in Fig. 6 for $Pr=0.7$, $Sc=0.22$ and $N=0.5$. Again, it is observed that the results match those of [7]. In particular, the oscillating trend in the skin friction coefficient for near the stagnation region can be observed.

5. Conclusion

The purpose of the current study was to develop a bivariate Lagrange polynomial based spectral collocation method for solving system of coupled non-linear partial differential equations. The applicability of the proposed method, termed bivariate spectral local linearisation method (BSLLM) was tested on the well-known problem of unsteady mixed convection flow over a vertical cone due to impulsive motion. The validity of the approximate numerical results was confirmed against known results from literature. The results of this study were found to be qualitatively congruent with those from published literature. The study revealed that the proposed method can be used as a viable approach for solving coupled partial differential equations with fluid mechanics applications.

Appendix

Definition of coefficients

$$a_{1,r} = \frac{\eta}{2}(1-\xi) + \beta_1(\xi) f_r - \beta_2(\xi)\frac{\partial f_r}{\partial \xi}, \tag{26}$$

$$a_{2,r} = -\frac{2m}{3}\xi f_r' + \beta_2(\xi)\frac{\partial f_r'}{\partial \xi}, \tag{27}$$

$$a_{3,r} = \beta_1(\xi) f_r'', \tag{28}$$

$$a_{4,r} = -\xi(1-\xi) + \beta_2(\xi) f_r', \tag{29}$$

$$a_{5,r} = -\beta_2(\xi) f_r'', \tag{30}$$

$$R_{1,r} = \beta_1(\xi) f_r f_r'' - \frac{m}{3}\xi\left[1+(f_r')^2\right] - \lambda\xi(\theta_r + N\phi_r) - \beta_2(\xi)\left[f_r''\frac{\partial f_r}{\partial \xi} - f_r'\frac{\partial f_r'}{\partial \xi}\right], \tag{31}$$

$$\beta_1(\xi) = \xi\left(\frac{m+3}{6}\right) - (1-\xi)\left(\frac{m-3}{6}\right)\log(1-\xi), \tag{32}$$

$$\beta_2(\xi) = \xi(1-\xi)\log(1-\xi)\frac{(m-3)}{3}, \tag{33}$$

$$b_{1,r} = \frac{\eta}{2}Pr(1-\xi) + Pr\beta_1(\xi)f_r - Pr\beta_2(\xi)\frac{\partial f_r}{\partial \xi}, \tag{34}$$

$$b_{2,r} = -Pr\frac{(2m-3)}{3}\xi f_r', \tag{35}$$

$$b_{3,r} = -\xi(1-\xi)Pr + Pr\beta_2(\xi)f_r', \tag{36}$$

$$c_{1,r} = \frac{\eta}{2}Sc(1-\xi) + Sc\beta_1(\xi)f_r - Sc\beta_2(\xi)\frac{\partial f_r}{\partial \xi}, \tag{37}$$

$$c_{2,r} = -Sc\frac{(2m-3)}{3}\xi f_r', \tag{38}$$

$$c_{3,r} = -\xi(1-\xi)Sc + Sc\beta_2(\xi)f_r', \tag{39}$$

Author details

Sandile Motsa*

Address all correspondence to: sandilemotsa@gmail.com

School of Mathematics, Statistics and Computer Science, University of KwaZulu-Natal,
Private Bag X, Scottsville, Pietermaritzburg, South Africa

References

[1] R.E. Bellman and R.E. Kalaba, Quasi-linearisation and nonlinear boundary-value problems, Elsevier, New York, 1965.

[2] C. Canuto, M.Y. Hussaini, A. Quarteroni, and T.A. Zang, Spectral Methods in Fluid Dynamics, Springer-Verlag, Berlin, 1988.

[3] K. Inoyue, A. Tate, Finite differences version of quasilinearization applied to boundary layer equations, AIAA J. 12 (1974) 558-560.

[4] S.S. Motsa, A new spectral local linearization method for nonlinear boundary layer flow problems, J. Applied Math. vol. 2013, Article ID 423628, 15 pages, 2013. doi: 10.1155/2013/423628

[5] S.S.Motsa, On the practical use of the spectral homotopy analysis method and local linearisation method for unsteady boundary-layer flows caused by an impulsively stretching plate, Numer. Algor. 66 (2014) 865-883

[6] R. Seshadri, N. Sreeshylan, G. Nath, Unsteady mixed convection flow in the stagnation region of a heated vertical plate due to impulsive motion, Int. J. Heat Mass Transfer 45 (2002) 1345-1352.

[7] P.R. Singh, S. Roy, Unsteady mixed convection flow over a vertical cone due to impulsive motion, International Journal of Heat and Mass Transfer 50 (2007) 949-959

[8] L. N. Trefethen, Spectral Methods in MATLAB, SIAM, 2000.

[9] J.C. William, T.B. Rhyne, Boundary layer development on a wedge impulsively set into motion, SIAM J. Appl. Math. 38 (1980) 215-224.

Chapter 2

Mass Transfer Mechanisms and Transport Resistances in Membrane Separation Process

Amira Abdelrasoul, Huu Doan, Ali Lohi and
Chil-Hung Cheng

Additional information is available at the end of the chapter

http://dx.doi.org/10.5772/60866

Abstract

One of the major obstacles preventing a more widespread application of membrane technology is the fact that the filtration performance inevitably decreases with filtration time. The understanding of causes of flux decline and the ability of predicting the flux performance is crucial for more extensive membrane applications. Therefore, this review focused on the analysis of the interrelated dynamics of membrane fouling and mass transport in the filtration/separation process. Furthermore, findings from various studies undertaken by many researchers to investigate various aspects of these complex phenomena, were analyzed and discussed. These previous studies form the foundation essential for the alleviation of adverse effect of membrane fouling and emphasize the fact that the development of a complex overlapping approach is needed. Investigations of the mechanisms of mass transfer in low and high pressure membranes, analyses of diffusion mechanisms in the membrane pore together with identifications of transport resistances resulting from membrane fouling will allow for a comprehensive understanding and in-depth knowledge of the fouling phenomenon and applicable mass transfer mechanisms.

Keywords: mass transfer, modeling, diffusion, boundary layer, transport resistances, membrane fouling

1. Introduction

Today membrane technology is considered an important tool for sustainable growth in the industry due to its simplicity in concept and operation, modularity for an easy scale-up, potential to reclaim both permeate and retentate for recycling purposes, and reduced energy demand, all of which make it attractive for a more rational utilization of raw materials and waste minimization. Various membrane operations are currently available for a wide spectrum of industrial applications, where most of them can be used as unit operations in pressure driven processes, such as: microfiltration (MF), ultrafiltation (UF), nanofiltration (NF), reverse osmosis (RO), and membrane distillation (MD). Membrane operations show potential in molecular separation, clarification, fractionation, and concentration in liquid and gas phases. Nevertheless, one of the major obstacles preventing a more widespread application of membrane technology is the fact that the filtration performance inevitably decreases with filtration time. This phenomenon is known as membrane fouling and is considered to be the most serious problem affecting system performance and the primary challenge in membrane development. As such, membrane fouling leads to lower mass transfer rate, higher operating cost, higher energy demand, reduced membrane life time, and increased cleaning frequency.

The reduction of membrane flux below that of the corresponding pure water flux, or more generally, pure solvent flux can be divided into two separate components. First, the concentration polarization, which is a natural consequence of the membrane's selectivity [1]. This phenomenon leads to an accumulation of particles or solutes in a mass transfer boundary layer adjacent to the membrane surface. The dissolved molecules accumulating at the surface hinder the solvent transport, which in turn lowers the solvent flow through the membrane. Second, due to the blockage of membrane pores during the filtration process by the combination of sieving and adsorption of particulates and compounds onto the membrane internal surface or within the membrane pores. During this process additional hydraulic resistance is added to the permeate flux. Fouling leads to an increase in resistance, resulting in less flux for a given transmembrane pressure (TMP), or a higher TMP if flux is kept invariant [2]. Understanding the concentration polarization resistance is important when attempting to distinguish a reduction in the driving force across the membrane from the increase in resistance due to the fouling of the membrane [3, 4]. As the material passes through the membrane, it has to be transfered to the surface, diffused through the membrane, and finally transfered from the other side of the membrane to the bulk phase. When the material dissolves within the membrane, then the components are in equilibrium at the surfaces corresponding to their solubility in the membrane. The solute mass transfer through the membranes is controlled by diffusion as a result of the concentration gradient across the membrane surface. In our previously developed mechanistic model for membrane fouling, the mass of fouling attached to the pore wall was a function of the mass transfer coefficient, which, in turn, was dependent on the diffusion coefficient of the foulants in water, particle sizes, and membrane pore sizes [5, 6].

Researchers have invested a lot of effort in seeking new accurate models for the prediction of membrane performance. In most applications, the system equations were derived based on simplifications and assumptions, which resulted in limited practical application of these models.

Nevertheless, these models provide sufficient basis for an incorporation of more parameters for more realistic scenarios. While so far no universally accepted model exists for describing diffusion-controlled membrane processes, understanding the multiple factors affecting membrane mass transfer would certainly help to develop better predictive models. There are many different theories and models describing mass transfer in diffusion-controlled membrane processes, however, several fundamental principles or theories are used as the basis for the majority of these models: convection, diffusion, film theory, and electroneutrality [7, 8]. Most mass transport models assume constant mass transfer coefficients (MTCs) based on a homogeneous membrane surface. Recent innovative studies evaluated mass transfer processes by incorporating membrane surface morphology into a diffusion-based model while assuming that MTCs are dependent on the thickness variation of the membrane's active layer [9]. A non-homogeneous diffusion model (NHDM) was then developed in order to account for the surface variations in the active layer [10]. Notably, concentration polarization (CP) is also affected by this non-homogeneous surface property. As a consequence, the NHDM was modified by incorporating the CP factor. Recent studies have likewise shown that the membrane surface morphology influences colloidal fouling behavior. Therefore, the main objectives of this chapter are to investigate the mechanisms of mass transfer, to critically analyze the different diffusion mechanisms in membrane pores, to identify different transport resistances resulting from membrane fouling, and to discuss various models of mass transfer, in order to obtain a comprehensive understanding of the factors affecting mass transfer phenomenon in membrane and help to develop a comprehensive model predicting the membrane performance.

2. Mass transfer and modeling of the filtration process in the absence of fouling

For an in-depth analysis of the transport resistances in the filtration/separation process due to membrane fouling, it is necessary to understand the mass transfer occurring through membranes in the absence of fouling. This type of transport in membranes can be generally classified into two types of diffusion: first is the diffusion through a dense membrane, which follows the Fick's law and does not depend primarily on the structure of the solid membrane; and second is the diffusion in porous membrane where the porous structure and channel type are important. This study will briefly consider both types of this diffusion.

2.1. Solution diffusion theory through dense membranes

The solution-diffusion process, as illustrated in Figure 1, is the most common mechanism for mass transport through nonporous membranes [11]. It is generally suggested that the component permeation through a homogeneous membrane consists of five fundamental mutually dependent processes: (1) the solute molecules must first be transported or diffused through the liquid film (or gas film; in the later case the mass transfer resistance of the boundary layer is negligible causing this step to be omitted) of the feed phase on the feed side of the membrane, as shown in Figure 1 (B); (2) the solution of the solute molecule in the upstream surface of the membrane; (3) diffusion of the dissolved species across the membrane matrix occurs; (4) desorption of the solute molecules in the downstream side (permeate side) of the membrane; and (5) diffusion through the boundary layer of the permeate phase. The first and the fifth steps can be omitted when there are insignificant mass transfer resistances between the liquid and membrane phases. This assumption is valid for gas permeation or liquid permeation with high flow rates in the fluid phases on both sides of the membranes.

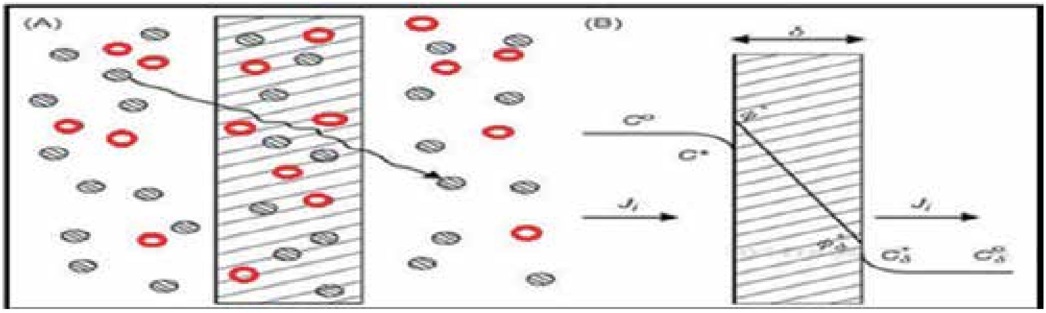

Figure 1. (A) Mass transport through dense membrane (B) Concentration Profile

Fick's first law relates the diffusive flux to the concentration under the assumption of steady state. It postulates that the flux goes from regions of high concentration to regions of low concentration, with a magnitude that is proportional to the concentration gradient [12]. Fick's first law of diffusion is mathematically expressed in Equation (1):

$$J = -D\frac{dC}{dZ} \tag{1}$$

where J is the rate of transfer per unit area of the membrane, C is the concentration of diffusing substances, and Z is the space coordinate measured normal to the membrane.

2.2. Convective transport through a porous membrane layer

As the basis of the pore flow model, pressure-driven convective flow is most commonly used to describe the flow in capillary tubes. The key mechanism at the core of both microfiltration and ultrafiltration is the sieving process, which effectively rejects molecules with the size greater than that of the membrane's pores. Commonly, two approaches are utilized as a way of describing permeability through porous membranes. In the first case, when the membrane resembles an arrangement of near-spherical particles, then the Carman–Kozeny equation can be applied [12], as illustrated in Equation (2):

$$J = \frac{\varepsilon^3}{K.\,\mu.\,S^2\left(1-\ \varepsilon\right)^2}\cdot\frac{\Delta p}{l_{pore}} \tag{2}$$

where J is the permeate flux, ε is surface porosity, μ is the dynamic viscosity of the permeate, K is a constant, l_{pore} is the thickness of the porous layer, ΔP is the pressure drop, and S is the specific area per unit volume. Both K and S depend upon the nature of the membrane porous structure. The permeability constant, K, is a function of the membrane structure, including characteristics such as pore size distribution, and porosity of the membrane, as well as the viscosity of the permeate.

In the second approach, the laminar fluid flow through the capillaries can be described by means of the differential momentum balance equation, Newton's law of viscosity [13, 14]. After integration, the well-known Hagen-Poiseuille equation for the average convective velocity through the porous membrane was obtained to calculate the permeate flux, as described by Equation (3):

$$J = \frac{\varepsilon .\, d_{pore}^2}{32.\, \mu .\, \tau} \cdot \frac{\Delta p}{l_{pore}} \tag{3}$$

where τ is the tortuosity of the capillaries and d_{pore} is the diameter of the capillaries. Once again the flux is inversely proportional to the viscosity of the permeate. In addition, for the porous medium, Darcy law is the basic equation that can be utilized in order to describe the rate of fluid flow and thus allowing calculating the membrane area for a targeted separation at given conditions [12], as showed in Equation 4:

$$Q = \frac{-k\, A}{\mu} \cdot \frac{\left(P_b - P_a\right)}{L} \tag{4}$$

where Q is the total discharge, [m^3/s], k [m^2] is the empirical constant representing permeability of the medium, (A) [m^2] is the cross-sectional area to flow, ($P_b - P_a$) is the pressure drop, μ [kg/(m s) or Pa s] is the viscosity, and L [m] is the membrane thickness.

3. Mass transfer boundary layer and membrane fouling

The rejection of contaminated particles results in a higher concentration in the mass transfer boundary layer. The process of mass accumulation in the mass transfer boundary region is called concentration polarization (CP). CP is a natural consequence of membrane selectivity, which leads to a reduction in the permeate flux because of the gel layer formation [15]. As a result of the high concentration of the rejected component, a back-diffusion occurs from the thin layer adjacent to the membrane back into the bulk [16], as shown in Figure 2. The reduction of membrane performance can be represented as a reduction in the effective TMP driving force due to an osmotic pressure difference between the filtrate and the feed solution immediately adjacent to the membrane surface [11]. As shown in Figure (2), $J_{1,\, con}$, $J_{2,\, con}$, and $J_{2,\, diff}$ [kmol/

m^2.s] represent the convective flux of the solution, the convective flux of the solute, and the diffusion flux of the solute, respectively. The following assumptions were made in order to obtain a mass balance on the feed side of the membrane: steady state, Fickian diffusion, the absence of chemical reaction, negligible concentration gradient parallel to the membrane, and constant density and diffusion coefficient independent of solute concentration [17]. Therefore, the net flux of the solute is the difference between the convective flux and back diffusion flux of the solute.

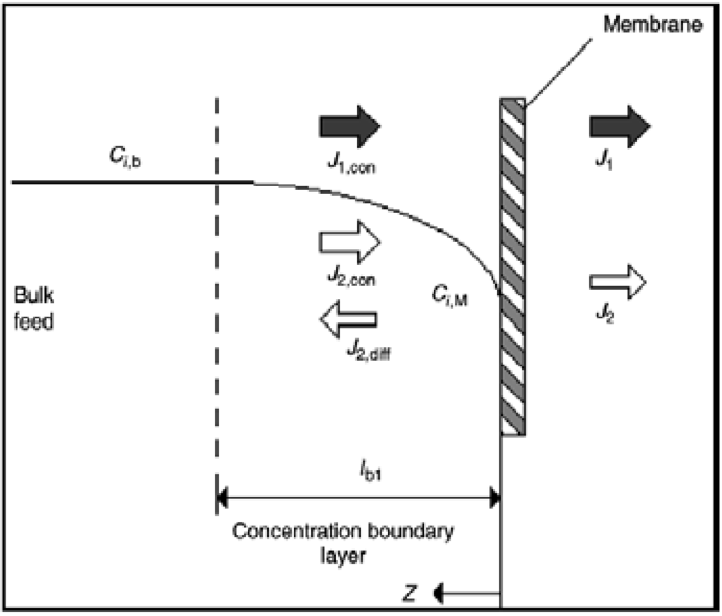

Figure 2. Schematic diagram of concentration polarization

Thus, in general the overall mass balance equation of a component i can be written as:

$$J.\,C_i = J.\,C_{i,p} - D_{ji}\frac{dC_i}{dZ} \tag{5}$$

where J is the volumetric permeate flux, C_i is the concentration of solute i . D_{ji} is the diffusivity of component i, and l_{bl} is the thickness of the mass transfer boundary layer [18]. Integration of Equation (5) gives the well-known polarization equation as below:

$$\left(C_{i,M} - C_{i,P}\right) = \left(C_{i,b} - C_{i,P}\right).\exp\frac{J.\,l_{bl}}{D_{ji}} \tag{6}$$

The subscripts *M*, *b*, and *p* refer to the membrane surface, bulk and permeate respectively. In Equation (5), the term (D_{ji}/l_{bl}) is defined as the mass transfer coefficient $k_{i,b}$. If the permeate flux is based on a limited mass transport and the diffusion is Brownian, then the back diffusivity for small colloids and macromolecules may be calculated from the Stokes-Einstein Equation (7), as follows:

$$D_S = \frac{\mathrm{K}T}{6\pi\,\mu r_p} \tag{7}$$

where K is Boltzmann constant, *T* is the absolute temperature, r_{p} is the particle radius, and μ is the solution viscosity.

The curvature of the concentration profile depends on the flux and so does the relationship between the mass transfer coefficients [19]. The mass transfer coefficient may be obtained from experiments using Equation (8), which is rearranged from Equation (6) with the assumption that the solute concentration in the permeate is very small compared to that of the feed and that at the membrane surface.

$$J = k_{i,b} \,.\, \ln\left(\frac{C_{i,M}}{C_{i,b}}\right) \tag{8}$$

The mass transfer boundary layer thickness is equal to $D_{ji} / k_{i,b}$. When D_{ji} is small compared to the mass transfer coefficient $k_{i,b}$, the boundary layer is thin, especially for macromolecules. D_{ji} is exceedingly small and the boundary layer is thus very thin [20]. This causes severely localized high solute concentration at the membrane surface, which facilitates fouling.

Furthermore, fouling may be due to adsorption, pore blockage, deposition, and gel layer formation. The adsorption occurs whenever there are interactions between the membrane and the solute or particles. If the degree of adsorption is concentration-dependent, then the CP exacerbates the amount of adsorption creating an extra transport resistance [1]. Notably, the monolayer of particles and solute leads to an additional hydraulic resistance. The membrane surface hydrophilicity is the primary factor affecting particle-to-membrane attachments [21–23]. The deposit of particles can grow thicker by additional layers on top of the membrane's surface, leading to a significant hydraulic resistance, often referred to as a cake resistance. For certain macromolecules, CP may lead to gel formation in the immediate vicinity of the membrane surface. Furthermore, the size of contaminated particles plays a major role in the membrane pore blockage, which leads to a reduction in flux due to the partial closure of pores [5, 6]. In general terms, membrane fouling models are concerned with the non-dissolved materials that are either deposited on the membrane surface, or deposited in the membrane pores.

4. Modeling of porous membrane filtration in the presence of fouling

Membrane fouling provides additional transport resistance during the separation process. As a consequence, permeate flux and TMP are the best indicators of membrane fouling phenomenon [2]. The transport resistance created by the membrane fouling leads to a significant increase in hydraulic resistance, manifested as a permeate flux decline or TMP increase when the process is operated under constant-TMP or constant-flux conditions. The flux through most fouled membranes cannot be described by the idealized equation of Hagen-Poiseuille. It should also be noted that if a solute is present, then there will be CP. The following equation is used to describe the flux in the absence of any fouling cake layer:

$$J = \frac{\Delta p - \Delta \pi}{\mu R_m} \tag{9}$$

where R_m is the empirically measured membrane resistance, Δp is the pressure drop, and $\Delta \pi$ is the osmotic pressure difference between upstream and downstream of the membrane. In general, the driving force ΔP that exists between the bulk feed on one side and the solution on the permeate side will be reduced by the osmotic pressure differences that occurs due to solute rejection. An alternative to Equation (9) can be defined as follows, with R_{cp} as the resistance of the CP layer:

$$J = \frac{\Delta p - \Delta \pi}{\mu \left(R_m + R_{cp} \right)} \tag{10}$$

It was illustrated by Wijmans et al. (1985) that the two expressions are thermodynamically equivalent with the concentration boundary layer impeding the flow of the solvent and thus "consuming" part of the overall driving force [3]. While the value of $\Delta \pi$ can be calculated from equations for osmotic pressure of known concentration solutions, the value of R_{cp} can only be inferred from experimental data. Additional terms can be added to account for the hydraulic resistance that is caused by the material accumulation on the membrane's surface and/or in the membrane's pores, as shown in Equation (11). The pore diffusion transport model (PDTM) developed by Tu et al. (2005) allows to predict the flux decline and provides meaningful insight into the mechanisms affecting it. The model is intrinsically based on the presence of simultaneous fouling, being a joint function of CP, internal pore blocking, and gel or cake formation [19]. Although CP and internal pore fouling are effective factors for membrane fouling at the beginning of the filtration process however, according to PDTM surface fouling is insignificant since no gel layer is formed on the membrane's surface [24, 25]. A short time after the beginning of filtration, a gel layer is formed on the membrane surface due to the accumulation of the contaminated particles. At steady-state, no flux decline takes place due to the presence of a permanent gel layer. Equation (11) illustrates the overall hydraulic resistances, due to membrane fouling:

$$J = \frac{\Delta p - \Delta \pi}{\mu\left(R_m + R_{ads} + R_{irrev}\right)} \tag{11}$$

The first of the additional hydraulic resistances, R_{ads}, is due to surface or pore adsorption that occurs independently of the flux. This resistance R_{ads} is estimated by measuring the permeate flux at a given TMP when the complete fouling occurs, after the estimation of membrane resistance R_m [26]. The increased resistance can be classified into reversible or irreversible based on the attachment strength of particles to the membrane surface. R_{ads} represents the sum of reversible and irreversible fouling. The reversible resistance occurs due to reversible fouling and disappears during the backwash process. On the other hand, the irreversible resistance, R_{irrev}, reflects the irreversible deposition after cleaning process. R_{cp} was insignificant in Equation (11).

When considering these fouling mechanisms, the critical flux, at which fouling is first observed for a given feed concentration and given crossflow velocity, should be a design consideration for all pressure-driven processes [27]. A model of critical flux, J_{cs}, has been developed in order to discriminate the un-fouling conditions (where R_m is the only resistance in Equation (11)) from fouling conditions where other resistances apply and the osmotic pressure is assumed negligible.

$$\text{For} < J_{cs} : J = \frac{\Delta p}{\mu R_m} \tag{12}$$

$$\text{For} > J_{cs} : J = \frac{\Delta p}{\mu\left(R_m + \left(R_{rev} + R_{irrev}\right)\right)} \tag{13}$$

For low J_{cs}, at least one of R_{rev} or R_{irrev} is non-zero and R_{ads} is considered to be negligible. For UF, the flux through the membrane can be described as analogous to that through a MF membrane with allowance for osmotic effects due to CP. The alternative form of the resistance-in-series model is presented in Equation (14).

$$J = \frac{\Delta p}{\mu\left(K_m + K_c + K_p\right)} \tag{14}$$

where K_m, K_c, K_p are the resistance coefficient for membrane, cake layer, and pore constriction, and μ is Dynamic viscosity. The pore constriction resistance coefficient K_p can be negligible for small pore membranes such as NF. The resistance in a series model is a very useful and convenient concept to understand which resistance component is dominant and what should be performed in improving the flux. In bench scale studies, the cake layer resistance coefficient K_c can be calculated using the Kozney equation for flow through a granular medium utilizing monodisperse spherical latex particle [27, 28]:

$$K_c = \frac{36\ K_K\ \delta_c \left(1-\varepsilon\right)^2}{\varepsilon^3 d_p^2} \tag{15}$$

where K_K [dimensionless] is Kozeny coefficient (typically 5), ε [dimensionless] is the cake porosity, δ_c [m] is the thickness of cake layer, and d_p [m] is the diameter of retained particles.

Several filtration models have been developed to describe the dynamics that frame the fouling process at a constant TMP. These models relate the permeate flow (Q), peremrate volume (V), the time (t) with the filtration constants for each model (K_{bc}, K_{ic}, K_{sc}, K_{dc}), and the initial permeate flow (Q_0). The mathematical expressions of these models and their assumptions are shown in Table 1.

Model	Equation	Assumption
Complete blocking filtration	$Q = Q_o - K_{bc} V$	Particles are not superimposed on one another; the blocked surface area is proportional to the permeate volume.
Intermediate blocking filtration	$\frac{1}{Q} = K_{ic} t + \frac{1}{Q_o}$	Particles can overlap each other; not every deposited particle block the pores.
Standard blocking filtration	$Q^{1/2} = Q_o^{1/2} - \left(\frac{K_{sc}\ V\ Q_o^{1/2}}{2}\right)$	Particles are small enough to enter the pores; the decrease of pore volume is proportional to the permeate volume.
Cake filtration	$\frac{1}{Q} = \frac{1}{Q_o} + K_{cc} V$	Particles are big enough to not enter the pores; and therefore forms a cake layer on the surface

Table 1. Constant pressure filtration model

Applications of these models were examined in numerous recent publications [29–33]. Lim investigated the fouling behavior of microfiltration membranes in an activated sludge system [29]. The results show that the main types of membrane fouling in this case were attributed to initial pore blocking (standard blocking filtration model) followed by cake formation (cake filtration model) [29]. Bolton (2006) compared these four models in application to microfiltration and ultrafiltration of biological fluids, the conclusion is the combined cake filtration model and the complete blocking model resulted in the best fit of experimental data [30]. In a cross flow ultrafiltration experiment conducted by Tarabara (2004), cake formation was investigated under variable particle size and solution ionic strength. The results revealed that in all cases, there is a dense layer of the colloidal deposit adjacent to the membrane with an abrupt transition to a much more porous layer near the membrane-suspension interface [31]. This observation implies that different models should be considered at different phases of fouling.

5. Diffusion models in the presence of fouling

There is general consensus among research scholars that the solute mass transfer through RO and NF membranes is controlled by diffusion as a result of the concentration gradient across the membrane surface [34–38]. Researchers have invested extensive efforts in seeking new, comprehensive and accurate diffusion models capable of predicting membrane performance in cases involving membrane fouling. In most cases, the models were derived based on simplifications and assumptions, rendering limitation of the application of the models to practice. However, the diffusion models provide the basis and opportunity for incorporation of more complicated and realistic scenarios. Thus far, there is no universally accepted model for describing diffusion-controlled membrane processes, but understanding the factors affecting membrane mass transfer will certainly help with developing a better predictive model.

5.1. Homogeneous solution diffusion model (HSDM)

The homogeneous solution diffusion model (HSDM) is one of the basic models describing mass transfer as a function of concentration gradient and the pressure difference across the membrane's film. The HSDM assumes a homogeneous feed stream and homogeneous membrane surface that are linearly correlated to the average feed concentration and system recovery [39, 40]. This model is utilized to predict the permeate concentration, with a given solvent and solute mass transfer coefficient (MTC), overall recovery, transmembrane pressure, and feed concentration over a single element. The HSDM final formulation is given in Equation (16) [41, 42]:

$$C_p = \frac{k_s C_f}{F_W\left(\frac{2-2Rc}{2-Rc}\right)+k_S} \tag{16}$$

where C_p is the permeate concentration, Fw is the water permeate flux, C_f is the feed concentration, k_g is solute MTC, and Rc is the overall recovery, which is the ratio of permeate flow rate to feed flow rate. The solute MTCs were found to be related to membrane feed water qualities and membrane properties. They can be theoretically determined using Fick's first law described in Equation (1) assuming a steady state within a thin film.

Duranceau (2011) developed a model correlating the solute MTCs to the solute charge and molecular weight with a normal distribution [41, 42]. Furthermore, Zhao (2005) investigated the influence of membrane surface properties and feed water qualities on solute MTCs. It was found that the MTC increased as the surface roughness and contact angle were increased. Also, the amount of natural organic matter (NOM) in the feed water appeared to positively affect the MTC [35]. The HSDM has been modified to incorporate the osmotic pressure in an integrated incremental model by Zhao [38]. The model considered the osmotic pressure increase as a result of enhanced salt concentration in the membrane channel. Duranceau (2009) has modified the HSDM to predict multi-stage membrane systems [37]. Absar (2010) modified the diffusion model by comparing the effects of co-current and counter-current permeate flow with respect to the feed stream. It was concluded that the counter-current flow pattern, especially during the concentrating process, has a better overall efficiency [43].

5.2. Nonhomogeneous diffusion model development

Previous diffusion models had typically assumed a constant mass transfer rate across a non-porous, smooth, flat membrane surface. Nevertheless, the membrane surface characterization has been shown to affect the membrane's performance, as well as the overall fouling process [32, 33]. Therefore, non-homogeneous mass transfer model introduced an additional variable affecting mass transport that can be quantified by considering the non-uniform structure of the membrane surface. Research conducted by Mendret (2010) demonstrated that random distribution models may be used to effectively describe the heterogeneity of surfaces [28].

The HSDM can be modified by incorporating the effects of a non-uniform membrane surfaces on the solute permeability so as to obtain a non-homogeneous diffusion model. In addition, Sung (1993) has incorporated the film-theory factors accounting for the CP to develop the non-homogeneous diffusion model (NHDM), as presented in Equation (17)[39]. Notably, the k_s' is the back mass transfer coefficient was also incorporated:

$$C_p = \frac{C_f\, k_s'\, e^{F_W/k_s}}{k_W\, \left(\Delta p - \Delta\pi\right)\left(\dfrac{2-2Rc}{2-Rc}\right) + k_s'\, e^{F_W/k}s} \tag{17}$$

where C_p [mg/L] is the solute concentration in the permeate, C_f is the feed concentration, k_s [m/s] is the solute mass transfer coefficient, k_W [m/s.psi] mass transfer coefficient and F_w [gal/sfd] is the solvent permeate flux. k_s is assumed to be related to the membrane surface morphology and therefore a variable parameter. Under laminar flow conditions, the back diffusion coefficient, ks, is related to the cross flow velocity and the geometry of the membrane channel [10]:

$$k_s' = 1.86\left(\frac{D}{d_h}\right)^{0.67}\left(v\right)^{0.33} \tag{18}$$

where k_s' [m/s] is the back diffusion mass transfer coefficient, d_h [m] is the hydraulic diameter of the membrane channel, v [m/s] is the cross flow velocity, and D [m^2/s] is the salt diffusion coefficient. The advantages of the non-homogeneous approach include the model's capacity to predict the hydraulic flow and solute concentration gradient in the bulk flow and on the membrane's surface, with a known solute concentration in the permeate. The overall back mass transfer coefficient was derived from a one-dimensional convective-diffusive mass balance, and was then integrated individually across the cake layer and the salt concentration boundary layer [27], as shown in Equation (19):

$$k_s' = \left[\delta_c \left(\frac{1}{D_s} - \frac{1}{\mathrm{D}\infty} \right) + \frac{1}{k_s} \right]^{-1} \tag{19}$$

where δ_c is cake thickness, D_s is the back diffusivity, D^∞ is bulk diffusivity, and k_s is the solute mass transfer coefficient.

Mendret (2010) developed a model that considered two dimensional flow of a particle suspension in the membrane's channel in order to investigate the growth of a cake on a non-uniform permeability membrane [28]. The overall mass transfer coefficient (k_t) can be determined as below:

$$\frac{e_t}{k_t} = \frac{e_d}{k_d} + \frac{e_m}{k_m} \tag{20}$$

where e_t, e_d, e_m are the total thickness of the porous sub-domain, the deposit thickness, and the membrane thickness, and k_d, k_m are the deposit permeability and the membrane permeability, respectively.

The NHDM and HSDM were verified using pilot plant data from a brackish groundwater plant located in Florida. It was found that the NHDM predictions were in close agreement with actual permeate concentrations. The results likewise indicated that the NHDM provides a more accurate prediction of solute concentration with a high concentration in the feed stream. This can be explained by the role of CP effects on the mass transfer with different feed solute concentration, since the CP appears to be more significant in determining the salt passage in instances when the solute feed concentration is higher. Although it was found that the fouling behavior was related to the degree of surface roughness [2, 44–46], incorporating the surface roughness into the diffusion models and evaluating its impact has not been comprehensively studied yet.

6. Dimensionless mass transfer coefficient models

The mass transfer coefficient (k) is the most widely used parameter when it comes to the design of pressure-driven membrane separation systems. The mass transfer coefficient can be estimated from a dimensionless correlation using the Sherwood number [47]. Most models used in the description of the CP phenomena during cross-flow membrane filtration require the knowledge of mass transfer coefficient [12]. Such an expression of the mass transfer coefficient should be able to represent the effects of changing conditions in the systems that are being used for membrane filtration. The value of the mass transfer coefficient *k* can be calculated using Sherwood relations [47, 48], generally represented as:

$$\mathrm{Sh} = \frac{k\, d_h}{D} = \mathrm{B}\, Re^{q} Sc^{r} \tag{21}$$

where d_h is the hydraulic diameter of the system; *D* is the diffusion coefficient; *Re* is the Reynolds number; S_C is the Schmidt number; and *B*, *q*, and *r* are the adjustable parameters. Usually, the description of the mass transfer coefficient is given for laminar and turbulent conditions separately. In literature, a number of different values for *B*, *q*, and *r* can be found depending on the operating conditions (laminar/turbulent conditions), the value of the Reynolds and Schmidt numbers [12]. The addition of the Sherwood relations to non-Newtonian fluids, as well as the laminar flow case, indicate that choosing a relationship that accurately describes a certain system is very difficult. The major limitations of such Sherwood number relationships include: (1) the failure to take into account the variations of physical properties (e.g., solution density, solute diffusivity, etc.) with concentrations due to concentration polarization; (2) the neglected effects of suction in the presence of a porous membrane; (3) the assumption that the mass transfer boundary layer is fully developed, which may not be the case in most of the conduits during macromolecular ultrafiltration (UF); and (4) the effects of pressure on the mass transfer coefficient, which may be present during ultrafiltration, have not been considered. Numerous Sherwood number relationships have been proposed and extensively reviewed [9]. In these reviews, it was identified that the standard correlations needed to be modified depending on the context of the limitations discussed earlier. In fact, it was suggested that alternative techniques, such as the velocity variation technique or the combined osmotic pressure-film theory model, may be utilized to estimate the mass transfer coefficient. However, both of these techniques have their respective disadvantages. To circumvent this problem a detailed numerical solution based on the governing momentum and solute mass balance equations with pertinent boundary conditions may be used [9]. But this method could appear problematic for design purposes due to certain inherent complexities and rigorous computational requirements. Another alternative approach proposes a second correlation for polarized layer resistance with operating conditions. However, such relationships are solute, system specific, and overall not general enough to encompass a wider variety of solute-membrane systems [3]. In addition, working with two correlations simultaneously increases the range of potential points of uncertainty and inaccuracy during the prediction.

Sirshendu and Bhattacharya [9] proposed new Sherwood number relationships that incorporate the effects of suction of a membrane for laminar flow in rectangular, radial, and tubular geometries. However, in this research study, the variations in physical properties brought about by concentration, and which become dominant under highly polarized conditions in a UF process, were not taken into consideration during the analysis. The large number of experimental variables and corrections that are associated with the mass transfer relations provide a valid reason for directly determining the mass transfer coefficient experimentally [49]. Based on the data already available in the literature, the variables that have the capacity to influence the value of the mass transfer coefficient can be expected to include: the applied transmembrane pressure, the cross-flow velocity, the flux, the type of solute, the hydraulic dimensions of the module, and the characteristics of the membrane [48].

The commonly used Sherwood number correlation is that from Deissler, as shown in Equation (26). For solutes such as BSA and Dextrans (SC= 13,000-22,000), the mass transfer coefficient can be calculated from Harriott and Hamilton's equation [44].

$$1 << Sc << 1000(\text{Deissler});\ \text{Sh} = 0.023\ Re^{0.875} Sc^{0.25} \tag{22}$$

$$\text{Sc} > 1000(\text{Harriott} - \text{ Hamilton});\ \text{Sh} = 0.0096\ Re^{0.91}\ Sc^{0.35} \tag{23}$$

6.1. The velocity variation method

The Sherwood relations for *k*, depending on the cross-flow velocity of the type $k= bv^a$, where "*a*" is about 0.33 for laminar conditions and around 0.75–0.91 for turbulent conditions. Therefore, to obtain the mass transfer coefficient an experimental based model was developed for the retention, as follows:

$$\ln\left[\frac{(1-R_{obs})}{R_{obs}}\right] = \ln\left[\frac{(1-R)}{R}\right] + J\big/(bv^a) \tag{24}$$

where R_{obs} [dimensionless] is the observed retention coefficient and R is the intrinsic retention coefficient. By plotting the experimental values of $\ln\left[\frac{(1-R_{obs})}{R_{obs}}\right]$ as a function of J/v^a, where the value of the exponent *(a)* should be chosen in advance based on the flow regime, the intrinsic retention and the constant *b* can be determined graphically. The relation for the mass transfer coefficient as a function of the various experimental variables can then be obtained by accurately fitting the data found in the different experimental circumstances. A considerable disadvantage of this semi-empirical method is the necessity for an incomplete retention. While in practical circumstances for many solutes the retention is preferably complete and equal one, in this case the retention is relatively low.

The velocity variation method is not absolutely reliable when it comes to determining the mass transfer coefficient, primarily because its sensitivity to the experimental parameter values. The best experimental method for determining the mass transfer coefficient remains that of evaluation of the observed retention at varying velocities. Therefore, the use of normal mass transfer relations can be equally reliable and much easier than the velocity variation method [44]. The velocity variation method can be recommended for practice when one or more of the parameters in the conventional mass transfer coefficient relationships are unknown.

6.2. The modified Sherwood relation

The modified Sherwood number relationships, including the effects of suction during vacuum filtration and variations in properties brought about by concentration, may be a more adequate representation of concentration polarization phenomena during ultrafiltration of macromolecules [44]. Such a relationship is formulated for laminar flow in a rectangular geometry. The developed model is then employed to predict permeate flux of the ultrafiltration process of BSA and dextran. The value of the exponent in Equation (25) is found to be 0.01 for all operating conditions of BSA, and 0.013 for dextran at 5 kgm^{-3} and 0.026 at 10 kg m^{-3}. The present model is able to accommodate incomplete solute retention by the membrane and can be effectively applied during the simultaneous prediction of permeate flux and observed retention.

$$\mathrm{Sh_m} = \mathrm{Sh}\left(\frac{Sc}{Sc_m}\right)^n \tag{25}$$

7. Gas transport through membranes

A number of phenomenological and physiochemical models have been developed for gas transport, each of them suited specifically to particular types of penetrating membrane systems over limited pressure and temperature ranges [12]. Gas transport through membranes has been categorized as transport in homogeneous membranes, porous membranes, asymmetric, and composite membranes. The relationship between the permeation, flux, and operating conditions in general can be described by:

$$J = \frac{\mathrm{P}}{L} \times \left(p_h - p_i\right) \tag{26}$$

where J is permeation flux, p_h is feed side pressure, p_i is permeate side pressure, P is permeability, L is membrane thickness.

The permeability value, P depends on the membrane material type and the variety of operating conditions used. Transport in homogeneous membranes can be assessed using the solution diffusion model (for rubbery polymer), Dual sorption model (for glassy polymer), and Free Volume Theory. The transport in porous membranes can be evaluated using the Pore model. On the other hand, transport in asymmetric and composite membranes, which are membranes that consist of several barrier layers with distinct nature, can be determined using the Resistance model [12]. Unlike asymmetric membranes, the composite membrane has a clear discontinuity at the boundary of two neighboring barrier layers, either in the chemical structure or in the morphology of the material.

The permeation rate, Q_i for a component i through a homogeneous membrane can be written as:

$$Q_i = J_{\mathrm{i}} \times A = \frac{P}{L} \times A \times \left(p_h - p_i\right) = \frac{P}{L} \times A \times \Delta p \tag{27}$$

In this case, the permeation rate, *Qi*, can be calculated as a function of the driving force, which is the pressure difference Δp and R' is the resistance to the flow, as in Equation (28):

$$Qi = \frac{\Delta p}{R'} \tag{28}$$

The resistances in composite membranes are usually connected in a following manner: series, parallel, and two resistance arms. Two resistances are connected in series whenever two layers of membranes are combined in a series, as shown in Figure 3 (a). Two resistances are connected in parallel whenever the material of the membrane is different and connected along the same layer of the membrane's surface, as shown in Figure 3 (b). The parallel combination of two resistance models is used when a homogeneous film of relatively high permeability is laminated on top of the membrane, as shown in Figure 3 (c).

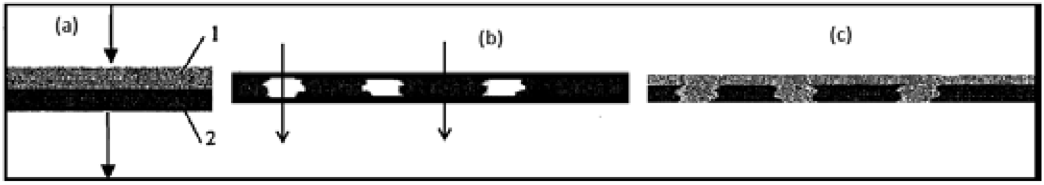

Figure 3. The connection of the transport resistances in composite membranes

The mass transport through a porous layer has been extensively studied. Its specific type depends on the pore size and its comparison to the mean path of the transported molecules. In the case of gas transport, three regions are distinguished regarding the transport [50]: (1) molecular and/or viscous flow, occurring when the mean free path of gas molecules is less than the pore size; (2) Knudsen diffusion, occuring when the pore size is larger than the size of transport species, but less than the mean free path of the gas molecule; and (3) molecular sieving transport (configurational diffusion), which tends to occur when the pore size is the same size as that of the transported species [51].

Molecular diffusion and/or viscous flow are dominated by the interaction between the transported molecules whenever the pore diameter is considerably larger than the mean free path. The viscous flow can be calculated according to Hagen-Poiseuille (Equation (2)), as illustrated in Equation (29):

$$J_i = v \frac{p_i}{\mathrm{R}T} = -\frac{p_i}{\mathrm{R}T} \frac{\varepsilon}{\tau} \frac{d_p^2}{32} \frac{dp}{dy} \tag{29}$$

where p is the total pressure, p_i is the partial pressure and v is the convective velocity of the molecules. When both the molecular and the viscous flows exist, the total mass transfer rate is expressed through the sum of these two flow rates:

$$J_i = -\frac{1}{\mathrm{RT}}\left(\frac{\varepsilon}{\tau}\frac{d_p^2}{32}p_i\frac{dp}{dy} + D_i\frac{dp_i}{dy}\right) \tag{30}$$

After integration, it can be obtained for the mass transfer rate:

$$J_i = \frac{1}{\delta}\left(\frac{\varepsilon}{\tau}\frac{d_p^2}{32}C_t + \frac{D_i}{RT}\right)\left(p_{e,i} - p_{t,i}\right) \tag{31}$$

where subscript e and t denote the feed side and the permeate side, and C_t is the total concentration (kmol/m^3).

In case of Knudsen diffusion, flux can be calculated as follows:

$$J_i = -D_{K,i}\frac{dC_i}{dy} \equiv -\frac{D_{K,i}}{RT}\frac{dp_i}{dy} \tag{32}$$

where J_i is the mass transfer flux (kmol/m^{2}s). The partial pressure gradient, dp_i/dy, is the driving force of the transport. The coefficient of Knudsen diffusion, $D_{K,i}$, can be estimated from [52]:

$$D_{K,i} = \frac{d_p}{3}\frac{\varepsilon}{\tau}\sqrt{\frac{8\mathrm{R}T}{\pi M_i}} \tag{33}$$

where R is the gas constant, M_i is the molecular weight of species i (kg/kmol),and d_p is the pore size (m).

If the pore diameters approach the range comparable to that of the molecule sizes, then the configurational diffusion regime is reached [53]. The corresponding flux density can be described by [54]:

$$J_i = -\frac{1}{RT}\frac{\varepsilon}{\tau}D\frac{dp_i}{dz} \tag{34}$$

$$D = \rho_g d_p\sqrt{\frac{8RT}{\pi M_i}}\,e^{-\left(E_i^c/RT\right)} \tag{35}$$

where D is the diffusion coefficient (m^2/s) and E_i^c is activation energy of diffusion (kJ/kmol). There are no fully-accepted formulas available for the prediction of the diffusivity [53].

In the regions with very small pores compared with the solute molecular size, the effects of the surface diffusion might be significant. The surface diffusion flux can also be critical when it comes to the mass transport through pores in the Knudsen regime due to the adsorption [53, 54]. The most general approach for multicomponent surface diffusion was proposed by Krishna and Wesselingh [55]. Based on the physical picture of molecules moving on the surface, the generalized Maxwell À Stefan equations were applied so as to describe the interactions mechanistically [54, 55].

8. Conclusion

In membrane operations, there are several key issues that influence membrane separation and transport, which in turn affects the performance and the economy of the overall process. Membrane fouling is the major obstacle that inevitably decreases the membrane performance and cause flux decline due to the presence of external and internal membrane fouling. The understanding of causes of flux decline and the ability of predicting the flux performance is essential for more extensive membrane applications. Therefore, this review focused on the analysis of the interrelated dynamics of membrane fouling, flux decline, and mass transport in the filtration/separation process. In addition, this study illustrates that extensive efforts have been undertaken by many researchers to investigate various aspects of these complex phenomena. These studies form the foundation necessary for the alleviation of adverse effect of membrane fouling and emphasize the fact that the development of a complex overlapping approach is needed. Investigations of the mechanisms of mass transfer in high and low pressure membranes, analyses of diffusion mechanisms in membrane pores together with identifications of transport resistances resulting from membrane fouling will allow for a comprehensive understanding and in-depth knowledge of the fouling phenomenon and applicable mass transfer mechanism.

Several mathematical models have been developed over the years in order to describe the solute and solvent mass transport in membrane processes based on a homogeneous membrane surface. In addition, the effect of the morphology of the membrane active layer on solvent and solute mass transport was incorporated. It was determined that solute mass transport is controlled by the non-homogeneous diffusion in the thinner regions of the active layer. This non-uniform surface also affects the concentration polarization layer, where more solutes tend to accumulate on the valleys rather than on the ridges. The NHDM was developed, taking into account the membrane surface property, so as to describe the non-homogeneous phenomenon while accommodating the fact that solute and solvent MTCs vary with active layer thickness. Based on the same conceptual the dynamic model, which is a non-homogeneous diffusion model, was developed with and without the CP effect, and then compared with the HSDM. It was found that the mass transport across the membrane film was affected by the morphology of the membrane surface.

Nomenclature

Symbol	**Physical Meaning**
A	Cross-sectional area to flow [m^2]
B	Constant depending on flow patterns [dimensionless]
C	concentration of diffusing substances [kg/m^3]
$C_{i,\mathrm{M}}$	Concentration of solute *i* at the membrane surface [kg/m^3]
$C_{i,\mathrm{b}}$	Concentration of solute *i* at the bulk [kg/m^3]
$C_{i,\mathrm{p}}$	Concentration of solute *i* at the permeate [kg/m^3]
$\mathrm{C_f}$	Feed concentration [kg/m^3]
D_{ji}	Diffusivity of component *i* [m^2/s]
D_s	Back diffusivity [m^2/s]
D^{∞}	Bulk diffusivity [m^2/s]
d_{pore}	Diameter of the capillaries [m]
d_p	Diameter of retained particles [m]
d_h	Hydraulic diameter of the membrane channel [m]
E_i^c	Activation energy of diffusion [kJ/kmol]
e_t	Total thickness of the porous sub-domain [m]
e_d	Deposit thickness [m]
e_m	Membrane thickness [m]
F_w	Water permeate flux [m^3/m^{2}s]
J	Permeate flux [m^3/m^{2}s]
J_w	Permeate flux of pure water [m^3/m^{2}s]
k_m	Resistance coefficient for membrane
k_c	Resistance coefficient for cake layer
k_p	Resistance coefficient for pore constriction
k_k	Kozeny coefficient (typically 5) [dimensionless]
K	Permeability constant [m^2]
$k_{i,b}$	Mass transfer coefficient [m/s]
k_d	Deposit permeability [m^2]
k_s	Solute mass transfer coefficient [m/s]
k_s'	Back mass transfer coefficient [m/s]
K_{bc}	Filtration constant of complete blocking model [dimensionless]

Symbol	Physical Meaning
K_{ic}	Filtration constant of intermediate blocking model [dimensionless]
K_{sc}	Filtration constant of standard blocking model [dimensionless]
K_{dc}	Filtration constant of cake model [dimensionless]
K	Boltzman constant [dimensionless]
L	Membrane thickness [m]
l_{pore}	Thickness of the porous layer [m]
l_{bl}	Thickness of the mass transfer boundary layer [m]
μ	Dynamic viscosity of the permeate [kg/(m·s) or Pa·s]
ΔP	Pressure drop [psi]
$(P_b - P_a)$	Pressure drop [psi]
P	Permeability [m^2]
Q	Total discharge [m^3/s]
Q_0	Initial permeate flow [m^3/s]
q	Constant depending on flow patterns [dimensionless]
Re	Reynolds number [dimensionless] $\left(\rho v L / \mu \right)$
r	Constant depending on flow patterns [dimensionless]
r_p	Particle radius [m]
R_m	Membrane resistance [m^{-1}]
R_{cp}	Resistance of the concentration polarization layer [m^{-1}]
R_{ads}	Hydraulic resistances, due to surface or pore adsorption [m^{-1}]
R_{irrev}	Irreversible resistance due to irreversible deposition [m^{-1}]
Rc	Overall recovery [%]
R_{obs}	Observed retention coefficient [dimensionless]
R	Intrinsic retention coefficient [dimensionless]
R'	Resistance to flow
R	Gas constant [J/mol. K]
S	Specific area per unit volume [m^2/m^3]
Sc	Schmidt number [dimensionless] $(\mu / \rho L)$
Sh	Sherwood number [dimensionless] $\left(kL / D \right)$
T	Absolute temperature [K]
τ	Tortuosity of the capillaries [dimensionless]
t	Filtration time [seconds]

Symbol	Physical Meaning
V	Permeate volume [m^3]
v	Cross-flow velocity [m/s]
Z	Space coordinate measured normal to the membrane [dimensionless]
$\Delta\pi$	Osmotic pressure [atm]
$\Delta\pi_m{}^*$	Osmotic pressure difference [atm]
ε	Surface porosity [dimensionless]
δ_c	Thickness of cake layer [m]

Author details

Amira Abdelrasoul*, Huu Doan, Ali Lohi and Chil-Hung Cheng

*Address all correspondence to: amira.abdelrasoul@ryerson.ca

Department of Chemical Engineering, Ryerson University, Toronto, Ontario, Canada

References

[1] Gekas V, Hallstrom B. Mass transfer in the membrane concentration polarization layer under turbulent cross flow, Critical literature review and adaptation of existing Sherwood correlations to membrane operations. *J. Membr. Sci.* 1987;80:153–170.

[2] Abdelrasoul A, Doan H, Lohi A. Fouling in membrane filtration and remediation methods. *Mass Transfer - Advances in Sustainable Energy and Environment Oriented Numerical Modeling*, Dr. Hironori Nakajima (Ed.). Intech Open Access Publisher. 2013;195–218.

[3] Wijmans JG, Nakao S, Van Den Berg J, Troelstra FR, Smolders CA. Hydrodynamic resistance of concentration polarization boundary layers in ultrafiltration. *J.Membr. Sci.* 1985;22:117–135.

[4] Vasan SS, Field RW. On maintaining consistency between the film model and the profile of the concentration polarisation layer. *J. Membr. Sci.* 2006;279:434–438.

[5] Abdelrasoul A, Doan H, Lohi A. A mechanistic model for ultrafiltration membrane fouling by latex. *J. Membr. Sci.* 2013;433:88–99.

[6] Abdelrasoul A, Doan H, Lohi A, Cheng CH. Modeling development for ultrafiltration membrane fouling of heterogeneous membranes with non-uniform pore size. *Can. J. Chem. Eng.* 2014;92 (11):1926–1938.

[7] Jennifer A. Model studies of diffusion-controlled (2-hydroxyethyl methacrylate) HEMA hydrogel membranes for controlled release of proteins, State University of New York at Buffalo, 2012;327.

[8] Mirando J, Campos J. Mass transfer in the vicinity of a separation membrane the applicability of the stagnant film theory. *J. Membr. Sci.* 2002;202:137–150.

[9] Sirshendu D, Bhattacharya P. Mass transfer coefficient with suction including property variations in applications of cross-flow ultrafiltration. *Sep. Purif. Technol.* 1999;16:61–73.

[10] Fang Y. Study of the effect of surface morphology on mass transfer and fouling behavior of reverse osmosis and nanofiltration membrane processes, University of Central Florida, Orlando, Florida, 2013.

[11] Lonsdale HK. The growth of membrane and technology. *J. Membr. Sci.* 1982;11:81–181.

[12] Nagy E. *Basic Equations of the Mass Transport through a Membrane Layer*, Elsevier, 2012.

[13] Bird RB, Stewart W, Lightfoot EN. Transport phenomena, John Wiley and Sons, New York, 1960.

[14] Geankoplis CJ. Transport processes and separation process principles, 4th ed. Prentice Hall, New Jersey, 2003.

[15] Goosen M, Sablani S, Al-Maskari S, Al-Belushi R, Wilf M. Effect of feed temperature on permeate flux and mass transfer coefficient in spiral-wound reverse osmosis systems. *Desalination*. 2002;144:367–372.

[16] Duranceau S, Taylor J. Solute charge and molecular weight modeling for predicting of solute MTCs. Proceedings AWWA MTC. Baltimore, MD, 1993.

[17] Merten U. Transport Properties of Osmotic Membranes, *Desalination by Reverse Osmosis,* U.

[18] Merten, ed., pp. 15–54, MIT Press, Cambridge, Mass. 1966.

[19] Morineau-Thomas O, Jaouen P, Legentilhomme P. Modeling of fouling in three ultrafiltration cell configurations: Swirl, plane and axial annular. *Chem. Eng. Technol.* 2001;24:1521–4125.

[20] Tu SC, Ravindran V, Pirbazari M. A pore diffusion transport model for forecasting the performance of membrane processes. *J. Membr. Sci.* 2005;265 29–50.

[21] Coskun A, Yasemin K, Zeren B, Vergili I. Evaluation of membrane fouling and flux decline related with mass transport in nanofiltration of tartrazine solution. *J. Chem. Technol. Biotechnol.* 2010;85:1229–1240.

[22] Abdelrasoul A, Doan H, Lohi A, Cheng CH. Modeling of fouling and foulant attachments on heterogeneous membranes in ultrafiltration of latex solution. *Sep. Purif. Technol.* 2014;135:199–210.

[23] Abdelrasoul A, Doan H, Lohi A, Cheng CH. Modeling of fouling and fouling attachments as a function of the zeta potential of heterogeneous membranes surfaces in ultrafiltration of latex solution. *Ind.& Eng. Chem. Res.* 2014;53: 9897−9908.

[24] Benitez F, Acero J, Leal A, Gonzalez M. The use of ultrafiltration and nanofiltration membranes for the purification of cork processing wastewater. *J. Hazard. Mater.* 2009;162:1438–1445.

[25] Field RW, Wu D, Howell J, Gupta B. Critical flux concept for microfiltration fouling. *J. Membr. Sci.* 1995;100:259–272.

[26] Bacchin P, Aimar P, Field R. Critical and sustainable fluxes fundamentals of fouling review: Theory, experiments and applications. *J. Membr. Sci.* 2006;281:42–69.

[27] Zhao Y, Taylor J. Assessment of ASTM D4516 for evaluation of reverse osmosis membrane performance. *Desalination.* 2005;180:231-244.

[28] Mohammadi T, Kazeminoghadam M, Saadabadi M. Modeling of membrane fouling and flux decline in reverse osmosis during separation of oil in water emulsions. *Desalination.* 2003;157:369–375.

[29] Mendret J, Guigui C, Cabassud C. Numerical investigation of the effect of non-uniform membrane permeability on the deposit formation and filtration process. *Desalination*. 2010;263:122–132.

[30] Lim A, Bai R. Membrane fouling and cleaning in microfiltration of activated sludge wastewater. *J. Membr. Sci.* 2003;216:279–290.

[31] Bolton G, LaCasse D, Kuriyel R. Combined models of membranes fouling: Development and application to microfiltration and ultrafiltration of biological fluids. *J. Membr. Sci.* 2006;277(1–4):75–84.

[32] Tarabara V, Koyuncu I, Wiesner M. Effect of hydrodynamics and solution ionic strength on permeate flux in cross-flow filtration: Direct experimental observation of filter cake cross-sections. *J. Membr. Sci.* 2004;241(1):65–78.

[33] Sioutopoulos S, Yiantsios DG, Karabelas AJ. Relation between fouling characteristics of RO and UF membranes in experiments with colloidal organic and inorganic species. *J. Membr. Sci.* 2010;350:62–82.

[34] Belfort G, Davis R, Zydney A. The behavior of suspensions and macromolecular solutions in crossflow microfiltration. *J. Membr. Sci.* 1994;96(28):1–58.

[35] ZhaoY, Taylor J. Combined influence of membrane surface properties and feed water qualities on RO/NF mass transfer, a pilot study. *Water Res.* 2005;39:1233–1244.

[36] ZhaoY, Taylor J. Incorporation of osmostic pressure in an integrated incremental model for predicting RO or NF permeate concentration. *Desalination.* 2005;174:145–159.

[37] Jamal K, Khan MA, Kamil M. Mathematical modelin of reverse osmosis system. *Desalination.* 2004;160:29–42.

[38] Duranceau S. Modeling the permeate transient response to perturbation from steady state in a nanofiltration process. *Desalin. Water Treat.* 2009;1:7–16.

[39] Zhao Y, Taylor JS, Chellam S. Predicting RO/NF water quality by modified solution diffusion model and artificial neural networks. *J. Membr. Sci.* 2005;263:38–46.

[40] Sung LK. *Film-theory and ion coupling models for diffusion controlled membrane processes*. Ph.D dissertation: University of Central Florida, 1993.

[41] Taylor J, Jacob EP. *Reverse osmosis and nanofiltration in water treatment membrane Processes*, McGraw-Hill, 1996, Chapter 9.

[42] Duranceau S, Taylor JS. Membranes. In J. Edzwald, Water Quality and Treatment. Denver, Colorado: American Water Works Association, 2011, Chapter 11, 11.4–11.9.

[43] Duranceau S. *Modeling of mass transfer and synthetic organic compound removal in a membrane softening process*. Ph.D dissertation: University of Central Florida, 1990.

[44] Absar B, Belhamiti O. Reverse osmosis modeling with orthogonal collocation of finite element method. *Desalin. Water Treat.* 2010;21:23–32.

[45] Boussu K, Brlpaire A, Volodin A, Haesendonck C, Van der Meeren P, Vandecasteele C. Influence of membrane and colloid characteristics on fouling of nanofiltration membranes. *J. Membr. Sci.* 2007;289:220–230.

[46] Norberg D, Hong S, Taylor J, Zhao Y. Surface characterization and performance evaluation of commercial fouling resistant low-pressure RO membranes. *Desalination.* 2007;2002:45–52.

[47] Warsinger DM, Swaminathan J, Guillen-Burrieza E, Arafat HA, Lienhard JH. Scaling and fouling in membrane distillation for desalination applications: A review. *Desalination.* 2014;356:1–20.

[48] Sherwood TK, Brian P, Fisher R, Dresner L. Salt concentration at phase boundaries in desalination by reverse osmosis. *Ind. & Eng. Chem. Fundamentals*. 1965;4:113–118.

[49] Crittenden JC, Trussell R, Hand DW. *Water Treatment Principles and Design*. New Jersey: Jonh Wiley & Sons. Inc, 2012.

[50] Berg GB, Racz IG, Smolders CA. Mass Transfer Coefficients in cross flow ultrafiltration. *J. Membr. Sci.* 1989;47:25–51.

[51] Seidel-Morgenstern A. *Membrane Reactors*. Wiley-VCH, Weinheim, 2010.

[52] Lawson KW, Lloyd DR. Membrane distillation: Review. *J. Membr. Sci.* 1997;124:1–25.

[53] Mason EA, Malinauskas AP. *Gas Transport in Porous Media: The Dusty Gas Model*. Elsevier, Amsterdam, 1983.

[54] Thomas S, Schafer R, Caro J, Seidel-Morgenstern A. Investigation of mass transfer through inorganic membrane with several layers. *Catalysis Today.* 2001;67:205–216.

[55] Tuchlenski A, Uchytil P, Seidel-Morgenstern A. An experimental study of combined gas phase and surface diffusion in porous glass. *J. Membr. Sci.* 2001;140:165–184.

[56] Krishna R, Wesselingh JA. The Maxwell-Stefan approach to mass transfer. Chem. Eng. Sci. 1997;52:861–911.

Chapter 3

Computational Fluid Dynamics Method for the Analysis of the Hydrodynamic Performance in Swimming

Ahlem Arfaoui and Guillaume Polidori

Additional information is available at the end of the chapter

http://dx.doi.org/10.5772/61176

Abstract

Numerical simulations of the flow around a swimmer during the different swimming phases were carried out to understand the drag force. In mechanics of swimming, the reduction of forces, which oppose to the swimmers advancement, plays a very important part in the improvement of the performances. As a consequence, the performance improvement requires a better understanding of the structure of the fluid flow around swimmers and a good knowledge of the pressure fields and wall shear stress encountered to minimize them. This chapter will focus on computational fluid dynamics (CFD) procedures and results for this practical implication in swimming and will aim at highlighting details on numerical schemes, validations, and results showing the way CFD can be used as a powerful tool in swimming understanding.

Keywords: CFD, swimming, standard *kk*–*ωω* turbulence model, underwater surface patterns, head positions

1. Introduction

In the mechanics of swimming, the study of the flow features around the swimmer during the different swimming phases is of great importance. The hydrodynamic performance in swimming depends strongly on the technique adopted by the swimmers during the different phases of swimming as well as on the resistance of advancement encountered during their movements in water. Three drag forces are noted when the swimmer advances in water, namely, friction drag due to the viscosity of water, pressure drag due to the complex shape of the human body, and wave drag created at the surface of the water. The performance improvement requires a better understanding of the structure of the fluid flow around swimmers and a good knowledge of the pressure fields and wall shear stress encountered to minimize them.

In literature, research in swimming was poor until 1970. Some authors measured the total drag on the swimmer's whole body and estimated the influence of various parameters such as the morphology of swimmer, the position of swimmer, or the velocity on the level of the drag and on analysis of performance. In the quest for higher levels of performance in swimming, many research strategies have been adopted to reduce drag to optimize and coordinate the different movements. Due to the complexity in the use of different experimental measurement techniques, researchers are oriented toward the numerical simulation using computational fluid dynamics (CFD) method. The CFD method is increasingly used in the domain of biomechanics notably to study the flow around a different parts of swimmer's body.

In swimming, the first study that used the CFD method on a real model is that of Bixler and Riewald [1]. They have used CFD to approach the flow around the hand and forearm of a swimmer. The numerical modeling was to calculate the forces and hydrodynamic coefficients for different angles of attack. In same time, the flow around the hand and forearm was also studied by Sato and Hino [2] using the CFD. The purpose of their work was to establish a method to predict the thrust force and optimize the movement of the swimmer while swimming.

In 2006, Rouboa et al. [3] used CFD in order to calculate the drag and lift coefficients for the hand and forearm of a swimmer in steady and unsteady cases, as well as to assess the effect of accelerating the hand and forearm on generating the propulsion force. The model of the hand and forearm used in the numerical simulation was built using a CAD (Computer Aided Design) based on the dimensions of a model of the hand and forearm of a male subject. Since then, the CFD method has been used by several authors in the swimming field.

This chapter will focus on CFD procedures and results for this practical implication in swimming and will aim at highlighting details on numerical schemes, validations, and results showing the way CFD can be used as a powerful tool in swimming understanding.

2. Mathematical modeling

When an elongated element is studied such as a swimmer for example, the flow around this element becomes unstable and turbulent. This instability occurs when Re is about 5×10^5 for streamlined bodies. Therefore, the turbulent fluid flow is controlled by the Reynolds averaged Navier–Stokes equations. These equations are obtained by decomposing each instantaneous variable (velocity, pressure, etc.) into a mean component and a fluctuating component, and by time averaging the instantaneous governing equations. This method is based on the spatial integration of the conservation equations over finite control volumes.

The way to choose the turbulence model is of great importance to highlight vortex structures and recirculation zones in the vicinity of the swimmer's body.

2.1. Governing equations

In fluid mechanics, one of the fundamental parameters used when a fluid is in relative motion to a surface is the Reynolds number (Re), including the fluid properties of density and viscosity, plus a velocity and a characteristic dimension:

$$R_e = \frac{inertialforces}{viscousforces} = \frac{\rho \mathbf{v} L}{\mu} = \frac{\mathbf{v} L}{\nu}$$

where **v** is the mean velocity of the object relative to the fluid (SI units: m/s), L is a characteristic linear dimension (m), and ν is the kinematic viscosity (m^2/s).

The resulting system of equations to be solved for this two-dimensional incompressible flow in steady-state regime is as follows:

Continuity equation:

$$\frac{\partial}{\partial x_i}(\overline{U_i}) = 0 \tag{1}$$

Navier–Stokes (momentum) equations:

$$\frac{\partial}{\partial x_j}(\rho\, \bar{U}_i\, \bar{U}_j) = -\frac{\partial \bar{p}}{\partial x_i} + \frac{\partial}{\partial x_j}\left[\mu\left(\frac{\partial \bar{U}_i}{\partial x_j} + \frac{\partial \bar{U}_j}{\partial x_i}\right) - \rho\, \overline{u_i\, u_j}\right] \tag{2}$$

Boussinesq hypothesis:

$$-\rho\, \overline{u_i\, u_j} = \mu_t \left(\frac{\partial \bar{U}_i}{\partial x_j} + \frac{\partial \overline{U_j}}{\partial x_i}\right) - \frac{2}{3}\delta_{ij} \rho\, k \tag{3}$$

where $U_i(t) \equiv U_i = \overline{U_i} + u_i$: instantaneous velocity component in the i direction (m/s); $\overline{\boldsymbol{U}}_i$: mean (time-averaged) velocity component in the i direction (m/s); u_i: fluctuating velocity component in the i direction (m/s); i, j: directions; μ_t: turbulent viscosity (kg/ms); and ρ: fluid density (kg/m^3)

A new term, $-\rho\overline{u_i u_j}$, due to the correlation between the fluctuations of the velocity components appears in the time-averaged governing equations. This term, also called Reynolds stresses, is problematic as the number of unknowns becomes greater than the number of equations. The aim of the various turbulence models proposed in the literature is to model the Reynolds stresses in order to close the system of equations to be solved. The Boussinesq hypothesis can be used to approach the Reynolds stresses [4]. This hypothesis consists in directly linking the correlations with the time-averaged velocity components by the introduction of the concept of turbulent viscosity (μ_t). The turbulent viscosity is not a property of the fluid itself but depends on the dynamic characteristics of the turbulent flow. Modeling the turbulent viscosity from the time-averaged dynamical characteristics of the turbulent flow is the aim of first-order turbulence models that are presented in the next subsection.

2.2. Turbulence models

The choice of the turbulence model largely depends on its ability to represent correctly the different physical phenomena governing the flow. First-order turbulence models, based on the introduction of a turbulent viscosity, are widely used. The closure of the problem is then obtained by using 0, 1, or 2 additional transport equations. In the following subsections, five first-order turbulence models that will be used to simulate the flow around the swimmer are briefly described with their respective advantages and drawbacks. All these models are implemented in the fluent CFD code used to carry out the numerical simulations of this study.

2.2.1. Standard kk–εε model

The standard *k*–*ε* model is the most known of the turbulence models presented in this paper. It is widely used as it offers a good compromise between the numerical effort (CPU time) and the accuracy of the solution. This is a semiempirical model that was first proposed by Launder and Spalding [5]. This model needs to solve two additional transport equations in order to determine the turbulent viscosity. These two additional transport equations concern the turbulent kinetic energy (*k*) and its dissipation rate (*ε*) and are written as follows (Equations 4 and 5):

Standard *k*–*ε* equations:

$$\overline{U_i}\frac{\partial k}{\partial x_i} = \frac{1}{\rho}\frac{\partial}{\partial x_i}\left(\frac{\mu_t}{\sigma_k}\frac{\partial k}{\partial x_i}\right) + P_k - \varepsilon \tag{4}$$

$$\overline{U_i}\frac{\partial \varepsilon}{\partial x_i} = \frac{1}{\rho}\frac{\partial}{\partial x_i}\left(\frac{\mu_t}{\sigma_\varepsilon}\frac{\partial \varepsilon}{\partial x_i}\right) + c_1\frac{\varepsilon}{k}P_k - c_2\frac{\varepsilon^2}{k} \tag{5}$$

with $P_k = \frac{\mu_t}{\rho}\left(\frac{\partial \overline{U_i}}{\partial x_j} + \frac{\partial \overline{U_j}}{\partial x_i}\right)\frac{\partial \overline{U_i}}{\partial x_j}$

The turbulent viscosity is calculated by using the following relationship (Equation 6):

$$\mu_t = \rho c_\mu \frac{k^2}{\varepsilon} \tag{6}$$

where C_μ is a constant.

The constants of the standard *k*–*ω* model have been determined from numerous experiments. Their values are summarized in Table 1.

c_μ	c_1	c_2	σ_k	σ_ε
0,09	1,44	1,92	1,0	1,3

Table 1. Constants of the standard k-ε turbulence model

From now on, the standard k–ε model is nearly the only model that was used during CFD simulations of flows in human swimming [1, 3, 6]. Nevertheless, this model presents some weak points such as the simulation of curved boundary layers or vortical flows. Recirculations can hardly be found by this model.

Furthermore, turbulent flows are significantly affected by the presence of a wall (the body surface in the case of a swimmer) where the molecular viscosity plays an important role. Indeed, velocity fluctuations are notably reduced by the effect of the viscosity in the near-wall region, while the standard k–ε model assumes a fully turbulent flow in the whole fluid domain. As a result, a specific treatment of the near-wall region is required to account for the turbulence modifications in the near-wall region when using the standard k–ε model. In the present study, this was done by using the "nonequilibrium wall function."

The above-mentioned limitations of the standard k–ε model are first indications that this model may not be the most appropriate to predict the flow structure around the swimmer. This is the reason why four other first-order turbulence models in order to determine the most suitable model for such a problem can be tested.

2.2.2. RNG k–ε model

This model was derived from the unsteady Navier–Stokes equations by using a statistical mathematical method called "ReNormalization Group" [7]. A new term is added in the dissipation rate (ε) transport equation. In this model, an effective turbulent viscosity is introduced that varies with the effective Reynolds number. The RNG model is similar to the standard model. For high Reynolds numbers, the effective turbulence equation is the same as with the standard k–ε model. However, the additional term carries out a significant improvement in the accuracy of the simulations of flows with abrupt changes of direction or with strong shearing. Furthermore, it allows a better modeling for low Reynolds numbers and near the wall (or body), while the standard k–ε model is more suited to high Reynolds number flows.

2.2.3. Realizable k2.2.3 Realizable k–ε model

The word "realizable" means that this model satisfies some mathematical criteria concerning the Reynolds stresses, logical with the physics of turbulent flows [8]. In this model, the kinetic energy equation is the same as in the standard model, except for the constants, whereas the dissipation rate equation differs. The turbulent viscosity is determined by using the same formula as with the standard model, but the coefficient C_μ is no longer constant and depends on the flow characteristics. This model provides better performances in the case of flow simulations with boundary layers under strong adverse pressure gradients, reticulating zones or separating boundary layers.

2.2.4. Standard k–ω model

This is a model based on two additional transport equations like the standard k–ε model: one for the kinetic energy (k) and the other for the specific dissipation rate (ω) of the turbulence [9].

As previously mentioned, the dissipation rate (ε) is difficult to specify near the wall. Therefore, in order to overcome this difficulty, one may solve the transport equation of another quantity such as ω. The standard k–ω model is well suited to wall-bounded flows and free shear flows.

2.2.5. Spalart–Allmaras model

This model was proposed by Spalart and Allmaras [10]. Unlike the other turbulence models, which express the turbulent viscosity as a secondary unknown, only one transport equation is solved directly and takes into account the effect of the wall in order to determine the turbulent viscosity. This model was specifically designed for applications implying flows limited by walls. This model is well suited for boundary layers subjected to adverse pressure gradients.

2.2.6. Criterion for choosing a turbulence model

The aim of the present section is to specify which turbulence model is the most appropriate for the numerical study of the flow around a swimmer during underwater swimming. The influence of the choice of the turbulence model on the results of the numerical simulations will be examined. Numerical simulations of the flow around the swimmer have been carried out by using the five different turbulence models described in Section 2. The numerical parameters are the same as those used in a previous study [4] except for the meshing. The meshing was refined in the vicinity of the swimmer in order to better visualize the vortical structures developing along the swimmer's body.

One of the criteria used is the numerical simulation of hydrodynamic special areas where vertical structures occur. The reference used comes from experimental visualizations obtained by the tuft method, showing the location of where separation and reattachment of main vortices appears (Figure 1).

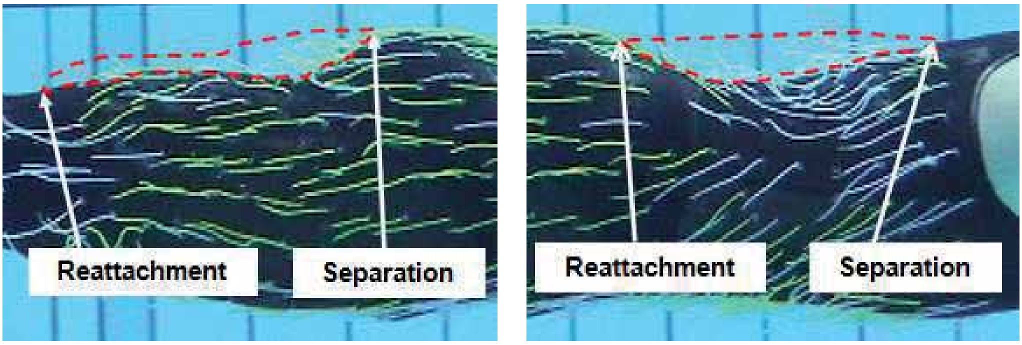

(a) Vortical structure (separation) at the buttocks level.

(b) Vortical structure (separation) at the back level.

Figure 1. Experimental visualizations of vortical structures at the back and buttocks levels during underwater swimming. Swimmer's speed: U_O=2.2 m/s.

Numerical streamline patterns of the resulting flows around the swimmer's head and body are plotted in Figure 2. One may note that all the turbulence models are able to catch three vortical regions around the swimmer's head. Two main large-scale vortices are observed on both sides of the head, especially in the neck and nape regions. One may clearly observe a separation of the flow at the back of the head with its reattachment on the upper part of the back as well as another flow separation starting at the tip of the nose with its reattachment on the breast. A secondary small-scale vortex acting like a junction vortex is present at the arm/head corner, whatever the model used. The presence of this particular vortex is obviously not physically correct; it is only a consequence of the 2D modeling, which considers the arm as a direct extension of the head.

These three regions are very similar in shape and size for the five turbulence models. As a result, it may be concluded that the study of the flow structure around the sole head is not sufficient to assess the efficiency of the turbulence models. Indeed, the locations where flow separations and reattachments occur are imposed by the shape of the head. The similar behaviors noticed around the head for all turbulence models are no longer observed along the body, especially in the back and the buttocks regions. In these regions, one may note large discrepancies among the numerical results obtained with the different turbulence models.

As can be seen in Figure 2, the standard k–ε model provides streamline patterns, indicating a flow that follows closely the shape of the body. No boundary-layer separation and, consequently, no vortical structure are obtained along the swimmer's body. This is in contradiction with the experimental observations given in Figure 1. The vortical structure in the buttocks region has been captured by the four other turbulence models, namely, the RNG model, the realizable k–ε model, the Spalart–Allmaras (SA) model, and the standard k–ω model. However, we may observe that the separation zone behind the buttocks varies as a function of the turbulence model. Three of these models (RNG, realizable, and SA) indicate a smaller separation zone than that visualized during the experiments. As concerns the standard k–ω model, the size of the separation zone at the buttocks level corresponds approximately to that observed experimentally. The locations of the flow separation and of the flow reattachment are very close.

In the back region, turbulence models have more difficulties to find the vortical structures observed experimentally. The standard k–ω is the sole turbulence model that is really able to catch such a structure. The SA model provides only a tiny recirculation zone whereas the two other models (RNG and realizable) are unable to catch any structure in that region. However, the separation zone captured by the k–ω model in the back region remains underestimated by the numerical simulation.

In continuity, Arfaoui et al. [11] have compared the CFD simulations using the standard k–ω turbulence model with the results of experiments by investigating the characteristics of the flow around a female swimmer. The experimental protocol has been performed in the swimming pools of the National Institute of Sports and Physical Education in Paris. Flow visualizations were performed by using the tufts method. The tufts were fixed directly to the swimsuit, and their length was chosen (0.08 m) to highlight the structure of the flow around the swimmer's body and to respond promptly to changes in the direction of the flow with a specific gravity equal to that of the water ensuring neutral buoyancy. Numerical streamlines reveal that complex turbulent zones were generated, particularly in the regions with sudden changes in the body shape such as head, shoulders, and buttocks. The results of these experiments confirmed the 3D numerical simulations using the standard k–ω turbulence model in CFD.

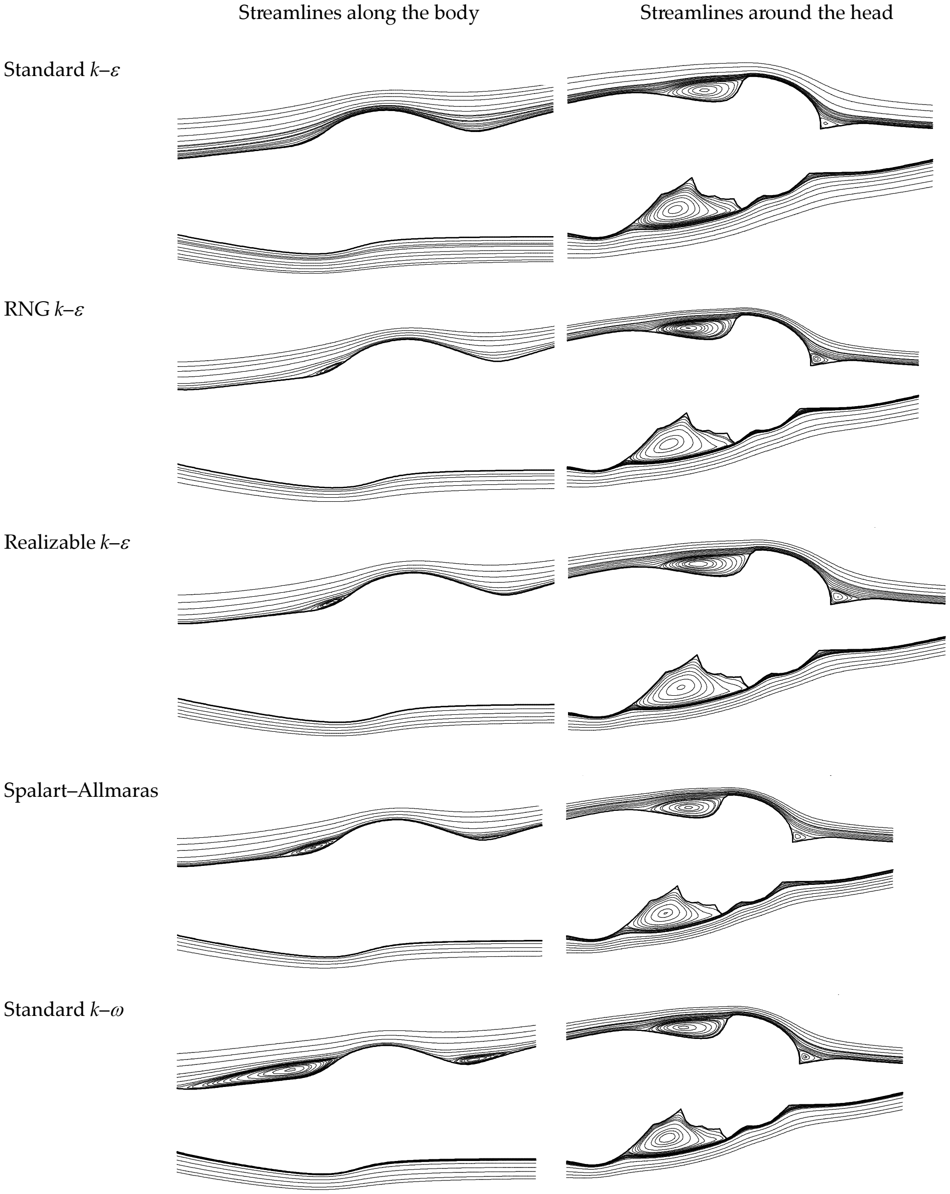

Figure 2. Streamline patterns around the swimmer's body. Swimmer's speed: $U_O = 2.2$ m/s.

3. Numerical approach

3.1. Construction of the swimmer's geometry

Realistic models of swimmers are required for finely studying the vortex flow around body. For this reason, the construction of the 3D geometric model must be meticulous. The first numerical work dedicated to 3D geometry was directed by Lyttle and Keys [12]. The objective was to prescribe the elite swimmers a stroke technique optimally feet starting phase "casting" and phase back after the turn to improve the thrust. To do this, they have chosen a high-level swimmer as a model for this study. Building the model of the swimmer has been performed using a 3D scanner "WBX Cyberware" high resolution, and the geometry has been constructed at once to a position corresponding to the sliding stage with a shaped body and arms outstretched.

In 2010, Zaïdi et al. [13] studied a national-level female swimmer model for their numerical simulation. The construction of the 3D geometric was conducted by a Konica Minoltas scanner (Figure 3).

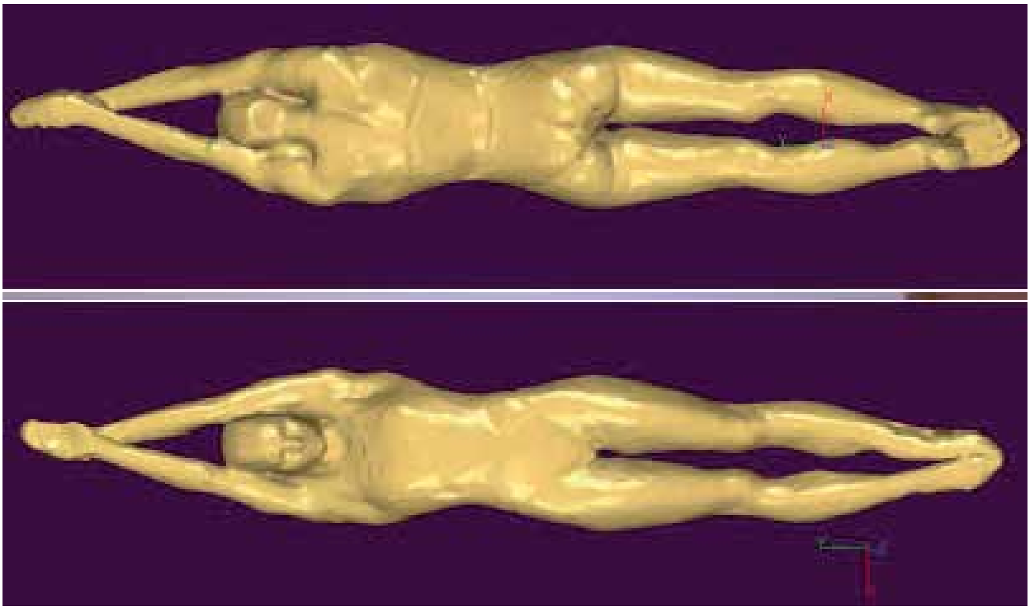

Figure 3. Geometry of the female swimmer obtained from a laser scan.

3.2. Construction of the fluid domain around the swimmer

After constructing the swimmer's geometry, the next stage consists in building the fluid domain around the swimmer. The dimensions of the fluid field around the swimmer are chosen so as to ensure the independence of the numerical results. In numerical simulation, the choice of the size of the computational domain plays an important role on the fidelity of numerical results. It must be large enough to overcome the influence of the boundaries of the fluid field on the flow. If the swimmer is placed very close to the entrance, it disturbs the flow and imposes a speed profile unreal to the surface of the swimmer. If it is placed very close to the exit, it prevents the establishment of the flow and deteriorates the performance. Numerical simulations on areas of different sizes have been carried out in order to specify the size of the fluid domain necessary to ensure the independence of the numerical results.

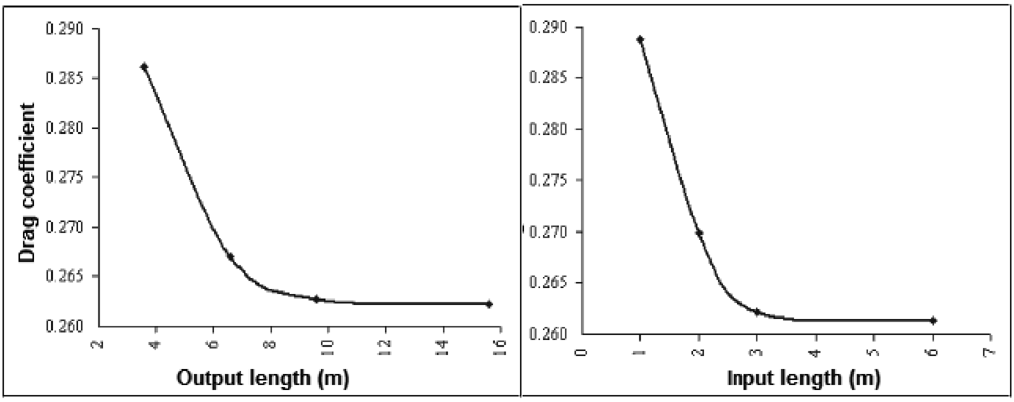

Figure 4. Front and back of the swimmer geometry obtained from a laser scan of the athlete.

In order to ensure the independence of the results from the output and the output length, Zaidi et al. (2008) varied the input and output lengths to avoid their effects on the independence of the numerical results, and they have carried out simulations for such various lengths. They have shown that the drag coefficient becomes stable from 3.0 m of the inlet and one of a distance of 9.6 m from the outlet (Figure 4).

3.3. Grid of the fluid domain

In numerical modeling, the grid of the area plays a leading role on the reliability of the results. The choice of this meshing depends on the expected accuracy of the calculation and the available computing resources. Using a coarse mesh gives erroneous results, while a fine meshing increases the computing time and requires a lot of storage capacity when processing results. The purpose is to find a mesh that occupies less space and time and provides independent results. To assess the influence of the fineness of the mesh on the results, calculation series were conducted to mesh sizes. All tested meshes are progressive, that is to say refined near the surface of the swimmer and released away from the latter. In the study by Zaidi et al. [13], the mesh of the fluid was realized by TGrids software. The mesh was refined near the swimmer and less refined elsewhere so to reduce the computational time.

Figure 5 shows the surface meshing of the swimmer's body and a cross section of the fluid around the swimmer. When a nonstructured grid is used, the flow is not lined up with the grid cells.

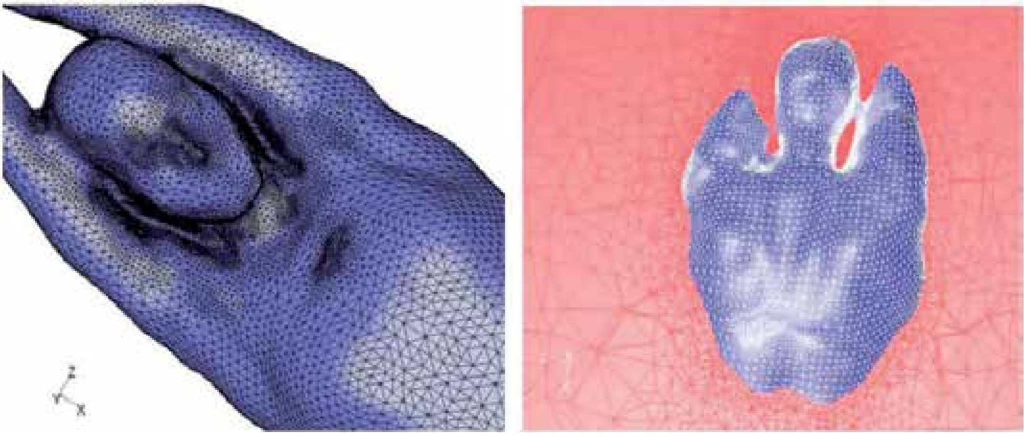

Figure 5. Body surface grid (left) and view of the fluid progressive grid in a plane around the swimmer's body (right).

3.4. Boundary conditions

Once the geometry and meshing defined, it is necessary to choose the geometric areas on which one may apply the boundary conditions used in the numerical simulation. The choice of boundary conditions corresponds to the real problematic. Indeed, special attention should be turned toward the understanding of swimmer's movement in the water.

Popa et al. [14] studied the flow dynamics around a competitive swimmer during underwater glide phases occurring at the start and at turns. The problem is considered as 3D and in steady hydrodynamic state. Three velocities (1.4 m/s, 2.2 m/s, and 3.1 m/s) that correspond to interregional, national, and international swimming levels were studied (Figure 6). The boundary conditions used for the numerical simulations In the study of Popa et al. are :

- At the entrance of the fluid domain: They chose a uniform velocity profile.
- At the exit of the fluid area: They chose mass conservation law.
- On left, right, upper and lower limits of the fluid domain: They chose the condition of symmetry is imposed. Symmetry boundary conditions are used to model zero-shear slip walls in viscous flows and to avoid the boundary layers that develop on the walls of the domain and which are not real.
- On the surface of the swimmer: The no-slip condition is used.

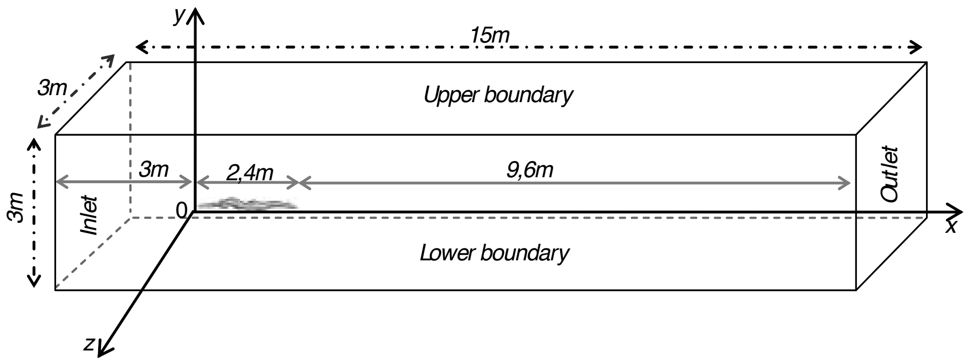

Figure 6. View of the external boundaries of the fluid area around the swimmer.

4. Hydrodynamic drag forces

Numerical simulations of the flow around a swimmer during the different swimming phases were carried out to understand the drag force. In mechanics of swimming, the reduction of drag forces opposed to the swimmers movement plays an important role in the improvement of the performances. For this reason, optimization of the position and movement of the swimmer is necessary in order to determine the optimal parameters that correspond to the minimal drag forces. The total resistance, also called total drag, is composed by three main components:

- Viscous drag or friction due to the viscosity of the fluid medium pressure
- Pressure drag, mainly due to the complex shape of the human body
- Wave drag caused by the wave field that accompanies the moving body and extending gradually over a considerable area of the free surface [15–18].

The pressure drag and the viscous drag depend on the Reynolds number.

In fluid dynamics, the drag equation is as follows:

$$F_D = \frac{1}{2}\rho u^2 C_D A \tag{7}$$

where F_D is the drag force: force component in the direction of the flow velocity; ρ is the mass density of the fluid; u is the flow velocity relative to the object; C_D is the drag coefficient—a dimensionless coefficient related to the object's geometry; and A is the reference area.

The reference area A is typically defined as the area of the orthographic projection of the swimmer on a plane perpendicular to the direction of motion.

Rouboa et al. [3] used a turbulent model to calculate the drag and lift coefficients of the hand/forearm both under steady and unsteady flow conditions. They determined the effect of the acceleration of the hand/forearm on the generation of the propulsive force. Sato and Hino [2] carried out unsteady CFD simulations in order to consider the effects of acceleration and transient motions of the hand in predicting swimmer's thrust. Gardano and Dabnichki [6] estimated the hydrodynamic drag and lift forces. Their work constituted an important projection toward the use of CFD in the simulation of swimming in unsteady regime.

The contribution of these three drag forces in swimming varies depending on both swimming speed and depth. According to Rushall et al. [17], a doubling of swimming speed increases twice the friction drag, four times the drag, and eight times the wave drag. Toussaint et al. (2002) assumed that for a swimming speed of 1 m/s, contributions of the three drag components in the total drag are 3% for the friction drag, 95% for the form drag, and 2% for the wave drag. These values respectively become 3%, 77%, and 20% at a speed of 2 m/s. They also indicate that the contribution of the friction drag does not exceed 5% of the total drag. An increased wave drag increases the form drag, while the friction drag is considered independent of the first two. The two streaks of form and wave are dependent. Increasing wave drag increases the form drag, while the friction drag is considered independent of the drag of form and wave.

In order to analyze the effect of the position of the swimmer's head on the hydrodynamic performances in swimming and in evolution of drag, Zaïdi et al. [4, 19] neglected wave drag because the underwater glide phases occurring at the start and at turns were placed away from the free surface (the swimmer is placed at a depth of 1.5 m) [16, 20].

Figure 7 shows the variation of the pressure, viscous, and total drag forces calculated for the three head positions and for velocities ranging between 1.4 and 3.1 m/s. One may observe that the position of the head aligned with the body (position 2) is the one that offers less resistance. In the case of position 2 and for a speed of 3.1 m/s, the viscous drag accounts for 20% whereas the form drag accounts for 80% of the total drag.

The curves show that a change in the head position induces an important modification of the total drag in the velocity range of 1.4 to 3.1 m/s. The total drag vary from 4% according to the head position and this whatever the speed of the swimmer. This difference in drag is very important in high-level competition.

4.1. 2D versus 3D modeling

In complex problem of fluid dynamics where complex phenomena occur, many restrictions were noted in the use of 2D modeling. The 2D study is insufficient and the 3D study seems inevitable to be able to model vortex structures and separation areas.

Figure 8 shows comparison between the numerical results of a 3D study with the k–ω model and the 2D study carried out by Zaïdi et al. [4, 19] using both the k–ε and the k–ω turbulence models. On the same Figure 8, the 3D experimental results obtained by Bixler et al. [21] and Vennell et al. [16] are also presented. The 2D study appears to be limited as it does not enable to evaluate correctly the drag forces, and that the 2D study is unavoidable in swimming analysis. Indeed, the total drag values calculated in the case of the 2D study are much higher

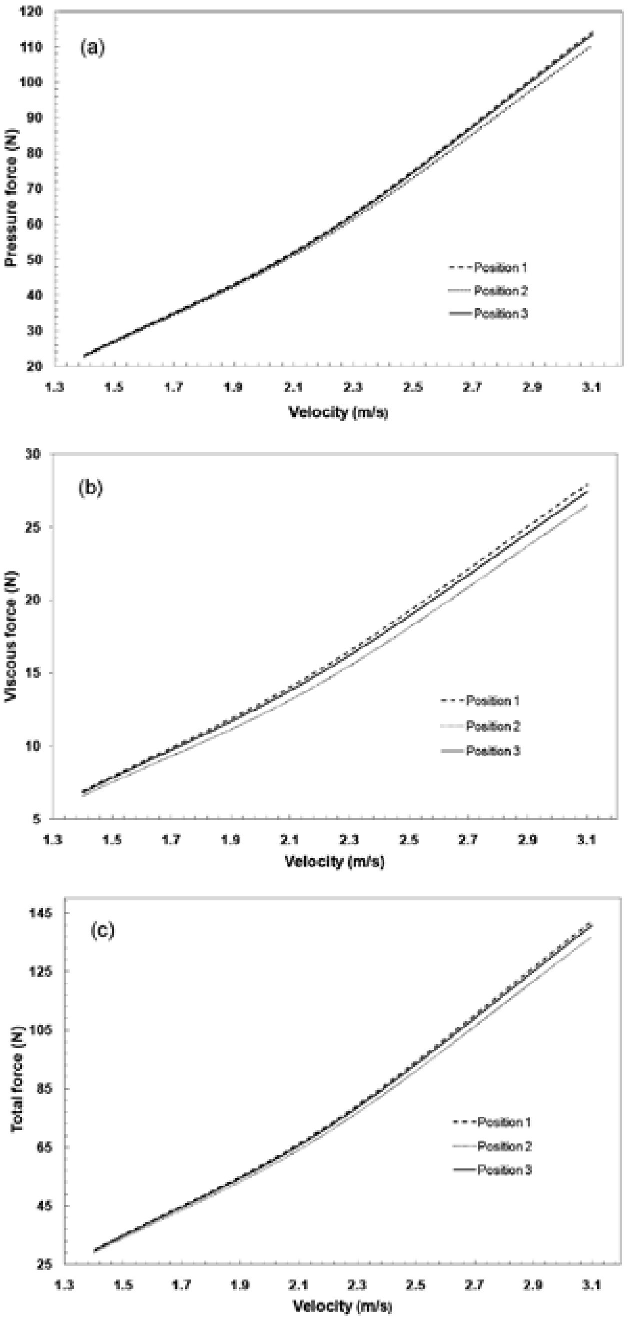

Figure 7. Evolution of the pressure (a), viscous (b), and total (c) force as a function of the head position and velocity.

than the ones calculated in the case of the 3D study, whatever model of turbulence has been used.

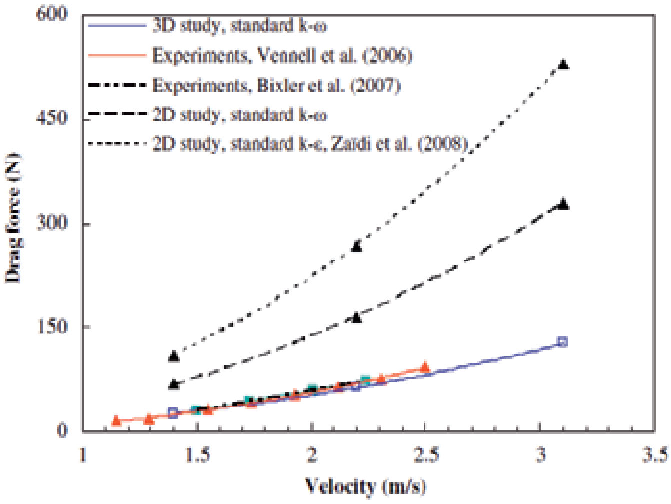

Figure 8. Comparison between the experiments of Vennel et al. [16, 19] and the 2D and 3D numerical results.

4.2. Position influence

Several authors carried out measurements on the whole body of the swimmer and estimated the influence of various parameters such as the swimmer's position or morphology on the intensity of the drag [22]. Other investigators studied the effect of the hand/forearm position on the propulsion effect of a swimmer [23]. Berger et al. [24] measured the drag and lift forces on two hand/forearm models by using the quasi-static approach. The results were compared for velocities, various sizes, and orientations. Bixler and Riewald [1] were the first who used the CFD method to simulate the water flow around a swimmer's hand and forearm (Figure 9). They estimated the drag forces and coefficients around a swimmer's hand and forearm for different angles of attack.

Rouboua et al. [3] have calculated numerically the drag and lift coefficients for a swimmer's hand and forearm in both the steady- and the unsteady-state cases. They studied the effect of the acceleration of the hand and forearm on the generation of the propulsion force. Gardano et al. [6] have also calculated numerically the importance of the flow analysis around the whole arm of a swimmer, and they have estimated the propulsion and the drag forces. More recently, the numerical results obtained by Zaïdi et al. [4] in a 2D geometry case have revealed that the position of the head had a noticeable effect on the hydrodynamic performances. The analysis of these results made it possible to propose an optimal position of the swimmer head in underwater swimming.

In this section, numerical simulations of the flow around a swimmer during underwater swimming corresponding to the starting phase (after the start dive) or following a turn are presented. The aim is to optimize the performance among high-level swimmers by reducing drag effects considering the position of the swimmer's head. Three positions of the head are investigated: lifted up, aligned, or lowered. The length of the swimmer, with arms and hands

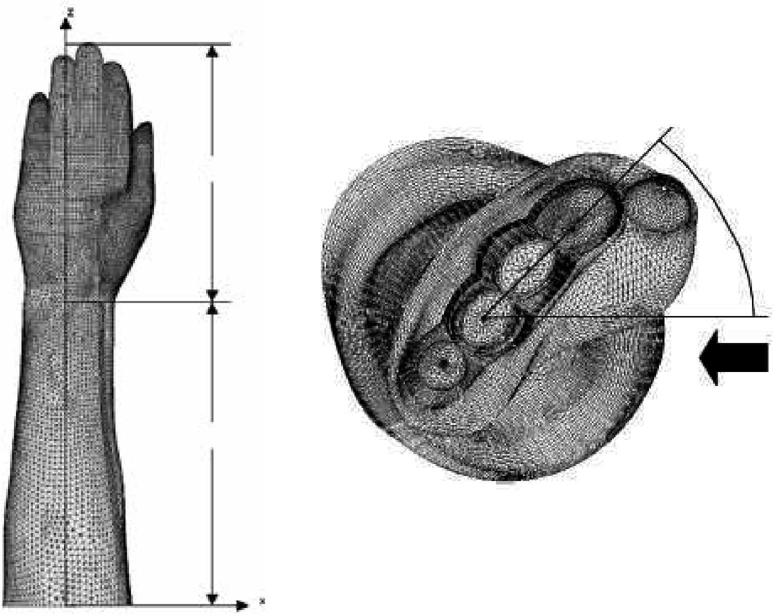

Figure 9. CFD surface mesh of hand and arm with coordinate system [1] and angle of attack defined.

outstretched corresponding to the position of the swimmer in the underwater starting phase, is 2.4 m. In this study, three positions of the head have been investigated: lifted up, aligned, and lowered corresponding to positions 1, 2, and 3 schematized in Figure 10. Only the head modifies the general posture.

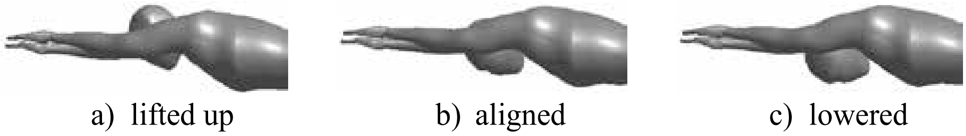

Figure 10. Positions of the head.

5. Streamline patterns

Improving the swimming performance leads also to understand the behavior of the water circulating around the swimmer. A swimmer in streamlined position will not generate the same wake as a swimmer in an unoptimized position. The vortex structures will differ in size and position, as well as areas of vortex separation and attachment. Collapse near this wake allows to reduce the drag force and thus to enhance the performance. In such a way, CFD is a powerful tool to study the flow around swimmers as it avoids making for very complicated

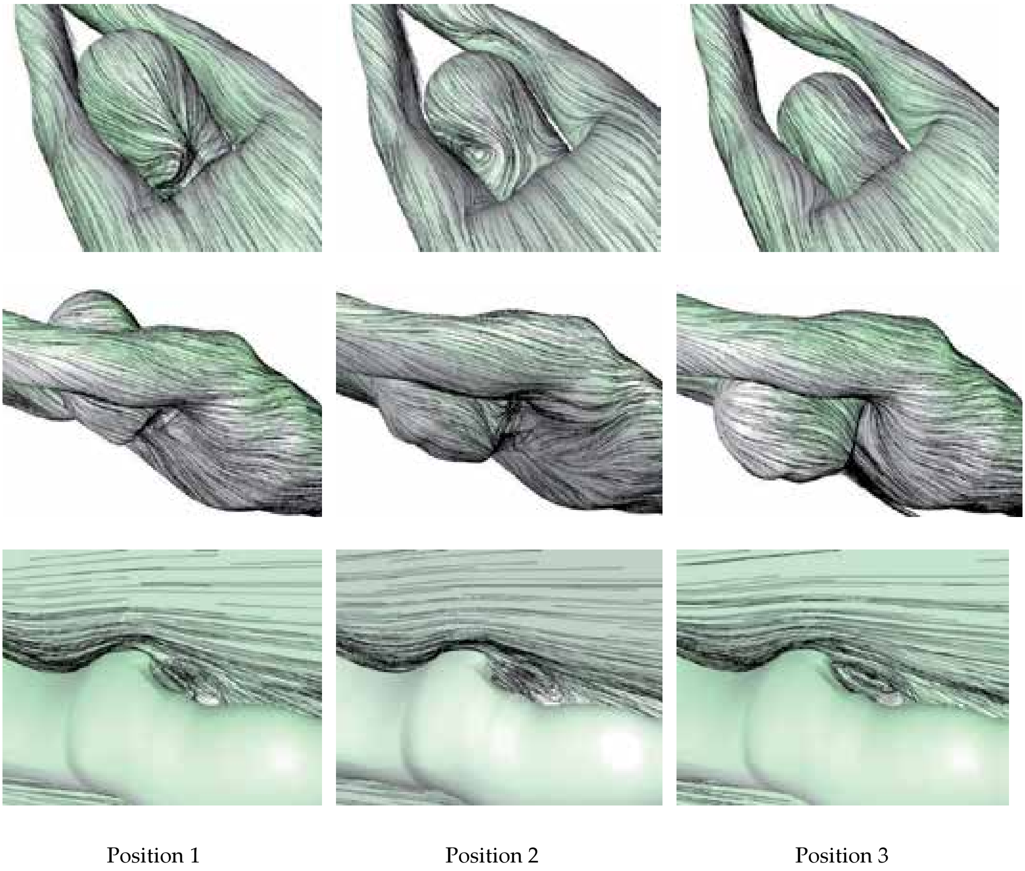

Figure 11. Streamline patterns around the swimmer for three head positions and U_0 = 3.1 m/s [26].

experiments to achieve. Because of the nonuniformity and complexity of the human body, complex turbulent zones are generated around the swimmer's body [20], particularly in the regions with sudden changes in the body shape such as head, shoulders, elbows, hips, knees, buttocks, and feet [25].

Popa et al. [26] showed in Figure 11 streamline patterns to highlight the flow structure around the swimmer's neck, chin, and buttocks for each of the three head positions and for a velocity of 3.1 m/s. One may observe recirculation zones around the swimmer's neck, chin, and buttocks according to the position of the head. For example, when the head is lifted up or aligned with the body, two upper and lower separated points induce vortices.

One may note that these closed vortices are located in the concave geometry of the body, namely, the nape of the neck for the upper surface and the chin/breast area for the lower surface. On the contrary, for the position of the head lowered (position 3), there is no recirculation zones in the neck or under the chin. Because of the nonuniformity of the body on the swimmer's head, shoulders, elbows, hips, knees, and buttocks, complex turbulent zones are generated around the swimmer's body. In this study, Popa et al. [26] noted a recirculation zone on the swimmer's buttocks with a larger recirculation zone when the head is lifted up whatever the head position. The numerical results show that the position of the head plays a very important role for high swimming velocities on the hydrodynamic performances. The position of the head aligned with the body is the one that offers less force drag in comparison with positions with head lowered or lifted up. Complex turbulent zones due to the nonuniformity of the human body are generated around the swimmer's body. This occurs particularly in the regions with sudden changes in the body shape such as the chin, neck and buttocks when the head is lifted up or aligned.

6. Velocity profiles and wall shear stress

The resistance force of advancement strongly depends on the pressure fields and the wall shear stress around the swimmer. The performance improvement requires a better understanding of the structure of the fluid flow around swimmers and a good knowledge of the pressure fields and wall shear stress encountered to minimize them.

Wall shear stress and static pressure are fundamental parameters in high-level swimming. When a swimmer moves in the aquatic environment because of the nonuniformity and complexity of the human body, negative pressure gradients and turbulence zones are generated around the swimmer's body [20], particularly in the regions where the body suddenly changes shape as head, shoulders, elbows, hips, knees, and feet [25].

In the study of Popa et al. [14], the wall shear stress increases with the velocity and consequently the resistance force of advancement increases as well. Also, the wall shear is important in the areas where the body shape suddenly changes, such as the head, the shoulders, the buttocks, the heel, and the chest. Figures 12 and 13 represent the surface shear stress on the swimmer's body for three positions of the head, namely, lifted up (position 1), aligned (position 2), and lowered (position 3) in back and front views. To achieve this, they have chosen a high velocity ($u_0 = 3.1$ m/s) that corresponds to an international level swimmer. The wall shear stress is higher behind the head for position 1 (Figure 12(a)) and on the forehead in position 3 (Figure 13(c)). Figures 14 and 15 present the back and front views of the pressure field for each of the three head positions and u_0 = 3.1 m/s. They observed the negative pressure gradients behind the head for position 1 (Figure 14(a)) and on the forehead in position 3 (Figure 15(c)), which indicate that there are separation zones in these areas.

In a previous study, Zaïdi et al. [19] have found that the position of the head aligned is the one that offers less resistance in underwater swimming in comparison with the positions of the head lifted up and lowered. The pressure gradient between the different parts of the swimmer generates a resistance force that acts perpendicular to the surface of the body which slows the swimmer [17]. The more the resistance force to the advancement, the more wall shear stress observed. The wall shear stress increases with velocity and consequently the resistance force to advancement increases. Also, the wall shear stress is important in the regions where the body shape suddenly changes, such as the head, the shoulders, and the buttocks. In these regions, flow separations occur and the pressure decreases sharply.

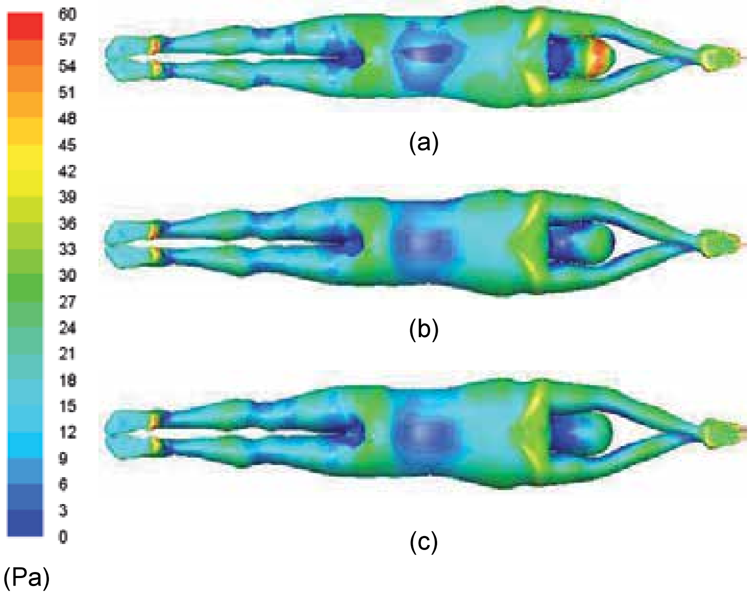

Figure 12. Wall shear stress for three head positions (lifted up, aligned, and lowered) and U_0 =3.1 m/s on the back view of the swimmer (Popa et al. [14]).

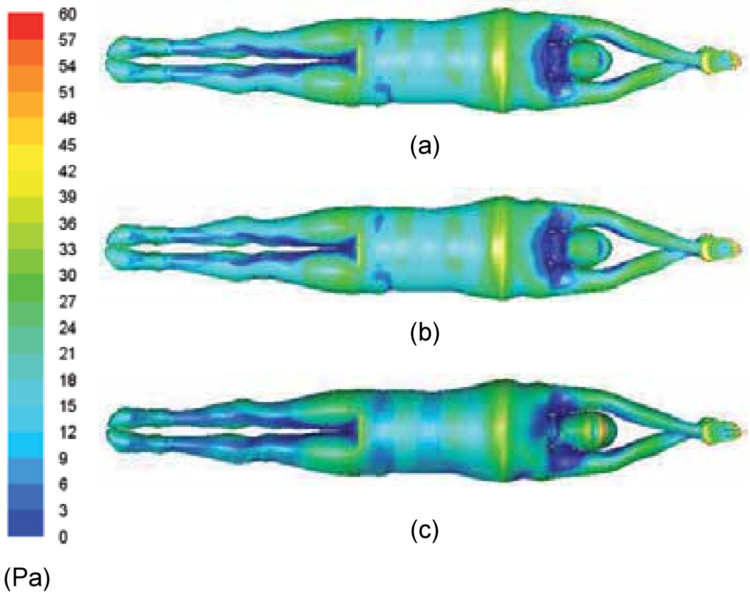

Figure 13. Wall shear stress for three head positions (lifted up, aligned, and lowered) and U_0 =3.1 m/s on the face view of the swimmer (Popa et al. [14]).

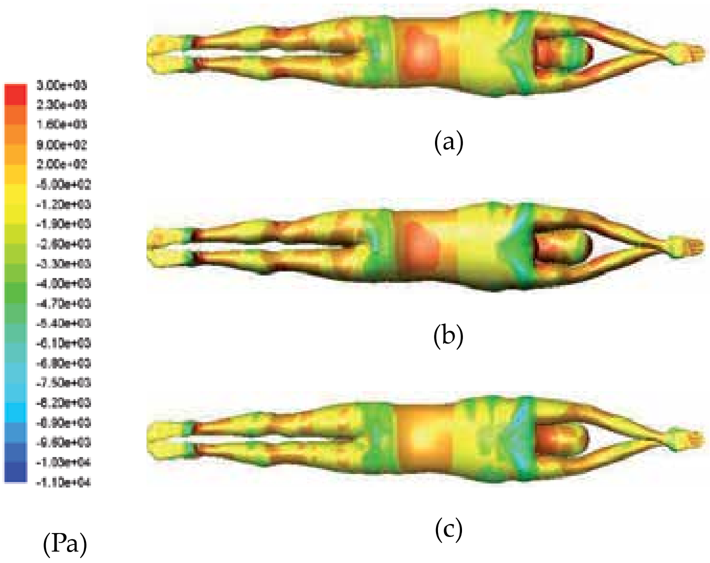

Figure 14. Pressure field for three head positions (lifted up, aligned, and lowered) and U_0 =3.1 m/s on the back view of the swimmer (Popa et al. [14]).

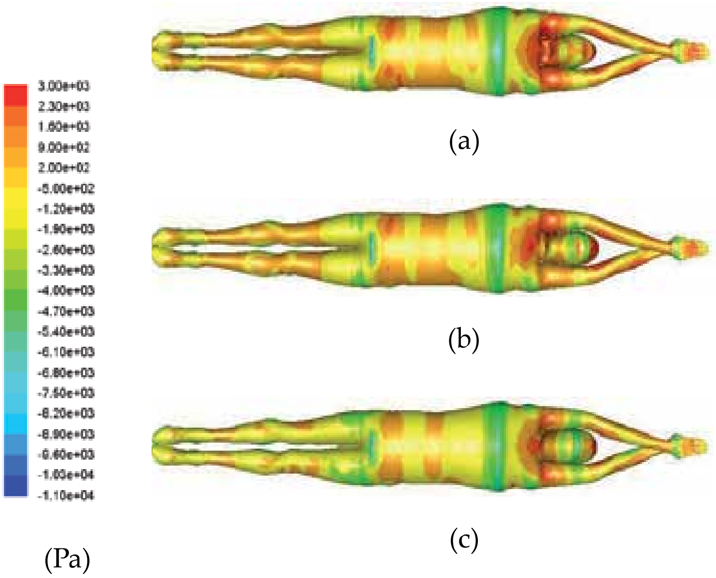

Figure 15. Pressure field for three head positions (lifted up, aligned, and lowered) and U_0 =3.1 m/s on the face view of the swimmer (Popa et al. [14]).

To consolidate these findings, Popa et al. [26] studied the dimensionless longitudinal velocity profiles plotted for six plane locations, for the three positions of the head and for U_0 = 2.2 m/s.

Note that the aspect of the velocity profiles along the body is strongly affected by the change in the head position (Figure 16(a) and (b)).

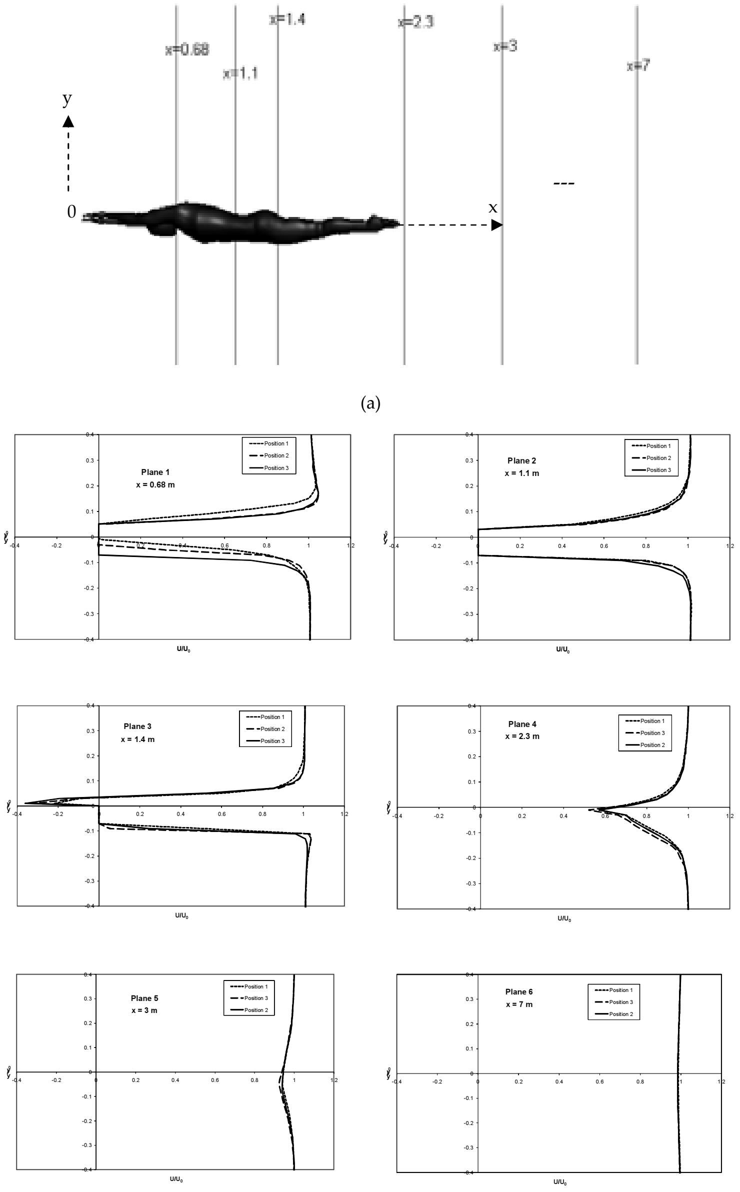

(a)

(b)

Figure 16. (a). Planes position in the fluid domain (z = 0) from Popa et al. [26]. (b). Dimensionless longitudinal velocity profiles in planes 1–6 for U_0 = 2.2 m/s (Re = 6.4 × × 10^6) from Popa et al. [26].

On plane 1, a pronounced increase is noted in the velocity at the upper body surface for lowered and aligned head positions. However, the velocity is greater for lifted up head position. On plane 2, located at the trunk, there are no differences between the three head positions. In the buttock area (plane 3), at $0 < y/y_0 < 0.04$, negative velocities were observed irrespective of the head positions. This indicates that there are recirculation zones in the buttock area that have the same width. In plane 3, the maximum longitudinal velocity is 40% higher for the third head position (lowered) compared to the first head position (lifted up).

In the wake zone, downstream the swimmer, a deceleration of the fluid is noted (loss of kinetic energy). The differences between the velocity profiles in the wake zone characterize the velocity deficit. This dimensionless longitudinal velocity profiles reveals the importance of the head position in the dynamics of the flow in underwater swimming phases (start dive or turns).

7. Conclusion

The main objective of this work was the numerical study of flow around swimmers to improve their hydrodynamic performance. The performance improvement requires a better understanding of the structure of the fluid flow around swimmers and a good knowledge of mechanics of swimming. This chapter focuses on computational fluid dynamics (CFD) procedures and results for this practical implication in swimming and aims to give more details on numerical models. We may note that the CFD can be used as a powerful tool in swimming understanding if the boundary conditions are well studied and chosen. The study of the flow features around the swimmer during the different swimming phases showed that the reduction of forces, which oppose to the swimmers advancement, plays great importance part in the improvement of the performances.

Author details

Ahlem Arfaoui[1*] and Guillaume Polidori[2]

*Address all correspondence to: ahlem.arfaoui@univ-reims.fr

1 Biomechanics Team/Research Group in Engineering Sciences (GRESPI EA4694), University of Reims, France

2 Thermomechanics team/Research Group in Engineering Sciences (GRESPI EA4694), University of Reims, France

References

[1] Bixler, B., Riewald, S., 2002. Analysis of swimmer's hand and arm in steady flow conditions using computational fluid dynamics. Journal of Biomechanics 35, 713–717.

[2] Sato, Y., Hino, T., 2002. Estimation of Thrust of Swimmer's Hand Using CFD National Maritime Research Institute, Center for CFD Research, Shinkawa 6-38-1, Mitaka, Tokyo 181-0004, Japan.

[3] Rouboa, A., Silva, A., Leal, L., Rocha, J., Alves, F., 2006. The effect of swimmer's hand/forearm acceleration on propulsive forces generation using computational fluid dynamics. Journal of Biomechanics 39, 1239–1248.

[4] Zaïdi, H., Taïar, R., Fohanno, S., Polidori, G., 2008. Analysis of the effect of swimmer's head position on swimming performance using computational fluid dynamics. Journal of Biomechanics 41, 1350–1358.

[5] Launder, B. E., Spalding, D. B., 1972. Lectures in Mathematical Models of Turbulence. Academic Press, London, England.

[6] Gardano, P., Dabnichki, P., 2006. On hydrodynamics of drag and lift of the human arm. Journal of Biomechanics 39, 2767–2773.

[7] Choudhury, D., 1993. Introduction to the Renormalization Group Method and Turbulence Modeling. Fluent Inc. Technical Memorandum TM-107.

[8] Shih, T.-H., Liou, W. W., Shabbir, A., Yang, Z., Zhu, J. A., 1995. New k–ε eddy-viscosity model for high Reynolds number turbulent flows. Model development and validation. Computers and Fluids 24, 227–238.

[9] Wilcox, D. C., 1998. Turbulence Modeling for CFD. DCW Industries, Inc., La Canada, California.

[10] Spalart, P., Allmaras, S., 1992. A one-equation turbulence model for aerodynamic flows. Technical Report AIAA-92-0439, American Institute of Aeronautics and Astronautics.

[11] Arfaoui, A., Popa, C.V., Taiar, R., Polidori, G., Fohanno, S., 2012. Numerical streamline patterns at swimmer's surface using RANS equations. Journal of Applied Biomechanics, 28 (3), 279–283.

[12] Lyttle, A., Keys, M., 2004. The use of computational fluids dynamics to optimize underwater kicking performance. In Proceedings of the XXIInd International Symposium on Biomechanics in Sports (p. 403–411). Ottawa, Canada: Imprimerie Impression.

[13] Zaïdi, H., Taïar, R., Fohanno, S., Polidori, G., 2010. Turbulence model choice for the calculation of drag forces when using the CFD method. Journal of Biomechanics 43, 405–411.

[14] Popa, C.V., Zaidi, H., Arfaoui A., Polidori, G., Taïar, R., Fohanno, S., 2011. Wall shear stress analysis around a competitive swimmer using 3D Navier–Stokes equations in CFD, Acta of Bioengineering and Biomechanics 13(1), 3–11.

[15] Polidori G., Taïar R., Fohanno S., Mai T.H. Lodini A., 2006. Skin-friction drag analysis from the forced convection modeling in simplified underwater swimming. Journal of Biomechanics 39, 2535–2541.

[16] Vennel, R., Pease, D., Wilson, B., 2006.Wave drag on human swimmers. Journal of Biomechanics 39, 664–671.

[17] Rushall, B. S., Holt, L. E., Sprigings, E. J., Cappaert, J. M., 1994. A re-evaluation of forces in swimming. Journal of Swimming Research 10, 6–30.

[18] Sheehan, D. P., Laughrin, D. M., 1992. Device for qualitative measurements of hydrodynamic drag on swimmers. Journal of Swimming Research 8, 30–34.

[19] Zaïdi, H., Taïar, R., Fohanno, S., Polidori, G., 2009.An evaluation of turbulence models in CFD simulations of underwater swimming. Series in Biomechanics 24, 5–14.

[20] Lyttle, A.D., 1999. Hydrodynamics of the Human Body During the Freestyle Tumble Turn. Published doctoral dissertation, The University of Western Australia, Nedlands, Australia.

[21] Bixler, B., Pease, D., Fairhurst, F., 2007. The accuracy of computational fluid dynamics analysis of the passive drag of a male swimmer. Sports Biomechanics 6, 81–98.

[22] Huijing, P.A., Toussaint, H.M., Clarys, J.P., Groot, G., de., Hollander, A.P., Vervoorn, K., Mackay, R., Savelberg, H.H.C.M., 1988. Active drag related to body dimensions. In: B.E. Ungerechts, K. Reischle, K. Wilke (Eds.), Swimming Science V, 31–37. Champaign, IL: Human Kinetics Books.

[23] Schleihauf, R.E., 1979. A Hydrodynamic Analysis of Swimming Propulsion, Swimming III. International Series of Sports Sciences 8, pp. 70–109. Baltimore: University Park Press.

[24] Berger, M.A.M., Groot, G., Hollander, A.P., 1995. Hydrodynamic drag and lift forces on human hand arm models. Journal of Biomechanics, 28, 125–133.

[25] Clarys, J.P., 1979. Human morphology and hydrodynamics. In: J. Terauds and E. W. Bedingfield (Eds.), International Series on Sports Science 8; Swimming III, pp. 3–41, Baltimore, MD: University Park Press.

[26] Popa, C.V., Arfaoui A., Fohanno, S., Taïar, R., 2011 Polidori, G., 2014. Influence of a postural change of the swimmer's head in hydrodynamic performances using three dimensional CFD. Computer Methods in Biomechanics and Biomedical Engineering, 17(4), 344–351. CFD simulations of underwater swimming. Series in Biomechanics 24, 5–14.

Chapter 4

Double-Diffusive Natural Convection with Cross-Diffusion Effects in an Anisotropic Porous Enclosure Using ISPH Method

Abdelraheem M. Aly and Mitsuteru Asai

Additional information is available at the end of the chapter

http://dx.doi.org/10.5772/60879

Abstract

A study on heat and mass transfer behaviour on an anisotropic porous medium embedded in square cavity/annulus is conducted using Incompressibe Smoothed Particle Hydrodynamics (ISPH) method. In the case of square cavity, the left wall has hot temperature T_h and mass C_h and the right wall has cool temperature T_c and mass C_c and both of the top and bottom walls are adiabatic. While in the case of square annulus, the inner surface wall is considered to have a cool temperature T_c and mass C_c while the outer surface is exposed to a hot temperature T_h and mass C_h. The governing partial differential equations are transformed to non-dimensional governing equations and are solved using ISPH method. The results present the influences of the Dufour and Soret effects on the heat and mass transfer. The effects of various physical parameters such as Darcy parameter, permeability ratio, inclination angle of permeability and Rayleigh numbers on the temperature and concentration profiles together with the local Nusselt and Sherwood numbers are presented graphically. The results from the current ISPH method are well validated and have favorable comparisons with previously published results and solutions by the finite volume method.

Keywords: Anisotropic porous media, Double-diffusive, Dufour number, ISPH, Natural convection, Non-Darcy flow, Soret number, Square annulus

1. Introduction

The enormous interest in the double diffusive convection in the recent years has led researchers to an extensive study on this topic due to its applicability in the industry as well as in engineering fields. The various aspects related to the heat and mass transfer have been addressed in the extensive literature [1-12]. The thermal diffusion (Soret) and diffusion-thermo (Dufour) effects in the combined heat and mass transfer affect the flow field in free convection significantly [13]. Thus both Soret and Dufour effects have considerable implications on the flow field. Aly and his co-authors [14-17] introduced several studies related to the effects of thermal diffusion (Soret) and diffusion-thermo (Dufour) in the combined heat and mass transfer. Mansour et al. [14] investigated the effects of chemical reaction, thermal stratification, Soret number and Dufour number on MHD free convective heat and mass transfer of a viscous, incompressible and electrically conducting fluid on a vertical stretching surface embedded in a saturated porous medium. Chamkha et al. [15] studied unsteady double-diffusive natural convective MHD flow along a vertical cylinder in the presence of chemical reaction, thermal radiation and Soret and Dufour effects. Chamkha and Aly [16] solved numerically the steady boundary-layer stagnation-point flow of a polar fluid towards a stretching surface embedded in porous media in the presence of the effects of Soret and Dufour numbers and first-order homogeneous chemical reaction. Aly et al. [17] studied the effects of soret and Dufour numbers on free convection over two different types of flows, namely isothermal and adiabatic stretching surfaces embedded in porous media in the presence of a homogeneous first-order chemical reaction. A study made by Nithyadevi and Yang [18] and Weaver and Viskanta [19] discovered that the Soret and Dufour effects will become very significant when the temperature and concentration gradients are high. The fluid velocity and heat transfer rates increase when Dufour parameter is very high. For Soret effect, as the parameter is high, the mass transfer increases but the velocity decreases.

On the other hand, the natural convection in an anisotropic porous medium is an important area of research due to its wide range of applications including thermal insulation, flow in mushy region of a solidifying alloy [20] and flow past heat exchanger tubes [21]. The non-Darcy effects on natural convection in porous media have also received significant attention as a result of the experiments conducted with several combinations of solids and fluids. These experiments covered wide ranges of governing parameters that indicate that the experimental data for systems other than glass water at low Rayleigh numbers do not agree with the theoretical predictions based on the Darcy flow model. This divergence in the heat transfer results has been reviewed in detail in Cheng [22] and Prasad et al. [23], among others. Thus, extensive efforts are being made to include the inertia and viscous diffusion terms in the flow equations and to examine their effects in order to develop a reasonably accurate mathematical model for convective transport in porous media. Detailed accounts of the research into non-Darcy convection have been reported in Tien and Hong [24], Cheng [25], Prasad et al. [26], and Kiadias and Prasad [27]. Nield and Bejan [28] provided an excellent summary of the subject regarding porous media models. The numerical studies of the natural convection flow in anisotropic porous media were conducted by use of Brinkman equation [29] or Brinkman-Forchheimer equation with permeability tensor [30]. They demonstrated that their formulations were accurate in predicting the flow and heat transfer for various inclinations of the principal permeability direction, permeability ratios, and Darcy numbers. The natural convective flow and heat transfer in a fluid saturated anisotropic porous medium have been investigated using the generalized non-Darcy models Nithiarasu et al. [31].

In recent years, the SPH method had been applied into compressible and incompressible viscous fluid flow problems [32, 33]. The SPH was originally developed in compressible flow, and then some special treatment was required to satisfy the incompressible condition. A proposal for developing an incompressible SPH (ISPH) model has been introduced, which pressure is implicitly calculated by solving a discretized pressure Poisson equation at every time step [34-38]. Cummins and Rudman [34] introduced a new formulation for enforcing incompressibility in Smoothed Particle Hydrodynamics (SPH). The method uses a fractional step with the velocity field integrated forward in time without enforcing incompressibility. The resulting intermediate velocity field is then projected onto a divergence-free space by solving a pressure Poisson equation derived from an approximate pressure projection. Asai et al. [35] introduced the stabilized incompressible SPH method by relaxing the density invariance condition. Aly et al. [36-38] applied the stabilized incompressible SPH method to simulate multi-fluid problems, fluid-structure interaction and fluid-soil-structure interactions. Aly et al. [36] modeled the surface tension force for free surface flows and an eddy viscosity based on the Smagorinsky sub-grid scale model using ISPH (Incompressible smoothed particle hydrodynamics) method. They declared that, the eddy viscosity has clear effects in adjusting the splashes and reduces the deformation of free surface in the interaction between the two fluids. In addition, Aly et al. [37] applied the stabilized incompressible SPH method to simulate free falling of rigid body and water entry/exit of circular cylinder into water tank. Aly [38] discussed in details the simulation of fluid-soil-structure interactions using an improved ISPH method.

Numerical modeling of transient natural convection by using SPH method has also been investigated. Chaniotis et al. [39] proposed a remeshing algorithm based on weakly compressible flow approach and performed a comprehensive study for non-isothermal flows. SPH simulation of flow and energy transport using SPH was performed by Szewc et al. [40]. In their study, natural convection in a square cavity problem with a Boussinesq and a non-Boussinesq formulation was performed. They introduced a new variant of the Smoothed Particle Hydrodynamics (SPH) simulations of the natural convection phenomena. Danis et al. [41] modeled the transient and laminar natural convection in a square cavity using SPH method with a discretization tool on uniform Eulerian grids. Recently, Aly [42] modelled the multi-phase flow and natural convection in a square/cubic cavity using ISPH method in two and three dimensions. Rayleigh-Taylor instability between two and three adjacent fluid layers has been simulated and also the natural convection in a square/cubic cavity has been introduced with a good agreement compared to benchmark tests. Aly and Asai [43] modelled non-Darcy flows through porous media using an extended ISPH method. In their study, unsteady lid-Driven flow, natural convection in non-Darcy porous cavities and natural convection in porous medium-fluid interface are examined separately by using ISPH method. In addition, Aly and Sameh [44] modelled the non-Darcy flows through anisotropic porous media for natural/mixed convection and heat transfer in a cavity using ISPH method.

In this study, we presented a generalized porous medium model based on the ISPH method for natural convection and heat and mass transfer in cavity saturated with anisotropic porous media under the effects of Soret and Dufour numbers. Here, we described the implementation of the projection method procedure for a more general hydrodynamically, thermally and diffusion anisotropic porous medium. A semi-implicit time integration scheme is applied for double-diffusive natural convection with anisotropic porous media under the effects of Soret and Dufour numbers. Here, two different cases of boundary condition for the square cavity have been studied numerically using ISPH method. The first case considers natural convection in a square cavity, in which the left wall has hot temperature T_h and mass C_h and the right wall has cool temperature T_c and mass C_c and both of the top and bottom walls are adiabatic. While the second case considers natural convection in square annulus, in which the inner surface wall is considered to have a cool temperature T_c and mass C_c and the outer surface is exposed to a hot temperature T_h and mass C_h. The results present the influences of the Dufour and Soret effects on the heat and mass transfer. The effects of various physical parameters such as Darcy parameter, permeability ratio, inclination angle of permeability and Rayleigh numbers on the temperature and concentration profiles together with the local Nusselt and Sherwood numbers are presented graphically. The results from the current ISPH method are well validated and have favorable comparisons with previously published results and solutions by the finite volume method.

2. Problem description

Fig. 1 shows the physical model for the current problem for the natural convection in porous enclosure with two different cases. In the first case, it is assumed that, the left wall has hot temperature T_h and mass C_h and the right wall has cool temperature T_c and mass C_c. However, the horizontal walls are adiabatic. While for the second case, in square annulus the inner surface wall is considered to have a cool temperature T_c and mass C_c and the outer surface is exposed to a hot temperature T_h and mass C_h. In the both cases, the fluid and the porous medium are assumed to be in local thermodynamic equilibrium. The porous medium is anisotropic in permeability as well as in Forchheimer coefficient. The non-Darcy model is used to model this phenomenon. Also, the usual Boussinesq approximation is invoked to model the density variation in the buoyancy terms.

3. Mathematical analysis

The continuity, momentum, energy and concentration equations for the unsteady natural convection in the two-dimensional enclosure can be written in dimensional form as follows:

$$\nabla.\mathbf{V} = 0 \tag{1}$$

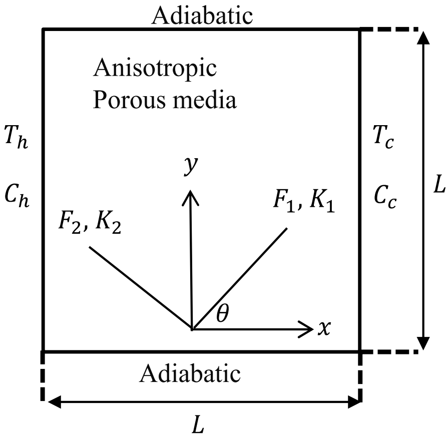

(a) First case: square cavity filled with anisotropic porous media

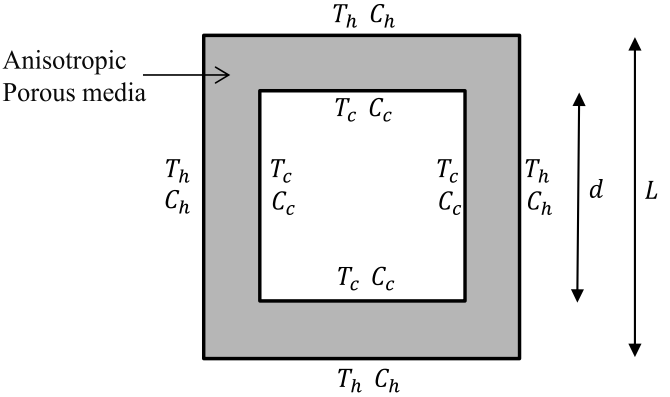

(b) Second case: square annulus filled with anisotropic porous media

Figure 1. Physical model for the porous enclosure (a) First case: square cavity filled with anisotropic porous media and (b) Second case: square annulus filled with anisotropic porous media.

$$\begin{aligned}&\frac{\partial \mathbf{V}}{\partial t}+\left(\frac{\mathbf{V}}{\varepsilon}\right)\cdot\nabla\mathbf{V} = \\ &= \frac{\varepsilon}{\rho}\left[-\nabla P+\frac{\mu}{\varepsilon}\left(\frac{\partial^2\mathbf{V}}{\partial x^2}+\frac{\partial^2\mathbf{V}}{\partial y^2}\right)-\frac{\mu}{\bar{\bar{K}}}\mathbf{V}-\bar{E}\rho\,\mathbf{V}\left|\mathbf{V}\right|+\rho\,\mathrm{g}\left(\beta_T\left(T'-T_l'\right)+\beta_C\left(C'-C_l'\right)\right)\right]\end{aligned} \tag{2}$$

$$\sigma\frac{\partial T'}{\partial t}+\mathbf{V}\cdot\nabla T'=\frac{1}{\rho C_P}\left(\nabla\cdot\left(\bar{k}\nabla T'\right)\right)+D_{TC}\left(\nabla\cdot\left(\nabla C'\right)\right), \tag{3}$$

$$\varepsilon\frac{\partial C'}{\partial t}+\mathbf{V}\cdot\nabla C'=\left(\nabla\cdot\left(\bar{D}\nabla C'\right)\right)+D_{CT}\left(\nabla\cdot\left(\nabla T'\right)\right), \tag{4}$$

where, $\boldsymbol{V}$ is the (Darcy) velocity vector, P is the fluid pressure, T' is the temperature, and ε is the porosity of the medium, σ is the ratio of heat capacities and C' is the concentration of species. D_{TC} is Dufour diffusivity and D_{CT} is Soret diffusivity.

The second order tensor of permeability, $\overline{K}$, Forchheimer coefficient $\overline{E}$, thermal diffusivity, $\overline{k}$, and mass diffusivity, $\overline{D}$, can be written in the following coordinate system as:

$$\overline{K} = \begin{bmatrix} K_1\cos^2\theta + K_2\sin^2\theta & (K_1 - K_2)\sin\theta\cos\theta \\ (K_1 - K_2)\sin\theta\cos\theta & K_2\cos^2\theta + K_1\sin^2\theta \end{bmatrix}, \tag{5}$$

$$K^* = \frac{K_1}{K_2}, \tag{6}$$

$$\overline{E} = \begin{bmatrix} E_1\cos^2\theta + E_2\sin^2\theta & (E_1 - E_2)\sin\theta\cos\theta \\ (E_1 - E_2)\sin\theta\cos\theta & E_2\cos^2\theta + E_1\sin^2\theta \end{bmatrix}, \tag{7}$$

$$E_1 = \frac{F_1}{\sqrt{K_1}}, E_2 = \frac{F_2}{\sqrt{K_2}}, \tag{8}$$

$$F^* = \frac{F_1}{F_2}, \tag{9}$$

$$E^* = \frac{E_1}{E_2} = \frac{F^*}{\sqrt{K^*}} \tag{10}$$

Substituting K^* (Eq. (6)) in Eq. (5) and by applying inverse, the permeability tensor can be reduced to:

$$\overline{K^{-1}} = \frac{1}{K_1}\begin{bmatrix} \cos^2\theta + K^*\sin^2\theta & (1 - K^*)\sin\theta\cos\theta \\ (1 - K^*)\sin\theta\cos\theta & K^*\cos^2\theta + \sin^2\theta \end{bmatrix}, \tag{11}$$

Substituting E^*. (Eq. (10)) in Eq. (7), the Forchheimer coefficient tensor can be reduced to:

$$\bar{E} = \frac{F_1}{\sqrt{K_1}} \begin{bmatrix} \cos^2\theta + \frac{\sqrt{K^*}}{F^*}\sin^2\theta & \left(1 - \frac{\sqrt{K^*}}{F^*}\right)\sin\theta\,\cos\theta \\ \left(1 - \frac{\sqrt{K^*}}{F^*}\right)\sin\theta\,\cos\theta & \frac{\sqrt{K^*}}{F^*}\cos^2\theta + \sin^2\theta \end{bmatrix}, \tag{12}$$

The second order of the thermal diffusivity, $\bar{k}$ can be written as:

$$\bar{k} = \begin{bmatrix} k_x & 0 \\ 0 & k_y \end{bmatrix}, \tag{13}$$

$$k^* = \frac{k_y}{k_x}, \tag{14}$$

Substituting k^* (Eq. (14)) in Eq. (13), the thermal conductivity tensor can be reduced to:

$$\bar{k} = k_x \begin{bmatrix} 1 & 0 \\ 0 & k^* \end{bmatrix}, \tag{15}$$

In similar manner, the second order tensor of mass diffusivity, $\bar{D}$, can be written as:

$$\bar{D} = \begin{bmatrix} D_x & 0 \\ 0 & D_y \end{bmatrix}, \tag{16}$$

$$D^* = \frac{D_y}{D_x}, \tag{17}$$

Substituting D^* (Eq. (17)) in Eq. (16), the mass diffusivity tensor can be reduced to:

$$\bar{D} = D_x \begin{bmatrix} 1 & 0 \\ 0 & D^* \end{bmatrix}, \tag{18}$$

The following dimensionless parameters are used to convert equations (1)-(4) to non-dimensional forms in natural convection case:

$$C=\frac{c'-c_l'}{\Delta c'},\ N=\frac{\beta_c\left(c_h'-c_l'\right)}{\beta_T\left(T_h'-T_l'\right)},\ L_e=\frac{a_x}{D_x} \tag{19}$$

Then, the dimensionless continuity, momentum, energy and mass equations are written as follows:

$$\frac{\partial U}{\partial X}+\frac{\partial V}{\partial Y}=0, \tag{20}$$

$$\begin{aligned}&\frac{1}{\in}\frac{\partial U}{\partial \tau}+\frac{U}{\in^2}\frac{\partial U}{\partial X}+\frac{V}{\in^2}\frac{\partial V}{\partial Y}=\\&-\frac{\partial P}{\partial X}+\frac{\Pr}{\in}\left[\frac{\partial^2 U}{\partial X^2}+\frac{\partial^2 U}{\partial Y^2}\right]-\frac{\Pr}{D_a}\left[U\left(\cos^2\theta+K^*\sin^2\theta\right)+\left(\left(1-K^*\right)\sin\theta\cos\theta\right)\right]-\\&-\frac{F_1}{\sqrt{D_a}}\left[U\left(\cos^2\theta+\frac{\sqrt{K^*}}{F^*}\sin^2\theta\right)+V\left(\left(1-\frac{\sqrt{K^*}}{F^*}\right)\sin\theta\cos\theta\right)\right]\sqrt{U^2+V^2},\end{aligned} \tag{21}$$

$$\begin{aligned}&\frac{1}{\in}\frac{\partial V}{\partial \tau}+\frac{U}{\in^2}\frac{\partial V}{\partial X}+\frac{V}{\in^2}\frac{\partial V}{\partial Y}=-\frac{\partial P}{\partial Y}+\frac{Pr}{\in}\left[\frac{\partial^2 V}{\partial X^2}+\frac{\partial^2 V}{\partial Y^2}\right]-\\&-\frac{Pr}{Da}\left[U\left(\left(1-K^*\right)\sin\theta\cos\theta\right)+V\left(K^*\cos^2\theta+\sin^2\theta\right)\right]-\\&-\frac{F_1}{\sqrt{D_a}}\left[U\left(\left(1-\frac{\sqrt{K^*}}{F^*}\right)\sin\theta\cos\theta\right)+V\left(\left(1-\frac{\sqrt{K^*}}{F^*}\right)\cos^2\theta\sin^2\theta\right)\right]\sqrt{U^2+V^2}+Ra\,Pr\left(T+NC\right),\end{aligned} \tag{22}$$

$$\sigma\frac{\partial T}{\partial \tau}+U\frac{\partial T}{\partial X}+V\frac{\partial T}{\partial Y}=\frac{\partial^2 T}{\partial X^2}+k^*\frac{\partial^2 T}{\partial Y^2}+Du\left(\frac{\partial^2 C}{\partial X^2}+\frac{\partial^2 C}{\partial Y^2}\right), \tag{23}$$

$$\varepsilon\frac{\partial C}{\partial \tau}+U\frac{\partial C}{\partial X}+V\frac{\partial C}{\partial Y}=\frac{1}{Le}\left(\frac{\partial^2 C}{\partial X^2}+D^*\frac{\partial^2 C}{\partial Y^2}\right)+Sr\left(\frac{\partial^2 T}{\partial X^2}+\frac{\partial^2 T}{\partial Y^2}\right) \tag{24}$$

where, *Pr* is the Prandtl number, *Ra* is the Rayleigh number and *Le* is Lewis number. $Du=\frac{D_{TC}\Delta C'}{\alpha_x\Delta T'}$ is Dufour number and $Sr=\frac{D_{CT}\Delta T'}{\alpha_x\Delta C'}$ is Soret number.

3.1. Boundary treatment

The dimensionless boundary conditions are:

a. First case (square cavity filled with anisotropic porous media):

$$\begin{array}{ll} U=0;\ V=0;\ T=1, C=1 & \text{for}\ \ X=0,\ \ 0\le Y\le 1 \\ U=0;\ V=0;\ T=0, C=0 & \text{for}\ \ X=1,\ \ 0\le Y\le 1 \\ U=0;\ V=0;\ \dfrac{\partial T}{\partial X}=0,\ \dfrac{\partial C}{\partial X}=0 & \text{for}\ \ Y=0,\ \ 0\le X\le 1 \\ U=0;\ V=0;\dfrac{\partial T}{\partial X}=0,\ \dfrac{\partial C}{\partial X}=0 & \text{for}\ \ Y=1,\ \ 0\le X\le 1 \end{array} \tag{25}$$

b. Second case (square annulus filled with anisotropic porous media)

$$\begin{array}{ll} U=0;\ V=0;\ T=1, C=1 & \text{for}\ \ X=0,\ \ 0\le Y\le 1 \\ U=0;\ V=0;\ T=1, C=1 & \text{for}\ \ X=1,\ \ 0\le Y\le 1 \\ U=0;\ V=0;\ T=1, C=1 & \text{for}\ \ Y=0,\ \ 0\le X\le 1 \\ U=0;\ V=0;T=1, C=1 & \text{for}\ \ Y=1,\ \ 0\le X\le 1 \\ U=0;\ V=0;T=1, C=1 & \text{for}\ \ Y=1,\ \ 0\le X\le 1 \\ U=0;\ V=0;\ T=0, C=0 & \text{for}\left(L-d\right)/2\le Y\le\left(L+d\right)/2,\ \ X=\left(L+d\right)/2, \\ U=0;\ V=0;\ T=0, C=0 & \text{for}\left(L-d\right)/2\le X\le\left(L+d\right)/2,\ \ Y=\left(L-d\right)/2, \\ U=0;\ V=0;\ T=0, C=0 & \text{for}\left(L-d\right)/2\le X\le\left(L+d\right)/2,\ \ Y=\left(L+d\right)/2, \end{array} \tag{26}$$

The local Nusselt number and local Sherwood number can be defined for the hot wall of square cavity as follows:

$$Nu=-\left.\frac{\partial T}{\partial X}\right|_{X=0}, \tag{27}$$

$$Sh=-\left.\frac{\partial C}{\partial X}\right|_{X=0}. \tag{28}$$

For the majority of design problems, the knowledge of the average Nusselt number is very useful. The average Nusselt number and average Sherwood number are obtained through the integration:

$$\overline{Nu}=-\frac{1}{L}\int_0^L\left(\frac{\partial T}{\partial X}\right)dY. \tag{29}$$

$$\overline{Sh} = -\frac{1}{L}\int_0^L \left(\frac{\partial C}{\partial X}\right) dY \tag{30}$$

The local Nusselt number and local Sherwood number can be defined for the square annulus as follows:

Horizontal hot walls:

$$Nu = -\left.\frac{\partial T}{\partial Y}\right|_{T=T_h},\ Sh = -\left.\frac{\partial C}{\partial Y}\right|_{T=T_h}, \tag{31}$$

Vertical hot walls:

$$Nu = -\left.\frac{\partial T}{\partial X}\right|_{T=T_h},\ Sh = -\left.\frac{\partial C}{\partial X}\right|_{T=T_h}, \tag{32}$$

For the square annulus case, the average Nusselt number and average Sherwood number are obtained through the following integration:

Average Nusselt and Sherwood numbers at the left hot surface:

$$\overline{Nu_L} = -\frac{1}{L}\int_0^L \left(\frac{\partial T}{\partial X}\right) dY, \overline{Sh_L} = -\frac{1}{L}\int_0^L \left(\frac{\partial C}{\partial X}\right) dY, \tag{33}$$

Average Nusselt and Sherwood numbers at the right hot surface:

$$\overline{Nu_R} = -\frac{1}{L}\int_0^L \left(\frac{\partial T}{\partial X}\right) dY, \overline{Sh_R} = -\frac{1}{L}\int_0^L \left(\frac{\partial C}{\partial X}\right) dY, \tag{34}$$

Average Nusselt and Sherwood numbers at the top hot surface:

$$\overline{Nu_T} = -\frac{1}{L}\int_0^L \left(\frac{\partial T}{\partial Y}\right) dX, \overline{Sh_R} = -\frac{1}{L}\int_0^L \left(\frac{\partial C}{\partial Y}\right) dX, \tag{35}$$

Average Nusselt and Sherwood numbers at the bottom hot surface:

$$\overline{Nu_B} = -\frac{1}{L}\int_0^L \left(\frac{\partial T}{\partial Y}\right) dX, \overline{Sh_B} = -\frac{1}{L}\int_0^L \left(\frac{\partial C}{\partial Y}\right) dX, \tag{36}$$

Then, the total average Nusselt and Sherwood numbers are defined as:

$$\overline{Nu_{Total}} = \frac{1}{4}\left(\overline{Nu_L} + \overline{Nu_R} + \overline{Nu_T} + \overline{Nu_B}\right), \tag{37}$$

$$\overline{Sh_{Total}} = \frac{1}{4}\left(\overline{Sh_L} + \overline{Sh_R} + \overline{Sh_T} + \overline{Sh_B}\right), \tag{38}$$

4. Numerical method

The dimensionless governing equations and boundary conditions were solved using both of finite volume method and ISPH method. Here, the finite volume method is introduced for the validation tests.

4.1. Finite volume method

The finite control volume method used here, was described in Patankar [45]. The combined continuity, momentum, energy and concentration equations have been solved numerically using the SIMPLE algorithm [45]. It is worth mentioning that, collocated, regular and orthogonal grids were used in this implementation. Also, Rhie-Chow interpolation was used. The algebraic equations resulting from this treatment are solved using alternating direct implicit (ADI) procedure. It is found that, the 121×121 grid is sufficiently enough to solve the system of equations. The unknowns dependent variables were calculated iteratively until the following criteria of convergence was fulfilled:

$$\sum_{i,j}\left|\chi_{i,j}^{new} - \chi_{i,j}^{old}\right| \le 10^{-6}, \tag{39}$$

4.2. ISPH method

The ISPH algorithm is implemented in a semi-implicit form in order to solve the incompressible viscous flow equations. In this section, the procedure for the solution of porous medium equations is described.

The ISPH method is based on the calculation of an intermediate velocity from a momentum equation where the pressure gradients are omitted. Then, the pressure is evaluated through solving the pressure Poisson equation (PPE). The PPE after SPH interpolation is solved by a preconditioned diagonal scaling Conjugate Gradient PCG method [46] with a convergence tolerance (=1.0x10^{-9}). Finally, the velocity is corrected using the evaluated pressure.

4.2.1. Temporal discretization

The momentum equation can be discretized in time using predictor-corrector scheme. Here, the momentum, energy and concentration equations are described in lagrangian description. In particular, the time discrete momentum equation in its semi-implicit form can be written as follows:

$$\begin{aligned}
&\frac{1}{\in}\left[\frac{U^{n+1}-U^{n}}{\Delta t}\right]=-\left(\frac{\partial P}{\partial X}\right)^{n+1}+\frac{\Pr}{\in}\left(\frac{\partial^2 U}{\partial X^2}+\frac{\partial^2 U}{\partial Y^2}\right)^{n}-\\
&-\left(\frac{\Pr}{Da}\left(\cos^2\theta+K^{*}\sin^2\theta\right)+\frac{F_1}{\sqrt{Da}}\left(\cos^2\theta+\frac{\sqrt{K^{*}}}{F^{*}}\sin^2\theta\right)\sqrt{U^2+V^2}\right)U^{n+1}-\\
&-\left(\left(\frac{\Pr}{Da}\left(1-K^{*}\right)\sin\theta\cos\theta\right)+\frac{F_1}{\sqrt{Da}}\left(\left(1-\frac{\sqrt{K^{*}}}{F^{*}}\right)\sin\theta\cos\theta\right)\sqrt{U^2+V^2}\right)V^{n}
\end{aligned}\tag{40}$$

$$\begin{aligned}
&\frac{1}{\in}\left[\frac{V^{n+1}-V^{n}}{\Delta t}\right]=-\left(\frac{\partial P}{\partial Y}\right)^{n+1}+\frac{\Pr}{\in}\left(\frac{\partial^2 U}{\partial X^2}+\frac{\partial^2 U}{\partial Y^2}\right)^{n}-\\
&-\left(\frac{\Pr}{Da}\left(\left(1-K^{*}\right)\sin\theta\cos\theta\right)+\frac{F_1}{\sqrt{Da}}\left(1-\frac{\sqrt{K^{*}}}{F^{*}}\sin^2\theta\cos\theta\right)\sqrt{U^2+V^2}\right)U^{n}-\\
&-\left(\frac{\Pr}{Da}\left(K^{*}\cos^2\theta+\sin^2\theta\right)+\frac{F_1}{\sqrt{Da}}\left(\frac{\sqrt{K^{*}}}{F^{*}}\cos^2\theta+\sin^2\theta\right)\sqrt{U^2+V^2}\right)V^{n+1}+\\
&+\Pr Ra\left(T^{n}+NC^{n}\right)
\end{aligned}\tag{41}$$

For simplicity,

$$\begin{aligned}
&\text{Porsy}=\frac{Pr}{Da}\left(K^{*}\cos^2\theta+\sin^2\theta\right)+\frac{F_1}{\sqrt{Da}}\left(\frac{\sqrt{K^{*}}}{F^{*}}\cos^2\theta+\sin^2\theta\right)\left(\sqrt{U^2+V^2}\right)^{n},\\
&\text{Porsr}=\left(\frac{Pr}{Da}\left(1-K^{*}\right)\sin\theta\cos\theta\right)+\frac{F_1}{\sqrt{Da}}\left(\left(1-\frac{\sqrt{K^{*}}}{F^{*}}\right)\sin\theta\cos\theta\right)\left(\sqrt{U^2+V^2}\right)^{n},
\end{aligned}\tag{42}$$

Then, equations (40) and (41) can be defined as follows:

$$\begin{aligned}
&\frac{\left(1+\epsilon\Delta t\ \text{Porsx}\right)U^{n+1}-\left(1+\epsilon\Delta t\ \text{Porsx}\right)U^{*}+\left(1+\epsilon\Delta t\ \text{Porsx}\right)U^{*}-U^{n}}{\epsilon\Delta t}=\\
&=-\left(\frac{\partial P}{\partial X}\right)^{n+1}+\frac{Pr}{\epsilon}\left(\frac{\partial^2 U}{\partial X^2}+\frac{\partial^2 U}{\partial Y^2}\right)^{n}-\text{Porsr}\ V^{n},
\end{aligned}\tag{43}$$

$$\frac{\left(1+\epsilon\Delta t\ \text{Porsy}\right)V^{n+1}-\left(1+\epsilon\Delta t\ \text{Porsy}\right)V^{*}+\left(1+\epsilon\Delta t\ \text{Porsy}\right)V^{*}-V^{n}}{\epsilon\Delta t}= \\ =-\left(\frac{\partial P}{\partial Y}\right)^{n+1}+\frac{Pr}{\epsilon}\left(\frac{\partial^2 V}{\partial X^2}+\frac{\partial^2 V}{\partial Y^2}\right)^{n}-\text{Porsr}\ U^{n}+\text{Pr}\,Ra\left(T^{n}+N\ C^{n}\right) \tag{44}$$

Step 1. Predict the velocity

The first step of the predictor-corrector scheme is the calculation of an intermediate velocity (U^{*}) from the momentum equation without including the pressure terms. Thus, the following is obtained:

$$\left(1+\epsilon\Delta t\ \text{Porsx}\right)U^{*}=U^{n}+\epsilon\Delta t\left(\frac{Pr}{\epsilon}\left(\frac{\partial^2 U}{\partial X^2}+\frac{\partial^2 U}{\partial Y^2}\right)^{n}-\text{Porsr}\ V^{n}\right), \tag{45}$$

$$\left(1+\epsilon\Delta t\ \text{Pors}y\right)V^{*}=\ V^{n}+\epsilon\Delta t\left(\frac{Pr}{\epsilon}\left(\frac{\partial^2 V}{\partial X^2}+\frac{\partial^2 V}{\partial Y^2}\right)^{n}+\text{Pr}\,Ra\left(T^{n}+N\ C^{n}\right)-\text{Porsr}\ U^{n}\right). \tag{46}$$

Step 2. Solving the pressure Poisson equation

In the second step, the pressure is calculated using the modified Poisson equation, which ensures that the continuity equation is satisfied, and for the generalized model can be written as follows:

$$\frac{\partial^2 P^{n+1}}{\partial X^2}+\frac{\partial^2 P^{n+1}}{\partial Y^2}=\left(\frac{\left(1+\epsilon\Delta t\ \text{Porsx}\right)}{\epsilon\Delta t}\left(\frac{\partial U^{*}}{\partial X}\right)+\frac{\left(1+\epsilon\Delta t\ \text{Porsy}\right)}{\epsilon\Delta t}\left(\frac{\partial V^{*}}{\partial Y}\right)\right)+\gamma\frac{\rho^{0}-<\rho^{*}>}{\rho^{0}\Delta t^{2}} \tag{47}$$

Note, the relaxation coefficient, γ, $(0\le\gamma\le1)$ can be decided from pre-analysis calculation as Asai et al. [35]. In this study, the particle size d_0 is taken as 2.0 cm and then the relaxation coefficient is decided as $\gamma=0.25$.

Step 3. Corrected velocity

In the third step, the real velocity values are obtained using the following correction:

$$\left(1+\epsilon\Delta t\ \text{Porsx}\right)U^{n+1}=\left(1+\epsilon\Delta t\ \text{Porsx}\right)U^{*}-\epsilon\Delta t\left[\frac{\partial P}{\partial X}\right]^{n+1}, \tag{48}$$

$$\left(1+\epsilon\Delta t\ \text{Porsy}\right)V^{n+1}=\left(1+\epsilon\Delta t\ \text{Porsy}\right)V^{*}-\epsilon\Delta t\left[\frac{\partial P}{\partial Y}\right]^{n+1}, \tag{49}$$

Step 4. Thermal flow problems:

In this step, the time discretization of the energy equation is introduced:

$$\sigma\left(\frac{T^{n+1}-T^{n}}{\Delta\tau}\right)=\left(\left(\frac{\partial^2 T}{\partial X^2}+k^*\frac{\partial^2 T}{\partial Y^2}\right)\right)^n+Du\left(\frac{\partial^2 C}{\partial X^2}+\frac{\partial^2 C}{\partial Y^2}\right)^n, \tag{50}$$

Step 5. Concentration flow problems:

In this step, the time discretization of the concentration equation is introduced:

$$\varepsilon\left(\frac{C^{n+1}-C^{n}}{\Delta\tau}\right)=\frac{1}{Le}\left(\left(\frac{\partial^2 C}{\partial X^2}+D^*\frac{\partial^2 C}{\partial Y^2}\right)\right)^n+Sr\left(\frac{\partial^2 T}{\partial X^2}+\frac{\partial^2 T}{\partial Y^2}\right)^n. \tag{51}$$

4.2.2. SPH Formulations

A spatial discretization using scattered particles, which is based on the SPH, is summarized. First, a physical scalar function $\phi(X_i, \tau)$ at a sampling point X_i can be represented by the following integral form:

$$\phi\left(X_i,\tau\right)=\int W\left(X_i-X_j,h\right)\phi\left(X_j,\tau\right)dv=\int W\left(R_{ij},h\right)\phi\left(X_j,\tau\right)dv, \tag{52}$$

where, W is a weight function called by smoothing kernel function in the SPH literature. In the smoothing kernel function, $R_{ij} = | X_i - X_j |$ and h are the distance between neighbor particles and smoothing length respectively. For SPH numerical analysis, the integral Eq. (52) is approximated by a summation of contributions from neighbor particles in the support domain.

$$\phi(X_i,\tau)\approx\left\langle\phi_i\right\rangle=\sum_j\frac{m_j}{\rho_j}W(R_{ij},h)\phi(X_j,\tau), \tag{53}$$

where, the subscripts i and j indicate positions of labeled particle, ρ_j and m_j mean density and representative mass related to particle j, respectively. Note that, the triangle bracket $\langle\phi_i\rangle$ means SPH approximation of a function ϕ. The gradient of the scalar function can be assumed by using the above defined SPH approximation as follows:

$$\nabla\phi(X_i)\approx\left\langle\nabla\phi_i\right\rangle=\frac{1}{\rho_i}\sum_j m_j(\phi_j-\phi_i)\nabla W(R_{ij},h). \tag{54}$$

Also, the other expression for the gradient can be represented by:

$$\nabla\phi(X_i)\approx\left\langle\nabla\phi_i\right\rangle=\rho_i\sum_j m_j\left(\frac{\phi_j}{\rho_j^2}+\frac{\phi_i}{\rho_i^2}\right)\nabla W(R_{ij},h). \tag{55}$$

In this study, quintic spline function is utilized as a kernel function

$$W\left(R_{ij},h\right)=\beta_d\begin{cases}\left(3-\frac{R_{ij}}{h}\right)^5-6\left(2-\frac{R_{ij}}{h}\right)^5+15\left(1-\frac{R_{ij}}{h}\right)^5 & 0\le R_{ij}<h\\ \left(3-\frac{R_{ij}}{h}\right)^5-6\left(2-\frac{R_{ij}}{h}\right)^5 & h\le R_{ij}<2h\\ \left(3-\frac{R_{ij}}{h}\right)^5 & 2h\le R_{ij}<3h\\ 0 & r_{ij}\ge 3h\end{cases}, \tag{56}$$

where β_d is $7/478\pi h^{\,2}$ and $3/358\pi h^{\,3}$, respectively, in two- and three dimension space.

4.2.3. Projection-based ISPH formulations

Here, the projection method for incompressible fluid problem, which is summarized in section 4, is discretized into particle quantities based on the SPH methodology. For this purpose, the gradient of pressure and the divergence of velocity are approximated as follows:

$$\nabla P(X_i)\approx\left\langle\nabla P_i\right\rangle=\rho_i\sum_j m_j\left(\frac{P_j}{\rho_j^2}+\frac{P_i}{\rho_i^2}\right)\nabla W(R_{ij},h), \tag{57}$$

$$\nabla.\boldsymbol{U}\left(X_i\right)\approx\langle\nabla.\boldsymbol{U}_i\rangle=\frac{1}{\rho_i}\sum_j m_j\left(\boldsymbol{U}_j-\boldsymbol{U}_i\right).\nabla W\left(R_{ij},h\right), \tag{58}$$

Although Laplacian could be derived directly from the original SPH approximation of a function in Eq. (58), this approach may lead to a loss of resolution. Then, the second derivative of velocity for viscous force and the Laplacian of pressure have been proposed by Morris et al. [33] by approximation expression as follows:

$$\nabla.\left(\upsilon\nabla\boldsymbol{U}\right)\left(X_i\right)\approx\langle\nabla.\left(\upsilon\nabla.\boldsymbol{U}_i\right)\rangle=\sum_j m_j\left(\frac{\rho_i\upsilon_i+\rho_j\upsilon_j}{\rho_i\rho_j}\frac{R_{ij}\cdot\nabla W\left(\left|R_i-R_j\right|,h\right)}{R_{ij}^2+\eta^2}\right)\boldsymbol{U}_{ij}, \tag{59}$$

where, η is a parameter to avoid a zero dominator, and its value is usually given by $\eta^2=0.0001h^2$. For the case of $\upsilon_i=\upsilon_j$ and $\rho_i=\rho_j$, the Laplacian term is simplified as:

$$\langle\nabla.\left(\upsilon\nabla.\boldsymbol{U}_i\right)\rangle=\frac{2\upsilon_i}{\rho_i}\sum_j m_j\left(\frac{R_{ij}\cdot\nabla W\left(\left|R_i-R_j\right|,h\right)}{R_{ij}^2+\eta^2}\right)\boldsymbol{U}_{ij}, \tag{60}$$

In this study, Laplacian of velocity is given by:

$$\nabla^2\boldsymbol{U}\left(X_i\right)\approx\langle\nabla^2\boldsymbol{U}_i\rangle=\frac{2}{\rho_i}\sum_j m_j\left(\frac{R_{ij}\cdot\nabla W\left(\left|R_i-R_j\right|,h\right)}{R_{ij}^2+\eta^2}\right)\boldsymbol{U}_{ij}, \tag{61}$$

Similarly, the Laplacian of pressure in pressure Poisson equation (PPE) is given by:

$$\nabla^2P(X_i)\approx\left\langle\nabla^2P_i\right\rangle=\frac{2}{\rho_i}\sum_j m_j\left(\frac{P_{ij}R_{ij}\cdot\nabla W\left(\left|R_i-R_j\right|,h\right)}{R_{ij}^2+\eta^2}\right). \tag{62}$$

The PPE after SPH interpolation is solved by a preconditioned (diagonal scaling) Conjugate Gradient (PCG) method [46] with a convergence tolerance (=1.0×10^{-9}).

The Laplacian operators for both of the temperature and concentration are given as:

$$\nabla^2T\left(X_i\right)\approx\langle\nabla^2T_i\rangle=\sum_j m_j\left(\frac{\rho_i+\rho_j}{\rho_i\rho_j}\frac{T_{ij}\ R_{ij}\cdot\nabla W(\left|R_i-R_j\right|,h)}{R_{ij}^2+\eta^2}\right), \tag{63}$$

$$\nabla^2C\left(X_i\right)\approx\langle\nabla^2C_i\rangle=\sum_j m_j\left(\frac{\rho_i+\rho_j}{\rho_i\rho_j}\frac{C_{ij}\ R_{ij}\cdot\nabla W(\left|R_i-R_j\right|,h)}{R_{ij}^2+\eta^2}\right), \tag{64}$$

5. Numerical validation tests

To check the accuracy of the numerical method employed for the solution of the problem under consideration, it was validated (after making the necessary modifications) with the problem of Nithiarasu et al. [31]. Comparison of average Nusselt number between Brinkman and Generalized porous medium models for Nithiarasu et al. [31], FVM and ISPH methods in the non-Darcy flow regime $Da=10^{-2}$ at buoyancy ratio $N=0$, has been introduced in table 1. In this table, the Rayleigh numbers was taken as Ra=10^4 with Darcy parameter, $Da=10^{-2}$. The current FVM and ISPH results agree well with the data from Nithiarasu et al. [31]. Note, the current comparison was reported before by Aly and Sameh [44].

θ	K^*	Ra	Nithiarasu et al. [31]	FVM	ISPH
0°	0.1	10^4	1.587	1.570	1.517
45°	0.1	10^4	1.573	1.563	1.522
90°	0.1	10^4	1.579	1.573	1.524
0°	10	10^4	1.106	1.110	1.132
45°	10	10^4	1.119	1.130	1.139
90°	10	10^4	1.106	1.111	1.134

Table 1. Comparison of average Nusselt number between generalized porous medium models for Nithiarasu et al. [31], FVM and ISPH method in the non-Darcy flow regime, $Da=10^{-2}$ with buoyancy ratio $N=0$.

Comparison of isotherms lines between FVM and ISPH methods under the effect of Rayleigh number and permeability ratio at Darcy number $Da=10^{-2}$, porosity parameter $\varepsilon=0.5$, buoyancy ratio $N=0$ and an inclination angle of permeability $\theta=0°$ is introduced in figure 2. In this figure, the isotherm lines are affected clearly by both of the Rayleigh number and permeability ratio. As the Rayleigh number increases, the heat conduction increases and the isotherms lines are strongly compressed in the bottom part of the left wall and in the top part of the right wall. As the permeability ratio increases from 0.1 to 10, then the heat conduction decreases.

6. Results and discussion

In this section, two different cases of boundary conditions for unsteady natural convection flow in square cavity saturated with anisotropic porous media under the effects of Soret and Dufour numbers have been discussed in details using ISPH method.

6.1. Natural convection in square cavity saturated with anisotropic porous media

In this study, the unsteady natural convection in square cavity saturated with anisotropic porous media under the effects of Soret and Dufour numbers has been solved numerically using ISPH method. It is assumed that, the vertical walls are kept at constant temperatures, T_h and T_c, where, T_h is the hot wall and T_c is cool wall and constant concentrations, C_h and C_c, where, $C_h > C_c$. However, the horizontal walls are adiabatic.

The effects of combined Soret and Dufour numbers on the isothermal lines, concentration lines and horizontal and vertical velocities contours at inclination angles $\theta=0°$ and $45°$ at permea-

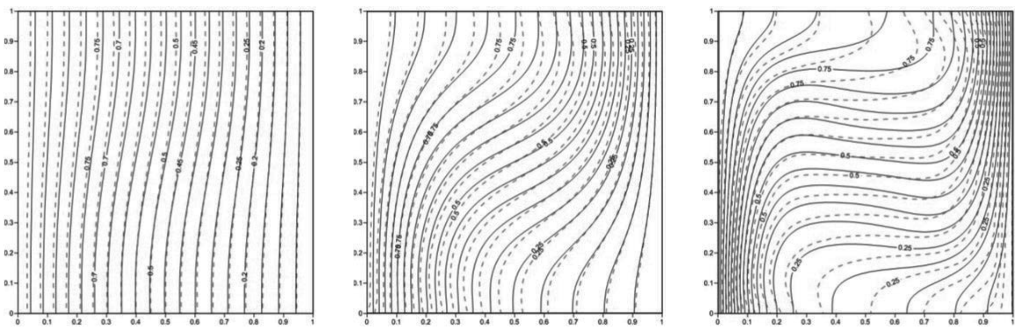

(a) $K^* = 0.1; Ra = 10^3$ $Ra = 10^4$ $Ra = 10^5$

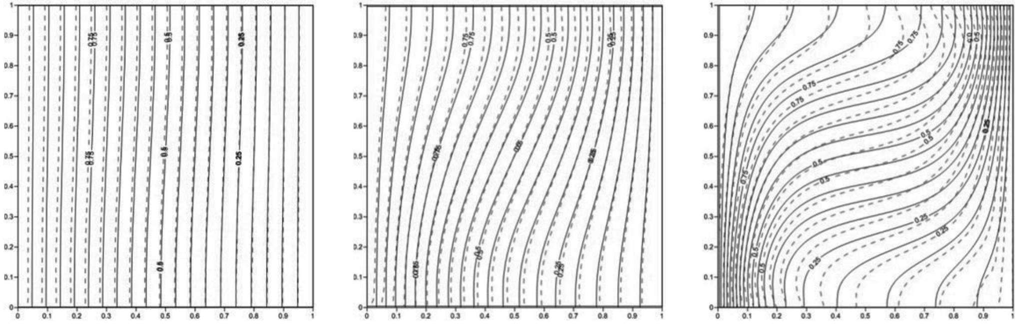

(b) $K^* = 10; Ra = 10^3$ $Ra = 10^4$ $Ra = 10^5$

Figure 2. Comparison of the isotherms lines between FVM method (—) and ISPH method (----) at buoyancy ratio $N=0$, Darcy number $Da=10^{-2}$, porosity parameter $\varepsilon=0.5$ and inclination angle $\theta=0^\circ$ in the absence of Soret and Dufour numbers effects.

bility ratio $K^*=0.1$, Darcy parameter $Da=10^{-2}$, porosity parameter $\varepsilon=0.5$, Rayleigh number $Ra=10^4$, buoyancy ratio $N=1.0$ and Lewis number $Le=1.0$ has been shown in figure 3.

It is observed that, in general, the isotherms lines gather beside the vertical walls, indicating thermals boundary layers beside the bottom of the left wall and top of the right wall of the cavity. As the Soret number increases with decrease in Dufour number, the isothermal lines are slightly increase the thermals boundary layers beside the bottom of the left wall and top of the right wall of the cavity. Regarding the solutal concentration lines, these contours are parallel to each other within the core of the cavity. Moreover, as the Soret number increases with decrease in Dufour number leads to the solutal concentration lines are highly affected and their contours are paralleled within the core of the cavity. The contours of horizontal velocity component formed in the shape of two vertically-extended clockwise and anticlockwise circular cells next to the bottom and top walls of the enclosure. On the contrary, the contours of the vertical velocity component formed in the shape of two horizontally-extended clockwise and anticlockwise circular cells next to left and right walls of the enclosure. Also, the horizontal and vertical velocity components contours become slightly stretch in case of increasing Soret number with decreasing Dufour number.

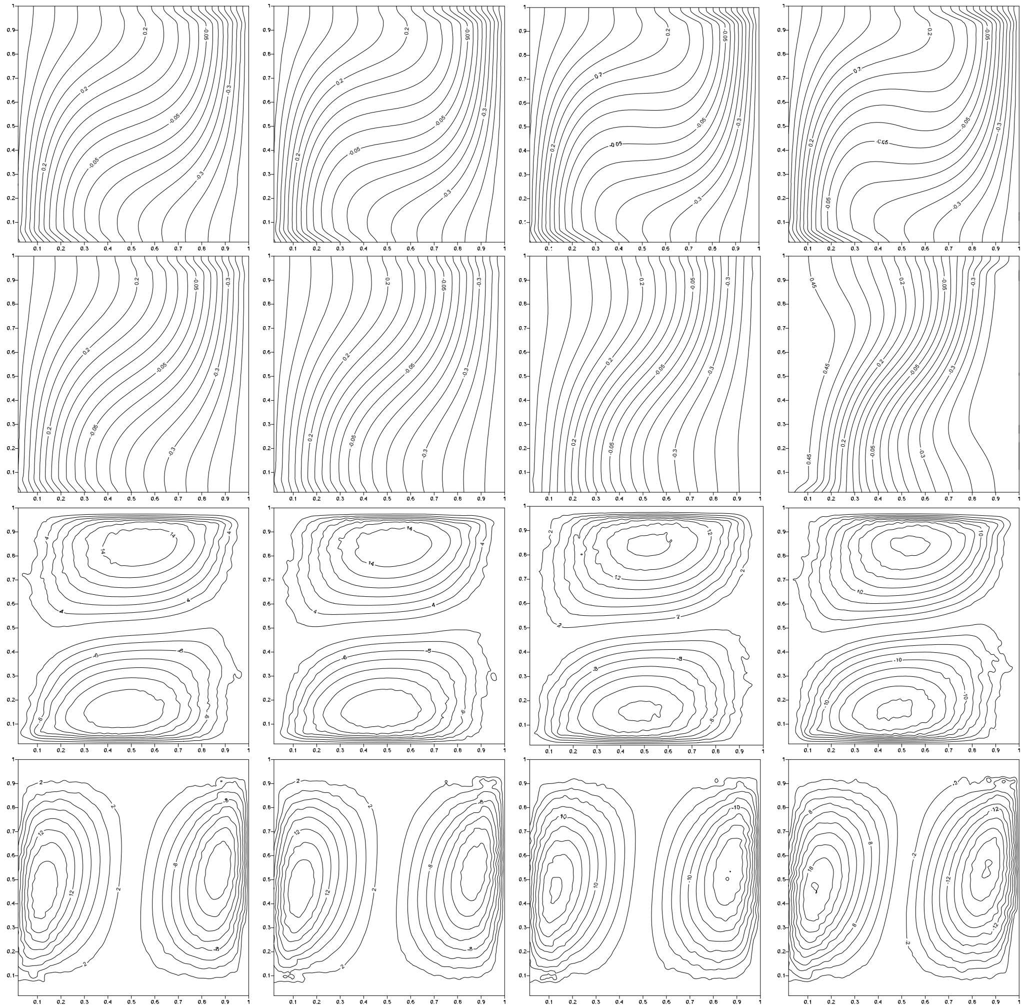

$Sr = 0.1$ and $Du = 0.6$ $Sr = 0.5$ and $Du = 0.3$ $Sr = 1$ and $Du = 0.12$ $Sr = 2$ and $Du = 0.03$

Figure 3. Presents isothermal lines, concentration lines, horizontal and vertical velocities contours under the effects of coupled Soret and Dufour numbers at inclination angle $\theta = 0°$, permeability ratio $K^{*} = 0.1$, $Da = 10^{-2}$, $\varepsilon = 0.5$, $Ra = 10^{4}$, $N = 1.0$ and $Le = 1.0$.

Fig. 4 presents the effects of Soret and Dufour numbers on temperature, solutal concentration, horizontal velocity profiles and vertical velocity profiles. It is noted that, an increase in Soret number accompanied by a decrease in Dufour number leads to increase both of fluid concentration and horizontal and vertical velocity profiles and decrease in fluid temperature.

The effects of Darcy number from 10^{-2} to 10^{-4} at inclination angles $\theta = 0°$, permeability ratio $K^{*} = 0.1$, porosity parameter $\varepsilon = 0.5$, Rayleigh number $Ra = 10^{4}$, buoyancy ratio $N = 1.0$, Soret number $Sr = 1.0$, Dufour number $Du = 0.12$ and Lewis number $Le = 1.0$ has been shown in figure 5. For the value of the buoyancy ratio N considered, the interaction between the thermal and

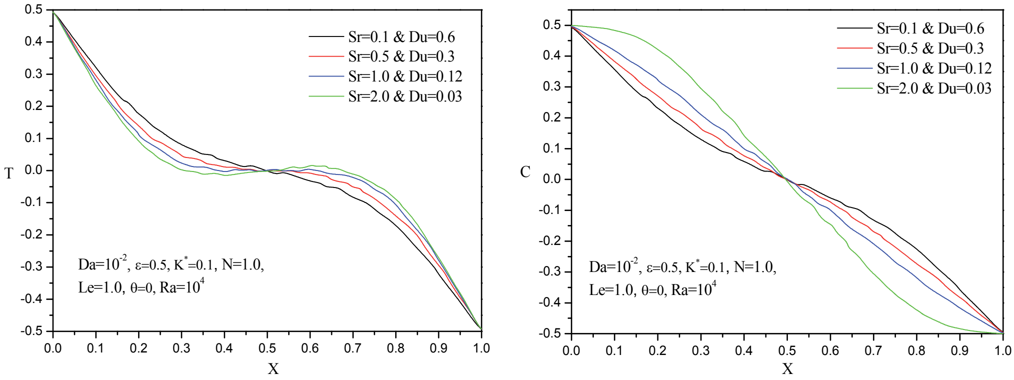

(a) Temperature profiles (b) Concentration profiles

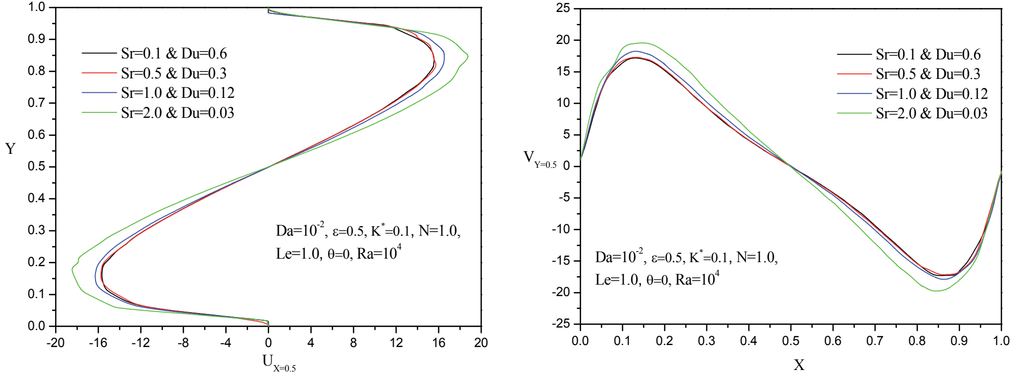

(c) Horizontal velocity profiles (d) Vertical velocity profiles

Figure 4. Presents the effects of combined Soret and Dufour numbers on the temperature, concentration, horizontal and vertical velocity profiles, respectively.

compositional buoyancy effects is significant. It is observed that, the heat and mass conduction in cavity are increase clearly and the flow moves faster at the case of increasing Darcy number from10^{-4} to 10^{-2}. In figure 5, as the inverse Darcy number Da^* increases from 10^2 to 10^4, the temperature and concentration contours become more parallel to the vertical walls and the horizontal and vertical values are decrease. Two parallel recirculations for both of horizontal and vertical velocities are formed near to the boundaries. It can be concluded that the main contributions of the presence of the porous medium for a buoyancy ratio of unity are predicted to be a flow retardation effect and a suppression of the overall heat transfer in the enclosure.

Fig. 6 depicts the effects of Darcy parameter on temperature, solutal concentration, horizontal velocity profiles and vertical velocity profiles at two values of Rayleigh number Ra=10^3 and 10^4. At the presence of the porous medium and Darcy number changes from 10^{-2} to 10^{-4}, both of the horizontal and vertical velocity profiles are decrease. The temperature and concentration profiles are decrease linearly as X increases. It is observed that, there is a region in the middle part of the cavity, where the temperature and concentration depart from its normal behavior, which can be called a reverse effect region. The temperature affected clearly by changing the

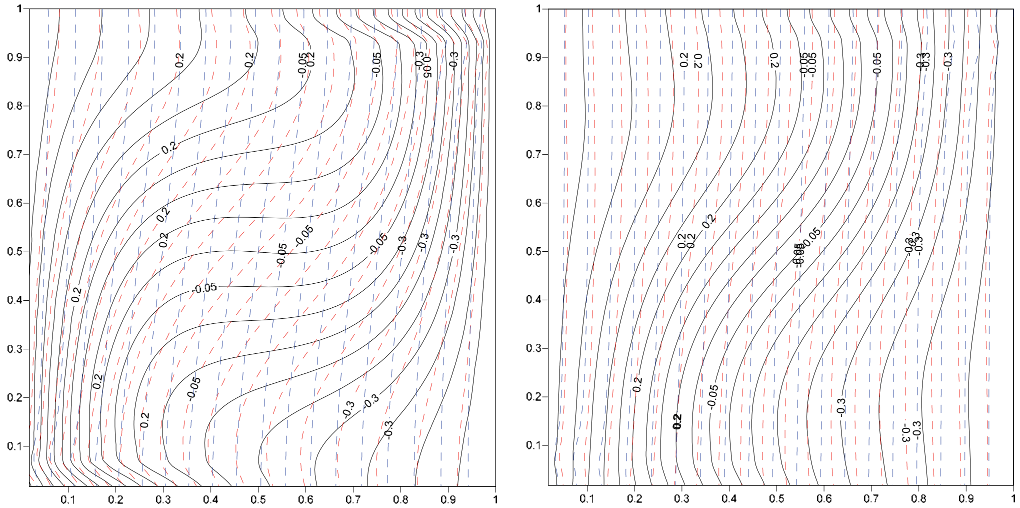

(a) isothermal lines (b) concentration lines

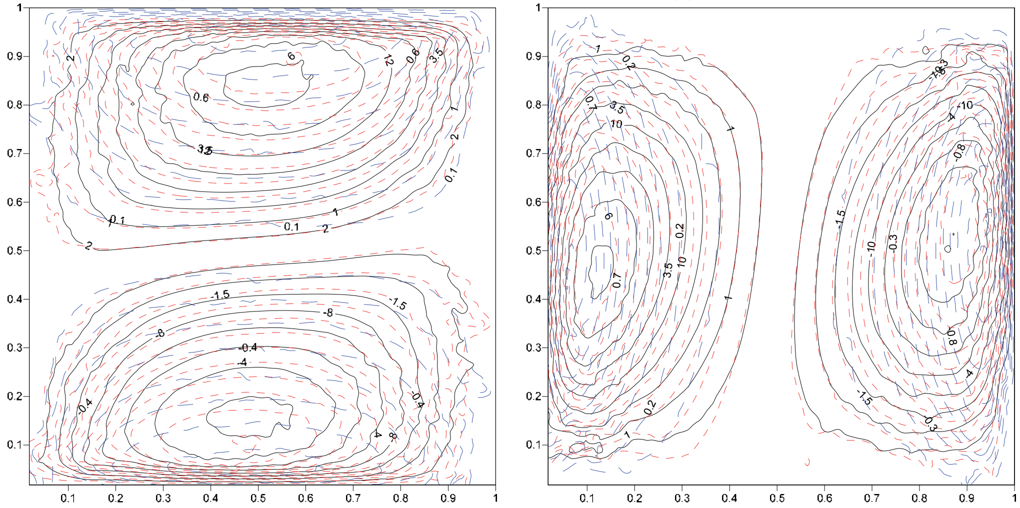

(c) horizontal velocity contours (d) vertical velocity contours

Figure 5. Presents isothermal lines, concentration lines, horizontal and vertical velocities contours under the effect of Darcy number 10^{-2} (—),10^{-3}(----) and 10^{-4}(----).

Rayleigh number. On the other hand, concentration profiles are affected slightly by changing the Rayleigh number. The horizontal velocity curves are symmetric, where the line $Y = 0.5$ represents the symmetrical axis and the variation of horizontal velocity increases as the Rayleigh number increases. Also, the vertical velocity curves are symmetric, where the line $X = 0.5$ represents the symmetrical axis and also the variation of vertical velocity increases as the Rayleigh number increases.

In order to demonstrate the variation in velocity, temperature and concentration fields under the effects of combined an inclination angle with permeability ratio parameter. The horizontal

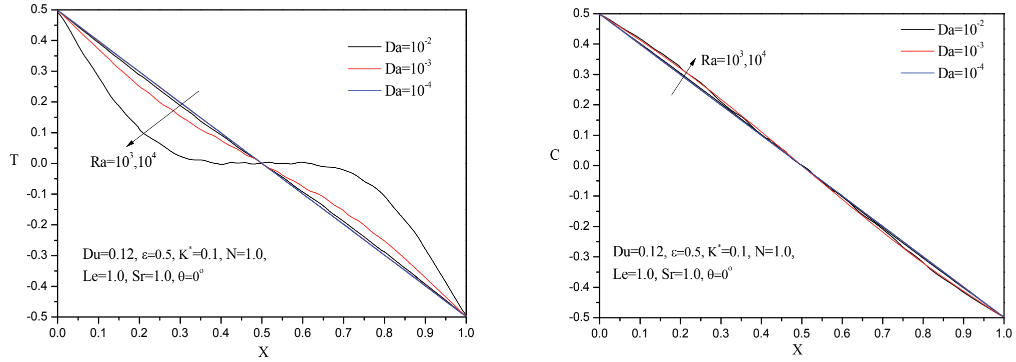

(a) Temperature profiles (b) Concentration profiles

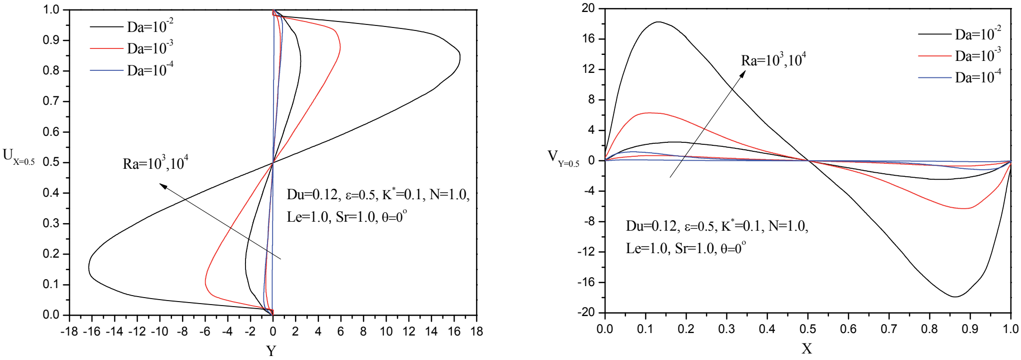

(c) Horizontal velocity profiles (d) Vertical velocity profiles

Figure 6. Depicts the effects of Darcy parameter on the temperature, concentration, horizontal and vertical velocity profiles, respectively at two values of Rayleigh number Ra=103 and 104.

and vertical velocity, temperature and concentration profiles and contours through the cavity under the effects of combined an inclination angle with permeability ratio parameter have been shown in Figs. 7 and 8.

In these figures, the permeability ratio parameter showed clear effects in isothermal lines, and horizontal and vertical velocities contours and also in temperature and horizontal and vertical velocity profiles compared to the effects of an inclination angle. As the permeability ratio parameter increases from 0.1 to 10, the temperature profiles are increase until their profiles become linear, this indicates the limit of no-flow. Also, the net fluid velocity in the vicinity of the heated wall is decrease. The concentration profiles are affected slightly by changing both of an inclination angle with permeability ratio parameter.

The time histories for the effects of the Darcy number with two values of Rayleigh number $Ra = 10^3$ and 10^4 and combined Soret with Dufour numbers on the average Nusselt number and the average Sherwood number are presented in Figs. 9 and 10. It is observed that, the average Nusselt number Nu has a decreasing trend with the presence of porous media by changing Darcy number from $Da = 10^{-2}$ to $Da = 10^{-4}$. Due to the opposing flow of solute concentration, the average Sherwood number has an increasing trend with the presence of porous media by

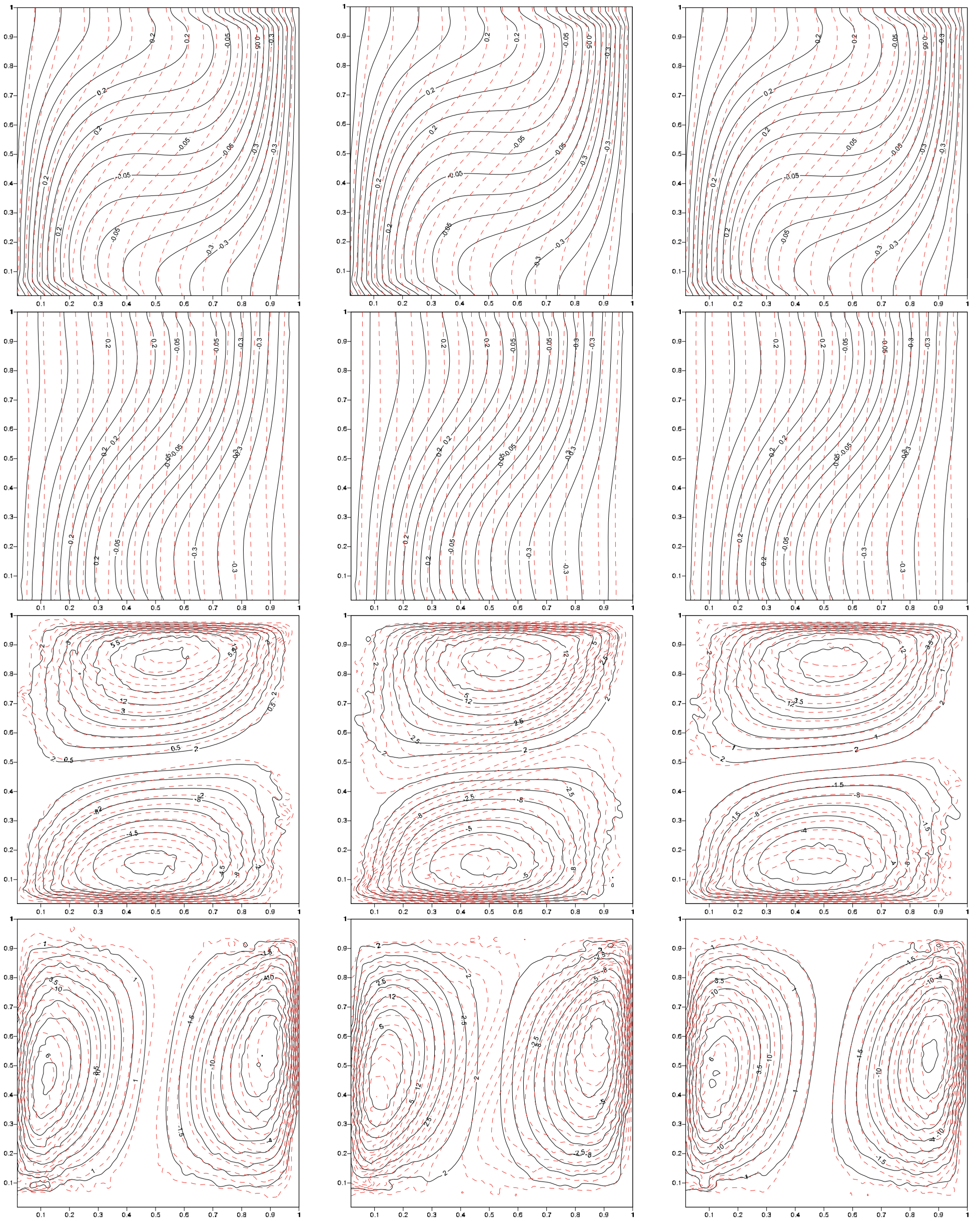

$\theta = 0°$ $\theta = 45°$ $\theta = 90°$

Figure 7. Presents isothermal lines, concentration lines, horizontal and vertical velocities contours under the effect of an inclination angle for two values of permeability ratio $K^{*}=0.1$ (—) and $K^{*}=10$ (----).

changing Darcy number from Da=10^{-2} to Da=10^{-4}. Also, the effects of Darcy number on both of average Nusselt and Sherwood numbers appears clearly at the high value of Rayleigh number $Ra=10^{4}$.

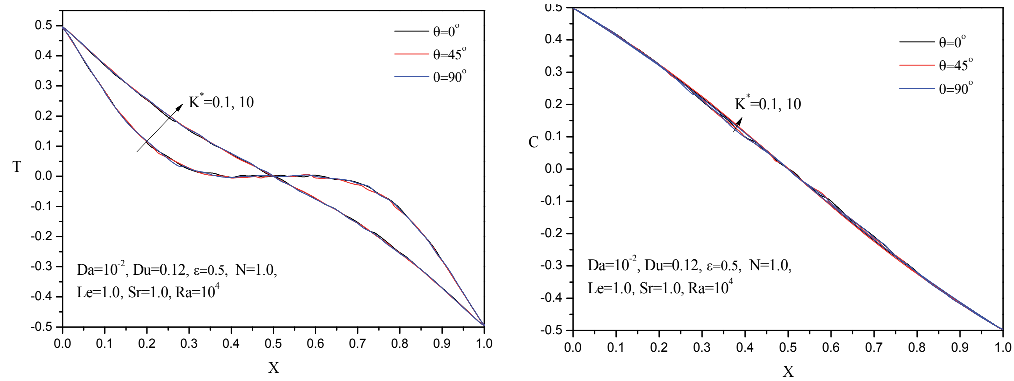

(a) Temperature profiles

(b) Concentration profiles

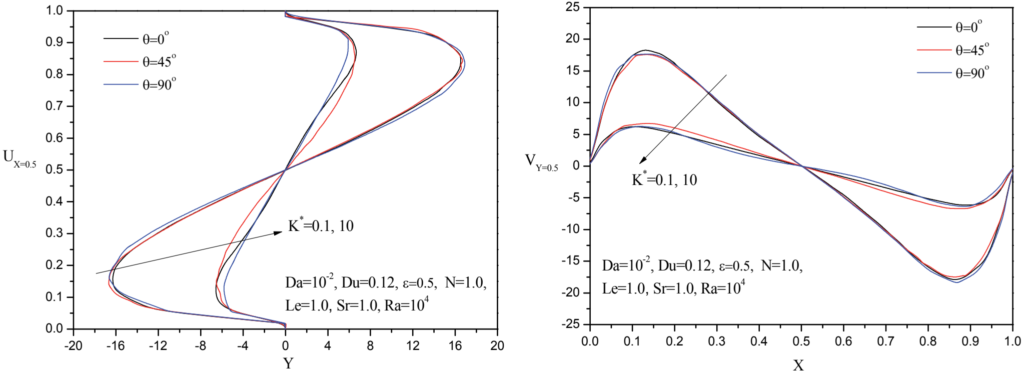

(c) Horizontal velocity profiles

(d) Vertical velocity profiles

Figure 8. Depicts the effects of an inclination angle on the temperature, concentration, horizontal and vertical velocity profiles, respectively at two values of permeability ratio $K^*=0.1$ and 10.

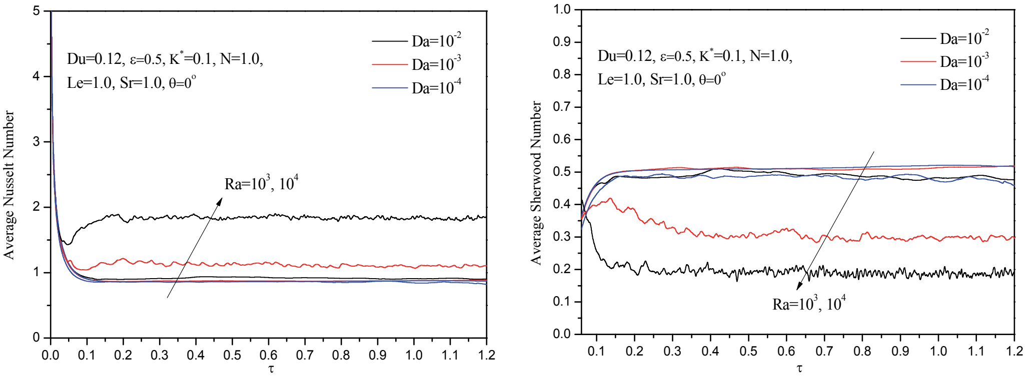

(a) Average Nusselt number

(b) Average Sherwood number

Figure 9. Time histories for the effects of Darcy number with two values of Rayleigh number on the average Nusselt and Sherwood numbers at the heated wall of the cavity.

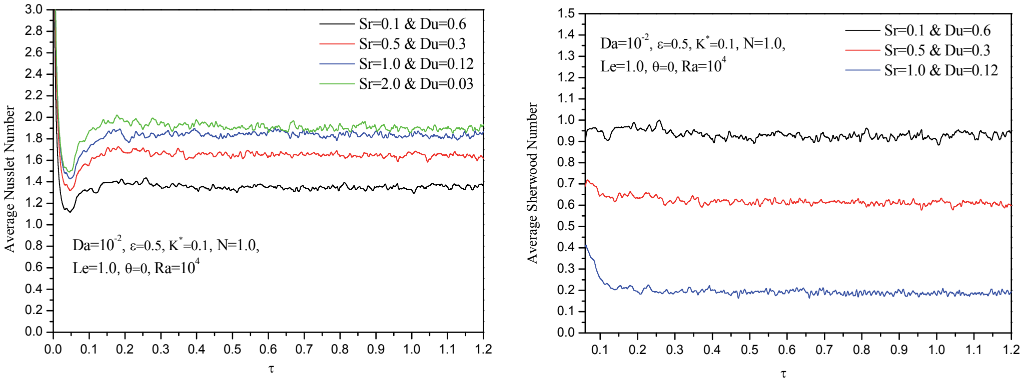

(a) Average Nusselt number (b) Average Sherwood number

Figure 10. Time histories for the effects of combined Soret number with Dufour number on the average Nusselt and Sherwood numbers at the heated wall of the cavity.

In addition, the average Nusselt number increases as the Soret number increases and Dufour number decreases. While, the average Sherwood number decreases as the Soret number increases and Dufour number decreases.

6.2. Natural convection in a square annulus filled with anisotropic porous media

In this section, we studied heat and mass behavior on a square annulus saturated with anisotropic porous media.

The effects of annulus length in the temperature, concentration, average Nusselt number and average Sherwood number have been introduced in Figs. 11 and 12. Fig. 11 Depicts the effects of annulus length on the isotherms lines, concentration lines and vertical and horizontal velocity contours, respectively at Darcy parameter $Da=10^{-2}$, $\varepsilon=0.5$, $Ra=10^{4}$, Sr=1.0, Du=0.12, $N=1.0$, Le=1.0 and $K^{*}=0.1$. In this figure, as the width ratio is increased, the oval shape becomes thinner and fluid activity at the top and bottom wall decreases. When the annulus length equals d= 0.75, there is almost no fluid activity at the top and bottom walls and from our observation due to restriction in space and movement of the fluid, the isotherms and concentration lines are almost equal under the effect of any parameter. Fig. 12 Depicts the time histories for the effects of annulus length on the average Nusselt number and average Sherwood number, respectively at Darcy parameter $Da=10^{-2}$, $\varepsilon=0.5$, $Ra=10^{4}$, Sr=1.0, Du=0.12, $N=1.0$, Le=1.0 and $K^{*}=0.1$. The bottom wall has higher average Nusselt and Sherwood numbers than the rest of the walls. The top wall has lower average Nusselt and Sherwood numbers than the rest of the walls.

Fig. 13 Depicts the time histories for the effects of combined Soret number with Dufour number on the average Nusselt number and average Sherwood number, respectively at annulus length 0.5, $Da=10^{-2}$, $\varepsilon=0.5$, $Ra=10^{4}$, $N=1.0$, Le=1.0 and $K^{*}=0.1$. In this figure, as the Soret number increases from 0.1 to 1.0 with decreasing the value of Dufour number from 0.6 to 0.12, the

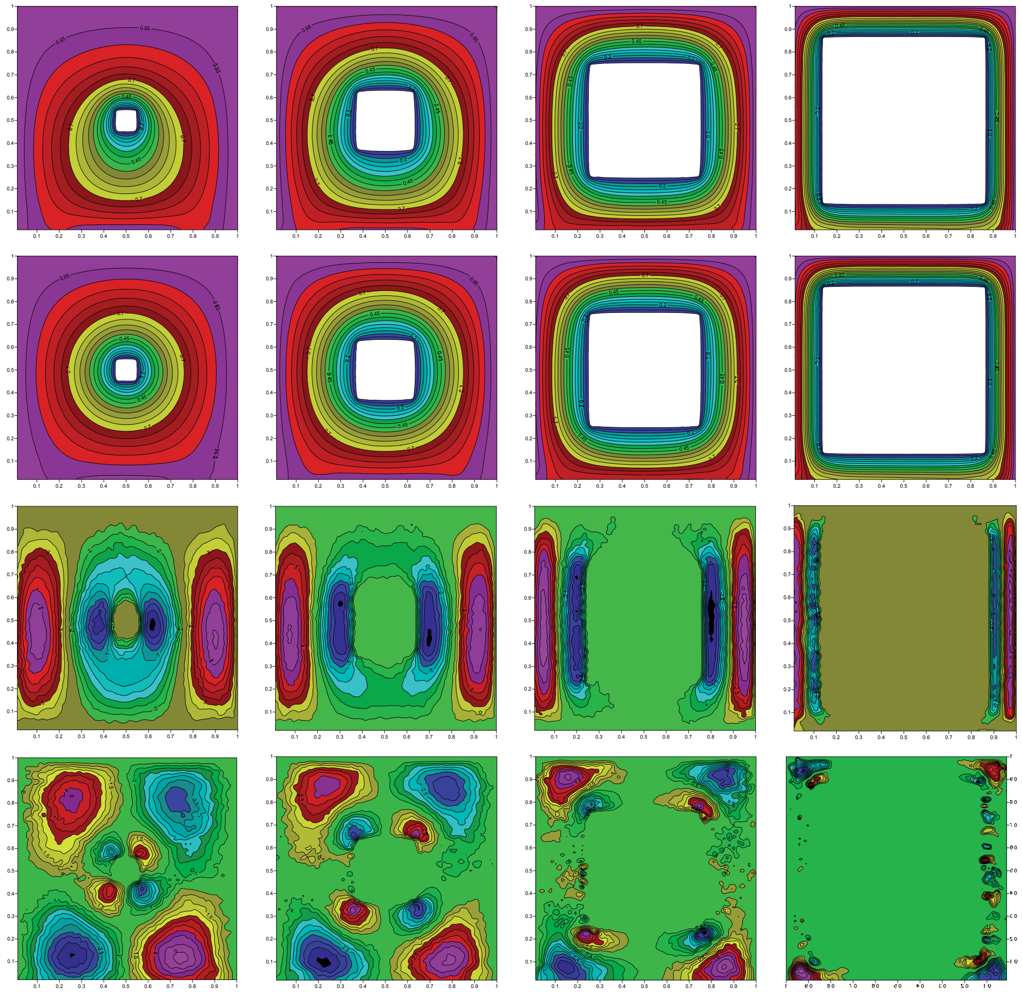

d=0.1 d=0.25 d=0.5 d=0.75

Figure 11. Depicts the effects of annulus length on the isotherms lines, concentration lines and vertical and horizontal velocity contours, respectively at Darcy parameter $\mathrm{Da}=10^{-2}$, $\varepsilon=0.5$, $\mathrm{Ra}=10^{4}$, $\mathrm{Sr}=1.0$, $\mathrm{Du}=0.12$, $N=1.0$, $\mathrm{Le}=1.0$ and $K^{*}=0.1$.

average Nusselt number increases. While, the average Sherwood number decreases as the Soret number increases with decreasing the Dufour number.

7. Conclusion

The unsteady Double-diffusive natural convection in an anisotropic porous square cavity/annulus has been investigated numerically using the stabilized ISPH method. In the current

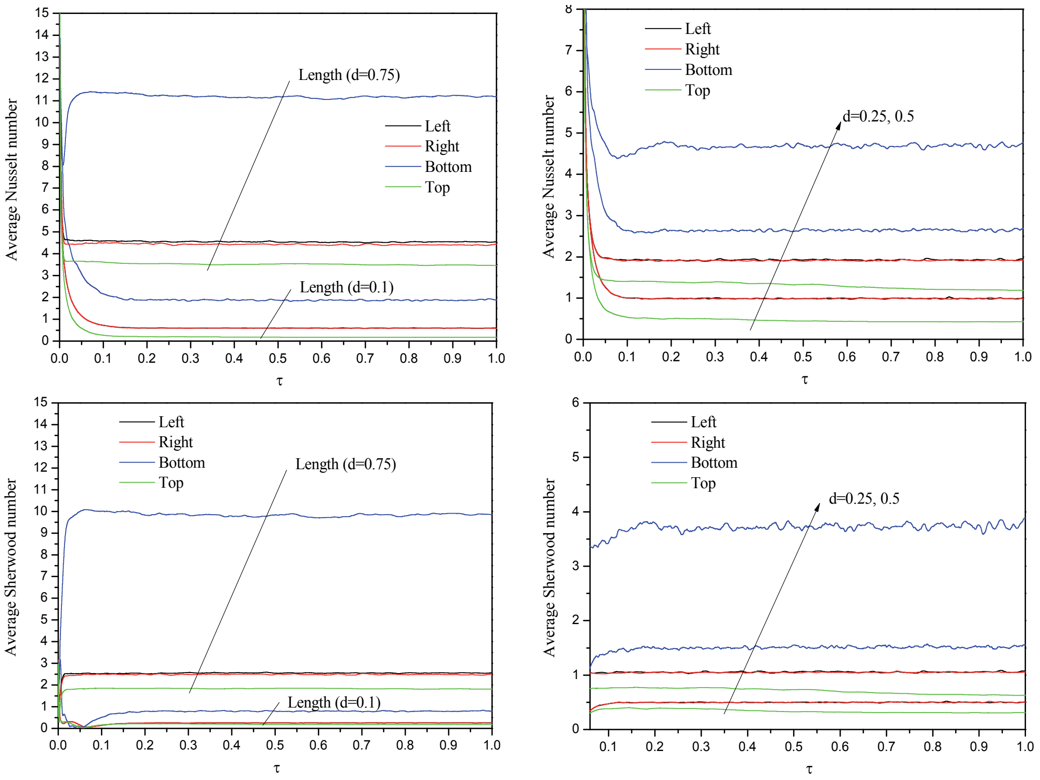

d= 0.1 and 0.75

d= 0.25 and 0. 5

Figure 12. Depicts the time histories for the effects of annulus length on the average Nusselt number and average Sherwood number, respectively at Darcy parameter $\mathrm{Da}=10^{-2}$, $\varepsilon=0.5$, $\mathrm{Ra}=10^4$, $\mathrm{Sr}=1.0$, $\mathrm{Du}=0.12$, $N=1.0$, $\mathrm{Le}=1.0$ and $K^*=0.1$.

ISPH algorithm, a semi-implicit velocity correction procedure was successfully used. The ISPH solution is validated by direct comparisons with previously published work and FVM solution on special cases of the problem, and the results show good agreements with these references. Graphic results for the temperature, concentration, horizontal velocity and vertical velocity contours and representative velocity, temperature, and concentration profiles at the cavity midsection for various parametric conditions were presented and discussed.

The following findings are summarized from the present investigation:

- The permeability ratio parameter increases leads to decrease in the both of heat conduction and flow regime.

- For the square annulus, the bottom wall has higher average Nusselt and Sherwood numbers than the rest of the walls. The top wall has lower average Nusselt and Sherwood numbers than the rest of the walls.

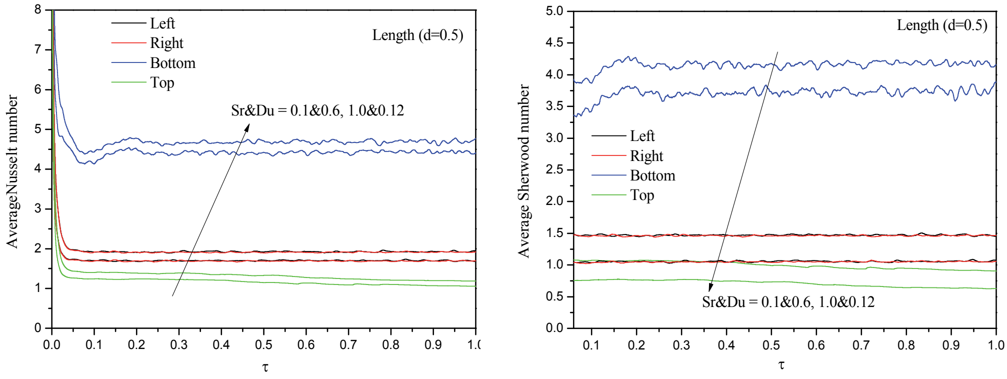

Average Nusselt number

Average Sherwood number

Figure 13. Depicts the time histories for the effects of combined Soret number with Dufour number on the average Nusselt number and average Sherwood number, respectively at annulus length 0.5, $\mathrm{Da}=10^{-2}$, $\varepsilon=0.5$, $\mathrm{Ra}=10^{4}$, $N=1.0$, $\mathrm{Le}=1.0$ and $K^{*}=0.1$.

- When the annulus length equals 0.75, there is almost no fluid activity at the top and bottom walls and from our observation due to restriction in space and movement of the fluid, the isotherms and concentration lines are almost equal under the effect of any parameter.

- As the Soret number increases with decreasing the value of Dufour number, the average Nusselt number increases. While, the average Sherwood number decreases as the Soret number increases with decreasing the Dufour number.

Nomenclature

C'	concentration of species	t	time
C	dimensionless species concentration	T'	temperature
C_p	specific heat	T	dimensionless temperature
Da	Darcy parameter	$U, \ V$	dimensionless velocity components
Du	Dufour number	$\boldsymbol{V}$	velocity vector
d	annulus length	$x, \ y$	Cartesian coordinates
d_0	particle size	$X, \ Y$	dimensionless coordinates
F	Forchheimer coefficient		**Greek symbols**
g	gravitational acceleration vector	α	thermal diffusivity
K	permeability	β_T	thermal expansion coefficient
k	thermal conductivity	β_C	compositional expansion coefficient

Nu	Nusselt number	ε	porosity
N	Buoyancy ratio	μ	viscosity
Le	Lewis number	υ	kinematic viscosity
P	pressure	σ	ratio of heat capacities
Pr	Prandtl number	ρ	density
Ra	Rayleigh number	τ	dimensionless time
Sh	Sherwood number	∇^2	Laplacian operator
Sr	Soret number		

Acknowledgements

This work was supported by JSPS KAKENHI Grant Numbers 26282106 and 13F03051.

Author details

Abdelraheem M. Aly[1,2*] and Mitsuteru Asai[1]

*Address all correspondence to: abdelreheam.abdallah@sci.svu.edu.eg

1 Department of Civil Engineering, Kyushu University, 744 Motooka, Nishi-ku, Fukuoka, Japan

2 Department of Mathematics, Faculty of Science, South Valley University, Qena, Egypt

References

[1] H. Demir, M. Mobedi, and S. Ülkü, "Effects of porosity on heat and mass transfer in a granular adsorbent bed," International Communications in Heat and Mass Transfer, vol. 36, no. 4, pp. 372-377, 2009.

[2] S. Han and R. J.Goldstein, "The heat/mass transfer analogy for a simulated turbine blade," International Journal of Heat and Mass Transfer, vol. 51, no. 21-22, pp. 5209-5225, 2008.

[3] S. Han and R. J. Goldstein, "The heat/mass transfer analogy for a simulated turbine end wall," International Journal of Heat and Mass Transfer, vol. 51, no. 11-12, pp. 3227-3244, 2008.

[4] G. Juncu, "Unsteady conjugate forced convection heat/mass transfer in ensembles of-Newtonian fluid spheres," International Journal of Heat and Mass Transfer, vol. 53, no. 13-14, pp. 2780- 2789, 2010.

[5] J.-S. Leu, J.-Y. Jang, and Y. Chou, "Heat and mass transfer for liquid film evaporation along a vertical plate covered with a thin porous layer," International Journal of Heat and Mass Transfer, vol. 49, no. 11-12, pp. 1937-1945, 2006.

[6] W. Pirompugd, C.-C.Wang, and S.Wongwises, "Finite circular fin method for heat and mass transfer characteristics for plain fin-and-tube heat exchangers under fully and partially wet surface conditions," International Journal of Heat and Mass Transfer, vol. 50, no. 3-4, pp. 552-565, 2007.

[7] W. Pirompugd, S. Wongwises, and C.-C. Wang, "Simultaneous heat and mass transfer characteristics for wavy fin-and-tube heat exchangers under dehumidifying conditions," International Journal of Heat and Mass Transfer, vol. 49,no. 1-2, pp. 132-143, 2006.

[8] M. Suresh and A. Mani, "Heat and mass transfer studies on R134a bubble absorber in R134a/DMF solution based on phenomenological theory," International Journal of Heat and Mass Transfer, vol. 53, no. 13-14, pp. 2813-2825, 2010.

[9] P. Talukdar, C.R. Iskra, and C. J. Simonson, "Combined heat and mass transfer for laminar flow of moist air in a 3D rectangular duct: CFD simulation and validation with experimental data," International Journal of Heat and Mass Transfer, vol. 51, no. 11- 12, pp. 3091-3102, 2008.

[10] L.-Z. Zhang, "Heat and mass transfer in plate-fin sinusoidal passages with vapor-permeable wall materials," International Journal of Heat and Mass Transfer, vol. 51, no. 3-4, pp. 618-629, 2008.

[11] L.-Z. Zhang, "Coupled heat and mass transfer in an application scale cross-flow hollow fiber membrane module for air humidification," International Journal of Heat and Mass Transfer, vol. 55, no. 21-22, pp. 5861-5869, 2012.

[12] F.-Y. Zhao, D. Liu, and G.-F. Tang, "Application issues of the streamline, heatline and massline for conjugate heat and mass transfer," International Journal of Heat and Mass Transfer, vol. 50, no. 1-2, pp. 320-334, 2007.

[13] A. Mahdy, "MHD non-Darcian free convection from a vertical wavy surface embedded in porous media in the presence of Soret and Dufour effect," International Communications in Heat and Mass Transfer, vol. 36, no. 10, pp. 1067-1074, 2009.

[14] M. A. Mansour, N. F. El-Anssary and A. M. Aly. Effects of Chemical Reaction and Thermal Stratification on MHD Free Convective Heat and Mass Transfer over a Vertical Stretching Surface Embedded in Porous Media Considering Soret and Dufour Numbers. Chemical Engineering Journal, vol. 145, pp. 340-345, 2008.

[15] A. J. Chamkha, M. F. Al-Amin, A. M. Aly, Unsteady double-diffusive natural convective MHD flow along a vertical cylinder in the presence of chemical reaction, thermal

radiation and Soret and Dufour effects. Journal of Naval Architecture and Marine Engineering, Vol 8, No 1, 2011.

[16] A. J. Chamkha and A. M. Aly, Heat and mass transfer in stagnation-point flow of a polar fluid towards a stretching surface in porous media in the presence of Soret, Dufour and chemical reaction effects. Chemical Engineering Communications, vol. 198, Issue 2, pp. 214-234, 2010.

[17] A. M. Aly, M. A. Mansour, Ali J. Chamkha. Effects of soret and Dufour numbers on free convection over isothermal and adiabatic stretching surfaces embedded in porous media, Journal of Porous Media, vol. 14, pp. 67-72, 2011.

[18] N. Nithyadevi and R.-J. Yang, "Double diffusive natural convection in a partially heated enclosure with Soret and Dufour effects," International Journal of Heat and Fluid Flow, vol. 30, no. 5, pp. 902-910, 2009.

[19] J. A. Weaver and R. Viskanta, "Natural convection due to horizontal temperature and concentration gradients—2. Species inter diffusion, Soret and Dufour effects," International Journal of Heat and Mass Transfer, vol. 34, no. 12, pp. 3121-3133, 1991.

[20] S. K. Sinha, T. Sundararajan, V.K. Garg, A variable property analysis of alloy solidification using the anisotropic porous medium approach, Int. J. Heat Mass Transfer Vol. 35, pp. 2865-2877, 1992.

[21] A. R. Chaudhuri, K.N. Seetharamu, T. Sundararajan, Modelling of steam surface condenser using finite element method, Comm. Numer. Meth. Engrg. Vol. 13, pp. 909-921, 1997.

[22] P. Cheng, Heat transfer in geothermal systems, Adu. Heat Transfer. vol. 14, pp. l-105, 1978.

[23] V. Prasad, F. A. Kulacki and M. Keyhani, Natural convection in porous media, J. Fluid Mech. vol. 150, pp. 89- 119, 1985.

[24] C. L. Tien and J. T. Hong, Natural convection in porous media under non-Darcian and non-uniform permeability conditions. In Natural Convection (Edited by S. Kakac, W. Aung and R. Viskanta). Hemisphere, Washington, DC, 1985.

[25] P. Cheng, Wall effects on fluid flow and heat transfer in porous media. Proc. ASME/JSME Heat Transfer Conf., pp. 297-303, 1987.

[26] V. Prasad, G. Lauriat and N. Kladias, Reexamination of Darcy-Brinkman solutions for free convection in porous media, Int. Symp. Convection in Porous Media: Non-Darcy Effects, Proc. 25th Nat. Heat Transfer Conf. vol. 1, pp. 569-580, 1988.

[27] N. Kladias and V. Prasad, Benard convection in porous media: effects of Darcy and Prandtl numbers, Int. Symp. Convection in Porous Media: Non-Darcy Effects, Proc. 25th Nat. Heat Transfer Conf. vol. 1, pp. 593-604, 1988.

[28] D. A. Nield and A. Bejan, Convection in Porous Media. Springer, New York, 1992.

[29] G. Degan, P. Vasseur, Boundary-layer regime in a vertical porous layer with anisotropic permeability and boundary effects, International Journal of Heat and Fluid Flow, Vol. 18, (3), pp. 334-343, 1997.

[30] P. Nithiarasu, K.N. Seetharamu, T. Sundararajan, Natural convective heat transfer in a fluid saturated variable porosity medium, International Journal of Heat and Mass Transfer, Vol. 40, (16), pp. 3955-3967, 1997.

[31] P. Nithiarasu, K. S. Sujatha, K. Ravindran, T. Sundararajan, K. N. Seetharamu, Non-Darcy natural convection in a hydrodynamically and thermally anisotropic porous medium, Computer Methods in Applied Mechanics and Engineering, Vol. 188, pp. 413-430, 2000.

[32] J. J. Monaghan. Simulating free surface flows with SPH. Journal of Computational Physics, 110(2):399 - 406, 1994.

[33] J. P. Morris, P. J. Fox, and Y. Zhu. Modeling low Reynolds number incompressible flows using SPH. Journal of Computational Physics, 136(1):214 - 226, 1997.

[34] S. J. Cummins and M. Rudman. An SPH projection method. Journal of Computational Physics, 152(2):584 - 607, 1999.

[35] M. Asai, A. M. Aly, Y. Sonoda and Y. Sakai. A Stabilized Incompressible SPH method by relaxing the Density invariance condition. Journal of Applied Mathematics, 2012; 2012: 24. doi:10.1155/2012/139583.

[36] A. M. Aly, M. Asai, Y. Sonoda. Modelling of surface tension force for free surface flows in ISPH method. International Journal of Numerical Methods for Heat & Fluid Flow, vol. 23 Iss: 3, pp.479-498, 2013.

[37] A. M. Aly, M. Asai, Y. Sonoda. Simulation of free falling rigid body into water by a stabilized incompressible SPH method. Ocean Systems Engineering, An International Journal, vol. 1(3): pp. 207-222, 2011.

[38] A. M. Aly, An Improved Incompressible Smoothed Particle Hydrodynamics to Simulate Fluid-Soil-Structure Interactions, Ph.D., Kyushu University, 2012.

[39] A. Chaniotis, D. Poulikakosand P. Koumoutsakos. Remeshed smoothed particle hydrodynamics for the simulationof viscous and heat conducting flows. Journal of ComputationalPhysics,182, no. 1: pp. 67-90, 2002.

[40] K. Szewc, J. Pozorski, and A. Tani`ere. Modeling of natural convection with smoothed particle hydrodynamics: Non-Boussinesq formulation. International Journal of Heat and Mass Transfer, vol. 54, no. 23-24: pp. 4807-16, 2011.

[41] M. E. Danis, M. Orhan and A. Ecder, ISPH modeling of transient natural convection, International Journal of Computational Fluid Dynamics, 27:1, pp. 15-31, 2013.

[42] A. M. Aly, Modeling of multi-phase flows and natural convection in a square cavity using an Incompressible Smoothed Particle Hydrodynamics, International Journal of Numerical Methods for Heat & Fluid Flow, vol. 25 (3), 2015.

[43] A. M. Aly, Mitsuteru Asai, Modelling of non-Darcy Flows through porous media using an extended Incompressible Smoothed Particle Hydrodynamics, Numerical Heat Transfer, Part B: Fundamentals, 2014, doi = 10.1080/10407790.2014.955772.

[44] A. M. Aly and S. E. Ahmed, An incompressible smoothed particle hydrodynamics method for natural/mixed convection in a non-Darcy anisotropic porous medium, Int. J. Heat Mass Transfer, vol. 77, pp. 1155-1168, 2014.

[45] S. V. Patankar, Numerical Heat Transfer and Fluid Flow, Hemisphere, McGraw-Hill, Washington DC, 1980.

[46] J. A. Meijerink and H. A. van der Vorst, An iterative solution method for linear systems of which the coefficient matrix is a symmetric M-matrix, l Mathematics of Computation, vol. 31, no. 137, pp. 148-162, 1977.

Evaluation of the New Phi-Plot Modeling Approach Optimization by Stepwise Solvent Gradient Simulated Moving Bed (SG-SMB) Simulator

Leôncio Diógenes Tavares Câmara

Additional information is available at the end of the chapter

http://dx.doi.org/10.5772/61252

Abstract

A new analytical design approach for operating conditions determination of solvent gradient simulated moving bed (SG-SMB) processes was proposed, which was based on the equilibrium theory. Also a new implemented simulator for SG-SMB was proposed to evaluate the new design approach. The simulator was totally developed in FORTRAN 90/95, assuming a stepwise modeling approach with a lumped mass transfer model between the solid adsorbent and liquid phase. The influence of the solvent modifier was considered by applying the Abel model, which takes into account the effect of modifier volume fraction over the partition coefficient. The optimal conditions determined from the new design approach were compared to the simulation results of a SG-SMB unit applied to the experimental separation of the amino acids phenylalanine and tryptophan. The new design approach, which is based on χ equation and phi-plot analysis, was able to predict a great number of operating conditions for complete separation of such molecules, which was validated by the simulations carried out by the new SG-SMB simulator. Such a SG-SMB simulator provides simulation results with very good agreement fitting the experimental data of the amino acid concentrations both in the extract as well as in the raffinate.

Keywords: Simulated moving bed, modeling, optimization

1. Introduction

The simulated moving bed (SMB) process has been used successfully in the separation of all kinds of molecules. It is a continuous process of interconnected chromatographic columns (HPLC), which can be used to separate molecule mixtures (enantiomeric and nonenantiomeric) with high purity and low solvent consumption. In the process, the positions of the two inlet

INTECH
open science | open minds

(feed and solvent) and the two outlet (extract and raffinate) streams are changed in the clockwise direction, leading to a simulated countercurrent movement of solid adsorbent phase. The extract and raffinate streams collect the more and less adsorbable enantiomer molecules, respectively. The solvent strength in the solvent gradient simulated moving bed (SG-SMB) process is modulated along the sections as the volume fraction of the modifier (ϕ) can be altered as can be seen in Fig. 1. The introduction of ethanol (modifier) in the desorbent stream leads to higher values of the modifier volume fraction at sections I and II, which reduces the adsorption affinity of the molecules in these regions. The contrary is observed in sections III and IV as the absence of ethanol in the inlet feed stream reduces the volume fraction of modifier in these regions, which consequently increase the adsorption affinity of molecules. Such procedures usually increase the purity of products as well as the productivity, reducing solvent consumption.

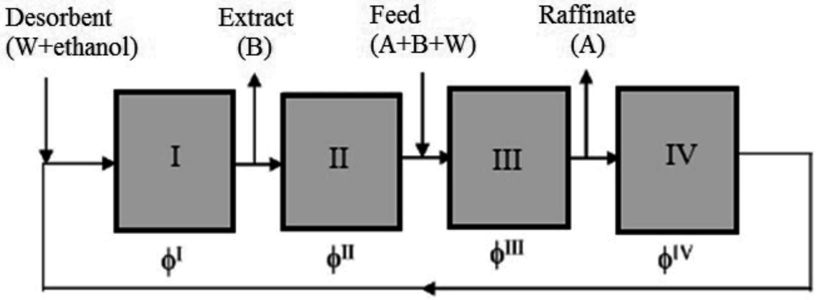

Figure 1. Schematic representation of SG-SMB

The application of gradients can be used in the performance improvement of simulated moving bed (SMB) as well as true moving bed (TMB) chromatography in which the most usual is the solvent-gradient method applied to SMB processes [1-15]. Other techniques include temperature gradients in SMB [16], micellar gradients in size-exclusion SMB [17], salt gradients in size-exchange SMB [18], pressure gradient in supercritical eluent SMB [19], voltage gradients in true moving bed (TMB) electrophoresis [20], etc. Migliorini et al. [16] showed the feasibility of temperature gradients applied in SMB, which may lead to significant advantages over the isothermal process mode. The authors observed an improvement in the productivity and a remarkable reduction in the solvent consumption with the possibility of tuning the enrichment by selection of proper temperature profile. Horneman et al. [17] showed the viability of surfactant-aided size-exclusion chromatography (SASEC) application on a SMB unit through selectivity modification by the addition of non-ionic micelles to the mobile phase. The use of a correct gradient leads to a significantly higher throughput of product concentration, which also leads to a lower solvent consumption if compared to a conventional SEC-SMB.

In the most common solvent-gradient simulated (SG-SMB) process as well as in other SMB gradient techniques, the main objective is the determination of flow rates and switching time, which leads to the full separation of molecules (high purity) with great productivity and low solvent consumption. Such a challenging objective can be achieved by utilizing, in general, either inverse problem optimization routines [1-4] or design criteria [5-8]. The application of inverse routines coupled with adequate mathematical mass transfer models [1-4] of the chromatographic column representations is desirable in the optimization problems for the achievement of optimal operating conditions. The inverse routine approach is interesting in the SG-SMB process optimization field as it can incorporate more realistic phenomenon effects such as mass transfer resistance, finite column efficiency, purity constrains, etc. The main disadvantages of such approaches are related to the high computational cost due to numerical simulations and to the algorithm accuracy and efficiency in the search for optimal solutions. The work of Nam et al. [1] is a good example as the authors utilized an inverse routine (based on genetic algorithm) combined with detailed mass transfer chromatographic rate models in the optimization of SG-SMB separation of phenylalanine and tryptophan. The optimization routine in this case was able to determine successfully the best operating conditions, which were further utilized and confirmed experimentally through a SG-SMB unit. The utilization of design criteria [5-8] is important in the determination of regions of complete separation. The design criteria approach is based on the frame of chromatography equilibrium theory or the so-called triangle theory in which the axial dispersion as well as the mass transfer resistance are neglected. Moreover, it is assumed that the separation performance of SG-TMB and SG-SMB is the same, and neither the main solvent nor the modifier interacts with the adsorbent phase. Abel et al. [7,8] provided design criteria and optimization results for the cases of linear and Langmuir isotherms, respectively. The authors carried out simulations from a mathematical mass transfer model with overall mass transfer and axial dispersion coefficients to confirm the validity of the theoretical analysis. In the work of Antos and Seidel-Morgenstern [5], a design criteria strategy, also based on the triangle theory, was coupled to mass transfer models (mixed cells in series) in the determination, through systematic numerical calculations, of suitable operating conditions as a function of averaged desorbent concentrations. The publication of Mazzotti et al. [19] in 1997 is maybe the first one in the literature which extends the isocratic concepts of the triangle theory to study and optimize a SMB gradient process or more specifically the pressure gradient mode in supercritical fluid SMB (SF-SMB).

The relevance and importance of the concepts of the triangle theory to study and evaluate the design criteria of solvent-gradient SMB (SG-SMB) processes were the motivation to proceed in the same direction applying such theory to establish a general project equation (χ equation) for optimal operating condition determination. The first step in such development, which was published recently [9] in a previous study (part I) showed the potential of the proposed screening strategy. It was used as the basis for further and deep studies for the present work (part II) in the analysis and evaluation of different operating conditions for performance improvement related to the separation of the amino acids phenylalanine and tryptophan. The proposed screening strategy was not used as usually described in the literature in the determination of regions of complete separation, but it was used in the minimization of the gradient of χ equation with the analysis of modifier volume fraction (Phi-plot) to determine the viability of separation (high purity in the extract and raffinate). A new implemented simulator for SG-SMB was also proposed to evaluate the new design approach, which assumed a stepwise modeling approach with a lumped mass transfer model between the solid adsorbent and liquid phase.

2. Phi-plot design criteria

Mazzotti et al. [4] proposed an approach, which is considered the classical procedure in the determination of the operating conditions of isocratic SMB process. The classical approach of Mazzotti et al. [4] was extended analogously to solvent gradient conditions (SG-SMB) considering the Henry's constant a function of the modifier volume fraction.

$$\mathbf{H}_{(+)}(\phi) < \mathbf{m}_{\mathrm{I}} < \infty \tag{1}$$

$$\mathbf{H}_{(-)}(\phi) < \mathbf{m}_{\mathrm{II}} < \mathbf{H}_{(+)}(\phi) \tag{2}$$

$$\mathbf{H}_{(-)}(\phi) < \mathbf{m}_{\mathrm{III}} < \mathbf{H}_{(+)}(\phi) \tag{3}$$

$$\frac{-\varepsilon_p}{(1-\varepsilon_p)} < \mathbf{m}_{\mathrm{IV}} < \mathbf{H}_{(-)}(\phi) \tag{4}$$

in which ε_p, m_i, $H_{(+)}$, and $H_{(-)}$ correspond to intraparticle porosity, flow rate ratios in each section i, and the Henry constants for the more and less adsorbable molecules, respectively.

Fig. 2A shows a typical volume fraction distribution of modifier along columns, assuming the introduction of modifier only in the desorbent inlet stream. As can be seen in Fig. 2A the modifier volume fraction reduces drastically in the forward positions after the feed inlet stream. Such a modifier volume fraction profile can be achieved assuming or not the adsorption of modifier by solid adsorbent phase. The results of Fig. 2A were obtained carrying out simulations through the proposed stepwise modeling of SG-SMB, which is described in the next section. In the proposed SG-SMB stepwise modeling approach the modifier adsorption by the adsorbent phase was not considered, and only the convection of ethanol (modifier) by a stepwise procedure (mixed cells in series) was assumed. In the work of Mun et al. [2], similar results of volume fraction of modifier along the columns were observed for the same condition of modifier introduction only in the desorbent inlet stream. The results are similar, but it should be noted that the authors assumed various phenomena for the ethanol (modifier) as convection, dispersion, film mass-transfer, intra-particle diffusion, and adsorption in a robust chromatographic mass transfer rate model. An important property in the design criteria is the average modifier volume fraction ($\hat{\phi}$), which is obtained from the arithmetic mean between the volume fraction of modifier in sections II (ϕ_{II}) and III (ϕ_{III}).

$$\hat{\phi} = \frac{\phi_{II} + \phi_{III}}{2} \tag{5}$$

The volume fraction of modifier in section II (ϕ_{II}) is equal to the volume fraction in the desorbent inlet stream (ϕ_0), and ϕ_{III} is obtained from the flow rate balance in the feed node (SG-SMB open loop case)

$$\phi_{III} = \frac{(\boldsymbol{F_D} - \boldsymbol{F_E})\phi_0}{(\boldsymbol{F_D} - \boldsymbol{F_E} + \boldsymbol{F_F})} \tag{6}$$

in which F_D, F_E, and F_F correspond to flow rate of desorbent, extract and feed, respectively.

The Henry values can be calculated according to volume fraction of modifier along the columns (Fig. 2A), and they can be plotted along the sections II and III as difference in terms of the inequalities of Eqs. 2 and 3 leading to the inversion of the profiles (Fig. 2B).

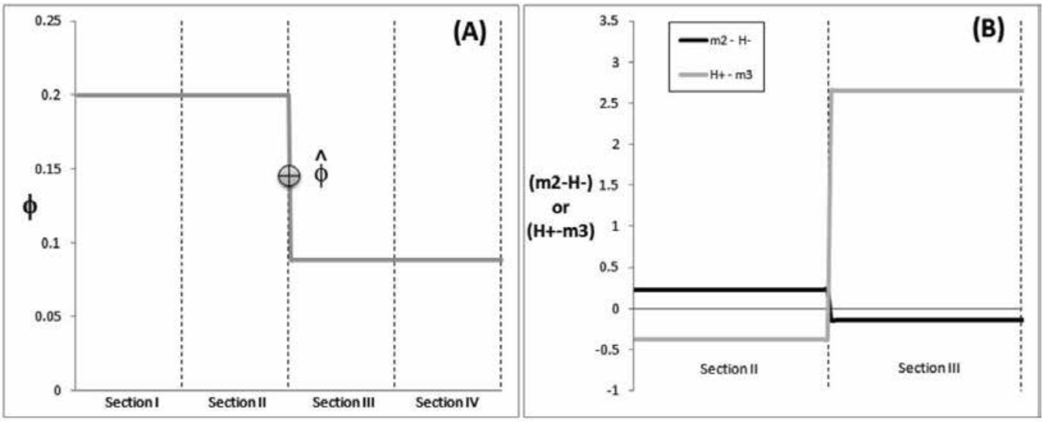

Figure 2. Modifier volume fraction along the sections (A); Inversion in the flow rates ratio difference near the feed inlet (B)

The inversion in the profiles of the difference (flow rate and Henry) along sections II and III is desirable, since for complete separation of the molecules the inequalities should be as follows:

$$\mathbf{m}_{\mathrm{II}} > \mathbf{H}_{(-)}(\phi_{\mathrm{II}}) \text{ and } \mathbf{H}_{(+)}(\phi_{\mathrm{III}}) > \mathbf{m}_{\mathrm{III}} \tag{7}$$

or

$$\mathbf{m}_{\mathrm{II}} - \mathbf{H}_{(-)}(\phi_{\mathrm{II}}) > 0 \text{ and } \mathbf{H}_{(+)}\left(\phi_{\mathrm{III}}\right) - \mathbf{m}_{\mathrm{III}} > 0 \tag{8}$$

At the feed entrance (limits of sections II and III), there is an intersection in the flow rate-Henry difference profiles so the above inequalities (Eq. 8) can be combined as

$$\mathbf{H}_{(+)}\left(\hat{\phi}\right)+\mathbf{H}_{(-)}\left(\hat{\phi}\right)=\mathbf{m}_{\mathrm{II}}+\mathbf{m}_{\mathrm{III}} \tag{9}$$

in which the Henry values for the more adsorbed molecules, $\mathbf{H}_{(+)}(\hat{\phi})$, and the less adsorbed molecules, $\mathbf{H}_{(-)}(\hat{\phi})$, are functions of the average volume fraction of modifier. The Eq. (9) is described as the difference of the terms leading to the project design equation (χ equation)

$$\chi=\mathbf{H}_{(+)}\left(\hat{\phi}\right)+\mathbf{H}_{(-)}\left(\hat{\phi}\right)-\mathbf{m}_{\mathrm{II}}+\mathbf{m}_{\mathrm{III}} \tag{10}$$

From Eq. (10) it can be noted that the best operating condition corresponds to that in which terms difference tends to zero ($\chi \rightarrow 0$).

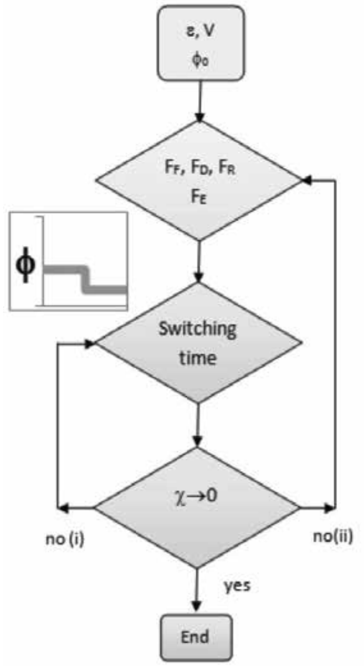

Figure 3. Flowchart of χ-equation design procedure

The flowchart of Fig. 3 describes the optimization routine, which starts with the specification of chromatographic columns volume, total porosity, and volume fraction of modifier at desorbent (ϕ_0). The next step is the specification of the volumetric flow rates followed by the switching time, which is the first one that can be varied to achieve the optimum condition of Eq. 10 ($\chi \rightarrow 0$). Both the switching time (way no (i)) as well as the volumetric flow rates (way no (ii)) can be varied in order to minimize the difference of terms in Eq. 10 ($\chi \rightarrow 0$). The evaluation of Eq. 10 is carried out analyzing at the same time the plot of the flow rate–Henry differences according to volume fraction of modifier (phi-plot). For complete separation of molecules (more and less adsorbable) it is necessary to locate both curves (one for each kind) in the positive region of the phi-plot graph. The proposed optimization routine can be implemented easily as an excel spreadsheet in such way that the user can alter manually the SG-SMB conditions and at the same time evaluate the separation performance.

3. Modeling approach of SG-SMB simulator

The chromatographic columns of the SG-SMB process are modeled as a discrete representation of *N* mixed cells in series [21]:

$$\frac{dC_i^p}{dt} + \frac{dq_i^p}{dt} = (C_{i0}^p - C_i^p)\sigma_i^p \tag{11}$$

In which $\mathbf{q_i^p}$, $\mathbf{C_i^p}$, $\mathbf{C_{i0}^p}$, and t represent the compound i concentration in the solid adsorbent phase, the compound i concentration in the liquid phase, the compound i concentration in the liquid phase at the mixed cell entrance, and the time, respectively, all at column p. In Eq. 11, $\boldsymbol{\sigma_i^p = F / V}$ with V, F, and ε representing the volume, the volumetric flow rate, and the total porosity of the mixed cell, respectively. In the Eq. 11 it is assumed that the molecules in the mass transfer between the liquid and solid phase stays at the interface inside the liquid phase so the same liquid volume is used in the calculation of concentrations. Therefore, the retention factor, *ki*, is equal to the equilibrium constant, *Keq*, since the volume is the same for the liquid and solid concentrations.

In such a modeling approach the ethanol adsorption on the solid adsorbent phase was not considered, so in the mass balance of modifier (Eq. 12) along the chromatographic column, the same stepwise model for the ethanol convection along chromatographic columns without the mass transfer resistance term was assumed.

$$\frac{d\phi^p}{dt} = (\phi_0^p - \phi^p)\sigma_i^p \tag{12}$$

In Eq. 11, a lumped mass transfer model representing all the effects of mass transfer between the liquid and the solid adsorbent phase is assumed. The isotherms were utilized only in the mass transfer parameters determination in the chromatographic column characterization step. Therefore, the slow mass transfer kinetic is the main and dominant effect of mass transfer between the phases (solid and liquid). The lumped mass transfer kinetic model is presented in Eq. 13, below, which depends on the concentrations as well as the mass transfer kinetic parameters of adsorption (η_{1i}) and desorption (λ_{2i}).

$$\frac{dq_i^p}{dt} = \eta_{1i} C_i^p - \lambda_{2i} q_i^p \tag{13}$$

The solute mass balances at the nodes of the SG-SMB process of Fig. 1 is solved incorporating the volumetric flow rates of each stream (Feed, Desorbent, Extract, and Raffinate). The new mass balance of solutes at the nodes is recalculated after each change in the configuration of the streams to be incorporated into the global mass balance equations of the columns. The Eqs. 11 to 13 are organized explicitly according to a simple finite difference approach and solved numerically utilizing a 4th order Runge-Kutta method, with a time step equal to 10^{-4}, utilizing Fortran90/95.

4. Results and discussions

4.1. Column characterization by SG-SMB simulator

The column characterization is the first step in the implementation of the SG-SMB simulator. The adapted experimental results of Nam et al. [22] in Fig. 4 show that the peak residence time of phenylalanine and tryptophan is a function of the volume fraction of modifier (ϕ). In such experimental results it can be observed reduction in the affinity of solutes with the adsorbent phase, increasing the volume fraction of adsorbent (ϕ), which reduces the elution time or residence time of molecules. As can be seen in Fig. 4, tryptophan (Fig. 4B) is the more adsorbed molecule due to higher values of residence time of the molecules in the chromatographic columns.

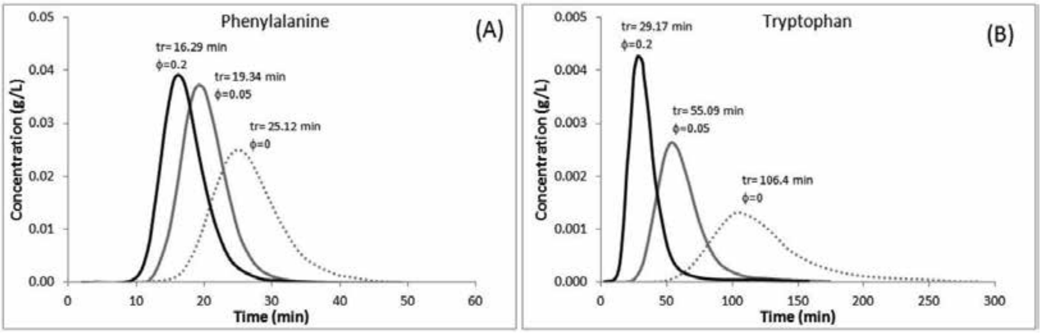

Figure 4. Adapted experimental results of Nam et al.[22]

The residence times of the two kinds of molecules (phenylalanine and tryptophan) in Fig. 4 were utilized in the column characterization for the determination of the mass transfer parameters of the lumped mass transfer model (Eq. 13). For each amino acid, in each condition of the volume fraction of modifier (ϕ=0, 0.05 and 0.2), it was determined the mass transfer parameters of adsorption and desorption that led to the same experimental value of residence time. In such procedures, an important property utilized was the partition coefficient (K), which was obtained by the Abel's model [1, 23]

$$\mathbf{K} = \frac{\mathbf{p}_1}{(1+\mathbf{p}_2\phi)^{\mathbf{p}_3}} \tag{14}$$

where p_1, p_2 and p_3 are the model parameters for each amino acid. The utilized model parameters p_1, p_2 and p_3 for tryptophan and phenylalanine were (11.6750, 11.980, 1.140) and (1.8817, 34.043, 0.623), respectively. It should be emphasized that the same Abel's model, with parameters for each amino acid, was utilized in the phi-plot design criteria (section 2) for the determination of the Henry's constants. After the acquiring of the mass transfer parameters (each ϕ value), linear interpolations in the modifier volume fraction domains for determination of the mass transfer parameter equations in the ϕ intervals were carried out. Eqs. 15 to 21 present the mass transfer parameter equations related to each ϕ interval, which were utilized in the proposed SG-SMB simulator. Such equations were applied in the calculations of the mass transfer parameters (according to ϕ values) utilized in the lumped mass transfer model of Eq. 13.

$$\eta_{1\text{ phenyl}} = -602.89\ \phi + 335.75\ \left(0.0 \le \phi \le \phi_0\right) \tag{15}$$

$$\eta_{1\text{ tryp}} = -7128.5\ \phi + 459.02\ \left(0.0 \le \phi < 0.05\right) \tag{16}$$

$$\eta_{1\text{ tryp}} = 938.32\phi + 55.68\ \left(0.05 \le \phi < \phi_0\right) \tag{17}$$

$$\lambda_{2\text{ phenyl}} = 2460.0\ \phi + 178.5\ \left(0.0 \le \phi < 0.05\right) \tag{18}$$

$$\lambda_{2\text{ phenyl}} = 733.33\ \phi + 264.83\ \left(0.05 \le \phi \le \phi_0\right) \tag{19}$$

$$\lambda_{2\text{ tryp}} = -486.0\ \phi + 39.3\ \left(0.0 \le \phi < 0.05\right) \tag{20}$$

$$\lambda_{2\text{ tryp}} = 460.0\ \phi - 8.0\ \left(0.05 \le \phi \le \phi_0\right) \tag{21}$$

4.2. Phi-plot design criteria evaluation by SG-SMB simulator

The next Table 1 presents the two conditions (cases 1 and 2) studied by Nam et al. [1] in performance optimization of SG-SMB separations of phenylalanine and tryptophan. The authors utilized distilled deionized water and ethanol as main solvent and modifier solvent. The adsorbent used was PVP resin (poly-4-vinylpyridine, cross linked) with intra-particle porosity of 0.55. The inter-particle porosity of the packed column was 0.33, obtained by tracer-molecule pulse tests. The conditions of Table 1 were utilized in the proposed design criteria approach, which was analyzed and evaluated through the new implemented SG-SMB simulator.

Zone flow rates (mL/min)	Case 1	Case 2
Q^{I}	10.00	10.00
Q^{II}	4.02	4.56
Q^{III}	9.06	11.21
Q^{IV}	3.62	4.52
Inlet/outlet flow rates (mL/min)		
Q_{feed}	5.04	6.65
Q_{des}	10.00	10.00
Q_{ext}	5.98	5.44
Q_{raf}	5.44	6.69
Switching time, t_{sw} (min)	25.95	21.97

Table 1. Optimized SG-SMB conditions studied by Nam et al. [1]

The two conditions of Table 1 were utilized in the phi-plot design criteria as well as in the SG-SMB simulator for three different values of porosity, the bed porosity (inter-particle), the intra-particle porosity and the total porosity, which correspond, respectively, to 0.33, 0.55 and 0.69. The last porosity value is the combination of both porosities, the inter-particle and the intra-particle. In the simulations carried out by Nam et al. [1] only the bed porosity and the intra-particle porosity were used in the robust modeling approach, respectively, in the mass transfer model of convection along the column combined with the mass transfer model inside the adsorbent pores. It should be noted that in the stepwise modeling approach applied in the present work only one porosity value is utilized in the model which is considered the total porosity. Therefore, any porosity value utilized in the present stepwise approach with lumped mass transfer model (SW-LM) is considered total porosity as such one assumes mass transfer phenomena in any kind of pore structure.

Table 2 presents the results of design criteria (χ equation) as well as of the SG-SMB simulator (purity values, productivity and solvent consumption) for three different values of total porosity, assuming the zone flow rates of case 1 in Table 1. As can be seen in Table 2, the best optimization result corresponds to that in which the χ equation tends to zero ($\chi \rightarrow 0$). This condition corresponds to the total porosity of 0.55, which is lower than the total porosity obtained by the bed porosity and the intra-particle porosity of PVP resin [1,23]. Such a porosity value led to purities in the extract and raffinate higher than 99% with higher productivity and lower solvent consumption.

Porosity	0.33	0.55	0.69
χ	-1.63	0.67	3.83
Raffinate purity (%)	69.38	99.99	99.21
Extract purity (%)	100.00	99.45	73.87
Productivity (g/h.L)	0.431	0.580	0.474
Solvent consumption (L/g)	3.264	2.426	2.967

Table 2. Porosity effect in the SG-SMB performance

The SG-SMB simulation results of Fig. 5 show the concentrations of phenylalanine and tryptophan along the columns for the three different values of total porosity (0.33, 0.55 and 0.69). Moreover, it can be seen in Fig. 5 the ethanol (modifier) volume fraction along the chromatographic columns, which has a significant reduction in the concentration in the regions after the feed (F). In the simulation results, utilizing the porosity equal to 0.33 (Fig. 5A), it can be observed the contamination of the raffinate (R) with both substances leading to a lower purity value of phenylalanie in the raffinate (see Table 2). The contrary is observed utilizing the porosity of 0.69 (Fig. 5C) in which the contamination is situated in the extract (E), which reduces the purity of tryptophan in such a region (see Table 2). In the porosity value of 0.55 (Fig. 5B), there is only tryptophan in the extract (E) and phenylalanine in the raffinate (R) so the respective purity is higher in both regions.

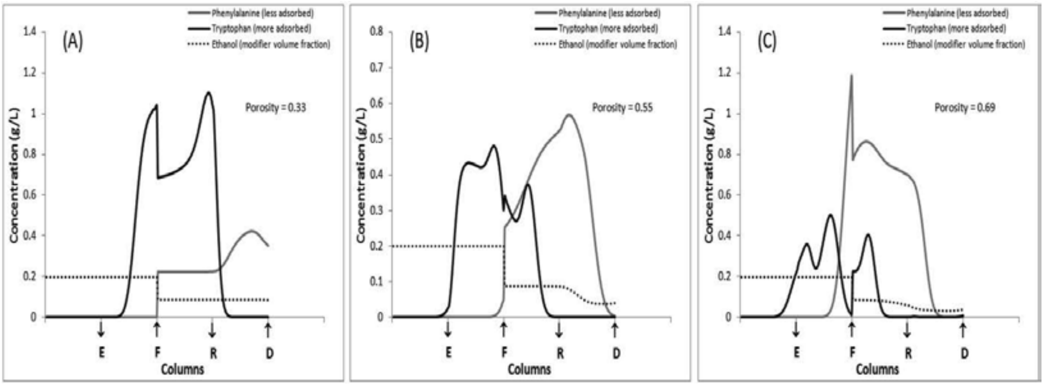

Figure 5. SG-SMB simulation results for the three studied values of total porosity

The design criteria results presented in Fig. 6 confirm the most favorable result for SG-SMB separation when utilizing the total porosity of 0.55 which led to the χ equation value of 0.63 (vide Table 2). The desirable inversion in the profiles (flow rate ratio–Henry difference) along sections II and III can be noted in Fig. 6A. The phi-plot results of Fig. 6B (volume fraction of modifier (ϕ) versus flow rate–Henry difference) are in the positive region of the graph, which indicates the viability of complete separation for both molecules. The grey triangle and the black square, which represent the flow rate–Henry difference in sections II and III, respectively, are also in the positive region, which validates the inequalities of Eq. 8. The analysis in terms of sections II and III is important as such regions represent a key role in the separation performance of SMB process. The inequalities of Eqs. 1 to 4 are plotted in Fig. 6C as the difference in terms of flow rate ratio–Henry (m-H or H-m). As can be seen in Fig. 6C, all the m-H and H-m difference quantities are positive, which indicate that the inequalities of Eqs 1 to 4 are true for complete separation. The volume fraction of modifier (ϕ) along columns obtained utilizing the flow rate balance of Eq. 6 is plotted in Fig. 6D, which shows the significant reduction in ϕ concentration after the feed (F).

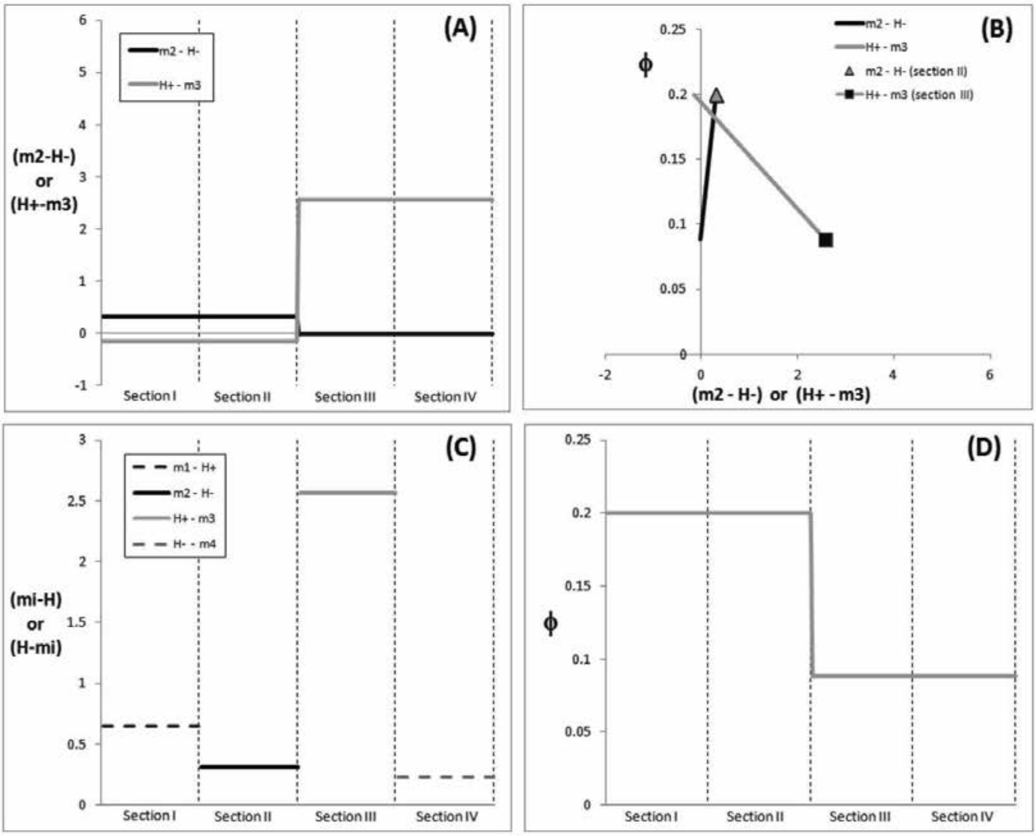

Figure 6. Design criteria approach with phi-plot results for total porosity of 0.55

Fig. 7 presents the design criteria results utilizing the ϕ distribution along the sections or columns (Fig. 7D) obtained not by the flow rate balance of Eq.6 but by the simulation results of the proposed SG-SMB simulator. Therefore, Fig. 6D and Fig. 7D were obtained, respectively, via the flow rate balance of Eq.6 and the SG-SMB simulator. Comparing both Figs. 6D and 7D it can be seen that the profiles of ϕ are very similar differing only in section IV. So it can be noted that both design criteria results of Fig. 6 and 7 are very similar and have the same conclusions as the ϕ concentration profiles are almost the same. It should be realized that the modifier volume fraction (ϕ) is the main data utilized in the determination of all the design criteria results.

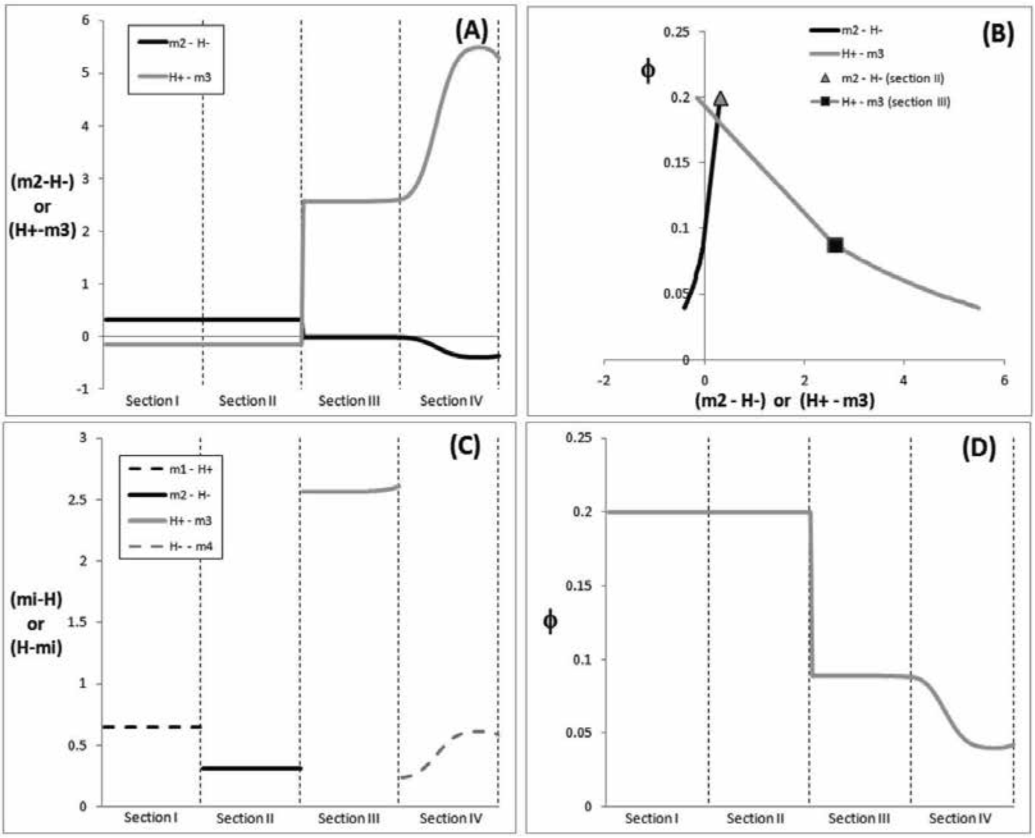

Figure 7. Design criteria approach with phi-plot results for total porosity of 0.55. The ϕ distribution obtained by SG-SMB simulator

Figs. 8 and 9 show the design criteria results for the two other porosity values in Table 2, 0.33, and 0.69, respectively. As can be seen in Table 2, the low porosity value of 0.33 led to a negative χ equation quantity (-1.63), which is far from the ideal ($\chi \rightarrow 0$) decreasing the purity in the raffinate. The low raffinate purity (see Fig. 5A) is due to the presence of both substances (phenylalanine and tryptophan) in raffinate (R) region after feed (F). Analyzing Fig. 8 it can be observed that the (H_+ - m_3) difference is not positive, so it is situated in the negative region of the phi-plot graph (Fig. 8B). The flow rate ratio in section 3 (m_3) is higher than the Henry constant as the (H_+ - m_3) difference is negative, therefore, the strong component (tryptophan) is carried upwards, contaminating the raffinate. Such a conclusion is evident in Fig. 5A as the concentration profile of tryptophan (black line) is wider for right positions if compared to the profile of the best condition of complete separation (Fig. 5B). Another implication due to the negative difference of (H_+ - m_3) is the non-intersection of the profiles in Fig. 8A. In Fig. 8C it can be observed that the flow rate ratio in section IV (m_4) is higher than the Henry constant for the less adsorbed component ($H_{(-)}$-m_4<0) so less adsorbed molecules (phenylalanine) are carried upwards by the liquid phase, increasing its concentration in the upwards position as can be observed in section IV of Fig. 5A.

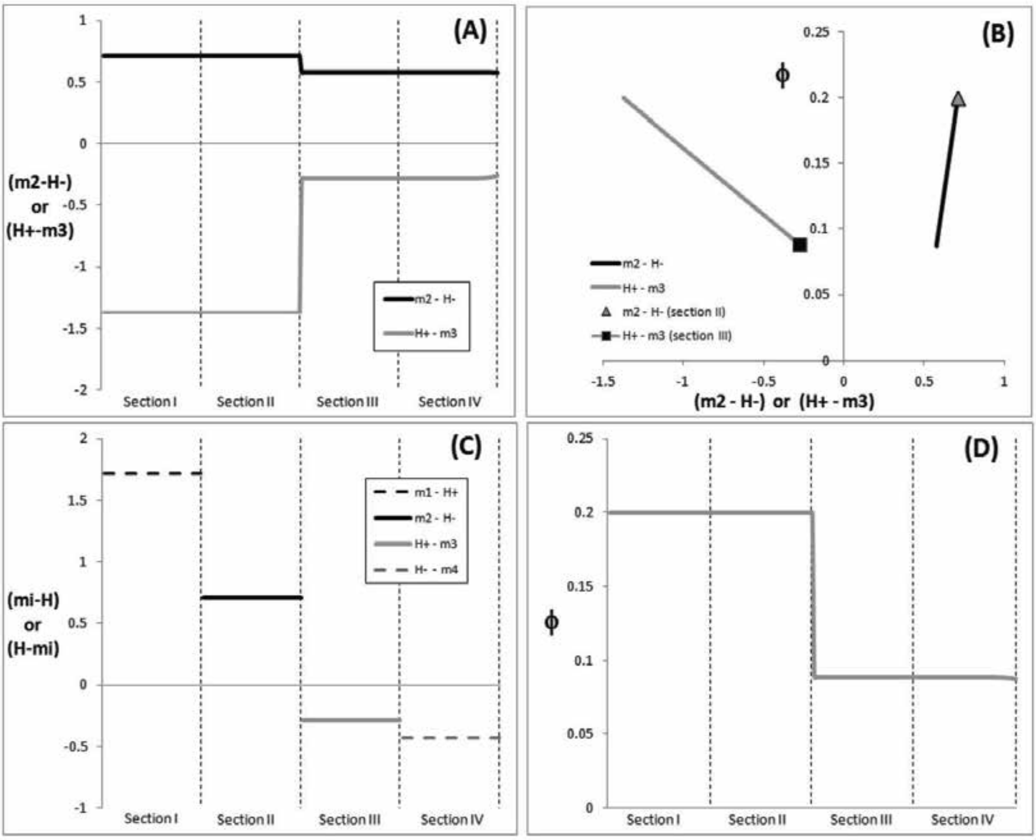

Figure 8. Design criteria approach with phi-plot results for total porosity of 0.33. The φ distribution obtained by SG-SMB simulator

The design criteria results for porosity equal to 0.69 are presented in Fig. 9 and it can be observed in the phi-plot of Fig. 9B that the (m_2-$H_{(-)}$) difference is negative so the Henry constant is higher than the flow rate ratio in section II. It means that the less adsorbed molecules (phenylalanine) are more retained in the solid adsorbent phase than it should be contaminating the extract port and reducing the purity. It is clear in Fig. 5C (porosity equal to 0.69) that the phenylalanine profile concentration (gray line) is wider (displaced to the left), reaching and contaminating the extract port. As can be seen in Table 2, the high porosity value of 0.69 led to a positive χ equation quantity (3.83), which is far from the ideal ($\chi \rightarrow 0$), decreasing the purity in the extract. Moreover in section I, the Henry constant for the more adsorbed is higher than the flow rate ratio as the (m_1-$H_{(+)}$) difference is negative (Fig. 9C). So in section I the tryptophan is more retained by the solid adsorbent phase than it should be. The implication is a wider concentration profile (displaced to the left) of the more adsorbed molecules, which can be visualized in Fig. 5C for the tryptophan (black line). Fig. 9A shows that the ideal intersection profile is not achieved as the requirements for complete separation are not fulfilled.

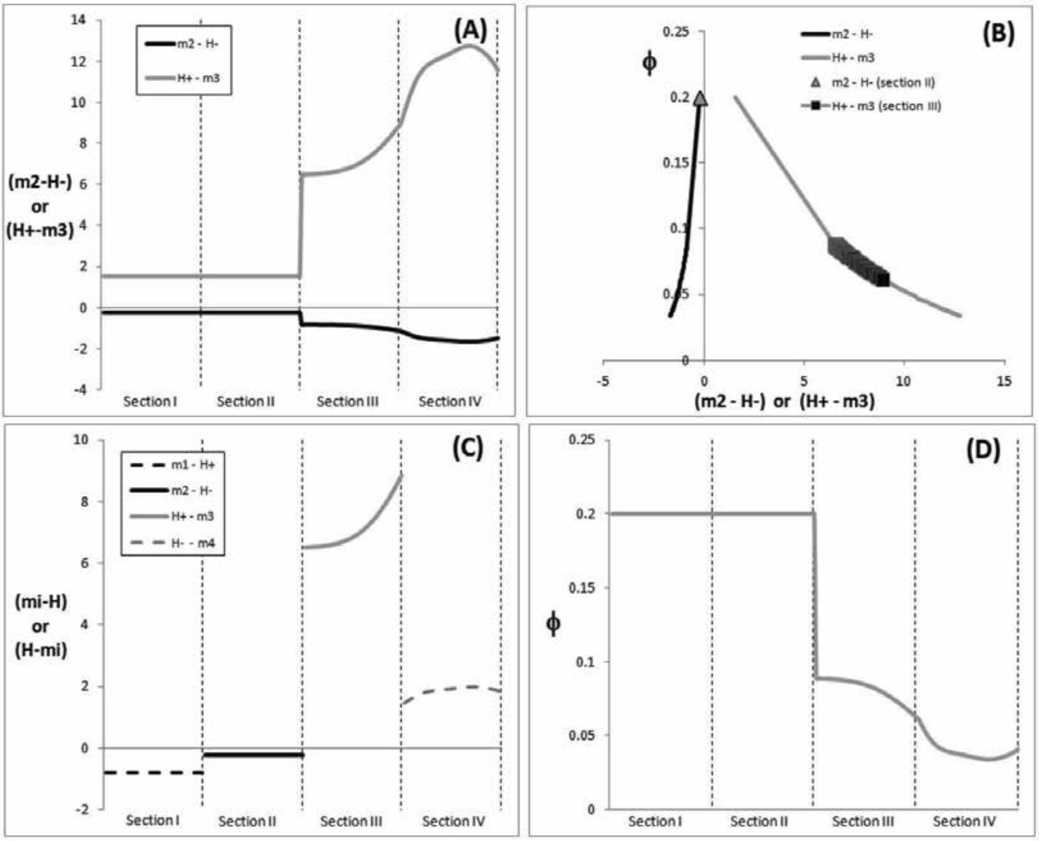

Figure 9. Design criteria approach with phi-plot results for total porosity of 0.69. The ϕ distribution obtained by SG-SMB simulator

The clockwise cyclic movement of the SG-SMB streams lead to cyclic concentration of molecules along time as can be seen in Fig. 10 for the two conditions of porosity, 0.55 (Fig. 10A) and 0.69 (Fig. 10B). Fig. 10 provides simulation results of concentration in the extract along time. In the condition of complete separation (Fig. 10A for porosity of 0.55), it can be observed the significant transient concentration of the more adsorbent molecule (tryptophan) if compared to the lower concentration of the less adsorbed (phenylalanine). The same separation performance is not achieved in the porosity condition of 0.69 (Fig. 10B) as both molecules have significant values of concentration. The periodic concentration of molecules in Figs. 10A and B can be visualized, respectively, through the concentration profiles along the columns in Figs. 5B and C. In each switch time period, the extract port varies from the right, near the Feed (F), to a left position in which there is a variation in the concentrations with time that depends on the concentration profiles of each solute along the columns (vide Figs. 5B and C).

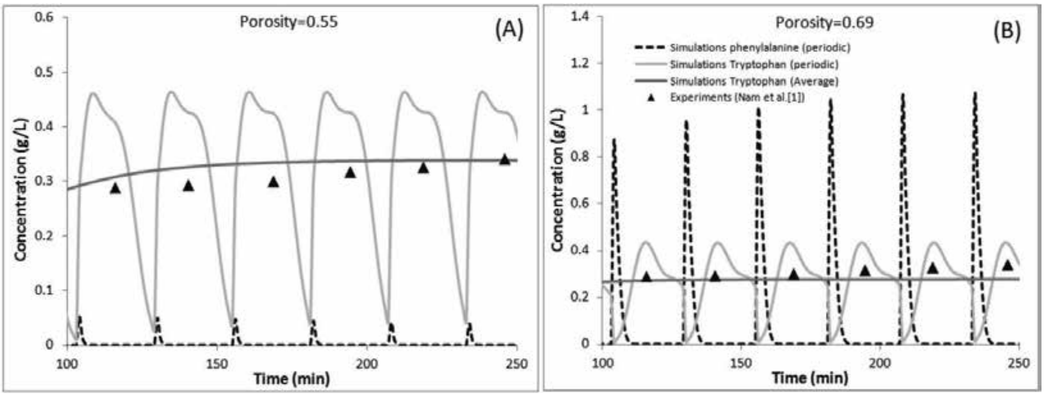

Figure 10. Concentrations along time in the extract of SG-SMB for porosity values of 0.55 (A) and of 0.69 (B)

Fig. 11 presents the correlations between the simulation results of the proposed SG-SMB simulator and the experimental data obtained by Nam et al. [1], who studied the separation performance of the amino acids phenylalanine and tryptophan in a SG-SMB unit. The simulations are plotted in terms of periodic (dotted lines) and average (solid line) concentrations along time in the extract as well as in the raffinate. From Fig. 11 it can be observed the good agreement between the average simulations and the experiments (black triangles) of Nam et al. [1] when utilizing the total porosity of 0.55. It must be remembered that there is no adjustment between the simulations and the experiments in Fig. 11 as it was utilized the mass transfer equations determined previously in the column characterization.

The two different operating conditions utilized by Nam et al. [1] and described in Table 1 were evaluated by the proposed SG-SMB simulator. The comparison results are presented in Table 3, and the close productivity values for both operating conditions studied can be seen. In terms of purity of extract and raffinate, the SG-SMB simulator provided values higher than those obtained by Nam et al. [1]. It can be observed that increasing the feed flow rate and reducing the switching time (second option) lead to a higher productivity with lower solvent consumption. The disadvantage in such a procedure is the reduction in both purities of the extract as well as raffinate.

New simulation results (SG-SMB simulator) for the optimization of productivity as well as solvent consumption were carried out increasing the feed flow rate as described in Table 4. In Table 4 it can be seen that it is possible to increase the productivity with solvent reduction by only adjusting the switching time. The purities had a small reduction, which was more evident in the extract stream. Also in Table 4 there are the design criteria results in terms of χ equation. As described in Table 4, the feed flow rate increase led to optimization conditions far from the ideal as the χ goes far from zero.

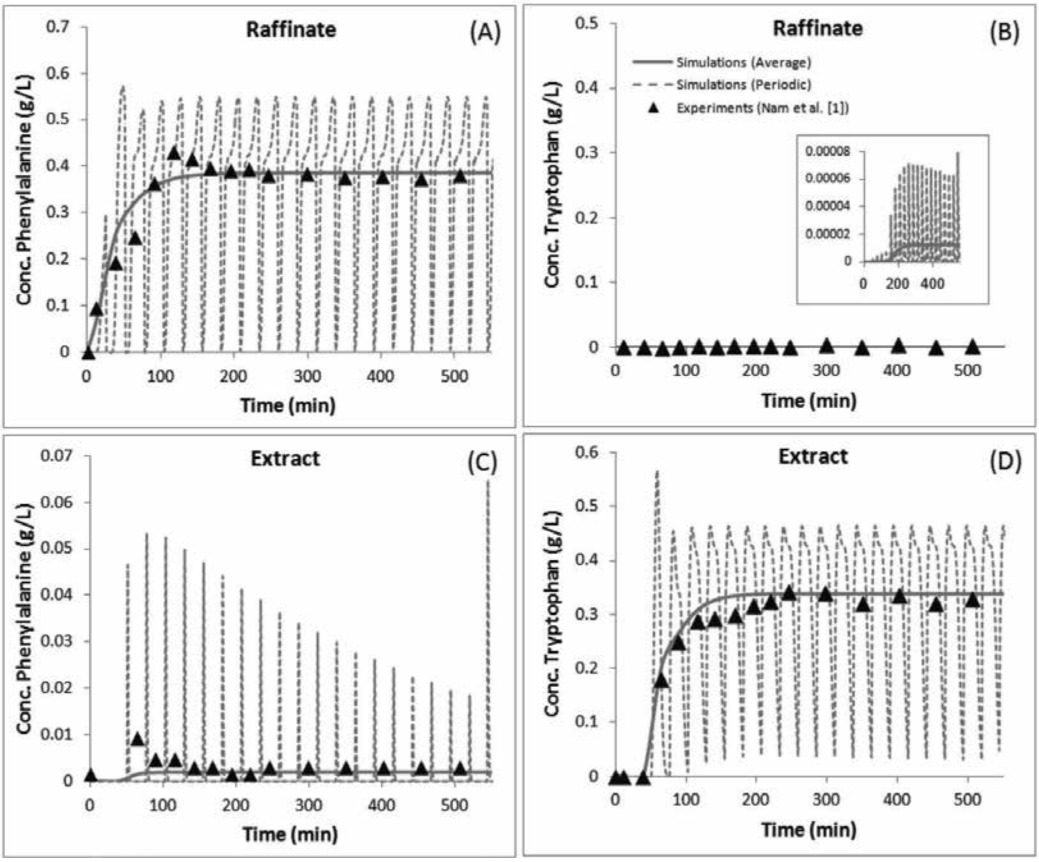

Figure 11. Comparisons between the simulation results from the SG-SMB simulator and the experimental data obtained by Nam et al. [1]; porosity equal to 0.55

	Nam et al.[1]	This work	Nam et al.[1]	This work
Feed flow rate (Q_{feed})	5.04	5.04	6.65	6.65
Switching time (min)	25.95	25.95	21.97	21.97
Raffinate purity (%)	98.00	99.99	97.40	99.85
Extract purity (%)	98.00	99.45	96.30	98.86
Productivity (g/h.L)	0.559	0.580	0.711	0.725
Solvent consumption (L/g)	-	2.426	-	1.943

Table 3. Separation performance of SG-SMB by comparison of two operating conditions

Feed flow rate (Q_{feed}) (mL/min)	**5.04**	**10**	**15**
Switching time (min)	25.95	28.00	25.00
χ	0.67	-2.36	-3.61
Raffinate purity (%)	99.99	99.91	99.91
Extract purity (%)	99.45	99.91	99.40
Productivity (g/h.L)	0.580	0.926	1.207
Solvent consumption (L/g)	2.426	1.522	1.167

Table 4. Improvement of productivity under feed flow rate increase (porosity equal to 0.55)

The phi-plot design criteria results related to feed flow rates of 10 and 15 mL/min (Table 4) are presented in Figs. 12A-B and 12C-D, respectively. According to Table 4 the χ equation values for feed flow rates of 10 and 15 mL/min were, respectively, equal to -2.36 and -3.61 so the higher feed flow rate corresponds to the inferior optimization condition (χ far from zero). In Fig. 12C such a conclusion is clear as the phi-plot of higher feed flow rate (15 mL/mi) is displaced to the left near the boundary of the positive region of the graph (compare Fig. 12A and C). Other results for the same feed flow rate (15 mL/min) show differences in the flow rate ratio–Henry (Fig. 12D) that are inferior in terms of domain if compared to those obtained using the feed flow rate of 10 mL/min (Fig. 12B). It should be emphasized that the optimization results from design criteria study are not a guarantee of complete separation of the molecules as the mass transfer effects of the real SG-SMB process are not assumed in such approach.

Different SG-SMB operating conditions were studied, comparing both the results of the SG-SMB simulator as well as of the design criteria approach. Table 5 presents the simulation results from the SG-SMB simulator as well as the design criteria approach studying four different operating conditions. As can be seen in Table 5, there is a strong relation between results of the design criteria and SG-SMB simulator as the last one confirmed the results obtained by the optimization approach. The design criteria results are in terms of separation performance in sections II (m_2 - $H_{(-)}$) and III ($H_{(+)}$ - m_3). In runs 1 and 2, such differences are positive, indicating complete separation of the molecules in the extract and raffinate. Such results are confirmed through the SG-SMB simulator that obtained simulation values of purities in the extract as well as in the raffinate higher than 99%. In run 3, the separation performance in section II (m_2 - $H_{(-)}$) is negative, indicating a contamination of the extract stream due to retention of the less adsorbed molecules (phenylalanine) on the solid adsorbent phase. This result is confirmed by the SG-SMB simulator, which presented a lower value of purity of the more adsorbed molecules (tryptophan) in the extract, which is equal to 65.03%. In run 4, the separation performance in section III ($H_{(+)}$ - m_3) is negative indicating a contamination of the raffinate stream due to convection transport of the more adsorbed molecules (tryptophan) by the liquid phase. This result is confirmed by the SG-SMB simulator, which presented a lower value of purity of the less adsorbed molecules (phenylalanine) in the raffinate, which is equal to 59.40%.

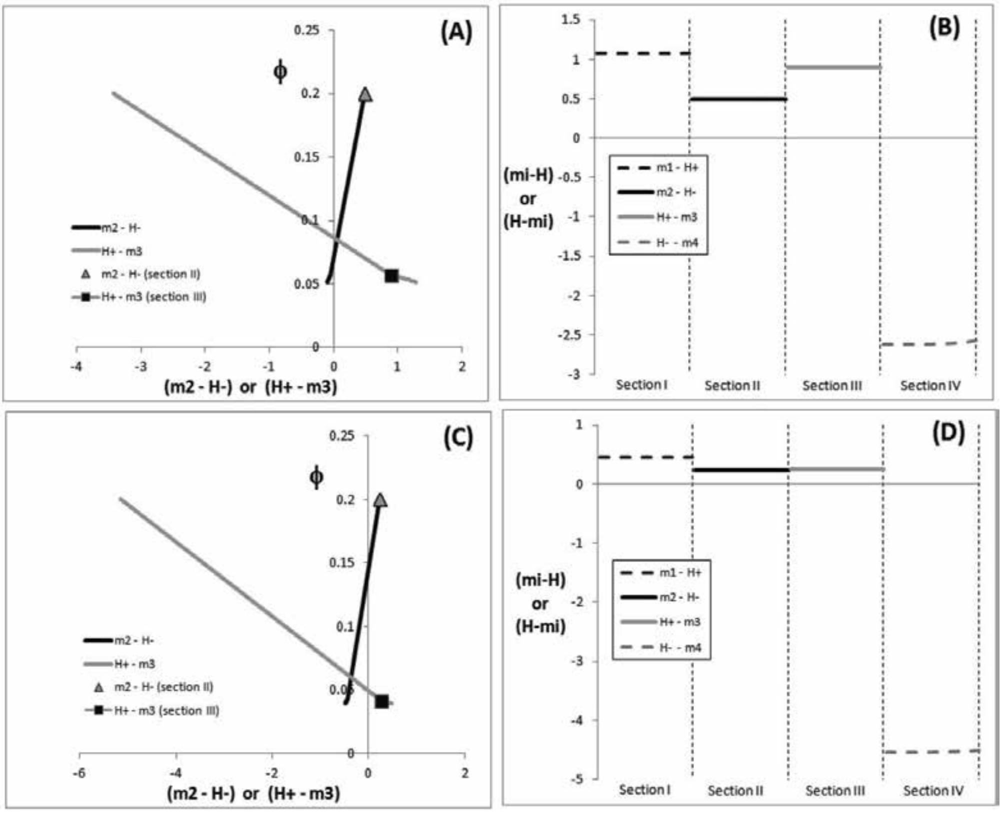

Figure 12. Phi-plot design criteria for feed flow rate of 10 mL/min (A and B) and 15 mL/min (C and D) related to simulation results in Table 4

	Run 1	Run 2	Run 3	Run 4
Q^{I} (mL/min)	15.0	7.0	7.0	12.0
Q^{II} (mL/min)	10.0	5.0	2.0	6.56
Q^{III} (mL/min)	20.0	8.0	12.0	18.56
Q^{IV} (mL/min)	15.0	6.0	7.0	11.87
Switching time (min)	15.5	34.5	37.0	25.0
porosity	0.7	0.7	0.7	0.55
$m_2 - H_{(-)}$	1.297	1.844	-1.238	1.560
$H_{(+)} - m_3$	3.732	3.292	7.012	-2.206
Raffinate purity (%)	99.85	99.87	99.84	59.40
Extract purity (%)	99.98	99.99	65.03	99.99
Productivity (g/h.L)	0.599	0.185	0.747	0.802
Solvent consumption (L/g)	3.523	5.326	1.319	2.108

Table 5. Separation performance of SG-SMB for several conditions (ϕ=0.2)

5. Conclusions

The new design approach, which is based on equilibrium theory and utilizes the χ equation and phi-plot analysis, was able to predict a great number of operating conditions for complete separation in the solvent gradient simulated moving bed (SG-SMB) process. Optimal results were validated by the simulations carried out by the new implemented SG-SMB simulator, which is based on a stepwise approach combined with a lumped mass transfer model (SW-LM). The influence of the solvent modifier was considered, applying the Abel model which takes into account the effect of modifier volume fraction over the partition coefficient. The optimal conditions determined from the new design approach were compared to the simulation results of a SG-SMB unit applied to the experimental separation of the amino acids phenylalanine and tryptophan. Such a SG-SMB simulator provided simulation results with very good agreement fitting the experimental data of the amino acids concentrations both in the extract as well as in the raffinate.

Acknowledgements

The author thanks UERJ, Faperj, CNPq, and Capes for the financial support.

Author details

Leôncio Diógenes Tavares Câmara

Address all correspondence to: dcamara@iprj.uerj.br; diogenescamara@gmail.com

Dep. Mechanical Eng. and Energy – DEMEC, Polytechnic Institute of the State University of Rio de Janeiro (IPRJ-UERJ), Nova Friburgo, Brazil

References

[1] H.-G. Nam, S.-H. Jo, C. Park, S. Mun, Experimental validation of the solvent-gradient simulated moving bed process for optimal separation of phenylalanine and tryptophan, Process Biochem. 47 (2012) 401-409.

[2] S. Mun and H.-H. L. Wang, Optimization of productivity in solvent gradient simulated moving bed for paclitaxel purification, Process Biochem. 43 (2008) 1407-1418.

[3] G. Ziomek, D. Antos, Stochastic optimization of simulated moving bed process sensitivity analysis for isocratic and gradient operation, Comput. Chem. Eng. 29 (2005) 1577-1589.

[4] G. Ziomek, M. Kaspereit, J. Jezowski, A. Seidel-Morgenstern, D. Antos, Effect of mobile phase composition on the SMB processes efficiency stochastic optimization of isocratic and gradient operation, J. Chromat. 1070 (2005) 111-124.

[5] D. Antos, A. Seidel-Morgenstern, Application of gradients in the simulated moving bed process, Chem. Eng. Sci. 56 (2001) 6667-6682.

[6] D. Antos, A. Seidel-Morgenstern, Two-step solvent gradient in simulated moving bed chromatography-Numerical study for linear equilibria, J. Chromat. A. 944 (2002) 77-91.

[7] S. Abel, M. Mazzotti, M. Morbidelli, Solvent gradient operation of simulated moving beds- I. Linear isotherms, J. Chromat. A. 944 (2002) 23-39.

[8] S. Abel, M. Mazzotti, M. Morbidelli, Solvent gradient operation of simulated moving beds- 2. Langmuir isotherms, J. Chromat. A. 1026 (2004) 47-55.

[9] L. D. T. Câmara, Optimization strategies in the modelling of SG-SMB applied to separation of phenylalanine and tryptophan, J. Phys.: Conf. Ser. 490 (2014) 012033.

[10] F. Wei, B. Shen, M. Chen, Y. Zhao, Study on a pseudo-simulated moving bed with solvent gradient for ternary separations, J. Chromat. A. 1225 (2012) 99-106.

[11] J.-G. Lu, Y.-X. Sun, Mathematical modelling of non-linear solvent-gradient simulated moving bed chromatographic separation processes, Dev. Chem. Eng. Mineral Process. 13/1-2 (2005) 193-202.

[12] N. V. D. Long, J. W. Lee, T.-H. Le, J.-I. Kim, Y.-M. Koo, Solvent-gradient SMB to separate o-xylene and p-xylene, Korean J. Chem. Eng. 28/4 (2011) 1110-1119.

[13] D. Antos, A. Seidel-Morgenstern, Application of gradients in the simulated moving bed process, Chem. Eng. Sci. 56 (2001) 6667-6682.

[14] M. Nagy, T. Szánya, Z. Molnár, G. Turza, G. Gál, L. Hanák, J. Argyelán, A. Aranyi, K. Temesvári, Z. Horváth, Separation of organic compounds by gradient simulated moving bed chromatography, Hung. J. Ind. Chem. 34 (2006) 21-26.

[15] W. Klaus, S. Arthur, S.-T. Henner, Modelling and validated simulation of solvent-gradient simulated moving bed (SG-SMB) processes for protein separation, in: L. Puigjaner (Ed.), ESCAPE - 15, Barcelona, 2005, pp. 313-304

[16] C. Migliorini, M. Wendlinger, M. Mazzotti, M. Morbidelli, Temperature gradient operation of a simulated moving bed unit, Ind. Eng. Chem. Res. 40 (2001) 2606-2617.

[17] D. A. Horneman, M. Ottens, J. T. F. Keurentjes, L. A. M. van der Wielen, Micellar gradients in size-exclusion simulated moving bed chromatography, J. Chromat. A. 1113 (2006) 130-139.

[18] J. Houwing, H. A. H. Billiet, L. A. M. van der Wielen, Optimization of azeotropic protein separations in gradient and isocratic ion-exchange simulated moving bed chromatography, j. Chromat. A. 944 (2002) 189-201.

[19] M. Mazzotti, G. Storti, M. Morbidelli, Supercritical fluid simulated moving bed chromatography, J. Chromat. A. 786 (1997) 309-320.

[20] B. M. Thome, C. F. Ivory, Continuous voltage gradients and their application to true moving bed electrophoresis, J. Chromat. A. 1129 (2006) 119-128.

[21] L. D. T. Câmara, Stepwise model evalution in simulated moving-bed separation of ketamine, Chem. Eng. Technol. 37/2 (2014) 301-309.

[22] H.-G. Nam, T.-H. Kim, S. Mun, Effect of ethanol content on adsorption equilibria of some useful amino acids in poly-4-vinylpyridine chromatography, J. Chem. Eng. Data. 55 (2010) 3327-3333.

Chapter 6

A Comparison of Mass Transfer Coefficients between Rotating Magnetic Field Mixer and Stirred Tank Reactor

Grzegorz Story, Marian Kordas and Rafał Rakoczy

Additional information is available at the end of the chapter

http://dx.doi.org/10.5772/61059

Abstract

The mass transfer process is the subject of many experimental studies in chemical engineering and also one of the most commonly used processes. Unfortunately, the mechanism of this process is still not fully understood, especially when nonstandard methods of intensification of mass transfer are used. In this investigation, the use of an alternating magnetic field action (AMFs) causing mass transfer was taking into consideration. As a result of the flow of electrically conductive fluid near the alternating magnetic field, electromagnetic forces can be generated within the liquid. These forces arise as a result of interaction between the magnetic field and the electric current. They are responsible for the rotation and consequently cause movement of the fluid on which they act. Therefore, there is the possibility of using these properties in the construction of a nonintrusive mixing stirrer.

The aim of this study is to determine the mixing time, the power consumption and the mixing efficiency in the mass transfer process that is induced under the action of RMF. The present study compared the mass transfer coefficient of two reactor types: RMF mixer and stirred tank reactor.

Keywords: Rotating magnetic field, mixing energy, mass transfer

1. Introduction

The mass transfer process is the subject of many experimental studies in chemical engineering and also one of the most commonly used processes. Unfortunately, the mechanism of this process is still not fully understood, especially when nonstandard methods of intensification of mass transfer are used. In this investigation, the use of an alternating magnetic field action (AMFs) causing mass transfer was taken into consideration. In many industries, static magnetic fields (MSSF) are mainly used as magnetic separators or electromagnetic brakes, while transverse rotating magnetic fields (TRMFs) are used in asynchronous electric motors or as an electromagnetic stirrer. As a result of the flow of electrically conductive fluid near the alternating magnetic field, electromagnetic forces can be generated within the liquid. These forces arise as a result of interaction between the magnetic field and the electric current, and they are called Lorentz or Laplace forces. They are responsible for the rotation and consequently cause movement of the fluid on which they act. Therefore, there is the possibility of using these properties in the construction of a nonintrusive mixing stirrer. The use of rotating magnetic field (RMF) acting on the conductive fluid is mainly used in the crystallization process and other processes in chemical engineering.

The application of the TRMF in chemical engineering processes has many advantages. Instead of using a mechanical mixer to increase the process intensity, it is possible the use static or rotating magnetic field (RMF). Generally, it is known that small particles having magnetic properties are arranged along the magnetic field lines and that they are also moving with movement of the magnetic field. The use of TRMF creates the possibility of using these particles and also controlling the hydrodynamic state of the magnetodispersion. Magnetic particles in the system, which are subjected to the influence of magnetic field, will behave as active microstirrers. Usually, the mixing process is carried out in the mixing tank or stirred vessel. The process performance can be evaluated on the basis of energy consumption and mixing time. However, when choosing the proper mixing equipment, the mixing time and energy of the system should not be considered separately. The minimum value of the mixing energy determines the optimum process conditions. Therefore, it is desirable to know value of the mixing energy during the design of the mixing device.

The aim of this study are to determine the mixing time, the power consumption and the mixing efficiency in the mass transfer process (dissolution of NaCl-cylindrical sample) that is induced under the action of RMF. The present study compared the mass transfer coefficient of two reactor types: RMF mixer and stirred tank reactor (STR) equipped with Rushton turbine. It is decided that in the present report, the influence of the mixing system consisting of the RMF generator or the mechanical stirrer on the mass transfer process is described by applying the nondimensional parameters, like Sherwood, Schmidt, and Reynolds numbers, and mixing energy. Mixing energy was calculated as a product of the mixing time and power input to the mixing liquid. These dimensionless numbers allow quantitative representation and characterization of the influence of the hydrodynamics state under the various hydrodynamic conditions on the mass transfer rate. The dimensionless groups are used to establish the effect of the various types of the mixing process on this operation in the form of the dimensionless correlation. Moreover, the comparison of the amount of energy input to reach the same mass transfer rate with two different devices (RMF mixer and STR) is discussed.

2. Theoretical background

There is one way of looking at the intensity of the external mass transfer, namely, the criterion of Sherwood, *Sh*. The physical meaning of the dimensionless Sherwood number lies in relating the actual flow of the component from boundary layer to the transverse flow in the stationary liquid layer with characteristic *L* dimension in accordance with concentration difference of this component. A relationship for the mass transfer process under convective conditions, based on the analogy to the heat transfer process, may be expected as a relationship between three dimensionless numbers, as follows [1]:

$$Sh = f\left(Re, Sc\right) \tag{1}$$

where

$Sh = \dfrac{(\beta)_V d_s^2}{\rho D}$ —dimensionless Sherwood number;

$Sc = \dfrac{v}{D}$ —dimensionless Schmidt number;

$Re = \dfrac{w\, l\, \rho}{\eta}$ —dimensionless Reynolds number.

In Eq. (1), a major role in mass transport has the following dimensionless numbers: Sherwood and Schmidt numbers. The first one (Sherwood number) describes the ratio of convective to diffusive mass transport [2], while the second one (Schmidt number) indicates physical parameters important for the analyzed setup. Furthermore, the Schmidt number is also the measure of the mass and momentum transport relative effectiveness by diffusion. In the basic Eq. (1), except the Sherwood and Schmidt numbers, additionally the Reynolds number can be found. The Reynolds number represents the ratio of convective to viscous momentum transport. The value of the Reynolds number determines the existence of laminar or turbulent regime of fluid flow. For small values of the Reynolds number, viscous forces are sufficiently large relative to inertia forces, and we have laminar flow. With increasing values of the Reynolds number, viscous effects become progressively less important relative to inertia effects, and we have turbulent flow.

It is clear that Eq. (1) in present form cannot be practical use. First, it must be rendered quantitative. It can be achieved by assuming that the functional relation is in the following form [3,4]:

$$Sh = aRe^b\, Sc^c \tag{2}$$

This is commonly known that the coefficient of the mass transfer process can be calculated using three dimensionless groups: Sherwood, Reynolds, and Schmidt numbers. Using Eq. (2), it is possible to combine a lot of data obtained from experimental measurements for many different operations. The *a*, *b*, and *c* coefficients of Eq. (2) are determined experimentally on the basis of the results of the measurements. Under forced convection conditions, this relationship can be presented in the form of [5]

$$Sh \propto Re^{0.5}\, Sc^{0.33} \tag{3}$$

The exponent upon of the Schmidt number is to be 0.33 [6–10] as there is some theoretical and experimental evidence for this value [11], although reported values vary from 0.56 [12] to 1.13 [13].

It should be also noted that for the mass transfer process under natural convection conditions, i.e., then, when the Reynolds number is unimportant, the general expression for the mass transfer has the following form:

$$Sh = f\left(Gr, Sc\right) \tag{4}$$

However, in the presented report, the mass transfer process proceeds under convective conditions; therefore, it is described by means of the following relationships:

- For the stirred vessel equipped with the mechanical stirrer $\left(\text{the Rushton turbine}\right)$,

$$Sh = f\left(Re_{STR}, Sc\right) \quad \Rightarrow \quad \left[\frac{\left(\beta\right)_V \left(\left\langle d_s \right\rangle\right)^2}{\rho D}\right] = f\left\{\left[\frac{n d_m^2}{\nu}\right], \left[\frac{\nu}{D}\right]\right\} \qquad \text{a}$$

- For the stirred vessel equipped with the RMF generator, $\left(\text{5b}\right)$

$$Sh = f\left(Re_{RMF}, Sc\right) \quad \Rightarrow \quad \left[\frac{\left(\beta\right)_V \left(\left\langle d_s \right\rangle\right)^2}{\rho D}\right] = f\left\{\left[\frac{w_{\mathrm{RMF}} D_{\mathrm{con}}}{\nu}\right], \left[\frac{\nu}{D}\right]\right\} \qquad \text{b}$$

$$(5)$$

The above dimensionless groups were calculated with the psychical properties of the tested fluid in the temperature 20°C. In this paper, we present results of the mass transfer process using similar dimensionless groups. In this case, the relationship between Sherwood number and two other numbers, which inform about hydrodynamic conditions in the system, Reynolds and Schmidt numbers, was slightly modified. The Reynolds numbers for the process realized with using the STR or RMF were defined by the following equations, respectively:

$$Re_{STR} = \frac{n d_m^2}{\nu_l} \tag{6}$$

$$Re_{RMF} = \frac{w_{\phi_{\max}} D_{con}}{\nu_l} \tag{7}$$

where

$$w_{\phi_{\max}} = B_{\max} D_{con} \sqrt{\frac{\omega_{RMF}\sigma_e}{\rho_l}},\ \mathrm{m\cdot s^{-1}} \tag{8}$$

In order to establish the effect of the hydrodynamic conditions on the mass transfer process in the tested experimental setups, we propose the following relationship:

$$\frac{Sh}{Sc^c} = aRe^b \tag{9}$$

The effect of mass transfer process can be described by using the variable $ShSc^{-c}$ proportional to the term aRe^b.

One of the parameters that describe the mixing process is the mixing time. This parameter determines the time needed to obtain required level of the mixture homogeneity. Therefore, the mixing time is a contractual value and depends on the mixture homogeneity definition. The homogenization time is often describe with a nondimensional module, defined as a required rotational impeller speed to obtain expected value of the mixing system homogeneity. Mixing time can be expressed as follows:

$$\Theta = \frac{\tau_{mix}\upsilon_0}{l_0^2} \tag{10}$$

To measure the level of the mixture homogeneity, the techniques based on put the system out of equilibrium are frequently used. Afterward, the time in which system returns to the equilibrium state is measured. Usually, one of the two techniques is used: a method that relies on the conductivity measurements [14–17] or thermal method [18,19]. Both of them are characterized by easy conduct of the experiment, and there are also relatively cheap. The conductometric method is based on adding to the system impulse influencing the change in the electrical conductivity of the mixed liquor. The second method is based on adding to the system signal in the form of the hot liquid. In this work, the thermal method of put the system out of equilibrium was used.

Another important parameter that determines the system cost of the process is the power consumption. This parameter can be used as a measure of energy consumption in the process. Power consumption for the mixing process can be calculated on the basis of the relationship between dimensionless number [20,21] as follows:

$$Ne = f\left(Re\right) \tag{11}$$

where Newton number is defined as

$$Ne = \frac{P_0}{n_0^2 l_0^5 \rho_0} \tag{12}$$

In the case of using a mechanical stirrer, *n* is defined as a frequency of rotation of the agitator, and a linear dimension, l_0, is substituted as a diameter of the stirrer, d_m.

In the case of influence, the rotating magnetic field *n* is defined as an angular velocity of the liquid, which is under the action of the RMF in the container, $n = \Omega_l D_{con}$. The magnetic Newton number, Ne_m, is describe as

$$Ne_m = \frac{P_0}{\left(\Omega_l D_{con}\right)^3 D_{con}{}^5 \rho_l} \tag{13}$$

Where

$$\Omega_{RMF} = \frac{w_{\phi_{\max}}}{D_{con}},\ \mathrm{s}^{-1} \tag{14}$$

The Reynolds numbers for the process realized with using the STR or RMF were defined before (Eqs. 6–8).

A parameter that connects both mixing time and power consumption is a mixing energy [22–26]. This parameter is defined as the product of the mixing time in relation to the volume of mixed liquor and power input:

$$e_{mix} = \tau_{mix} P_a,\ \mathrm{J} \tag{15}$$

This parameter can be presented as a dimensionless number:

$$e_{mix}^* = a_3 Re^{3+b_3} C^{b_3} \tag{16}$$

By calculating the dimensionless value of the mixing energy, it is possible to compare the efficiency of mixing between different systems.

To calculate dimensionless mixing energy for the both systems (Eq. 16), some relationships must be designated. First, from the measured experimental data of the mixing time, a function must be plotted. Then the approximation curve must be designated in the form of the following equations:

$$\begin{aligned} &\Theta_{RMF} = a_1 Re_{RMF}{}^{b_1} \quad \text{a} \\ &\Theta_{STR} = a_1 Re_{STR}{}^{b_1} \quad \text{b} \end{aligned} \tag{17}$$

Second, from the measured experimental data of the power consumption, a function given by the Eq. (11) must be plotted. Then the approximation curve must be designated in the form of the following equations:

$$\begin{aligned} &Ne_{RMF} = a_2 Re_{RMF}{}^{b_2} \quad \text{a} \\ &Ne_{STR} = a_2 Re_{STR}{}^{b_2} \quad \text{b} \end{aligned} \tag{18}$$

Considering the resulting equations (Eq. 17) and rearranging terms to Eq. (10), the following equations were obtained:

$$\begin{aligned} &\tau_{mix} = a_1 Re_{RMF}{}^{b_1}\left(\frac{D_{con}{}^2}{\nu_l}\right), \text{s} \quad \text{a} \\ &\tau_{mix} = a_1 Re_{STR}{}^{b_1}\left(\frac{D_{con}{}^2}{\nu_l}\right), \text{s} \quad \text{b} \end{aligned} \tag{19}$$

Substituting Eq. (12) into Eq. (18), we have

$$\begin{aligned} &P_a = a_2 Re_{RMF}{}^{b_2}\left(\left(\Omega_{RMF} D_{con}\right)^3 D_{con}{}^2 \rho_l\right), \text{W} \quad \text{a} \\ &P_{a,STR} = a_2 Re_{STR}{}^{b_2}\left(\left(n d_m\right)^3 d_m{}^2 \rho_l\right), \text{W} \quad \text{b} \end{aligned} \tag{20}$$

The obtained Eqs. (19) and (20) are then substituted in Eq. (15), and consequently we have the following relationships:

$$\begin{aligned} &e_{mix} = \left[a_1 Re_{RMF}{}^{b_1}\left(\frac{D_{con}{}^2}{\nu_l}\right)\right]\left[a_2 Re_{RMF}{}^{b_2}\left(\left(\Omega_{RMF} D_{con}\right)^3 D_{con}{}^2 \rho_l\right)\right], \text{J} \quad \text{a} \\ &e_{mix} = \left[a_1 Re_{STR}{}^{b_1}\left(\frac{D_{con}{}^2}{\nu_l}\right)\right]\left[a_2 Re_{STR}{}^{b_2}\left(\left(n d_m\right)^3 d_m{}^2 \rho_l\right)\right], \text{J} \quad \text{b} \end{aligned} \tag{21}$$

Transforming Eq. (21), it may be given in the dimensionless forms, as follows:

$$
\begin{aligned}
& e_{mix}=\tau_{mix}P_a \Rightarrow \left[a_1 {Re_{RMF}}^{b_1}\left(\frac{{D_{con}}^2}{\nu_l}\right)\right]\left[a_2 {Re_{RMF}}^{b_2}\left(\left(\Omega_{RMF}D_{con}\right)^3 {D_{con}}^2\rho_l\right)\right] \\
& \Rightarrow \left\{\left(\frac{{D_{con}}^2}{\nu_l}\right)\left(\left(\Omega_{RMF}D_{con}\right)^3 {D_{con}}^2\rho_l\right)\left(\frac{{\nu_l}^2}{{\nu_l}^2}\right)\right\} a_3 {Re_{RMF}}^{b_3} && \text{a} \\
& \Rightarrow e_{mix}=a_3 {Re_{RMF}}^{3+b_3}\left\{D\rho_l {\nu_l}^2\right\} \\
& e^*_{mix}=a_3 {Re_{RMF}}^{3+b_3}C^{b_3}=\frac{e_{mix}}{D_{con}\rho_l {\nu_l}^2} \\
& e_{mix}=\tau_{mix}P_{a,STR} \Rightarrow \left[a_1 {Re_{STR}}^{b_1}\left(\frac{{D_{con}}^2}{\nu_l}\right)\right]\left[a_2 {Re_{STR}}^{b_2}\left(\left(nd_m\right)^3 {d_m}^2\rho_l\right)\right] \\
& \Rightarrow \left\{\left(\frac{{D_{con}}^2}{\nu_l}\right)\left(\left(nd_m\right)^3 {d_m}^2\rho_l\right)\left(\frac{{\nu_l}^2}{{\nu_l}^2}\right)\left(\frac{d_m}{d_m}\right)\right\} a_3 {Re_{STR}}^{b_3} && \text{b} \\
& \Rightarrow e_{mix}=a_3 {Re_{STR}}^{3+b_3}\left\{\frac{{D_{con}}^2\rho_l {\nu_l}^2}{d_m}\right\} \\
& e^*_{mix}=a_3 {Re_{STR}}^{3+b_3}C^{b_3}=\frac{e_{mix}}{\frac{{D_{con}}^2\rho_l {\nu_l}^2}{d_m}}
\end{aligned}
\tag{22}
$$

3. Dissolution solid body in two reactor types

3.1. Literature survey

Many processes in chemical and related industries are carried out in heterogeneous solid–liquid systems. One of the most commonly used processes is the dissolution of a solid body in a liquid. The dissolution process of a solid body in a liquid can occur spontaneously or it can be intensified. One of the simplest methods of the mass transfer intensification is dissolution in mechanical mixers, i.e., apparatus with moving impellers [27,28]. Using the mechanical impeller should provide increase of the liquid turbulence, particularly at the boundary of the phases. The case of using mechanical mixers kinetic of the solid body dissolution depends on hydrodynamic conditions occurring inside the liquid volume, whereas hydrodynamics of the liquid depends on geometric configuration of the device. This is why the choice of the suitable impeller and mixing tank dimensions to the stirred medium, the type of the process, and the purpose of what we want to achieve are important issues. Except the result of research carried out for the well-known mechanical agitators, new constructional proposals of the mechanical mixers for performing solid dissolution process in a liquid can be found in the literature. This may have a positive effect on the mass transfer process, for example, using a reciprocating agitator [10,29–32]. Among other methods that are commonly used to intensify solid dissolution, a liquid pulsation [33], electrical discharges [34], other physical methods of the interaction [35], and dissolution on the solid or fluidized bed [36] can be found. In the case of dissolution process with chemical reaction an ultrasound can be used to the intensification [37–39]. In the last few years, a growth of interest in using of the magnetic fields in processes and unit operations in the scientific community was observed. Externally applied static magnetic field was used primarily to intensify the process of crystal growth [40,41] or during solidification of metal alloys [42,43]. The rotating magnetic field can be successfully used in the crystallization process [44–47], fluidization [48,49], metallurgy [50,51], or even to increase the intensity of the dissolution process, as an alternative for mechanical mixing. This type of magnetic field induces azimuthal forces, which are time averaged. If the stirred liquid is magnetically susceptible, then azimuthal forces make a circumferential flow. Lines of the magnetic field rotate in a horizontal direction with rotation frequency of the field, ω_{RMF}. Moreover, the rotation frequency of the field is equal to frequency of an alternating current. An electric field, $\bar{E}$, is generated perpendicularly to the magnetic field, $\bar{B}$. The magnetic Lorentz forces, $\overline{F_n}$, which are perpendicular to the electrical field, act as driving forces for the rotating liquid. TRMF can be generated by a stator from three-phase asynchronous electric motor. This construction of the RMF generator was used in several studies [52,53]. When the stirred liquid is magnetically susceptible, then the RMF induces currents inside it. These currents interact with the field of the inductor. As a result, the electromagnetic forces inside the mixed liquor are generated. The pattern of the flow hydrodynamic induced by TRMF in the volume of the stirred liquid depends on the number of inductor pole pair, p_{TRMF}. RMF can be used to generate a specific flow in the cylindrical volume of the liquid. The liquid moves in a circumferential direction around the axis of the tank. This flow is directed the same as the direction of magnetic field rotations. Subsequently, the fluid velocity reaches the maximum value near to the tank wall, i.e., in the place characterized by the highest values of the magnetic induction. This movement may influence to the heat or mass transfer inside volume of the liquid. Analyzing the results that are available in the literature, it was found that research has not focused on a comparison between the mass transfer processes during the solid body dissolution realized in different systems: RMF mixers and stirred tank reactors. In this paper, experimental studies were conducted, and the effects of RMF and Rushton turbine on the solid body dissolution process in a liquid were compared.

3.2. Preparation of samples

As a solid body, the NaCl-cylindrical samples were used. To obtain suitable samples, i.e., samples that are dissolving in uniform manner, all of them were subjected to hardening process. First, raw rock salt cylinders were placed in a container filled up with a NaCl saturated solution. Second, after 24 h, the samples were pulled out and left dry. This process was repeated two times to obtain homogeneous and smooth surface of the cylindrical samples. A short thread stainless steel rod was glued to the top surface of the sample, which allows to mount it in a selected position in volume of the stirred liquid. Finally, the samples were securing at the bottom and top surface of the cylinder by applying a thin layer of glue on it. The prepared samples were used to perform the measurements.

Before the solubility measuring, the samples were hardened again in saturated salt solution during 60 s and then dried with paper. It was necessary because the dry samples may have to collect moisture from the stirred water, which could have a negative impact on the solubility process. Before each measurement the samples were weighed. Moreover, their height and diameter were measured. The diameter of the sample was measured at five different high levels located in equal increments and taken three times for different angular position of the sample. The location of the places where the diameter was measured is schematically shown in Figure 1.

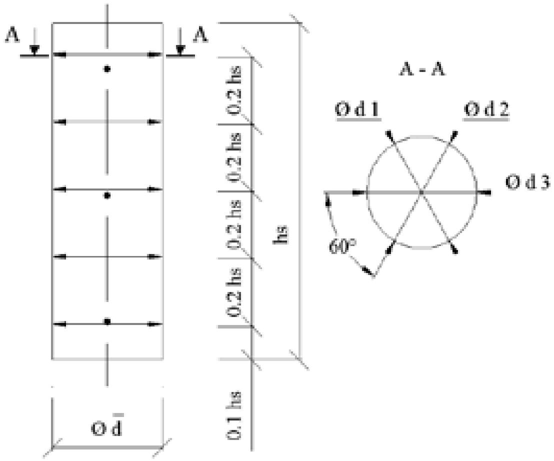

Figure 1. Location of the measurement levels on the solid sample.

Before the measurements in the magnetic stirrer were started, the magnetic field at a set point value of operating frequency of the stator was turned on. In the case of measurements for a mechanical mixer, first the impeller was set in motion on the requested rotation speed. Second, the conductivity measurement was switched. Then the sample was placed in a container filled up with tap water. In the case of a magnetic mixer, the sample was placed at the mid-height of electromagnetic laminations, where the most intensive magnetic field induction generated in a container takes place. Based on the literature data [54], it was found that it is also the place where the mass transfer process should proceed the fastest. The typical examples of the magnetic induction distribution in the form of the contours were presented in Figure 2.

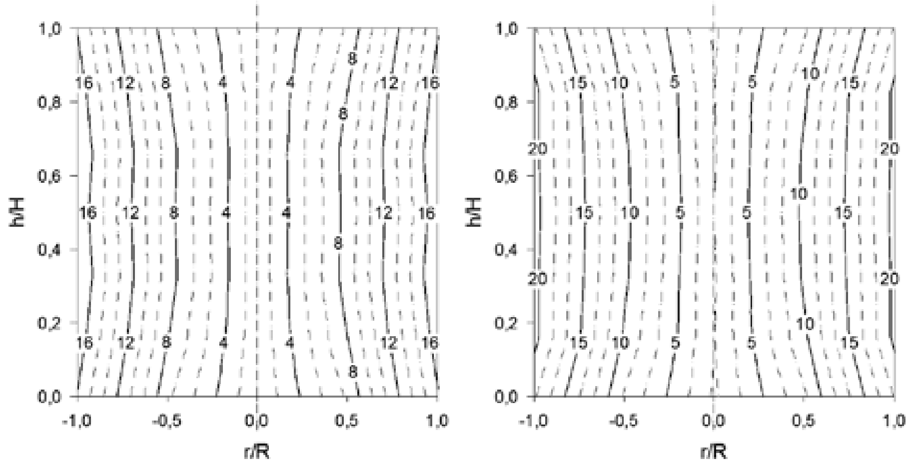

Figure 2. The typical example of the magnetic induction spatial distribution in the cross section of the RMF generator, $f_{RMF} = 20$ and $120\ s^{-1}$.

Every sample was dissolved once in short time equal to 5 s and then was pulled out of the system, dried by using the paper, measured, and weighed. For each sample, 13 replicates were performed. The number of repetition dissolution of the sample was chosen in a way to get appearance of the first pinholes. After the series of measurements, the data from multiparameter sensors were read. The water inside the container was replaced with a new one after every measurement series, keeping its temperature at constant level ($T = 22–23°C$).

3.3. Experimental setup

The first measurements of the NaCl-solid body dissolution were carried out in the RMF generator, which is shown in Figure 3. This experimental apparatus consists of a cylindrical glass container (2), a.c. transistorized inverter (3), and multifunctional computer meter (CX-701, Elmetron, Gliwice, Poland) (4). All of these elements are connected to the computer (5). The RMF generator was constructed of the stator, which was supplied from an electric motor with 50 Hz three-phase alternating current. The process parameters of the RMF generator were controlled using the special software. By controlling the inverter via a computer, it was possible to change the frequency of rotating magnetic field. In this case, the frequency was changed in the range of $f = 2–120\ s^{-1}$. The glass container was placed inside of the RMF generator and filled up with the tap water to the volume equal to 16 dm^3. Conductivity was measured by means of the conductivity electrodes and the multifunction meters CX-701. Voltage signals were registered digitally every 0.1 s. The conductivity probe was positioned diagonally on the top and bottom of the glass container. The localization of the probes and the measurement points in the RMF generator are shown in Figure 4.

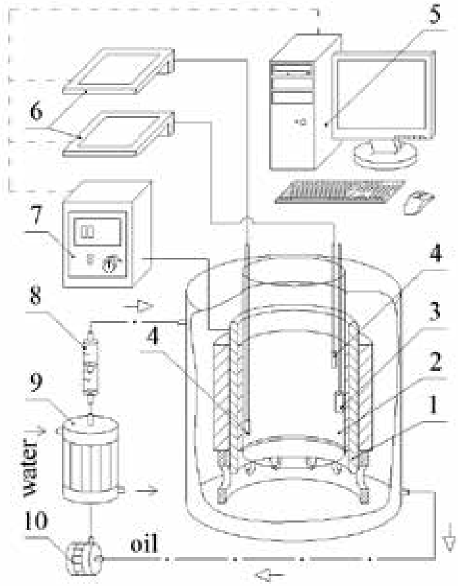

Figure 3. The sketch of the first experimental setup: 1—generator of rotating magnetic field, 2—glass container, 3—sample, 4—conductivity probes, 5—personal computer, 6—multifunctional computer meter, 7—a.c. transistorized inverter, 8—rotameter, 9—heat exchanger, 10—pump.

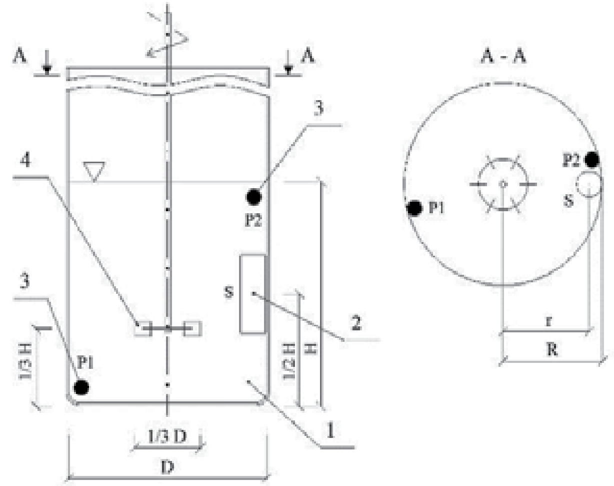

Figure 4. Localization of the probe and measurement points (where 1—glass container, 2—sample, 3—conductivity probes).

The second experimental apparatus are shown in Figure 5. It was the same glass vessel as in the first system; however, in this case, the mixing process was realized by using the mechanical high-speed impeller (Rushton disc turbine). The diameter of the agitator was equal to $d_m = 0.33D_{con}$. The distance from the impeller center to the bottom of the vessel was $z = 0.33H$. The experiments were conducted at nine different values of impeller speed in the range of $n = 0–3$ s^{-1}. The measurement points correspond to those defined for the RMF generator (see Figure 4).

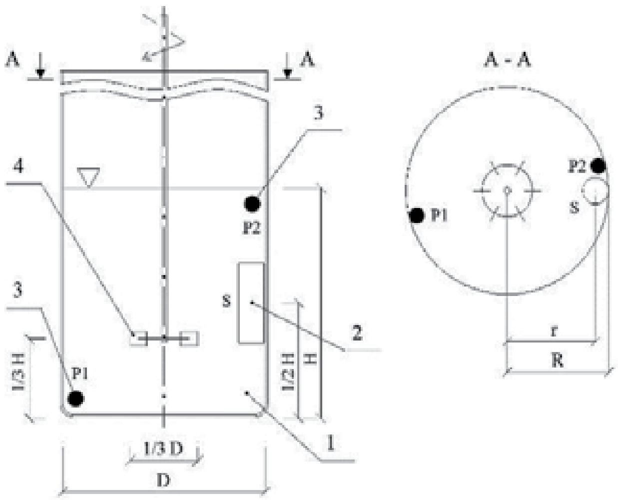

Figure 5. The sketches of the experimental setup with the mechanical mixer (where 1—glass container, 2—sample, 3—conductivity probes, 4—impeller).

3.4. Mixing time and power consumption measurements

The mixing time measurements for two systems were performed. The first mixer was under the action of the rotating magnetic field, and the second was equipped with the Rushton turbine mechanical impeller. The stirred vessel was filled up with a tap water (density 1000 kg m^{-3}, viscosity 1.002 mPa s, temperature 22–23°C). The geometric dimensions and process parameters for both systems are shown in Table 1.

Paramters	**Operating value**
Geometrical dimensions of mixer	
Vessel diameter, m	0.235
Agitator diameter, m	0.076
Time of dissolution, s	5
Height of liquid level in vessel, m	0.42
Operating conditions	
The frequency of rotation agitator, s^{-1}	0 – 3
Input power of agitator, W	0.002 - 26
Poles pair of generator RMF	2
The frequency of RMF, Hz	2 – 120
Input power of generator RMF, W	1 – 1050
Average diameter of sample, m	0.031
Average height of sample, m	0.074
Impulse temperature, °C	85
Electrical conductivity, (Ωm)$^{-1}$	$2.5 \cdot 10^{-4}$

Table 1. The main geometrical dimensions of mixers and operation conditions

In this investigation, a thermal method was used to mixing time determination. First, a specific volume of the liquid with much higher temperature comparing to the mixed liquid was added to the system. As a tracer, a 0.3-dm^3 tap water with temperature equal to 85°C was used. Then changes of the liquid temperature were measured by using special experimental apparatus. It was an LM35 temperature sensor with measuring test card, which can process an analog signal in the form of the voltage to a digital signal. The voltage signal from the temperature probe was recorded at a frequency of 0.01 s. When the measurement was finished, a content of the glass container was poured out, and the vessel was filled up again with a new tap water characterized by the initial temperature. The mixing process was regarded as complete when the temperature fluctuations on one level were established. In this experiment, the end point was reached, when changes of the temperature at two measurement points were less than ±5% of the overall temperature increase. The mixing time, τ_{95}, was defined as the time after which the temperature reaches a value equal to 95% of the final temperature of the liquid. It was assumed that this value of the mixing time will be achieved when the uniformity ratio of the temperature of the tracer, T_{tracer}, reaches a value equal to 0.05, according to the following equation:

$$T_{tracer} = \frac{T_{\infty} - T(\tau)}{T_{\infty} - T_0} \tag{23}$$

where T_0 is the initial temperature of the tracer, T_{∞} is the final temperature of the stirred liquid, and $T(\tau)$ is the temperature at the measuring point at a time τ. The distribution of the temperature probes was analogous to the position of the conductivity probe in the mass transport process. Consequently, the point of the heat pulse dosing in the same place where the sample of the dissolved solid body was placed. Examples of the curves obtained from the mixing time measurements are shown in Figure 6.

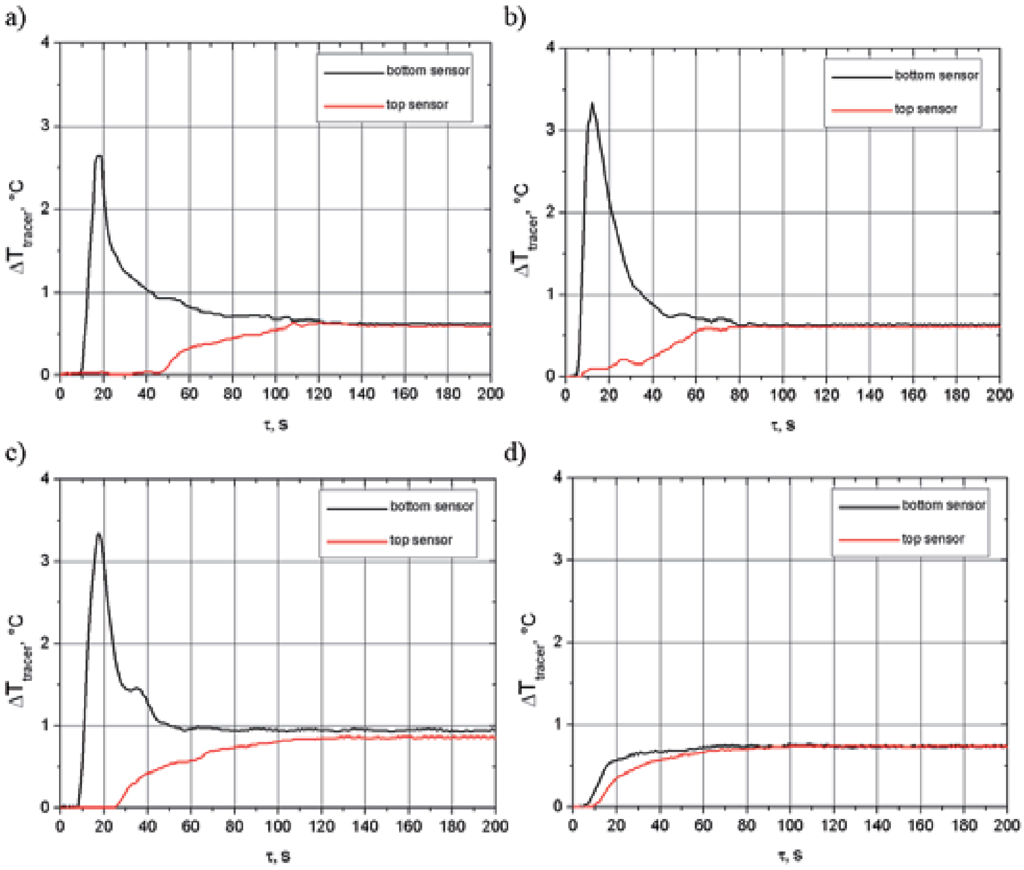

Figure 6. Typical example of temperature changes during mixing time investigations for (a) RMF $f = 20 s^{-1}$, (b) $f = 120\ s^{-1}$, (c) mechanical agitator $n = 0.33\ s^{-1}$, and (d) mechanical agitator $n = 3\ s^{-1}$.

Additionally, measurements of the active power input to the test system with a mechanical stirrer and RMF were performed. In the case of the mechanical stirrer, it was possible to read power consumption directly from the digital display stirrer drive, whereas in the case of the system comprising an RMF generator, it has to be measured by using the electricity meter (type C-52 Pafal), located between the magnetic agitator and the a.c. transistorized inverter. The data that were collected were then graphically shown in Figure 7, in the form of the power change depending on an increasing rate of the rotational impeller speed. A similar relationship for the RMF is shown in Figure 8, except that in this case, the power depends on the frequency of magnetic field rotation change.

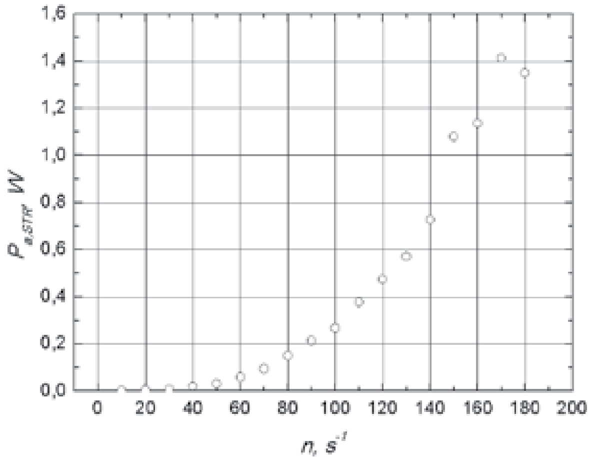

Figure 7. Power input measurements for mechanical mixer.

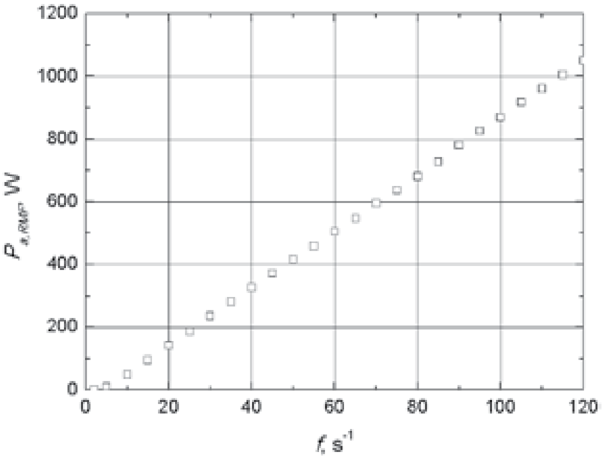

Figure 8. Power input measurements for the RMF generator.

4. Results and discussion

4.1. Influence of the Rushton turbine and the RMF on the mass transfer

The experimental results of the solid body dissolution are graphically shown in Figures 9 and 10. In Figure 9, results of the measurements for the mixing tank equipped with Rushton turbine impeller were presented. Furthermore, in the picture, an approximation of the experimental results and the proposed relationship were also presented. Analogous graph was prepared for the magnetic mixer and shown in Figure 10. Analyzing the plots, it was found that values of the mass transfer coefficients in the tested systems are depended on the Reynolds number. Additionally, a significant effect of the mixing method on the mass transfer process was observed. The higher impact of the Reynolds number value on the mass transfer coefficients in the STR was observed. In both systems, the mass transfer rate increased with increasing value of Reynolds number. However, the slope of the approximation curve was bigger in the case of the mechanical mixer than that in the case of the magnetic mixer. The proposed relationships were $Sh_{STR}\ Re_{STR}^{0.53}$ and $Sh_{RMF}\ Re_{RMF}^{0.26}$ for the STR and RMF generator, respectively.

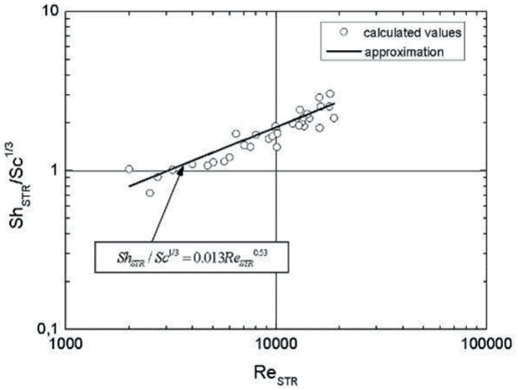

Figure 9. Mass transfer characteristics for Rushton turbine.

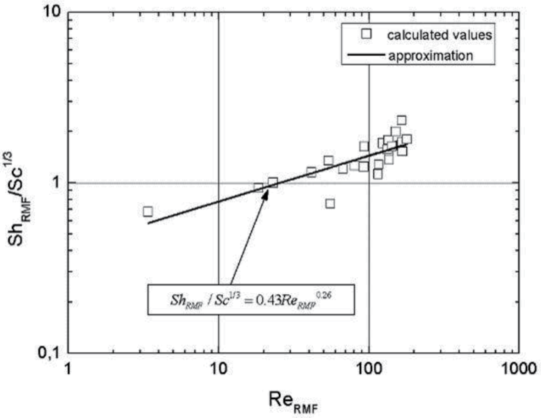

Figure 10. Mass transfer characteristics for the RMF generator.

4.2. Power characteristics for the Rushton turbine and the RMF

Power characteristics for both systems in Figures 11 and 12 were presented. As it could be seen, values of the power number for the STR system were much lower than those in the magnetic mixer. It is caused by the fact that in the case of the RMF generator, the power consumption was significantly higher, which consequently affects the calculated values of the Ne number. Based on the slope of the proposed approximation curve, in the case of mechanical mixer with increase value of the rotational impeller speed, the value of the Ne number was slightly decreasing. In the tested range, the proportionality $Ne_{STR}\ Re_{STR}^{-0.16}$ was found. A similar situation is in the case when the mixing process is carried out using the RMF generator. In that system, a slope of the approximation curve is also negative; however, the change in RMF frequency has a significant impact on the value of the Ne number. In the tested range, the proportionality $Ne_{RMF}\ Re_{RMF}^{-1.3}$ was found.

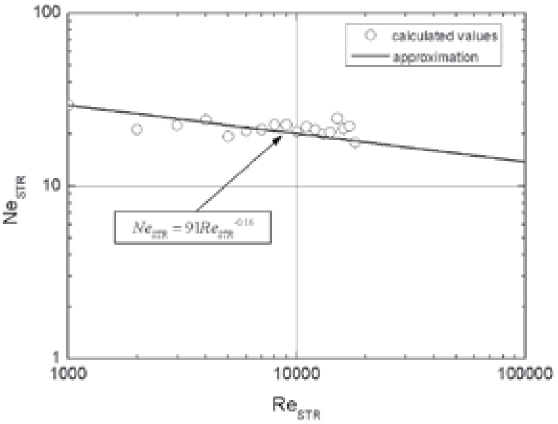

Figure 11. Power characteristic for Rushton turbine.

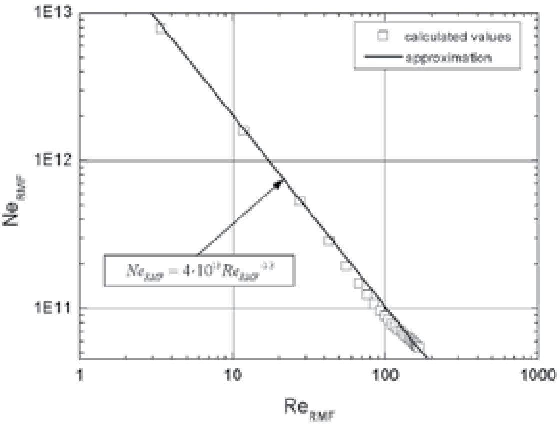

Figure 12. Power characteristic for the RMF generator.

4.3. Mixing time characteristics for the Rushton turbine and the RMF

In present consideration, the dimensionless mixing time was defined as

$$\Theta = \frac{\tau_0 v_0}{l_0^{\,2}} \Rightarrow \Theta = \frac{\tau_{mix} v_l}{D^2} \tag{24}$$

The mixing time may be analytically described using the relationship between the dimensionless mixing time and the Reynolds number. The experimental data obtained for the systems with the RMF generator or Rushton turbine in log–log graphs were presented (Figures 13 and 14). Analyzing the results shown in the graphs, it was found that values of the dimensionless mixing time decreased with increasing Reynolds number in both systems. Comparing results for both systems, it was found that smaller values of the dimensionless mixing time in the mixing process realized with using a Rushton turbine were obtained. Based on the curve slope, it can be assumed that the process using a mechanical impeller proceeds more intensively than that under the action of RMF. It should be noted that in the magnetic mixer, the process proceeds as a laminar, while the mechanical impeller induces a turbulent regime of the flow. According to that, using of an RMF mixer can be useful in a mixing process, when a turbulent flow of the fluid cannot be achieved, even if it will cause an increasing mixing time. An example can be here a bioprocess, where high shear forces connected with a turbulent flow can have a destructive impact on the microorganisms.

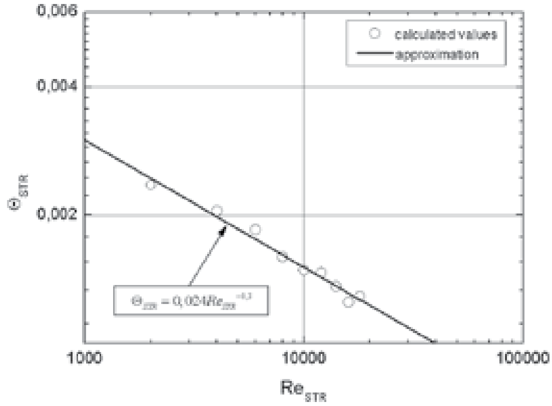

Figure 13. Dimensionless mixing time characteristic for Rushton turbine.

Additionally, values of the power number obtained from the experimental measurements and calculated on the basis of an approximating equation for the process under the action of the RMF are presented in the Figure 15 and compared.

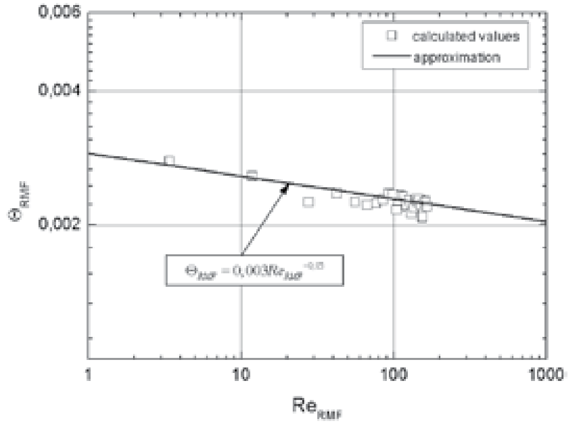

Figure 14. Dimensionless mixing time characteristic for the RMF generator.

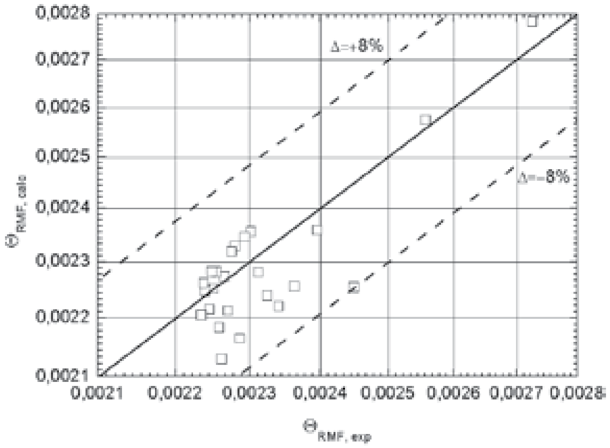

Figure 15. Comparison of the experimental and calculated values of the dimensionless mixing time for process under action of RMF.

5. Mixing energy

As mentioned before, an evaluation of the mixing process realized in different geometrical systems with a mixing energy parameter can be performed. Characteristics of the dimensionless mixing energy for both systems were graphically presented in Figures 16 and 17. As follows from the graphical analysis, lower values of the dimensionless mixing energy in the case of RT using were noted. The conclusion is that the rotational movements of mechanical impeller are more effective for the liquid mixing than the magnetic mixer in the whole tested range of the rotational impeller speed and RMF frequency. Nevertheless, the mixing process under the action of RMF is nonintrusive, which pose a huge advantage this type of mixer.

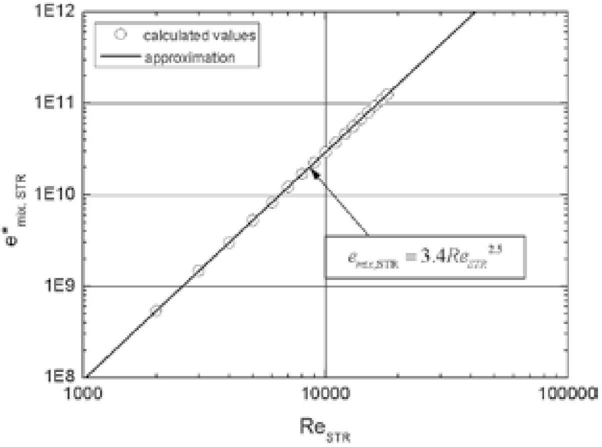

Figure 16. Dimensionless mixing energy characteristics for Rushton turbine.

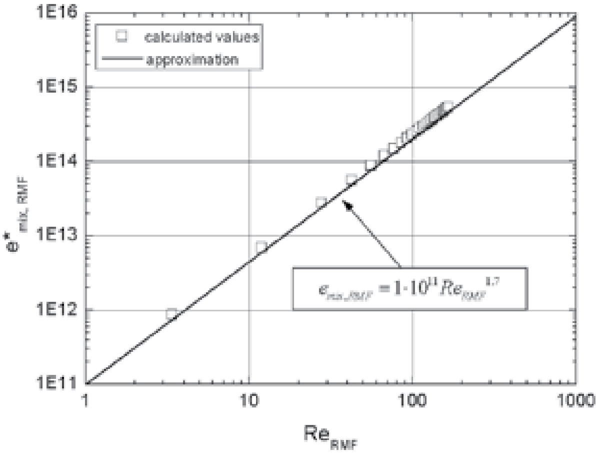

Figure 17. Dimensionless mixing energy characteristics for the RMF generator.

6. Conclusion

Obtained in this consideration, experimental and calculated results present an interesting effect of the rotating magnetic field and stirred tank reactor applications in the mass transfer process. Analyzing the obtained results reveals the following conclusions:

Values of the mass transfer coefficients increases with an increasing value of the rotational agitator speed and the magnetic field intensity. In the laminar regime of the flow, a stronger impact on the solid body dissolution in the case of magnetic mixer was observed, while in the turbulent regime of the flow, better results in the stirred tank with mechanical RT impeller were obtained.

In the STR system, values of the power number were much lower than those in the magnetic mixer. Based on the proposed approximation curves slope, with the increasing value of the rotational impeller speed or RMF frequency, the value of the *Ne* number decreases.

In both systems, the dimensionless mixing time decreased with increasing value of the Reynolds number. However, smaller values of the dimensionless mixing time in the mixing process realized with using a Rushton turbine were obtained. It must therefore be concluded that the process carried out with using a mechanical impeller proceeds more intensively than that under the action of RMF.

On the basis of the dimensionless mixing energy comparison for both systems, it was found from the economical point of view that using of the rotating magnetic field is less profitable due to high power consumption. In the future, additional experimental measurements should be carried out for the system with the RMF generator in order to find a way to reduce the calculated values of dimensionless mixing energy. One of the possibilities is using of the magnetic particles, which can be added to the mixed liquid.

In order to better understand the mechanism of the mass transfer process under the action of the rotating magnetic field further studies, both theoretical and experimental should be carried out.

Nomenclature

B; magnetic induction; kg A^{-1} s^{-2}

D; diffusion coefficient; m^2 s^{-1}

D_{con}; diameter of glass container; m

d_m; diameter of Rushton turbine; m

d_s; diameter of sample; m

e_{mix}; mixing energy; J

f; frequency of RMF; s^{-1}

h; height of sample; m

H; liquid level in glass container;m

l; characteristic dimension; m

m; mass; kg

n; rotational speed of agitator; s^{-1}

Pa; active power; W

r,R; radius; m

T; temperature; °C

V; volume; m^3

Greek letters

$(\beta)_V$; volumetric mass transfer coefficient; kg m^{-3} s^{-1}

w; liquid velocity; m s^{-1}

w_{RMF}; liquid velocity under the action of RMF; m s^{-1}

η; dynamic viscosity ; kg m^{-1} s^{-1}

ν; kinematic viscosity; m^2 s^{-1}

ρ; density; kg m^{-3}

σ_e; electrical conductivity; A s^3 kg^{-1} m^{-3}

τ; time; s

ω_{RMF}; angular velocity of rotating magnetic field; rad s^{-1}

Ω; angular velocity of liquid in container; rad s^{-1}

Dimensionless number

$e_{\mathrm{mix}}{}^*$; dimensionless mixing energy

Ne; Newton number

Re; Reynolds number

Sc; Schmidt number

Sh; Sherwood number

Θ; mixing time number

Subscripts

0; reference value

L; liquid

P; conductivity probe

S; sample

Abbreviations

mix; Mixing

RMF; rotating magnetic field

STR; Rushton turbine

Author details

Grzegorz Story, Marian Kordas and Rafał Rakoczy*

*Address all correspondence to: rrakoczy@zut.edu.pl

Faculty of Chemical Engineering, Institute of Chemical Engineering and Environmental Protection Processes, West Pomeranian University of Technology, Szczecin, Szczecin, Poland

References

[1] Incropera, F.P., DeWitt, D.P. Fundamentals of Heat and Mass Transfer. USA: John Wiley & Sons Inc.; 2011. ISBN: 978-0470-50197-9

[2] Basmadjian, D. Mass Transfer. Principles and Applications.USA: CRC Press LLC; 2004. ISBN 9780203503140

[3] Bird, R.B.; Stewart, W.E., Lightfoot, E.N. Transport Phenomena.USA: Wiley; 1966. ISBN: 978-0471073925

[4] Kays, W.M., Crawford, M.E. Convective Heat and Mass Transfer. USA: McGraw-Hill; 1980. ISBN 9780070334571

[5] Garner, F.H., Suckling, R.D. Mass transfer form a soluble solid sphere. American Institute of Chemical Engineers Journal. 1958;4(1):114–124. DOI: 10.1002/aic.690040120

[6] Condoret, J.S.; Riba, J.P., Angelino, H. Mass transfer in a particle bed with oscillating flow. Chemical Engineering Science. 1989;44(10):2107–2111. DOI: 10.1016/0009-2509(89)85145-0

[7] Jameson, G.J.Mass (or heat) transfer form an oscillating cylinder. Chemical Engineering Science. 1964;19:793–800. DOI: 10.1016/0009-2509(64)85090-9

[8] Lemcoff, N.O., Jameson, G.J. Solid–liquid mass transfer in a resonant bubble contractor. Chemical Engineering Science. 1975;30:363–367. DOI: 10.1016/0009-2509(75)85001-9.3

[9] Noordsij, P., Rotte, J.W. Mass transfer coefficients to a rotating and to a vibrating sphere. Chemical Engineering Science. 1967;22:1475–1481. DOI: 10.1016/0009-2509(67)80073-33

[10] Tojo K., Miyanami K., Minami I. Vibratory agitation in solid–liquid mixing. Chemical Engineering Science. 1981;36:279–284. DOI: 10.1016/0009-2509(81)85006-3

[11] Sugano, Y., Rutkowsky, D.A. Effect of transverse vibration upon the rate of mass transfer for horizontal cylinder. Chemical Engineering Science. 1968;23:707–716. DOI: 10.1016/0009-2509(68)85005-5

[12] Wong, P.F.Y., Ko, N.W.M., Yip, P.C. Mass transfer from large diameter vibrating cylinder. Transactions of the Institution of Chemical Engineers. 1978;56(3):214–216. ISSN: 0371-7496

[13] Lemlich, R., Levy, M.R. The effect of vibration on natural convective mass transfer. American Institute of Chemical Engineers Journal. 1961;7:240–241. DOI: 10.1002/aic.690070214

[14] Woziwodzki Sz., Broniarz-Press L., Ochowiak M. Effect of eccentricity on transitional mixing in vessel equipped with turbine impellers. Chemical Engineering Research and Design. 2010;88(12):1607–1614.DOI:10.1016/j.cherd.2010.04.007

[15] Kuzmanić N., Ljubičić B. Suspension of floating solids with up-pumping pitched blade impellers; mixing time and power characteristics. Chemical Engineering Journal. 2001;84(3):325–333.DOI: 10.1016/S1385–8947(00)00382-X

[16] Kuzmanić N., Žanetić R., Akrap M. Impact of floating suspended solids on the homogenisation of the liquid phase in dual-impeller agitated vessel. Chemical Engineering Process. 2008;47(4):663–669. DOI: 10.1016/j.cep.2006.12.010

[17] Delaplace G., Leuliet J.C., Relandeau V. Circulation and mixing times for helical ribbon impellers. Review and experiments. Experiments in Fluids. 2000;28:170–182. DOI: 10.1007/s003480050022

[18] Karcz J., Cudak M., Szoplik J. Stirring of a liquid in a stirred tank with an eccentrically located impeller. Chemical Engineering Science 2005;60(8–9):2369–2380. DOI: 10.1016/j.ces.2004.11.018

[19] Masiuk S. Mixing time for a reciprocating plate agitator with flapping blades. Chemical Engineering Journal 2000;79(1):23–30. DOI: 10.1016/S1385-8947(00)00141-8

[20] Zlokarnik M. Stirring—Theory and Practice. Weinheim: Wiley-VCH Verlag; 2001. ISBN 978-3-527-29996-3

[21] Harnby N., Edwards M.F., Nienow A.W. Mixing in the Process Industries. 2nd ed.UK: Butterworth-Heinemann, 2000.

[22] Rakoczy R. Mixing energy investigations in a liquid vessel that is mixed by using a rotating magnetic field. Chemical Engineering and Processing. 2013;66:1–11. DOI: 10.1016/j.cep.2013.01.012

[23] Masiuk, S., Kawecka-Typek, J. Mixing energy measurements in liquid vessel with pendulum agitators. Chemical Engineering and Processing. 2004;43(2):91–99. DOI: 10.1016/S0255-2701(03)00072-2

[24] Masiuk, S., Rakoczy, R., Kordas, M. Comparison density of maximal energy for mixing process using the same agitator in rotational and reciprocating movements. Chemical Engineering and Processing. 2008;47(8):1252–1260. DOI: 10.1016/j.cep.2007.04.004

[25] Nienow, A.W. On impeller circulation and mixing effectiveness in the turbulent flow regime. Chemical Engineering Science. 1997;52(15):2557–2565. DOI: 10.1016/S0009-2509(97)00072-9

[26] Bouaifi M., Roustan M. Power consumption, mixing time and homogenisation energy in dual-impeller agitated gas–liquid reactors. Chemical Engineering and Processing. 2001;40(2):87–95, DOI: 10.1016/S0255-2701(00)00128-8

[27] Hörmann T., SuzziD., Khinast J.G. Mixing and dissolution processes of pharmaceutical bulk materials in stirred tanks: experimental and numerical investigations. Industrial and Engineering Chemistry Research. 2011;50(21):12011–12025. DOI: 10.1021/ie2002523

[28] Hartmann H., Derksen J.J., van den Akker H.E.A. Numerical simulation of a dissolution process in a stirred tank reactor. Chemical Engineering Science. 2006;61:3025–3032. DOI: 10.1016/j.ces.2005.10.058

[29] Baird M.H.I., Rama Rao N.V., Vijayan S. Axial mixing and mass transfer in a vibrating perforated plate extraction column. Canadian Journal of Chemical Engineering. 1992;70:69–76. DOI: 10.1002/cjce.5450700111

[30] Kordas M., Rakoczy R., Grądzik P., Story G. Rozpuszczanie ciała stałego w mieszalniku z mieszadłem wykonującym ruch obrotowy i posuwisto-zwrotny. Inżynieria i Aparatura Chemiczna. 2012;51(6):346–347. (In Polish).

[31] Masiuk S. Dissolution of solid body in a tubular reactor with reciprocating plate agitator. Chemical Engineering Journal. 2001;83:139–144. DOI: 10.1016/S1385-8947(00)00268-0.

[32] Masiuk S., Rakoczy R. Power consumption, mixing time, heat and mass transfer measurements for liquid vessels that are mixed using reciprocating multiplates agitators. Chemical Engineering and Processing. 2007;46:89–98. DOI:10.1016/j.cep.2006.05.002

[33] NiX., GaoS. Scale-up correlation for mass transfer coefficients in pulsed baffled reactors. Chemical Engineering Journal and the Biochemical Engineering Journal. 1996;63(3):157–166. DOI:10.1016/S0923-0467(96)03120-X

[34] Coteaţă M., Schulze H.P., Slătineanu L. Drilling of difficult-to-cut steel by electrochemical discharge machining. Materials and Manufacturing Processes. 2011;26(12):1466–1472. DOI: 10.1080/10426914.2011.557286

[35] Tai C.Y., Chi-Kao W., Chang M.C. Effects of magnetic field on the crystallization of $CaCO_3$ using permanent magnets. Chemical Engineering Science. 2008;63:5606–5612. DOI: 10.1016/j.ces.2008.08.004

[36] Kalaga D.V., Dhar A., Dalvi S.V., Joshi J.B. Particle–liquid mass transfer in solid–liquid fluidized beds. Chemical Engineering Journal. 2014;245:323–341. DOI:10.1016/j.cej.2014.02.038

[37] Grénman H., Murzina E., Rönnholm M., Eränen K., Mikkola J., Lahtinen M., et al. Enhancement of solid dissolution by ultrasound. Chemical Engineering and Processing. 2007;46:862–869. DOI:10.1016/j.cep.2007.05.013

[38] Kannan A., Pathan S.K. Enhancement of solid dissolution process. Chemical Engineering Journal. 2004;102:45–49. DOI: 10.1016/j.cep.2009.11.004

[39] Sandilya K.D., Kannan A. Effect of ultrasound on the solubility limit of a sparingly soluble solid. Ultrasonics Sonochemistry. 2010;17:427–434. DOI:10.1016/j.ultsonch.2009.10.005

[40] Dold P., Szofran F.R., Benz K.W. Thermoelectromagnetic convection in vertical Bridgman grown germanium–silicon. Journal of Crystal Growth. 2006;291:1–7. DOI: 10.1016/j.jcrysgro.2006.02.055

[41] Kao, A., Djambazov, G., Pericleous, K. and Voller, V. Effects of magnetic fields on crystal growth. Proceedings in Applied Mathematics and Mechanics. 2007;7:4140015–4140016. DOI: 10.1002/pamm.200700922

[42] Du D., Hou L., Gagnoud A., Ren Z., Fautrelle Y. Cao G., Li X. Effect of an axial high magnetic field on Sn dendrite morphology of Pb–Sn alloys during directional solidification. Journal of Alloys and Compounds. 2014;588:190–198. DOI:10.1016/j.jallcom.2013.11.011

[43] Bouabdallah S., Bessaïh R. Effect of magnetic field on 3D flow and heat transfer during solidification from a melt. International Journal of Heat and Fluid Flow. 2012;37:154–166. DOI: 10.1016/j.ijheatfluidflow.2012.07.002

[44] Spitzer K.H. Application of rotating magnetic field in Czochralski crystal growth. Progress in Crystal Growth Characterization. 1999;38(1–4):59–71. DOI: 10.1016/S0960-8974(99)00008-X

[45] Dold P., Benz K.W. Rotating magnetic field: fluid flow and crystal growth applications. Progress in Crystal Growth Characterization of Materials. 1999;38:7–38, DOI 10.1016/S0960-8974(99)00007-8

[46] Walker J.S. Bridgman crystal growth with a strong, low-frequency, rotating magnetic field. Journal of Crystal Growth. 1998;192(1–2):318–327. DOI:10.1016/S0022-0248(98)00438-2

[47] Yang, M., Ma, N., Bliss, D.F., Bryant G.G. Melt motion during liquid-encapsulated Czochralski crystal growth in steady and rotating magnetic field. International Journal of Heat and Mass Transfer. 2007;28:768–776. DOI: 10.1016/j.ijheatfluidflow.2006.08.001

[48] Lu, X.S., Li, H. Fluidization of $CaCO_3$ and Fe_2O_3 particle mixtures in a transverse rotating magnetic field. Powder Technology. 2000;107:66–78. DOI: 10.1016/S0032-5910(99)00092-3

[49] Hristov J. Magnetic field assisted fluidization—dimensional analysis addressing the physical basis. China Particuology. 2007;5(1–2):103–110. DOI:10.1016/j.cpart.2007.03.002

[50] Nikrityuk, P.A., Eckert, K., Grundmann, R. A numerical study of unidirectional solidification of a binary metal alloy under influence of a rotating magnetic field. International Journal of Heat and Mass Transfer. 2006;49:1501–1515. DOI: 10.1016/j.ijheatmasstransfer.2005.08.035

[51] Willers, B., Eckert, S., Michel, U., Haase, I., Zouhar, G. The columnar-to-equiaxed transition in Pb–Sn alloys affected by electromagnetically driven convection. Materials Science and Engineering A. 2005;402(1–2):55–65, DOI: 10.1016/j.msea.2005.03.108

[52] Lu, X.S., Li, H. Fluidization of $CaCO_3$ and Fe_2O_3 particle mixtures in a transverse rotating magnetic field. Powder Technology. 2000;107:66–78. DOI: 10.1016/S0032-5910(99)00092-3

[53] Rakoczy, R., Masiuk, S. Influence of transverse rotating magnetic field on enhancement of solid dissolution process. American Institute of Chemical Engineers Journal. 2010;56:1416–1433. DOI: 10.1002/aic.12097

[54] Rakoczy R. Enhancement of solid dissolution process under the influence of rotating magnetic field. Chemical Engineering and Processing: Process Intensification. 2010:49(1):42–50. DOI: 10.1016/j.cep.2009.11.004

Chapter 7

Multiphase Mass Transfer in Iron and Steel Refining Processes

Lucas Teixeira Costa and Roberto Parreiras Tavares

Additional information is available at the end of the chapter

http://dx.doi.org/10.5772/60800

Abstract

In the present chapter, a computational fluid dynamics (CFD) model for multiphase flow was developed, allowing the simulation of two different processes, the desulfurization of hot metal in a ladle mechanically agitated by an impeller (KR process) and the desulfurization of steel in a gas-agitated ladle. The model gives important information to characterize the fluid flow conditions, to define the velocity profiles of the phases involved, and to predict the evolution of the sulfur content during the desulfurization treatments. An expression for the rate of transfer of sulfur from the metal to the slag was proposed. This expression can be used in processes where sulfur is transferred from the metal to the slag phase. The predictions of the variations of sulfur content of the metal phase with time were validated based on experimental data obtained in a Brazilian industrial plant for steel desulfurization. After the validation, the model was used to simulate the effects of several parameters and to optimize the processes. Based on these simulations, it was possible to set up the best operational conditions to improve the productivity of sulfur removal in the primary and secondary metallurgy.

Keywords: Mass transfer, CFD, desulfurization, hot metal, steel

1. Introduction

With the growing demand for high quality steels, several processes for hot metal and steel refining were developed for various purposes, such as decarburization, removal of inclusions, narrowing the range of chemical composition, thermal homogenization, and production of steels with low levels of impurities.

The efficiency and the productivity of these processes depend largely on the kinetics of the chemical reactions. Since these processes are usually developed at high temperatures, the rate-controlling step of the reactions involved is usually a mass transfer step.

In iron and steel refining, mass transfer is always a multiphase phenomenon. Different situations occur, depending on the phases involved, as follows:

- Liquid–liquid mass transfer, in the case of reactions involving liquid hot metal and steel and slag
- Liquid–gas mass transfer, when a gas is injected into or onto liquid hot metal and steel
- Liquid–solid mass transfer, when solid particles are injected into liquid hot metal and steel to promote refining reactions

In the present chapter, the importance of multiphase mass transfer in hot metal and steel refining processes will be emphasized. The fundamentals of multiphase mass transfer will be addressed, including the different techniques that are usually adopted to evaluate the mass transfer coefficient and to analyze the effects of the variables that affect its value.

Finally, two case studies, analyzing multiphase mass transfer rate during the desulfurization of hot metal and steel, will be presented and discussed.

Steels with ultralow sulfur contents are used in the manufacture of pipes for transporting oil and construction of offshore platforms, which require high impact strength and resistance to lamellar crack formation by interaction with hydrogen and sulfide inclusions.

It is well known that the efficiencies of the desulfurization of liquid hot metal and steel depends on the setting of the kinetic and thermodynamic factors that must be adjusted simultaneously to provide theoretical and practical ways to enable the optimization of the process parameters. In these case studies, a computational fluid dynamics (CFD) model for multiphase flow was developed, allowing the simulation of two different processes, the desulfurization of hot metal in a ladle mechanically agitated by an impeller and the desulfurization of steel in a gas-agitated ladle. The model gives important information to characterize the fluid flow conditions, to define the velocity profiles, and to predict the evolution of the sulfur content during the desulfurization treatments.

The model was able to predict the sulfur contents of hot metal and steel as a function of time. The predictions of the model were validated based on experimental data obtained in an industrial plant for steel desulfurization. After the validation, the model was used to simulate the effects of several parameters and to optimize the processes.

2. Multiphase mass transfer

The desulfurization of hot metal and steel is a reaction that occurs at the interface between liquid metal and liquid slag. Due to the high temperatures involved, the reaction rate is usually controlled by mass transfer between these two phases. To enhance the mass transfer rate, different methods of agitation are used. The most common are gas injection and mechanical agitation using an impeller.

The mass transfer rate of sulfur between metal and slag is usually determined by the following relationship [1]:

$$j_S = kA\left(C_S^m - C_S^i\right) \tag{1}$$

where

j_S is the sulfur transfer rate between metal and slag (kg/s),

k is the sulfur mass transfer coefficient (m/s),

A is the interface area (m^2),

C_S^m is the sulfur concentration in the metal phase (kg/m^3), and

C_S^i is the sulfur concentration at the metal–slag interface (kg/m^3).

To apply Equation (1) in the evaluation of the mass transfer rate, the sulfur mass transfer coefficient, the interface area, and the sulfur concentration at the metal–slag interface must be known. These parameters depend on the fluid flow patterns of both phases, on the geometry of the interface, and on the partition coefficient of sulfur between metal and slag. The sulfur concentration at the metal–slag interface is usually considered the equilibrium concentration since the chemical reaction at the interface is very fast at the temperatures at which these processes are developed. To estimate the equilibrium concentration, it is necessary to know the partition coefficient of sulfur between metal and slag. This partition coefficient is a thermodynamic variable that depends on the temperature and on the chemical composition of the slag and can be estimated using data available in the literature or using thermodynamic softwares (i.e., FactSage, Thermocalc, etc.).

The fluid flow patterns of the phases involved and the geometry of the metal–slag interface can be determined by simulations using computational fluid dynamics (CFD). Independent of the method of agitation, the procedure adopted to simulate the sulfur mass transfer during hot metal or steel refining followed the same sequence of steps:

- Evaluation of the fluid flow patterns of the phases involved, solving the turbulent form of the Navier–Stokes equations for multiphase systems. In this stage, the velocities and the turbulence parameters for all phases were determined. The geometry of the metal–slag interface was also obtained. Steady-state conditions are assumed in this step.
- Calculation of the partition coefficient of sulfur between the metal and the slag. The temperature and the slag composition must be specified. In the simulations presented here, the partition coefficients were determined based on information available in the literature.
- Simulation of the sulfur content variation in the metal during the desulfurization process. Using the results obtained on the previous steps, the transient mass conservation equation for sulfur was solved. The variation of sulfur concentration as a function of time and position in the simulation domain was calculated. The variation of the average sulfur concentration

in the liquid metal was then compared to some experimental results obtained in an industrial plant for validation purposes.

In the next section, two case studies of metal desulfurization are present and discussed.

3. Case studies

In this section, simulations of steel desulfurization in a gas-stirred ladle and hot metal desulfurization in a mechanically agitated ladle (KR-process) are presented and discussed. The validation of the predictions of the models using industrial data is also included. Finally, the effects of process variables on the desulfurization rate are analyzed.

3.1. Steel desulfurization in a gas-agitated ladle

Steel desulfurization is usually developed in a gas-stirred ladle. Different configurations of the gas injection system are adopted and that can affect the efficiency of the process. In the present case, the configuration considered was used in a Brazilian steelmaking industry.

3.1.1. CFD model

The ladle considered is schematically shown in Figure 1. Its main characteristics are presented in Table 1.

Parameter	Value
Height	3.3 m
Diameter at the bottom	2.32 m
Diameter at the top	2.50 m
Number of porous plugs	2
Diameter of the plugs	0.076 m
Nominal capacity	80 tons

Table 1. Main characteristics of the ladle.

Three phases were considered: liquid steel, liquid slag, and argon. The turbulent form of the conservation equations for mass, momentum, and turbulence quantities for each individual phase were solved using the commercial software Ansys-CFX. For turbulence, the standard k–ε model was used. One additional equation for sulfur mass conservation was included to simulate the transfer of sulfur between steel and slag. The transfer of sulfur to the gas phase was not considered.

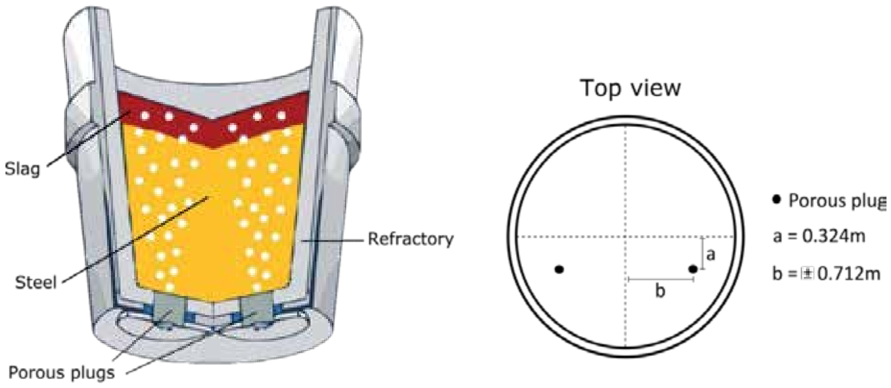

Figure 1. Schematic view of the ladle used for steel desulfurization with locations of the porous plugs at the bottom of the ladle.

Steel and slag were considered Newtonian fluids with constant density and viscosity. Argon was assumed as an ideal gas. Isothermal condition was considered in all simulations.

The diameter of the gas bubbles was considered uniform. It was evaluated using the equation proposed for liquid steel and argon [2]:

$$d_b = \left[\frac{3\sigma d_0}{\rho g} + \left(\frac{9\sigma^2 d_0^2}{\rho^2 g^2} + \frac{10Q^2 d_0}{g} \right)^{\frac{1}{2}} \right]^{\frac{1}{3}} \tag{2}$$

where

d_b is the diameter of the bubble (cm),

d_o is the diameter of the porous plug (cm),

Q is the gas flow rate (cm^3/s),

σ is the interfacial tension between liquid steel and argon (dyn/cm), and

ρ is the density of liquid steel (g/cm^3).

Nonslip conditions were assumed on all the solid walls of the ladle. At the porous plug, the gas flow rates were specified. Since the gas is injected at ambient temperature, the gas flow rates were adjusted considering the thermal expansion to the temperature of the domain. The top of the ladle was considered as an opening. The volumetric fractions of the three phases involved in the simulations were calculated in each of the control volumes of the domain. This enabled the evaluation of the contours of the phases and the interphase areas.

Grid-independent solutions were attained dividing the domain in approximately 1.5×10^6 volume elements. Figure 2 shows the mesh configuration adopted in the simulations.

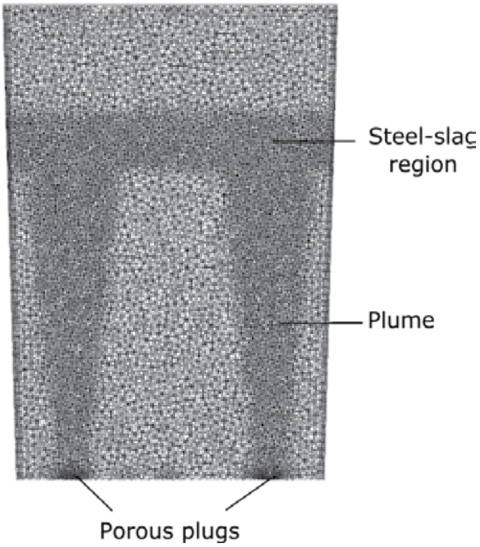

Figure 2. Mesh configuration considered in the simulations. Vertical plane passing through the porous plugs.

Nonuniform mesh was adopted, with smaller volume elements in the plume region and in the metal–slag interface.

3.1.2. Sulfur transfer model

An additional equation for sulfur transfer between metal and slag was incorporated into the model:

$$\frac{dM_S}{\mathrm{dt}} = -k_S A\left(C_{S,\mathrm{steel}} - \frac{C_{S,\mathrm{slag}}}{L_S}\right) \tag{3}$$

where

M_S the mass of sulfur transferred in the volume element interface(kg),

t is time (s),

k_S is the mass transfer coefficient for sulfur (m/s),

$C_{S,\mathrm{steel}}$ is the sulfur concentration in the metal (kg/m^3)

$C_{S,\mathrm{slag}}$ is the sulfur concentration in the slag (kg/m^3),

L_S is the partition coefficient for sulfur between slag and metal, and

A is the metal–slag interface area.

This equation was applied in every volume element where metal and slag coexisted. The metal–slag interface area and the volume of metal in each control volume were calculated by the Ansys-CFX software.

The partition coefficient was determined according to an equation proposed by Gaye et al. [3]. The mass transfer coefficient was estimated based on the correlation proposed by Incropera and DeWitt [4]:

$$Sh = 0.029\mathrm{R}^{4/5}Sc^{1/3} \tag{4}$$

where

Sh is the Sherwood number,

Re is the Reynolds number, and

Sc is the Schmidt number.

In this equation, most of the parameters depend on the physical properties of the liquid metal and are constant. Considering this, Equation (4) can be rewritten in the following form:

$$k_s = Cv_i^{4/5} \tag{5}$$

where

C is the constant and

v_i is the velocity of the metal in the interfacial region with the slag. This velocity is calculated during the CFD simulation.

The value of constant C was determined using industrial data in which samples of liquid steel were taken from the ladle desulfurization.

3.1.3. Validation of the model

To validate the predictions of the model, data from three industrial treatments were obtained. The information collected in these treatments included the following:

- Variation of the sulfur content of the liquid steel during the process (samples taken at intervals of five minutes)
- Mass of liquid steel being treated
- Mass and chemical composition of the slag
- Temperature of the process
- Argon flow rate in each porous plug

3.1.4. Results and discussion

The conditions adopted in all the CFD simulations are presented in Table 2.

Parameter	Value
Height of liquid steel	2.48 m
Mass of liquid steel	80.84 tons
Thickness of the slag layer	0.12 m
Mass of liquid slag	1430 kg
Argon flow rate	
Porous plug 1	13.2 Nm^3/h
Porous plug 2	4.8 Nm^3/h
Viscosity of liquid steel	6.5 x 10^{-3} Pa.s
Viscosity of liquid slag	0.65 Pa.s

Table 2. Conditions considered in the CFD simulations of desulfurization in a gas-stirred ladle.

Figure 3 illustrates the velocity profile of liquid steel in a vertical plane passing through the porous plugs. This profile is similar to those presented by Patil et al. [5].

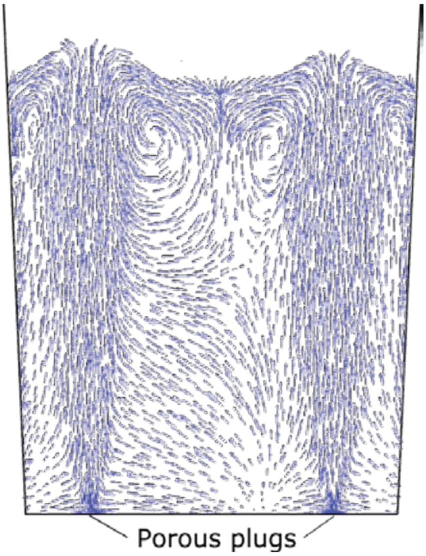

Figure 3. Velocity profile of liquid steel in a vertical plane passing through the porous plugs.

Figure 4 shows the regions of liquid steel, slag, and plume (argon) for the same vertical plane seen in Figure 3.

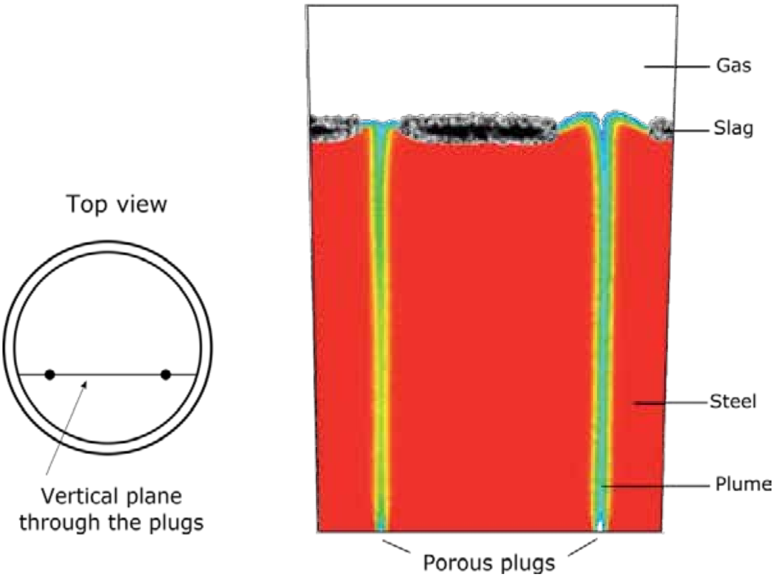

Figure 4. Regions of liquid steel, slag, and plume (argon) in a vertical plane passing through the nozzles.

For the conditions simulated, there is an "open eye" of liquid steel at the top of the ladle.

To estimate the value of constant C in Equation (5), samples of liquid steel were taken during a desulfurization treatment. The samples were taken at intervals of 5 minutes. Adjusting the simulation predictions to the experimental results, it was possible to determine the value of 1.45×10^{-3}. The composition of the slag used in this treatment was as follows (in weight percent): CaO, 54%; MgO, 5%; SiO_2, 19%; and Al_2O_3, 22%. The sulfur partition coefficient for this slag is 18.4 (according to the equation proposed by Gaye et al. [3]). With this value of constant *C*, it was possible to simulate the desulfurization process for other treatments. The results obtained for one of these treatments are illustrated in Figure 5. The experimental results are also included in the figure. In this case, the slag composition was as follows: CaO, 57%; MgO, 8%; SiO_2, 10%; and Al_2O_3, 25%. The partition coefficient was 52.

The model predictions reproduce very well the experimental data. Based on these results, the model was validated, and the effects of different parameters were analyzed. The effects of argon flow rate, slag composition, and slag thickness are presented here. These results were compared to the predictions using the conditions specified in Table2 (reference case).

Figure 6 shows the effect of the total argon flow rate on the variation of the sulfur content in the liquid steel. Only the last 15 minutes of the simulations are presented. In the range tested, there is only a slight effect of the argon flow rate on the sulfur contents. A significant increase in the argon flow rate does not have an important impact on the desulfurization but increases the area of the "open eye" of liquid steel, which can have deleterious effects on the steel quality.

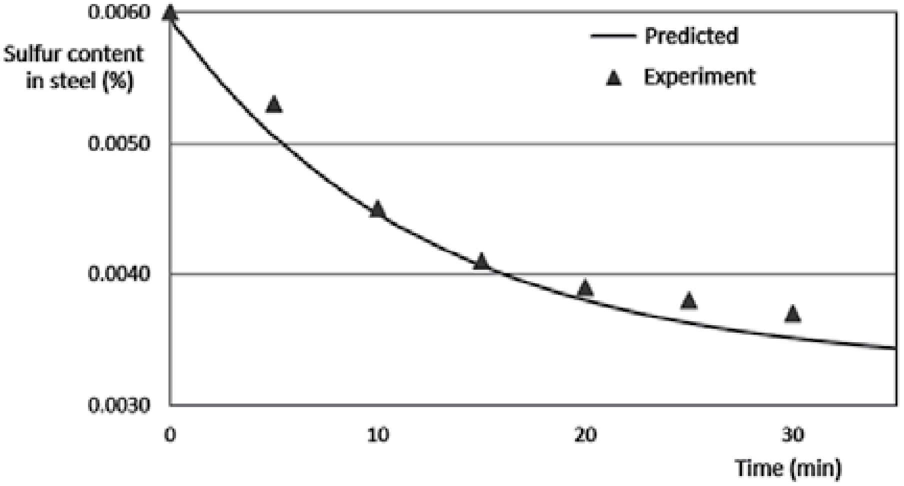

Figure 5. Comparison of the variations of sulfur content of the liquid steel as a function of time predicted by the model and determined in the experiment.

This effect of the argon flow rate can be explained in terms of the increase of velocities of the steel at the metal–slag interface, which increases the mass transfer coefficient, and in terms of faster homogenization of the sulfur content of the steel inside the ladle.

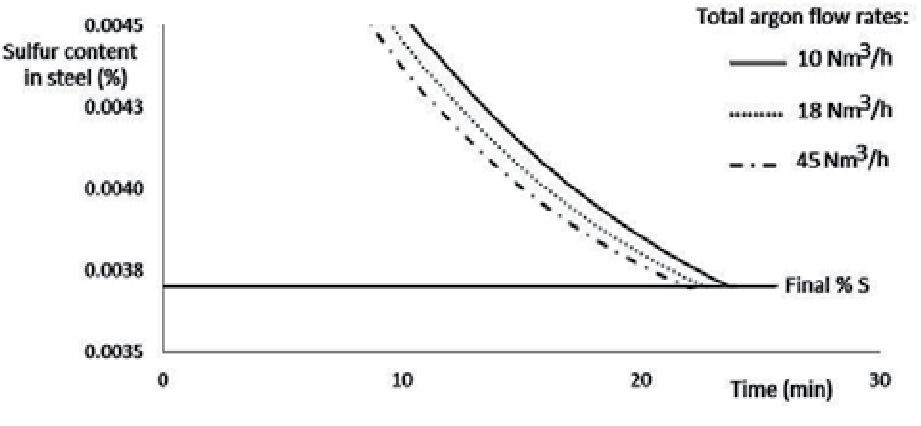

Figure 6. Effect of the total argon flow rate on the desulfurization process.

Figure 7 illustrates the effect of slag composition. Slag 1 is the one considered in Figure 5. Slag 2 has a partition coefficient of 52. An increase in the partition coefficient leads to a pronounced increase in the desulfurization rate. The time to reach a sulfur content of 35 ppm is 15 minutes for slag 2 and 24 minutes for slag 1. This could lead to a significant increase in productivity of the steel plant.

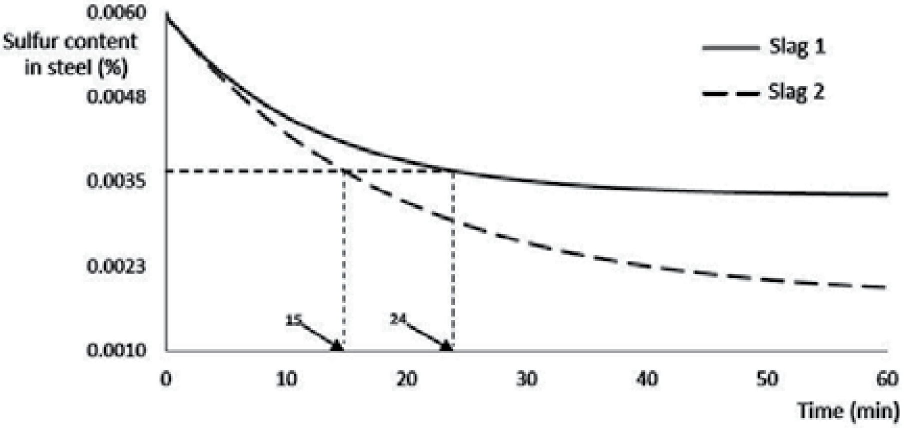

Figure 7. Effect of the slag partition coefficient on the desulfurization process.

Finally, the effect of the thickness of the slag layer is presented in Figure 8.

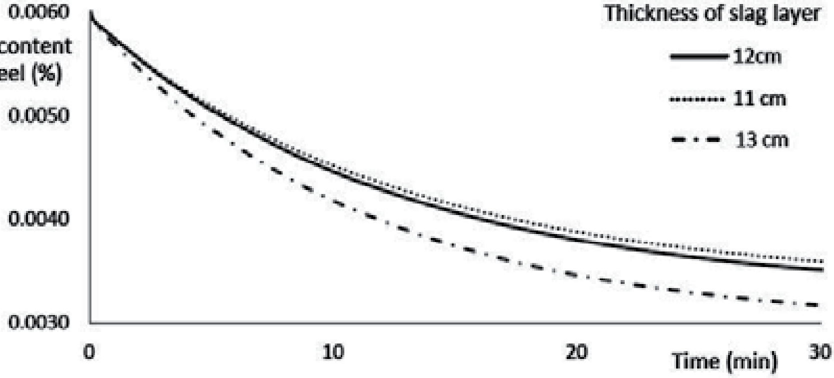

Figure 8. Variation of the sulfur content for different thicknesses of the slag layer.

As shown, an increase in the slag thickness has a positive effect on the desulfurization rate. With more slag, the sulfur concentration in the slag phase is smaller, and this leads to an increase in the driving force for sulfur transfer from steel to slag. Another benefit of a thicker slag layer is the reduction of the area of the "open eye."

3.2. Hot metal desulfurization in a mechanically agitated ladle

The KR process is largely used to promote hot metal desulfurization. In the process, an impeller is used to stir the liquid metal and to enhance the contact between metal and slag. Among the several variables that affect the desulfurization rate, the penetration in the liquid metal and position along the radius and the rotation speed of the impeller were chosen to be investigated.

The geometries of the ladle and of the impeller were specified according to the design currently being used in a Brazilian industry. The simulations followed the same steps described for the analysis of steel desulfurization in gas-stirred ladle.

3.2.1. CFD model

The geometries of the ladle and of the impeller are schematically shown in Figure 9. Their main dimensions are given in Table 3.

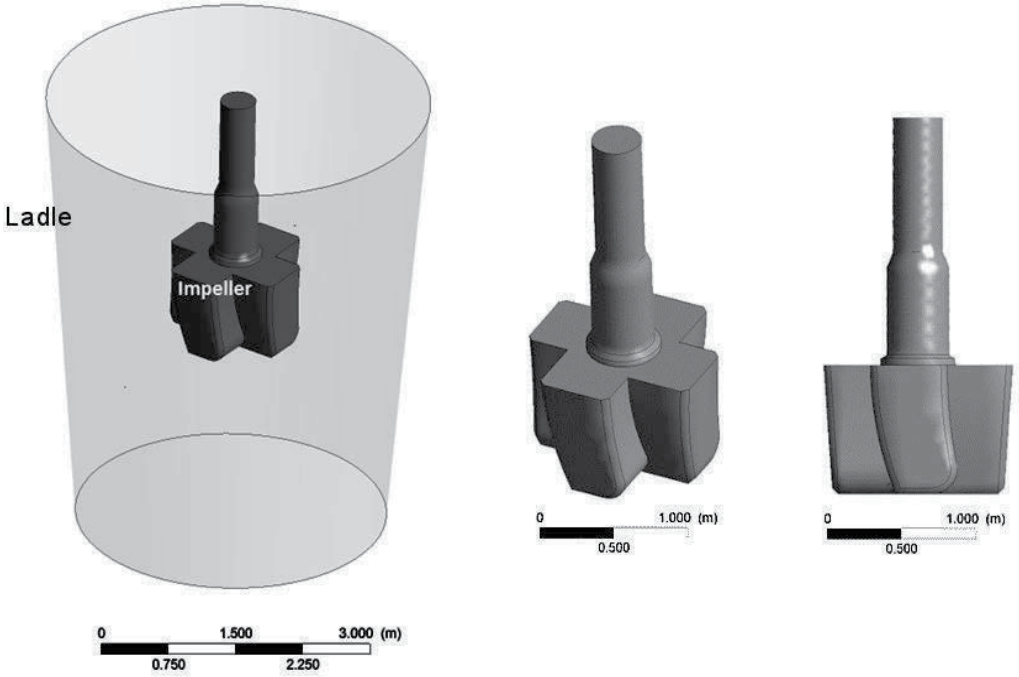

Figure 9. Schematic view of the ladle and of the impeller.

The CFD model is similar to that for steel desulfurization described previously. Since there is no gas injection in the KR process, the conservation equations were solved only for the hot metal and for the slag. A free surface model was implemented to identify the interfaces between the phases. The commercial software Ansys-CFX was used in all the simulations.

Hot metal and slag were assumed as Newtonian fluids with constant density and viscosity. These two phases were in thermal equilibrium.

For boundary conditions, nonslip conditions were considered on all the solid walls, including the surface of the impeller. The rotation speed of the impeller was specified.

The equation for sulfur transfer between the hot metal and the slag is similar to that used for desulfurization. The partition coefficient was also calculated using the same method shown

	Parameter	Value
Ladle	Height	5.10 m
	Diameter at the bottom	3.45 m
	Diameter at the top	4.30 m
	Nominal capacity	315 tons
Impeller	Top radius	1.50 m
	Bottom radius	1.35 m
	Length	1.00 m
	Radius of the axis	0.25 m

Table 3. Dimensions of the ladle and of the impeller.

by Gaye et al. [3]. The mass transfer coefficient was estimated according to Equation (5), with a value of 1.45×10^{-3} for C.

Grid-independent solutions were attained dividing the domain in approximately 1.2×10^6 volume elements. Figure 10 shows the mesh configuration adopted in the simulations.

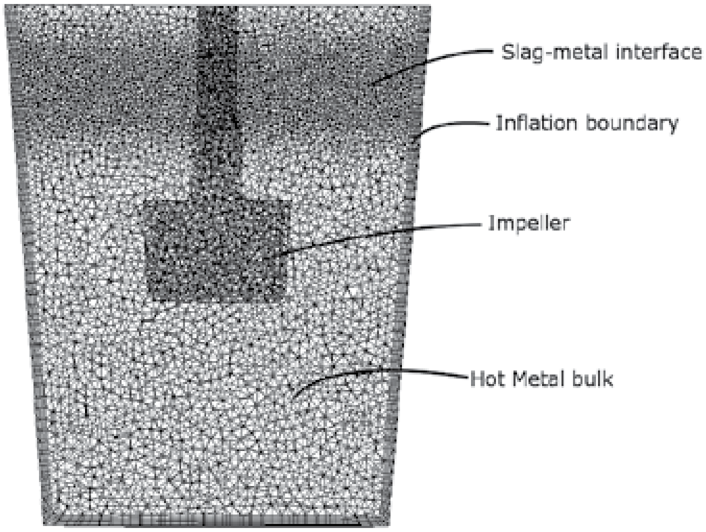

Figure 10. Mesh configuration considered in the simulations. Vertical plane passing the center of the ladle.

Nonuniform mesh was adopted, with smaller volume elements near the walls and in the metal–slag region.

3.2.2. Results and discussion

The conditions adopted in the CFD simulations are presented in Table 4.

Parameter	Value
Height of hot metal	4.20 m
Mass of hot metal	315 tons
Thickness of the slag layer	0.12 m
Mass of liquid slag	3500 kg
Viscosity of hot metal	6.5 x 10-3 Pa.s
Viscosity of liquid slag	0.65 Pa.s

Table 4. Conditions considered in the CFD simulations of desulfurization of hot metal in the KR process.

The impeller was located at the center of the ladle. The rotation speed was 40 rpm. The distance between the bottoms of the impeller and of the ladle was 2.5 m. These conditions are assumed as a reference to analyze the effects of some process variables.

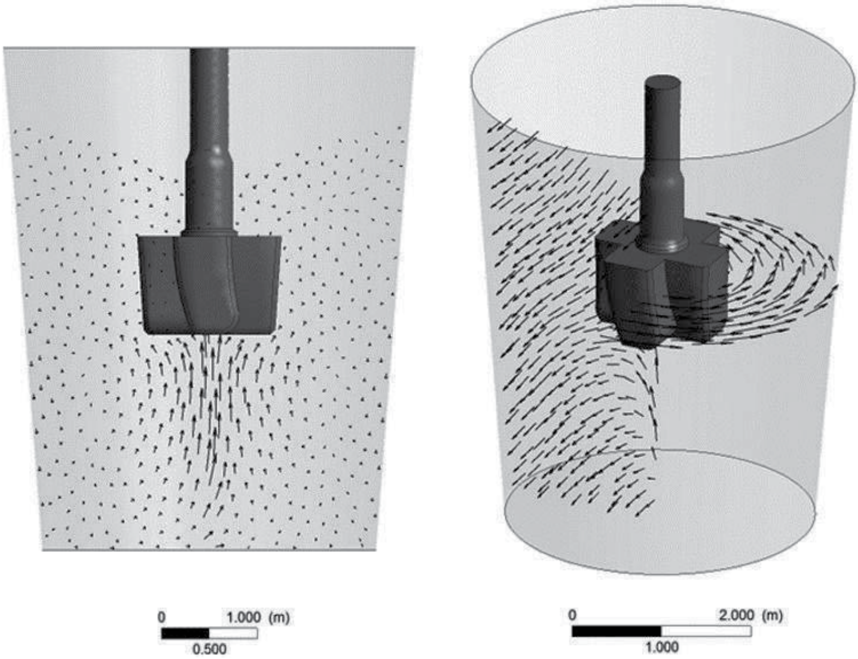

Figure 11. Velocity profiles of liquid hot metal in a vertical plane passing through the center of the ladle and in a horizontal plane passing through the impeller.

Figure 11 illustrates the velocity profile of liquid hot metal in a vertical plane passing through the center of the ladle and in a horizontal plane passing through the impeller. This profile is similar to those presented by Shao et al. [6]. There is an upward flow underneath the impeller. The rotation of the impeller also induces a rotation flow of hot metal. This rotation affects the pressure field and leads to a reduction of the level of hot metal in the center and an increase near the wall of the ladle, as seen in Figure 12, which shows the regions of liquid hot metal and slag for a vertical plane passing through the center of the ladle. This variation in the level of the hot metal significantly increases the interface area between metal and slag and increases the desulfurization rate.

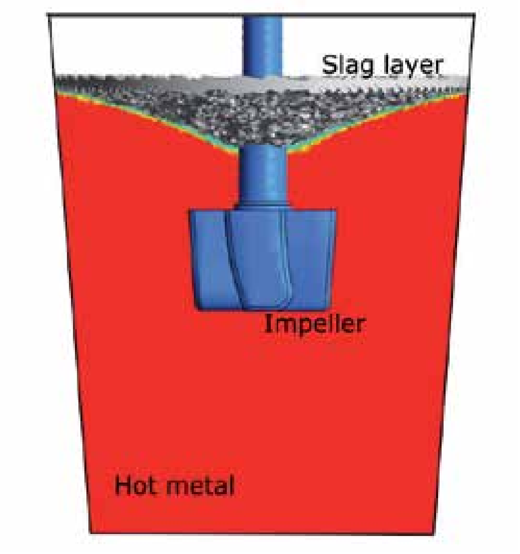

Figure 12. Regions of liquid hot metal and slag in a vertical plane passing through the center of the ladle.

Figure 13 shows the results of the simulation of the desulfurization of the hot metal for the reference conditions. The reduction of sulfur content is much faster than that observed with steel. The main reason for that is the higher initial sulfur content of the hot metal, which gives a more significant driving for sulfur transfer to the slag. As seen, a 5-minute treatment is sufficient to reduce the sulfur content from 300 to approximately 50 ppm. This result is consistent with data available in the literature [7–9].

Using the mathematical model, the effects of some process variables were investigated. Figure 14 shows the effect of positioning the impeller with its axis of rotation 40 cm off center. Compared to the impeller located at the center of the ladle, there is a slight reduction in the desulfurization rate. Although it was not considered in the model, locating the impeller off center might also increase refractory wear due to higher velocities near the wall of the ladle.

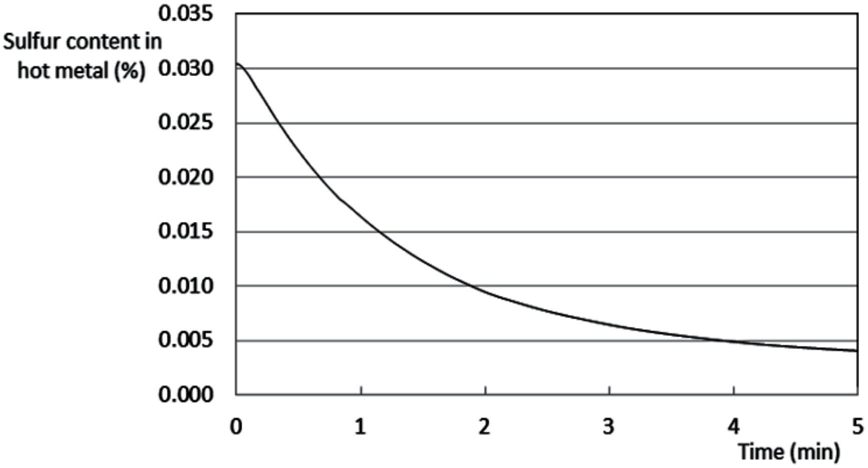

Figure 13. Variation of the sulfur content in the hot metal during the desulfurization. Reference conditions.

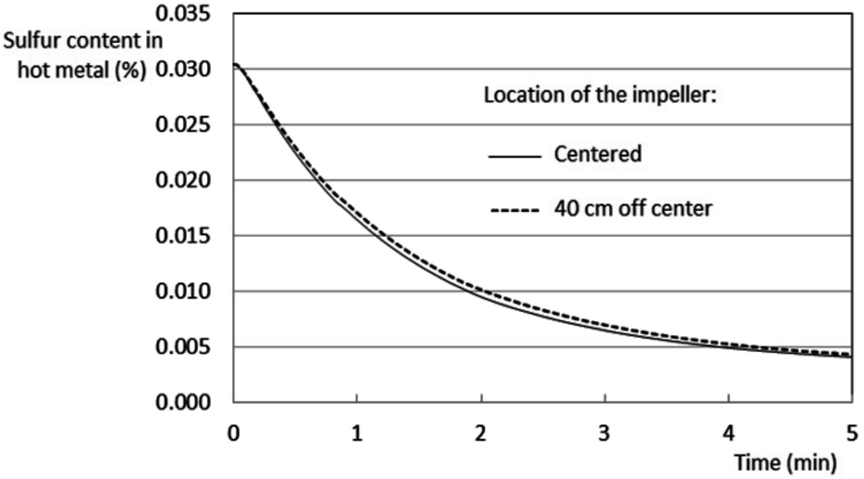

Figure 14. Effect of the location of the impeller on the variation of sulfur content of the hot metal.

The effect of the immersion depth of the impeller is presented in Figure 15. In this case, the immersion depth was increased in 40 cm (the distance between the bottoms of the impeller and of the ladle was reduced to 2.1 m). Increasing the immersion depth reduces the velocities in the region close to the interface between the hot metal and the slag. This leads to a decrease in the sulfur mass transfer coefficient and has a negative effect on the desulfurization rate.

Figure 16 illustrates the effect of an increase of 10 rpm in the rotation speed of the impeller (from 40 to 50 rpm). Among the variables analyzed, the rotation speed presented the most significant effect. With a rotation speed of 50 rpm, the velocities near the metal–slag interface increase and so does the mass transfer coefficient. Together with a faster homogenization of

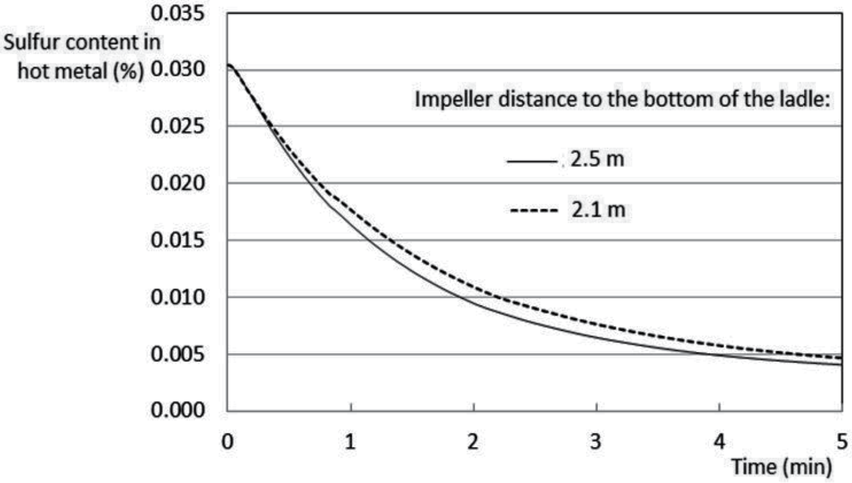

Figure 15. Variation of sulfur content of the hot metal for two immersion depths of the impeller.

the sulfur of the hot metal, the consequence is a faster desulfurization. Considering a final content of sulfur of 50 ppm, it is observed that an increase in the rotation speed to 50 rpm can lead to approximately a 1-minute reduction in the treatment time, with possible increase of productivity.

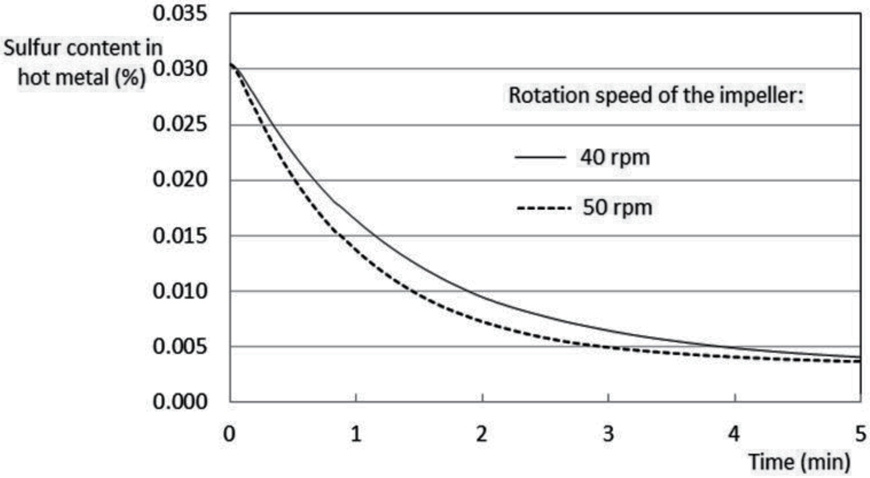

Figure 16. Effect of the rotation speed of the impeller on the variation of sulfur content of the hot metal.

Based on factor analysis, an equation to predict the sulfur content after a treatment of five minutes was determined:

$$S_{ppm} = 300.13 - 87.45d_B - 4.47r_S + 9d_{off} + 1.45d_Br_S \qquad (6)$$

where

S_{ppm} is the sulfur content after 5 minutes of treatment in the KR process (ppm),

d_{B} is the distance between the bottoms of the impeller and of the ladle (m),

r_{S} is the rotation speed of the impeller (rpm), and

d_{off} is the off-center distance of the axis of the impeller (m).

4. Conclusions

Mass transfer plays a significant role in the kinetics of steelmaking processes. In these processes, mass transfer is usually a multiphase phenomenon, and its rate is affected by the flow conditions of the phases involved.

In the production of high-quality steels, especially those with very low sulfur content, desulfurization must be implemented. The desulfurization of hot metal and liquid are both commonly used. In most processes, desulfurization is promoted by transferring sulfur from the metal to a refining slag.

In the present chapter, the desulfurization of steel in a gas-stirred ladle and of hot metal in the KR process was studied by mathematical modeling. The model developed involved the simulation of the flow field of the different phases involved, coupled with a mass conservation equation for sulfur, which included an expression for the rate of transfer of sulfur from the metal to the slag. The commercial software Ansys-CFX was used to solve the turbulent form of the Navier–Stokes equations for multiphase flows. The predictions of the model were validated using industrial data of steel desulfurization.

For the desulfurization of steel in a gas-stirred ladle, it was shown that increasing the sulfur partition coefficient and the thickness of the slag layer at the top of the ladle have both positive effects on the desulfurization rate. The gas flow rate, in the range tested, presented a minor effect, but very high gas flow rates lead to an increase in the "open eye" area of liquid steel at the top of the ladle, which can have deleterious effects on the steel quality.

For the desulfurization of hot metal in the KR process, the effects of variables related to the impeller position and rotation speed were investigated. The predictions of the model indicated that, in the ranges tested, the rotation of the impeller has the most significant effect. Increasing the penetration depth of the impeller and locating its axis of rotation off center in the ladle have slight negative effects on the desulfurization rate.

Acknowledgements

The financial support of FAPEMIG in the form of a research grant to R. P. Tavares (Process No. TEC-PPM-00118-13) is gratefully acknowledged. The authors also acknowledge the financial support of CAPES/PROEX to the graduate program. The scholarship from CNPq to the first author is also gratefully acknowledged.

Author details

Lucas Teixeira Costa and Roberto Parreiras Tavares*

*Address all correspondence to: rtavares@demet.ufmg.br

Federal University of Minas Gerais, Brazil

References

[1] Pomfret, R.J., Grieveson, P.. The kinetics of slag-metal reactions. Canadian Metallurgical Quarterly. 1983;2(22):287–299.

[2] Sano, M., Mori, K.. Bubble formation from single nozzles in liquid metals. Transactions JIM. 1976;(17):344–352.

[3] Gaye H., Gatellier C., Nadif R.P., Saleil J., Faral, M.. Réaction Métal-Laitier et Contrôle De La Composition Des Inclusions Résiduelles en Métallurgie Secondaire. Proceedings of the Clean Steel 3rd, Balatonfüred, Hungary. Institute of Metals. 1986;

[4] Incropera F., DeWitt D.. Fundamentals of Heat and Mass Transfer. 4th edition. John Wiley & Sons; 1996. DOI: 0-471-30460-3

[5] Patil S., Satish D., Peranandhanathan M., Mazumdar D.. Mixing models for slag covered, argon stirred ladles. ISIJ International. 2010;8(50):1117–1124.

[6] Shao P., Zhang T., Zhang Z., Liu Y.. Numerical simulation on gas–liquid flow in mechanical-gas injection coupled stirred system. ISIJ International. 2014;7(54):1507–1516.

[7] Kikuchi N., Nabeshima S., Takeuchi S., Yamauchi T., Kitano Y., Ogura S.. Effect of hot metal temperature and rotation speed on the rate of desulfurization rate by mechanical stirring process. Tetsu-To-Hagané. 2004;6(90):1883–2954.

[8] Nakai Y. Sumi I., Matsuno H., Kikuchi N., Kishimoto Y.. Effect of flux dispersion behavior on desulfurization of hot metal. ISIJ International. 2010;(50):403–410.

[9] Nakai Y., Kikuchi N., Miki Y., Kishimoto Y., Isawa T., Takeshi K.. Hot metal desulfurization behavior with dolomite flux. ISIJ International. 2013;6(53):1020–1027.

Disintegration Kinetics of Microbial Cells

Marek Solecki and Monika Solecka

Additional information is available at the end of the chapter

http://dx.doi.org/10.5772/60797

Abstract

Results of the disintegration of yeast *Saccharomyces cerevisiae* in the bead mill with a multi disk impeller are presented. The degree of disintegration was specified on the basis of absorbency measurements at the wavelength 260 nm. The process was investigated by two integrated methods. The experimental values of maximum absorbency A_{m2} appeared to be smaller than theoretical ones A_{m1}, which resulted from searching for the highest values of correlation coefficient between variables t and $\ln[A_{m1} / (A_{m1} - A)]$. A significant increase of the process rate constant was observed when the slurry concentration increased in the range from 0.05 to 0.20 g d.m./cm^3. This phenomenon was explained by an additional mechanism of cell destruction, which was induced by fragments of ground walls. The rate constant changed during the process due to a change of inner process conditions, and not directly as a result of a changing number of microbial cells. Modeling of the process in which the first-order differential equation is used to describe the kinetics is correct, with the process rate constant being a function of parameters that describe inner conditions changing during the process.

Keywords: Random transformation of dispersed matter, disintegration of microorganisms, bead mill, kinetics of the process

1. Introduction

Chemical compounds contained in microorganisms provide the opportunity, often the only one, to satisfy a whole range of human needs. Commercial importance was gained by, among others, intracellular enzymes used to shape and preserve functional properties of foodstuffs, conducting clinical analyses, antibiotic conversion, or therapy applied during cancer diseases [1]. The genetic modification of microorganisms allows for a further increase in the range of intracellular compounds' utilization. Such a possibility should lead to obtaining valuable components from microorganisms generally considered safe for people on an industrial scale [2].

The separation of compounds contained in microorganisms generally requires the destruction of cell walls and cytoplasmic membranes. The process is conducted in high pressure homogenizers and bead mills on a semitechnical and technical scale. The device type depends on the type of destroyed microorganisms. Homogenizers are recommended for the disintegration of some bacteria and yeasts, while mills are for yeasts, fungi, and algae [3]. High-energy consumption of the process carried out by mechanical methods is the cause to seek more economical technical means of its implementation. The use of chemical, biological, and other physical methods at the present stage of technology development is not economically justified. It is expected that the use of mechanical methods, combined with others, for the disintegration of more resistant microorganisms in future will be beneficial [3].

The research carried out on the process improvement realized in bead mills is difficult to a large number of phenomena occurring in circulating mill filling and their specificity. During the disintegration of microorganisms, there occurs disruption of cell walls and membranes, releasing and dissolving intracellular compounds; organelle disruption; milling fragments of cell walls, cytoplasmic membranes, and other cellular fragments; interaction between the released compounds and microorganisms; and unprotected organelles and their mutual interaction. While conducting the process, rheological properties change, both of a suspension and its continuous phase. Mutual relativity of occurrence times of separate events during disintegration can have very small (cell disruption—dissolving intracellular compounds) or very large values (cell disruption—cell autolysis). The process course is affected by a very large number of parameters: instrumental (e.g., mill design and size, filling ball diameter, filling degree, materials used, and surface condition), raw material (e.g., conditions for microorganisms growth, their size and morphological form), and process (e.g., mixer rotation speed, duration of the process, temperature, microorganisms' suspension flow rate under conditions of continuous operation, and initial concentration of microorganisms' cells). So far, there are several models leading to the mathematical description of the disintegration of microorganisms in bead mills by a first-order linear differential equation [1–10]. A dependency of the release rate of enzymes on their distribution in a cell has been shown [11]. Taking into account the consequences of events: disruption of the cells - release of intracellular compounds, led Melendres et al. [12] to a nonlinear description of the overall process assuming the linear course of component processes. Some researchers showed a dependency of the process rate constant on the initial microorganism concentration. Marffy and Kula [4] presented the results of the disintegration of brewer's yeasts *Saccharomyces carlsbergensis* in a horizontal mill with a multiple disc mixer with a working chamber volume of 600 cm^3 and indicated an almost twofold increase in the process rate constant at an increase in the suspended matter concentration described as the final amount of released protein from about 10 to 60 mg/cm^3. This effect was confirmed by Heim and Solecki [5] for the process carried out in a bead mill at a large concentration of *Saccharomyces cerevisiae* yeast suspension (0.14–0.20 g d.m./cm^3) and high rotational speeds of the mixer (2500–3500 rpm). On the other hand, the analysis of the presented by Currie et al. [6] values of rate constants dependent on the size of bed balls for the increased concentrations of *S. cerevisiae* yeast suspension in the range of 0.3 to 0.75 g yeasts/cm^3 indicates a continuous decrease in the obtained disintegration results. A rate constant decrease in a horizontal mill with a steel mixer at an increase in concentration from 0.15 to 0.30 kg yeasts/m^3 was demonstrated by Limon-Lason et al. [7]. The same tendency was demonstrated by the same authors in a horizontal mill with a polyurethane mixer with an increase in concentration from 0.15 to 0.75 kg yeasts/m^3. A dependency of the disintegration of microorganisms that results in changes in their concentration is explained by the authors by a change in rheological properties of the suspension [4, 7] or an additional mechanism to destroy microorganisms [5]. Of course, some researchers show in their publications that there is no effect of microorganism concentration on the process course [2, 8].

For researching, describing, and managing processes of random transformation of the dispersed matter in a limited space, the theory basics were developed [13–15]. They include the assumed possibility of shaping and transforming material set elements during mass exchange between dispersed types of volume differing in properties. It was assumed that these processes can occur as a result of physical, chemical, and biological factors in specified limited volumes, and their separate types are generated randomly in the space of material medium. For the assumed paradigm, there is a possibility to build phenomenological and mathematical process models. The basic description of matter formation assumes the form of a system of differential equations. Modeling methodology enables taking into account many phenomena and mechanisms appropriate for the investigated processes in the conducted analyses. The kinetics of matter formation description allows to recognize the effect of many factors and to develop the model of a given process at the desired level of complexity. Application areas of the theory, with its great potential, include numerous domains, such as medicine, biology, agriculture, environmental protection, and industry. The theory of random transformation of the distributed matter was already used for the description of the disintegration of microorganisms, inter alia, for the description of the effect of yeast cell size on the process course [13, 14]. The aim of this study is to apply the theory of a random transformation of the distributed matter in order to explain the dependency of the process rate constant on the initial microorganism concentration.

2. Theory

A bead mill is a tank filled with beads set in circulating motion by a rotating impeller. Microorganisms dispersed in liquid are broken as a result of the filling elements' impact on them. The type of mechanism to destroy cells results from the system of combined normal and tangential loading. Its three basic forms can be distinguished as caused by crushing, grinding, and rolling by means of balls. Generally, cell destruction mechanisms do not occur in a pure form in the circulating chamber filling. The process of the disintegration of microorganisms, a very complex one as it was presented in the introduction, is a random transformation of matter. In order to enable the specification and analysis of phenomena occurring during its course, the following phenomenological model of the disintegration of microorganisms in the circulating mill filling was developed [13–15]. The suspension of microorganisms constituting a set of material objects N occupies space in a mill V. In volume $V_{\alpha ti}$, being its part, volumes of transformation $V_{\gamma ji}$ are generated. It was assumed that the ith cell from the set N is destroyed after a relative transfer from volume V_α, where conditions are safe for it, to the *j*th volume $V_{\gamma ji}$. The transfer from volume $V_{\alpha ji}$ to volume $V_{\gamma ji}$ takes place through a boundary surface $F_{\gamma\alpha\rightarrow}$. The mathematical description result of the phenomenological model is a first-order differential equation (Eq. 1) [15], in which the rate constant is determined by Eq. (2).

$$dN_d = \frac{F_{\gamma\alpha\rightarrow}}{V_\alpha} u\left(N_0 - N_d\right) dt \tag{1}$$

$$k = \frac{F_{\gamma\alpha\rightarrow}}{V_\alpha} u \tag{2}$$

The increase in the process rate of the disintegration of microorganisms in suspensions with high concentrations presumably is caused by the occurrence of the additional mechanism to destroy cells [5]. As a result of high concentration, microorganisms affect each other. By blocking cells between colliding balls with high kinetic energy, they cause an increase in volume $V_{\gamma ji}$. Thus, greater values of the process rate constant for large concentrations and high impeller rotational speeds may result.

If the above hypothesis is true, then during the process with a reduction in the number of live cells, volume $V_{\gamma ji}$ should decrease, and consequently rate constant *k* as well. Its value describing the process for suspensions with large concentration, after obtaining a sufficiently large degree of disintegration, should be the same as in the case of suspensions with small concentration.

3. Bead mill

The process of disintegration was investigated in a horizontal bead mill with a multidisk impeller. The capacity of the working chamber 80 mm i.d. was 1 dm^3. Circular, full disks of the impeller of diameter 66 mm were placed every 30 mm. All parts of the mill were made from acid-resistant steel. The inside of the mill was filled in 80% with balls of diameter ranging from 0.8 to 1.0 mm made from leadless glass of density 2500 kg/m^3.

The shaft of the multidisk impeller was coupled with a d.c. motor. A voltage control system enabled smooth change of the impeller speed in the range from 0 to 3600 rpm. The cooling jacket of the mill was connected to a Fisherbrand FBC 735 thermostat (Fisher Scientific GmbH). The temperature of 50% water solution of ethylene glycol cooling the mill was 4°C at the inlet to the tank jacket. The slurry temperature was about 4°C.

4. Biological material

Investigations were made using the suspension of commercially available baker's yeast *S. cerevisiae* produced in the Silesian Yeast Factory "Polmos" at Wołczyn. Biological material from a single fermentation was transported to a laboratory after cooling for 36 h, which completed the technological process. All experiments were carried out within 14 days. Yeast cubes of 100 g were stored at a temperature of 4°C. The continuous phase of microbial slurry was a 0.1% aqueous solution of β-mercaptoethanol containing 0.01 M EDTA and 0.001 M PMSF. A pH of 7 was ensured by a phosphate buffer (NaH_2PO_4, Na_2HPO_4).

5. Range of investigation

Experiments were carried out batchwise (constant feed) at the rotational speed of the impeller ranging from 1000 to 3500 rpm. Thirteen experimental series were made for a suspension prepared from living yeast cells at concentrations ranging from 0.05 to 0.20 g d.m./cm^3. The series consists of two experiments carried out at the same parameters. In the experiments, a slurry was used for which the mean concentration value determined for five measurements did not differ from an assumed value by more than 5%.

Series	*n*	**Slurry 1**		**Slurry 2**		**Slurry mixture**	
		S	*X*	*S*	*X*	**Concentration of living cells**	**Total biomass concentration**
	rpm	g d.m./cm^3	%	g d.m./cm^3	%	g d.m./cm^3	g d.m. /cm^3
10	1000	0.1410	0	0.1974	99.5	0.0618	0.1727
11	2500	0.1393	0	0.1974	99.5	0.0599	0.1724
12	3500	0.1407	0	0.1940	99.5	0.0594	0.1711

Table 1. Parameters of a slurry made from living and previously disintegrated cells.

Three experimental series were carried out for a mixture of slurries characterized by total biomass concentration of about 0.17 g d.m./cm^3 and living cell concentration of about 0.06 g d.m./cm^3. The parameters of the slurry mixture and its components as well as the impeller speed during the process are given in Table 1. The slurry mixture was prepared by combining slurry 1 and slurry 2 in proper proportions. Microorganisms in slurry 2 were subjected to disintegration in the bead mill until reaching 99.5% disintegration degree. Rotational speed of the impeller during the disintegration of microbial cells in slurry 2 corresponded to the impeller speed used during the disintegration of yeast contained in the slurry mixture.

6. Methodology

Changes in the slurry state were analyzed on the basis of spectrophotometric measurements of light absorbency in the supernatant at the wavelength 260 nm. Near this value, there are maximum spectra of spectral nucleic acids. The measurements were carried out using a

Lambda 11 spectrophotometer (Perkin Elmer GmbH). The supernatant was obtained after 20 min centrifugation of slurry samples at the temperature 4°C with a centrifugal force of 34,000*g*. A 3K30 ultracentrifuge (B. Braun Biotech International GmbH) was used. The degree of microorganism disintegration after time *t* of the process duration (Eq. 3) was calculated from the ratio of relative absorbency A, determined for a sample to the maximum relative absorbency A_{m}, which was observed at total yeast cell disintegration. A reference liquid was the supernatant obtained from the slurry prior to the process.

$$X = \frac{A}{A_{\mathrm{m}}} = \frac{A^{'} \cdot r - A_{0}^{'} \cdot r_{0}}{A_{\mathrm{m}}^{'} \cdot r_{\mathrm{m}} - A_{0}^{'} \cdot r_{0}} \tag{3}$$

Depending on the cell disintegration degree, the slurry samples were diluted 0, 100, 200, or 400 times so that the measured absorbency did not exceed boundary values. Because of difficulties in using two parameters when describing the process kinetics, it was decided to convert the absorbency obtained at a given concentration into pure nucleic acids RNA released from the cell inside. Mean values for nucleotides used by Benthin et al. [16] were applied in the calculations. When solving the problem presented in this study, this simplifying assumption had no negative effects; however, the determined quantities of RNA could not be treated as precise values because of pollution of the supernatant with other intracellular components. In order to estimate the supernatant pollution, A/A_{250} and A/A_{280} ratios were studied. They were determined on the basis of the measurement of absorbencies A, A_{250}, and A_{280} identified for each sample in all experiments at the wavelengths 260, 250, and 280 nm, respectively. The effect of process conditions, and first of all the applied inhibitors of serine proteases and metaloproteases, was investigated by carrying out electrophoresis on 8% polyacryloamide gel SDS taken during slurry sample disintegration. The investigations were made for extreme concentrations of microorganisms at the impeller speed 2500 rpm.

The disintegration was investigated at different stages of the process, carrying out two experiments for fixed combinations of variable parameters. During the first experiment, 10 samples were taken in the time interval determined by the disintegration degree ranging from 0% to about 90%. On the basis of these data, a maximum amount of RNA possible to release, determined by the symbol C_{m1}, was obtained. At this amount, the correlation coefficient between variables t and $\ln[C_{m1}/(C_{\mathrm{m1}} - C)]$ was the highest. From the process description obtained in this way, using the regression line passing through 0 (Eq. 4), the process time in which disintegration degrees ranged from 98.0% to 99.5% was calculated. These were boundary values of the time interval in which 9 slurry samples were taken during the second experiment. Having the measured absorbency values and disintegration degrees calculated on the basis of k_1, a maximum amount of RNA C_{m2} was calculated for a given concentration, which would be observed after the disruption of yeast cell walls. Along with the data from the first experiment, this value was used to prepare again the process description by the regression line which passed through 0 (Eq. 5).

$$\ln \frac{C_{\mathrm{m1}}}{C_{\mathrm{m1}} - C} = k_{1} \cdot t \tag{4}$$

$$\ln \frac{C_{m2}}{C_{m2} - C} = k_2 \cdot t \tag{5}$$

The first part of the methodology, involving a maximum amount of the intracellular component determined as a result of the tendency to reach the best description of the process by the first-order differential equation, was used by Currie et al. [6]. It was also employed to describe part of the experiments with yeast *S. cerevisiae* disintegration in the vertical bead mill. According to the researchers, such necessity followed from the fact that it was impossible to obtain a satisfactory description of the process on the basis of a maximum amount of protein possible to release R_m, determined for microorganisms disintegrated in a high-pressure homogenizer. The authors quote that in five cases, they had to reject the data referring to the released protein R defined by the ratio R/R_m above 0.6, so that the first-order description was possible. In the subsequent six cases, such a description was not possible at all. A similar methodology was used by Limon-Lason et al. [7], who revealed the lack of any possibility to describe correctly the process carried out in the bead mill of volume 5 dm^3 basing on the amount of protein R_m specified in the mill of volume 0.6 dm^3. On the other hand, van Gaver et al. [8] in all investigated cases used only the values of R_m determined as a result of tending to achieve agreement between the experimental data and the assumed first-order process description. This decision was probably caused by much worse results obtained for experimentally determined maximum quantities of protein R_m. According to the authors, the experimental value of R_m was obtained after 10 cycles of slurry transition through the mill. In most publications, the maximum amount of measured intracellular components was determined experimentally.

7. Results and discussion

Results of the disintegration experiments performed in order to characterize biological material and the confirmation of its stability are given in Table 2. Strength properties of yeast cells derived from given fermentation were determined by means of parameters characteristic of the course of the disintegration process conducted for the extreme values of changed process parameters (S and n) in the assumed wider research plan [5, 9, 17]. Experimental series from the first to the fourth one were carried out at the beginning of the investigations, while those from the thirteenth to sixteenth at the end. In the two first columns, the values of variable parameters are quoted. In the subsequent columns, results obtained for the first (based on the value of C_{m1}) and second methods (based on the value of C_{m2}) are presented. The maximum concentrations of nucleic acids determined for 100% microorganism destruction, correlation coefficient, process rate constant, and its standard deviations are given in subsequent columns. On the basis of these results, it can be concluded that during storage, there were no changes in yeast cell sustainability to mechanical destruction in the bead mill significant for the investigations and changes that could distort the results of measurements.

Results of the investigations of process kinetics obtained by the first method revealed that the first-order differential equation, according to the present theory, described very well the

Series	S	n	C_{m1}	R_1	$k_1 \cdot 10^3$	C_{m1}	R_2	$k_2 \cdot 10^3$
	g d.m./cm^3	rpm	mg/cm^3	---	1/s	mg/cm^3	---	1/s
1	0.0513	1000	2.631	0.9983	1.307	2.317	0.9955	1.698
2	0.0491	3500	2.626	0.9984	6.024	2.434	0.9961	7.156
3	0.1991	1000	9.352	0.9937	1.817	8.725	0.9764	2.438
4	0.1991	3500	9.622	0.9971	9.632	8.745	0.9836	13.420
13	0.0485	1000	2.450	0.9997	1.348	2.263	0.9962	1.656
14	0.0485	3500	2.173	0.9996	6.986	2.252	0.9993	6.488
15	0.1957	1000	8.071	0.9907	2.149	7.935	0.9898	2.320
16	0.1957	3500	8.651	0.9962	10.429	8.106	0.9854	13.413

Table 2. Characteristics of biological material.

process run. The correlation coefficients for most of the experiments exceeded 0.9960. Only in two cases for slurry concentration 0.20 g d.m./cm^3 and impeller velocities 1000 rpm they were slightly lower (Table 2). Experimental results along with regression lines obtained for different slurry concentrations are shown in Fig. 1. On the basis of these results, it can be concluded that the process rate increases with an increase of the initial yeast slurry concentration. Rate constants for the highest slurry concentrations determined at the impeller speed 2500 and 3500 rpm are higher by over 60% than those obtained for the lowest concentrations. In the process performed at the impeller speed equal to 1000 rpm, the differences between the values of constant k_1 obtained for slurries at concentrations 0.05 and 0.20 g d.m./cm^3 are much smaller (about 40%) (Table 2). Standard deviations of the process rate constants for method 1 given in Table 3 are in the interval from 0.46% to 2.55%. In general, for higher slurry concentrations, higher values of the standard deviation were obtained. In the case of changes in the rotational speed of the impeller, the results are opposite.

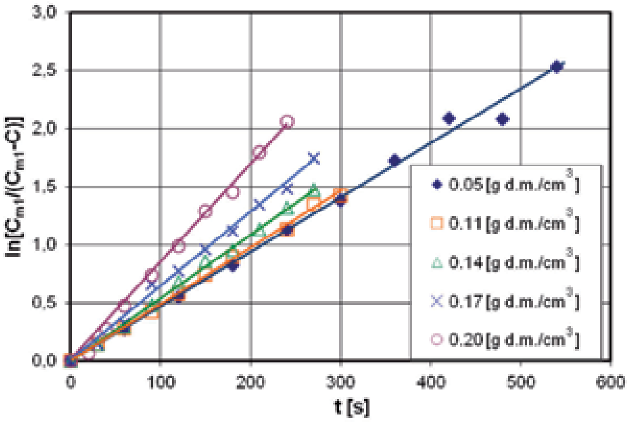

Figure 1. Microbial cell disintegration at different slurry concentrations (method 1, n = 2500 rpm).

Series	S	n	C_{m2}/C_{m1}	Standard deviation	
				Method 1	Method 2
	g d.m./cm^3	rpm	---	%	%
1	0.0513	1000	0.881	1.21	2.07
2	0.0485	1000	0.924	0.46	1.64
5	0.0491	2500	0.980	1.51	1.70
3	0.0491	3500	0.927	1.01	1.63
4	0.0485	3500	1.036	0.57	0.72
6	0.1102	2500	0.926	0.84	1.19
7	0.1431	2500	0.910	0.88	1.54
8	0.1645	2500	0.933	1.32	2.87
9	0.1991	1000	0.933	2.01	4.27
13	0.1957	1000	0.983	2.55	2.72
14	0.1974	2500	0.959	1.26	1.48
15	0.1991	3500	0.909	1.46	3.80
16	0.1957	3500	0.937	1.55	3.31

Table 3. Characteristics of experimental results.

Results of electrophoretic research carried out for the largest suspension concentration demonstrated clear separation of macroparticles, confirming the maximum limit of cutting proteins by enzymes released from highly specialized organelles. An increase of the disintegration effect with an increasing slurry concentration is not caused by an intensified supernatant pollution. Such a result was also confirmed by constant relations between absorbances being measured. Examples of the results obtained for experimental runs made for extreme parameters are shown in Table 4.

Series	S	n	A/A_{250}		A/A_{280}	
			Mean value	Standard deviation	Mean value	Standard deviation
	g d.m./cm^3	rpm	---	---	---	---
1	0.0513	1000	1.142	0.0036	1.797	0.0129
2	0.0491	3500	1.127	0.0073	1.748	0.0240
3	0.1991	1000	1.153	0.0022	1.790	0.0058
4	0.1991	3500	1.147	0.0032	1.767	0.0111
10	0.0618	1000	1.133	0.0039	1.721	0.0135
12	0.0594	3500	1.151	0.0030	1.789	0.0090

Table 4. Characteristics of the supernatant pollution degree.

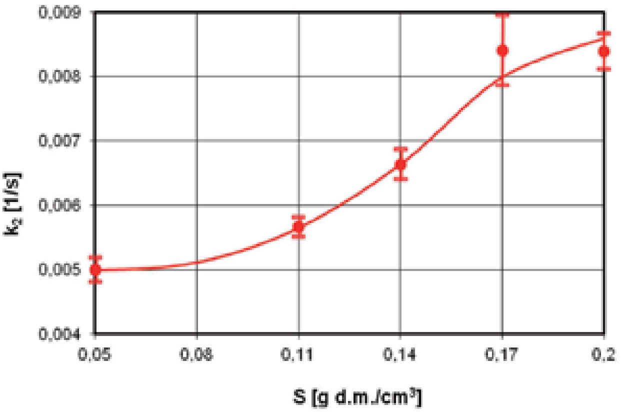

Figure 2. The effect of yeast slurry concentration on process rate constant at rotational speed of the impeller n = 2500 rpm (method 2, bottom and upper limits are marked for 95% of the confidence interval).

Changes of rate constants obtained by the second method, which take place at an increasing initial yeast cell concentration (Fig. 2, Table 2), are close to the ones obtained using method 1. Significant differences between values k_1 and k_2 were found. The process rate constants obtained by method 2 are from 7% to 39% higher than those obtained by method 1. An exception are the values obtained for slurry concentration 0.0485 g d.m./cm^3 at the impeller speed 3500 rpm (Table 1). The correlation coefficients obtained when describing the process by Eq. (5) are lower than R_1 (Table 2) and are in the range from 0.9764 to 0.9993. Much less advantageous are also standard deviations of the process rate constant (Table 3).

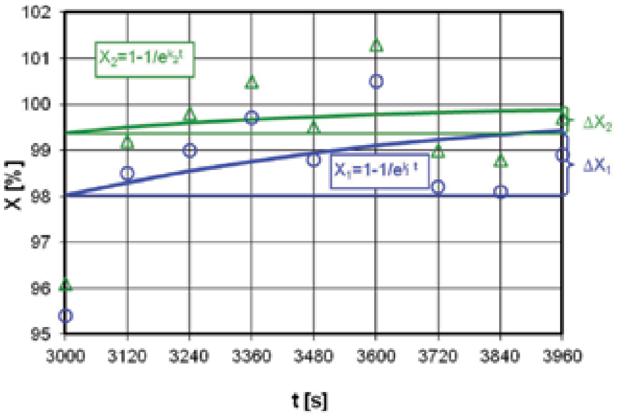

Figure 3. Changes of disintegration degree on the second stage of the process (S = 0.05 g d.m./cm^3, n = 1000 rpm).

Higher values of constant k_2 are due to the fact that values C_{m2} are lower than C_{m1}. They are compared in Table 3. The amount of nucleic acids C_{m2} for the slurry with disintegration degree

X=100% was determined based on the result of an experiment planned and carried out on the basis of the rate constant k_1. Therefore, values C_{m1} and C_{m2} should not differ very much and should reveal a typical statistical dispersion in relation to the real value. As it is not so, it was checked if the points used to determine C_{m2} were better described by the rate constant k_1 or k_2. Since the values of rate constant k_2 are higher than k_1, then in time interval Δt (time of process investigation in the second experiment), differences of the disintegration degree ΔX_2 are smaller than ΔX_1 (Fig. 3). For k_1 and k_2 in time, which determines slurry sampling, the disintegration degrees X_1 and X_2 were specified. On this basis and taking into account the measured values of absorbency A, A_{250}, and A_{280}, such values that would occur at 100% microorganism disintegration were identified. Only for three experiments, rate constant k_1 describes better absorbencies A, A_{250}, and A_{280}. In one experiment, the values of A are better described by rate constant k_1 and the values of A_{250} and A_{280} by rate constant k_2. In all other experiments, the values of standard deviation are lower than when rate constant k_2 is used to determine the value of relevant absorbencies, which occur when the total content of microbial cells is released. As differences between ΔX_2 and ΔX_1 were insignificant as compared to measuring errors of absorbency for the disintegration degree close to 100% [18], this result was assumed sufficient to claim that the rate constant k_2 described better the process tested in the second experiment. It follows that the values of C_{m2} should be closer to the real values at $X = 100\%$. The correlation coefficient for linear regression between variables C_{m1} and S was 0.9873, and between C_{m2} and S, it was 0.9949 (Fig. 4).

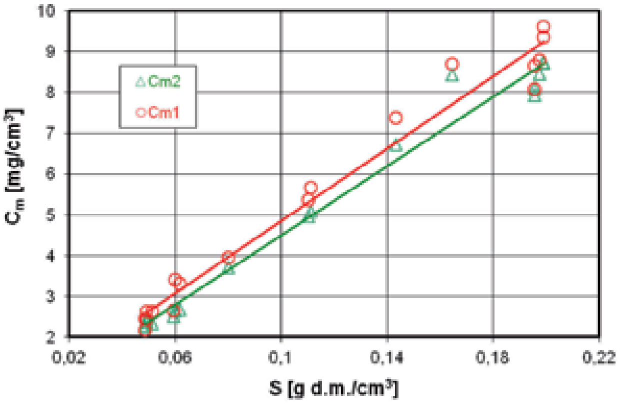

Figure 4. The effect of changes in the slurry concentration on determined values of C_m.

If in two separate time periods the process run can be described more precisely using different values of rate constant, then it may be assumed that the disintegration rate constant changes during the process. Fig. 5 shows experimental changes in the disintegration degree described on the basis of C_{m2}. The blue line denotes changes that result from the process description by Eq. (6) ($\Delta t = 0$).

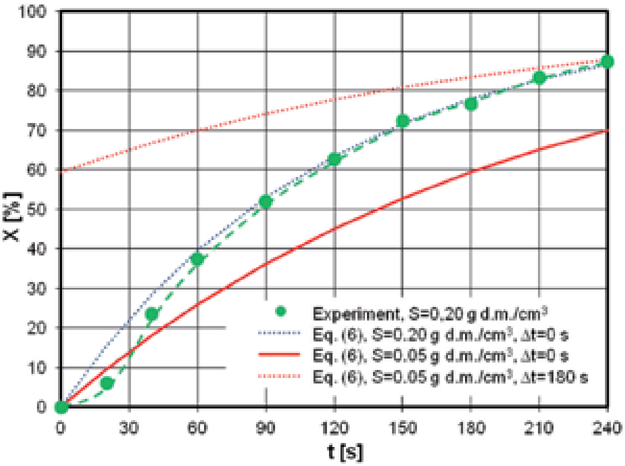

Figure 5. Changes of disintegration degree in the process carried out at slurry concentration 0.20 g d.m./cm^3 and impeller speed 2500 rpm.

$$X_2 = 1 - e^{-k_2(t+\Delta t)} \tag{6}$$

In first part of the process (from 0 to 120 s), the experimental points are located below the theoretical line, while in the second one, the results obtained are consistent. The position of the experimental points can be hardly taken as random. Real changes of the disintegration degree are close to the changes marked by the green line. Fig. 5 contains the process model obtained for the suspension concentration of 0.5 g d.m./cm^3 (red line). In this case, the dependency presented in Eq. (5) described the process course very well (Fig. 1).

During the cell disintegration in a suspension with concentration of 0.20 g d.m./cm^3, the process initially (up to 20 s) proceeds at a considerably slower pace than the model disintegration (blue line) determined at this concentration and at even slower pace than the process determined for 0.05 g d.m./cm^3. This can result from very large cell density at their largest concentration. The analysis of changes in the distance between geometrical centers of yeasts followed by an increase in their concentration was presented [5, 17]. In these considerations, the assumption of distributing cells in a close-packed hexagonal network was adopted because such a distribution provides the largest distances between microorganisms. The determined distances at such a distribution are boundary distances, the most favorable for minimizing interactions between microorganisms. Any other distribution of cells, including the actual one, causes a further increase in the intensity of their interaction. In accordance with the stated dependencies, at concentration of 0.20 g d.m./cm^3, the interaction between neighboring microorganisms is very large. The cell size distribution for yeasts used for the research in this work (Fig. 6) was very similar to the size distribution of microorganisms used in earlier works [5, 9, 13, 14, 17]. The comparison of results obtained in tests by means of laser particle size analyzers, with results obtained as a result of the computer analysis of microscopic images is included in the published work [19]. A cell before being disrupted is compressed between balls. Its dimensions in a plane perpendicular to the compression axis increase. This is a consequence of neighboring microorganisms being driven out from the danger zone when, e.g., two balls approach them. The result of this visible in Fig. 5 is the reduction in the cell disruption rate at the initial stage of the process. The described mechanism does not cause changes in the transformation volume $V_{\gamma ji}$ nor volume unavailable to a live *i*th cell $V_{\beta ji}$. In the developed theory basics [15], in order to simplify the initial considerations, independence of transformation events was assumed. In the case described above, the disruption of one cell increases the chance of saving the neighboring cell. The result of such impact will be deviations of the process course from linearity. Changes in the process rate constant at the time of its duration are shown in Fig. 5.

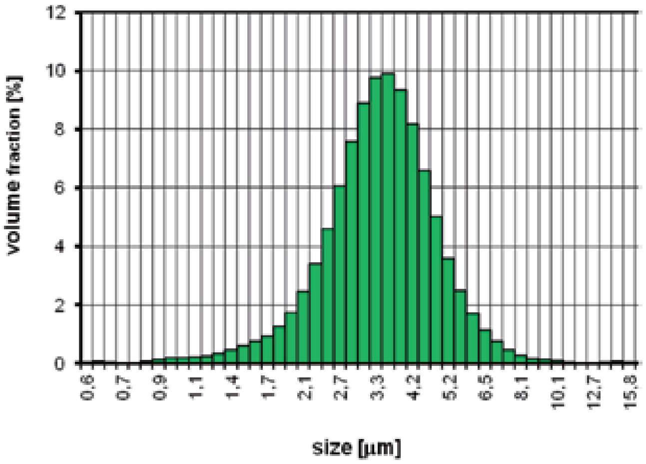

Figure 6. The yeast particle size distribution in the suspension.

In the suspension with a concentration of 0.20 g d.m./cm^3, the rate of microorganism disruption and release of intracellular compounds increases significantly from about 20 to 120 s of the process duration (Fig. 5). Is it greater than the cell disintegration rate in a suspension with concentration of 0.05 g d.m./cm^3 and also greater than the process course rate determined from Eq. (5) for the disintegration of microorganisms in the suspension with concentration of 0.20 g d.m./cm^3. Such an effect can result from an increase in the transformation volume $V_{\gamma ji}$ and volume $V_{\beta ji}$ unavailable to the live *i*th cell. Hypothetically, it is the result of blocking a cell in the danger zone by neighboring unthreatened microorganisms [5].

At the final stage of disintegration, the course of the process of the yeast cells disintegration carried out in the suspension with concentration of 0.20 g d.m./cm^3 is not in accordance with the course obtained for the suspension with concentration of 0.05 g d.m./cm^3. At the end of the process being carried out for the higher biomass concentration, there is a significant reduction in the number of viable cells. The rate constant is much higher than specified for the disintegration of the yeast cells at a concentration of 0.05 g d.m./cm^3.

Fig. 6 shows the graphic analysis of the process course for the cell disintegration in a mixture of slurries (Table 1, Series 11) analogical to the one presented above. In this case, due to less intensive interactions between neighboring yeast cells, there was probably no pushing out of cells from the danger zone by compressed microorganisms. The obtained values of rate constant (Table 5) are large over all the investigated time frame. They are much greater than those obtained with a suspension concentration of 0.05 g d.m./cm^3 (Fig. 7, red line). The values of the rate constant are similar to those obtained for the concentration of 0.17 g d.m./ cm^3 (Fig. 2).

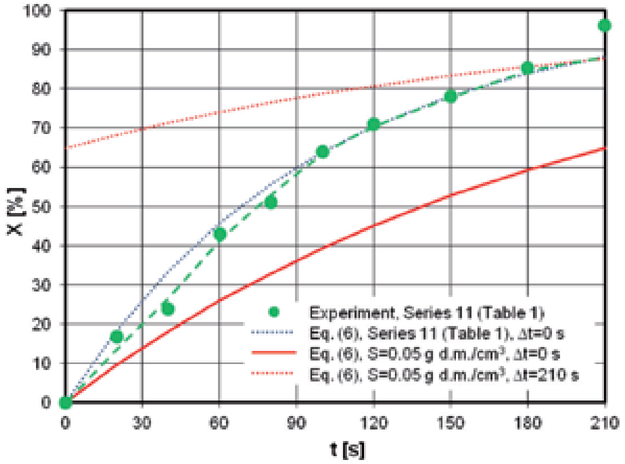

Figure 7. Changes of disintegration degree in the process carried out at biomass concentration 0.17 g d.m./cm^3, living cell concentration 0.05 g d.m./cm^3, and impeller speed 2500 rpm (Series 11, Table 1).

Such a process run, which is more or less distinct in all experiments performed, provides the evidence that the additional cell destruction mechanism is a result of the action of comminuted cell wall fragments, and not of the living microorganisms. The deviation of experimental points similar to the ones presented above was obtained by Melendres et al. [10], who investigated the process of disintegration on the basis of living cells specified using a hemocytometer. The results obtained by the researchers were a basis to develop a first-order mathematical model of the process based on the analogy to the theory of gas kinetics. Using their own data, Middelberg et al. [18] proved better agreement of the disintegration degree determined on the basis of the absorbency measurement (λ = 260 nm) and the number of living cells than that obtained from released proteins and living cells. According to Limon-Lason et al. [7], the process of disintegration is related to two phenomena: cell wall disruption and protein release. The latter phenomenon is much slower than the first one. According to the results obtained by Middelberg et al. [18], the difference between cell wall disruption rate and the rate of nucleic acid release is negligible.

Fig. 8 shows a graphical interpretation of disintegration kinetics described by Eq. (5). The regression line is not in agreement with experimental points. The real process run is not linear. Constant k_a at the onset of the process ($t \to 0$) is lower than the constant determined for time t = 200 s, and this in turn is smaller than constant k_m determined for time 1200 s. Changes in

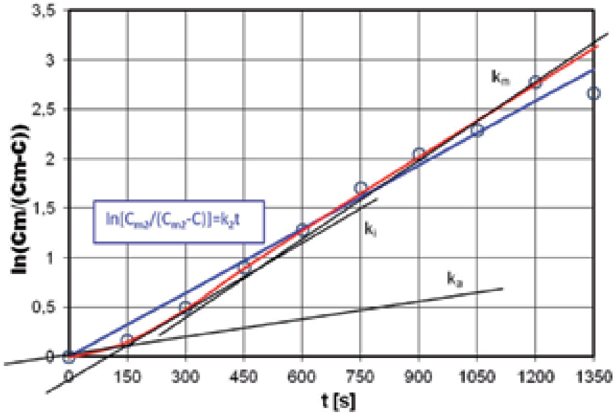

Figure 8. Yeast disintegration kinetics in the slurry at concentration 0.05 g d.m./cm^3 and impeller speed 1000 rpm.

the rate constant during the microorganism disintegration can be explained by an increase of the concentration of very fine fragments of cell walls. Irrespective of the initial slurry concentration, the rate constant at the beginning of the process k_a is always the same at lower concentrations. This is confirmed by the position of first experimental points obtained after starting the process. The mean value of k_a for slurries made exclusively from living cells of yeast disintegrated at the impeller speed 2500 rpm is 0.005146, and its standard deviation is 6.21%. For high concentrations of microbial slurry, the process rate increases significantly as a result of formation of numerous fine fragments of cell walls. The further run of the process is affected by their concentration, which depends on the rate of microgrinding and the amount of material being ground.

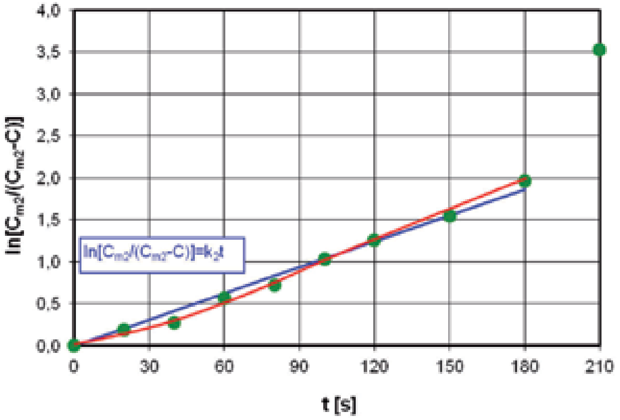

Figure 9. Yeast disintegration kinetics in the slurry mixture (biomass concentration 0.17 g/cm^3, living cell concentration 0.05 g/cm^3, n = 2500 rpm).

Series	n	C_{m1}	R_1	$k_1 \cdot 10^3$	C_{m2}	R_2	$k_2 \cdot 10^3$
	rpm	mg/cm^3	---	1/s	mg/cm^3	---	1/s
10	1000	2.803	0.9942	2.651	2.647	0.9912	3.203
11	2500	2.950	0.9970	8.078	2.621	0.9936	10.375
12	3500	2.742	0.9835	13.049	2.511	0.9682	19.964

Table 5. Results of microorganism disintegration in the slurry mixture.

In the case of the disintegration of microorganisms contained in the slurry mixture (experimental series 10, 11, and 12), much higher values of k_1 and k_2 (Table 5) were obtained than in the case of ordinary slurries with a comparable concentration of living cells. The change of conditions that define the increase of constant k during the process is determined not only by the presence of cell wall fragments but also by an increasing level of their comminution. Nonlinearity of the process kinetics (Fig. 9) is the evidence that the boundary value of concentration of small cell fragments has not been reached yet. The rate constant after starting the process is higher by 25% than constant k_a obtained for slurries made exclusively from living microorganisms. The correlation coefficients smaller than in other cases result from insignificant changes of absorbency during the process as compared to the initial absorbency.

8. Conclusions

At low concentrations of the suspension, cell disruption in the mill filling is an independent event. The process course is described very well by a linear first-order differential equation. During the disintegration of the microorganisms, disruption of the cells, release of intracellular compounds, and grinding of the fragments of broken walls take place.

An increase in the yeast suspension concentration in the range of 0.05 to 0.20 g d.m./cm^3 causes a significant reduction in distances between geometrical centers of neighboring cells and significant intensification of interactions between them.

At very high concentrations of the suspension, at the initial stage, that is, from the disintegration level 0% to 5%, the process course reveals deviations from linearity. An event consisting of cell disruption can affect the fate of neighboring cells. A cell being deformed as a result of compression pushes out cells adjacent to it from the danger zone. Thus, transformation events of objects from set N are not independent events. This effect does not cause an increase of the transformation volume and volume unavailable to the live ith cell. It seems that this phenomenon causes a significant decrease of the rate of cell disruption and release of intracellular compounds.

At high concentrations of the suspension, the process course reveals deviations from linearity. The cell disruption and the intracellular compound release rate are greater than the rate determined from the linear model for smallest concentration. At high initial concentration of microbes, reducing the number of cells during the disintegration does not reduce the rate constant of the process. Increasing the transformation volume and the volume inaccessible to the *i*th cell is to increase the rate of disintegration. It appears that increasing the amount of the intracellular compounds released or increasing the grinding degree of cell walls increases the volume of the transformation, and the volume is inaccessible to the *i*th cell.

At very high concentrations of the suspension, at the initial stage, that is, from the disintegration level 0% to 5%, the disintegration rate is influenced by both mentioned phenomena. In the case of the maximum concentration, the second mechanism, causing a significant reduction of the disintegration rate in comparison to the rate determined from the linear model, predominates.

Nomenclature

A; absorbency at wavelength $\lambda = 260$ nm

A_{m}; maximum absorbency determined for wavelength $\lambda = 260$ nm

A_{250}; absorbency at wavelength $\lambda = 250$ nm

A_{280}; absorbency at wavelength $\lambda = 280$ nm

A'; absorbency of the supernatant as related to distilled water

C; amount of pure nucleic acid corresponding to absorbency A, mg/cm^3

$F_{\gamma\alpha\rightarrow}$; slurry flow area from volume V_α to $V_{\gamma ji}$, m^2

k; process rate constant, 1/s

n; rotational speed of the impeller, rpm

N_{d}; number of disintegrated cells

N_{o}; initial number of living cells

$S_{;}$ concentration of microorganism slurry, g dry matter/cm^3

t; process duration, s

u; slurry transition rate from volume V_α to V_β, m/s

V; maximum slurry volume in working chamber of the mill, m^3

V_α; mill volume at physical conditions safe for microorganisms, m^3

$V_{\beta ji;}$ volume not available for nontransformed *i*th object from set N, m^3

$V_{\gamma ji;}$ the *j*th transformation volume of the *i*th material object from set N, m^3

X; cell disintegration degree, %

Author details

Marek Solecki[1*] and Monika Solecka[2]

*Address all correspondence to: marek.solecki@p.lodz.pl

1 Department of Process Equipment, Lodz University of Technology, Lodz, Poland

2 Institute of Fermentation Technology and Microbiology, Lodz University of Technology, Lodz, Poland

References

[1] Lilly MD. Mint: Applied Biochemistry and Bioengineering, Academic Press, New York, 1979; 2.

[2] Garrido F, Banerjee UC, Chisti Y, Moo-Young M. Mint: Disruption of a recombinant yeast for the release of β-galactosidase. Bioseparation. 1994; 4: 319–328.

[3] Chisti Y, Moo-Young M. Mint: Disruption of microbial cells for intercellular products. Enzyme Microb. Technol. 1986; 8: 194–204.

[4] Marffy F, Kula MR. Mint: Enzyme yields from cells of brewer's yeast disrupted by treatment in a horizontal disintegrator. Biotechnol. Bioeng. 1974; 16: 623–634.

[5] Heim A, Solecki M. Mint: Disintegration of microorganisms in bead mill with a multi-disc impeller. Powder Technol., 1999; 105: 390–396.

[6] Currie JA, Dunnill P, Lilly MD. Mint: release of protein from bakers' yeast (*Saccharomyces cerevisiae*) by disruption in an industrial agitator mill. Biotechnol. Bioeng. 1972; 14: 725–736.

[7] Limon-Lason J, Hoare M, Orsborn CB, Doyle DJ, Dunnill P. Mint: Reactor properties of a high-speed bead mill for microbial cell rupture. Biotechnol. Bioeng. 1979; 21: 745–774.

[8] van Gaver D, Huyghebaert A. Mint: Optimization of yeast cell disruption with a newly designed bead mill. Enzyme Microb. Technol. 1990; 13: 665–671.

[9] Heim A, Solecki M. Disintegration of microorganisms in a circulating bed of balls. In: Proceedings of the 3rd World Congress on Particle Technology (WCPT 3); 6–9 July 1998; Brighton: IchemE; 1998.

[10] Melendres AV, Honda H, Shiragami N, Unno H. Mint: A kinetic analysis of cell disruption by bead mill. Bioseparation. 1991; 2: 231–236.

[11] Hetherington PJ, Follows M, Dunnill P, Lilly MD. Mint: release of protein from baker's yeast (*Saccharomyces cerevisiae*) by disruption in an industrial homogeniser. Trans. Inst. Chem. Eng. 1971; 49: 142–148.

[12] Melendres AV, Honda H, Shiragami N, Unno H. Mint: enzyme release kinetics in a cell disruption chamber of a bead mill. J. Chem. Eng. Jap. 1993; 26: 2, 148–152.

[13] Solecki M. The release of compounds from microbial cells. In Nakajima H, editor. Mass Transfer—Advanced Aspects. 1st ed. Rijeka: InTech; 2011. p. 595–618.

[14] Solecki M. Mechanical disintegration of microbial cells. Zesz. Nauk. Politech. Łódz. 2012; 1114: 421, 1–95 (in Polish).

[15] Solecki M. The theory of random transformation of dispersed matter. In: Nakajima H, editor. Mass Transfer—Advances in Sustainable Energy and Environment Oriented Numerical Modeling. 1st ed. Rijeka: InTech; 2013. p. 3–30.

[16] Benthin S, Nielsen J, Villadssen J. Mint: A simple and reliable method for the determination of cellular RNA content. Biotechnol. Tech. 1991; 5: 1, 39–42.

[17] Heim A, Kamionowska U, Solecki M. The effect of microorganism concentration on yeast cell disruption in a bead mill. J. Food Eng. 2007; 83: 121–128.

[18] Middelberg APJ, O'Neill BK, Bogle IDL, Snoswell MA. Mint: a novel technique for the measurement of disruption in high-pressure homogenization: studies on *E. coli* containing recombinant inclusion bodies. Biotechnol. Bioeng. 1991; 38: 363–370.

[19] Solecki M. Analysis of methods for description of yeast cell morphology. In: Proceedings of the 5th World Congress on Particle Technology (WCPT5); 23–27 April 2006; Orlando: Florida.

Chapter 9

Mass Transfer in Multiphase Systems

Badie I. Morsi and Omar M. Basha

Additional information is available at the end of the chapter

http://dx.doi.org/10.5772/60516

Abstract

Mass transfer in reactive and non-reactive multiphase systems is of vital importance in chemical, petrochemical, and biological engineering applications. In this chapter, theories and models of mass transfer in gas-liquid, gas-solid and gas-liquid-solid systems with and without chemical reactions are briefly reviewed. Literature data on the mass transfer characteristics in multiphase reactors over the last two decades with applications to the Fischer-Tropsch (F-T) synthesis are summarized. Moreover, the F-T reactions are described and an overview of the use of Slurry Bubble Column Reactors (SBCRs) and Multitubular Fixed Bed Reactors (MTFBRs) for low temperature F-T (LTFT) synthesis are discussed. The important factors affecting the hydrodynamic (gas holdup, bubble size/distribution) and mass transfer parameters (volumetric mass transfer coefficients) in SBCRs for F-T synthesis, including operating conditions, gas-liquid-solid properties, reactor geometry and internals as well as gas distributors are also discussed. The discussion reveals that the performance of the LTFT SBCR operating in the churn-turbulent flow regime is controlled by the resistance in the liquid-side film and/or the F-T reaction kinetics depending on the operating conditions prevailing in the reactor. Also, there is a great need to understand the behavior and quantify the hydrodynamics and mass transfer in SBCRs operating with syngas (H_2 + CO) and F-T reactor wax in the presence of active catalyst (iron or cobalt) under typical F-T synthesis conditions in a large SBCR with an inside diameter ≥0.15m.

Keywords: Mass Transfer, Multiphase Systems, Fischer Tropsch, Slurry Bubble Column

1. Introduction

Mass transfer in multiphase (gas-liquid-solid) systems is one of the most critical processes occurring in chemical, petrochemical, and biological engineering applications. Generally, it entails transport of species among phases through diffusion (physical) and/or chemical reactions in a special unit operation (reactor), allowing such a process to take place. Chemical reactions, often used to speed up the mass transfer rate, occur whenever species of different chemical potentials are brought into contact. In multiphase systems, the species mass transfer rate is controlled not only by the system pressure and temperature, but also by the conductance of mass transfer, concentration gradients, reaction kinetics, activation energy, etc. In some cases, either the conductance of mass transfer or the reaction kinetics could control the overall mass transfer rate; and the slowest one will be the rate limiting or controlling step. For instance, oxygen transfer from the feed (gas) to the aqueous solution (liquid) in bioreactors could be the overall rate limiting step [1]. In any case, understanding mass transfer behavior in multiphase systems requires, among others, precise knowledge of all aspects affecting the overall mass transfer rate [2].

2. Mass transfer theories

There are different theories dealing with mass transfer among phases, such as the two-film theory, the penetration theory and the surface renewal theory. These theories are briefly discussed below.

2.1. Two-film theory

This is the oldest theory for gas-liquid mass transfer developed by Lewis and Whitman in 1924 [3]. The theory postulates the existence of a film of a thickness (δ) in both the gas and liquid phases separated by an interface. It is based on the following assumptions: (1) the mass transfer occurs by molecular diffusion through the film, beyond which the concentration (C_{Ab}) is homogeneous; (2) the mass transfer through the film occurs under steady state conditions; and (3) the flux is small and the mass transfer occurs at low concentration. Accordingly, for convective mass transfer, the concentration profile is linear as shown in Figure 1 and the liquid-side mass transfer coefficient is expressed by Equation (1):

$$k_L = \frac{D_{AB}}{\delta_L} \tag{1}$$

One should remember that the actual concentration profile is nonlinear as can be seen in Figure 1. In turbulent flow, however, attempts were made to relate the mass transfer coefficient with the turbulent diffusivity, which obviously is different from that in the laminar flow. Surprisingly, some experimental results were modeled with limited success using this simplistic model, where k_L values were found to be proportional to the diffusivity to the power one. However, one should keep in mind that the film theory does not provide a direct means for estimating the film thickness.

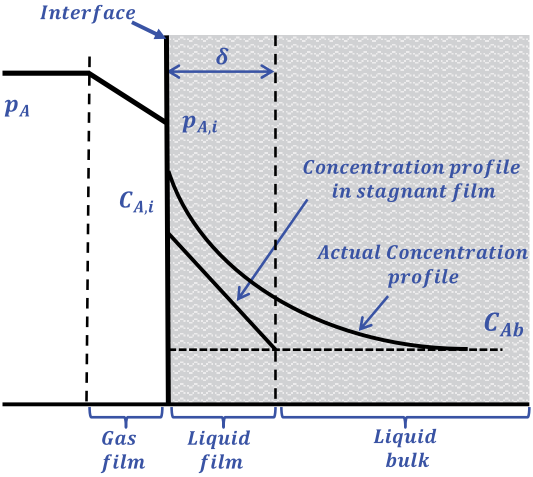

Figure 1. Schematic of two film theory

2.2. Penetration theory

The "penetration theory" or "Higbie's model" [4] assumes that each liquid element at the gas-liquid interface is exposed to the gas for a short time, as schematically shown in Figure 2. The basic assumptions of the theory are: (1) mass transfer from the gas into a liquid element occurs under unsteady-state conditions once they are in contact; (2) each of the liquid elements stays in contact with the gas for same time period; and (3) equilibrium exists at the gas-liquid interface. This theory was considered an improvement from the two-film theory since mass transfer occurs under unsteady-state conditions in many industrial processes. The penetration theory expresses the liquid-side mass transfer coefficient in terms of the contact time (θ) and the molecular diffusivity of the gas in the liquid according to Equation (2).

$$k_L = 2\left(\frac{D_{AB}}{\pi\theta}\right)^{0.5} \tag{2}$$

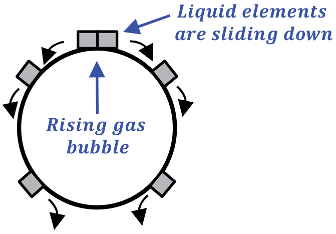

Figure 2. Schematic of Higbie's model

2.3. Surface renewal theory

The surface renewal theory, developed by Danckwerts [5], applies mathematics of the penetration theory to a more plausible situation, where the liquid is pictured as two regions, a large well mixed bulk region and an interfacial region, which is renewed so fast that it behaves as a thick film as shown in Figure 3. The basic assumptions of the theory are (1) liquid elements at the interface are being randomly swapped by fresh elements from the bulk; (2) at any moment, each of the liquid elements at the interface has the same probability of being substituted by a fresh element; and (3) mass transfer from the gas into the liquid element during its stay at the interface takes place under unsteady-state conditions. Thus, instead of using a constant contact time (θ), the differential liquid volume at the gas-liquid interface is renewed due to the turbulence around the interface, referred to as the surface renewal frequency (s). The surface renewal theory expresses the liquid-side mass transfer coefficient in terms of the surface renewal frequency (s) and the molecular diffusivity of the gas in the liquid according to Equation (3).

$$k_L = \left(D_{AB}s\right)^{0.5} \tag{3}$$

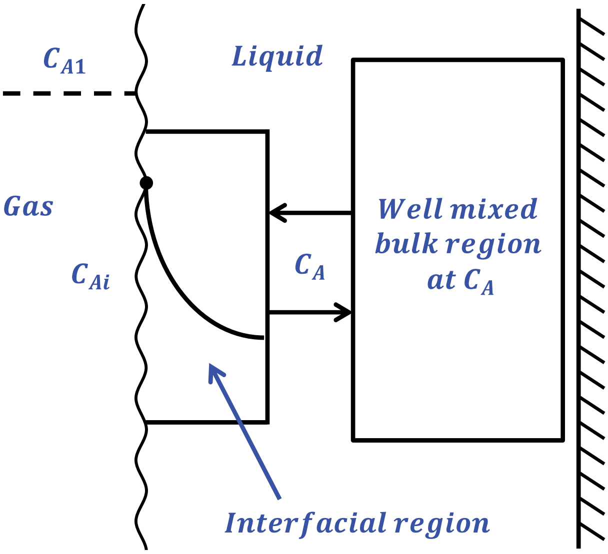

Figure 3. Schematic of surface renewal theory

In all three theories, D_{AB} is the molecular diffusivity of the gas (solute A) into the liquid (solvent B) at infinite dilution (up to 5 mol% of the solute in the solvent). However, one should keep in mind that the diffusivity depends to a large extent on the temperature, solvent viscosity as well as on the solvent composition and nature. A number of investigators related k_L to D_{AB} in the form $k_L \alpha \, (D_{AB})^{m}$ as given in Table 1.

Author	Variable	Diffusivity Exponent
Versteeg et al. [6]	k_L	0.33-0.5
Davies et al. [7]	k_L	0.46-0.60
Kuthan and Broz [8]	k_L	0.51-0.64
Kozinski and King [9]	k_L	0.5-0.6
Linek et al. [10]	k_L	0.46-0.66

Table 1. k_L relationship with diffusivity

3. Mass transfer with chemical reaction

3.1. Gas-liquid systems

In the absence of chemical reactions, the gas (A) diffuses into a liquid (B) and the mass transfer rate can be expressed using the following diffusivity equation:

$$\frac{\partial c_A}{\partial t} = -D_{AB}\frac{\partial^2 c_A}{\partial x^2} \tag{4}$$

The steady-state mass transfer flux through the liquid film can be described according to the film theory by Equation (5).

$$J_i = k_{L,i}a(C_i^* - C_{i,L}) \tag{5}$$

Where C_i^* represents the solute concentration at the gas-liquid interface, $C_{i,L}$ is the solute concentration in the liquid bulk, k_L is the liquid-side mass transfer coefficient, and a represents the gas-liquid interfacial area.

In the presence of chemical reactions, the film theory was also used to interpret gas-liquid mass transfer, however, modifications were required since the actual concentration profiles are no longer linear as can also be seen in Figure 4. This is due to the fact that chemical reactions could vary from slow to extremely fast, whereby instantaneous reactions occur at the interface; fast reactions occur in a narrow zone within the liquid film, and slow reactions spread through the film as well as the liquid bulk. Thus, in order to account for the effect of the chemical reaction on the solute mass transfer, an enhancement factor (E), defined as the ratio of the absorption rate with and without the reaction, is introduced as follows:

$$E = \frac{\text{Mass transfer rate with chemical reaction}}{\text{Mass transfer rate without chemical reaction}} \tag{6}$$

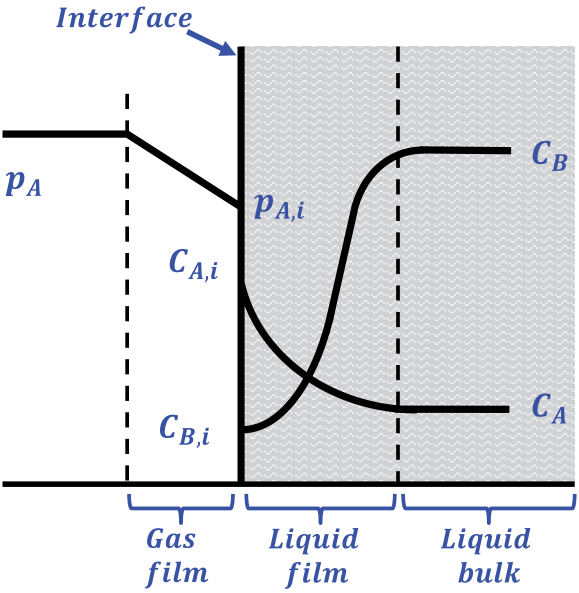

Figure 4. Mass transfer with chemical reaction in a gas-liquid system

An irreversible mth, nth orders chemical reaction can be expressed by the following equation:

$$mA + nB \rightarrow P(product) \tag{7}$$

The reaction rate can be written as:

$$-r_A = k_{m,n} C_A^m C_B^n \tag{8}$$

The enhancement factor has been extensively investigated with many approximations proposed for solving Equation (8). The most widely used approximation is the numerical solution proposed by van Krevelen and Hoftijzer [11], which estimates the value of the enhancement factor as a function of the Hatta number (Ha). Ha compares the rate of chemical reaction to that of diffusion through the film and the enhancement factor for an infinitely fast reaction (E_∞), is shown in Figure 5. For a chemical reaction expressed by Equation (8), Ha could be written as:

$$Ha = \frac{\sqrt{\frac{2}{(m+1)} k_{m,n} C_{A,i}^{m-1} C_{B,bulk}^{n} D_{A,B}}}{k_L} \tag{9}$$

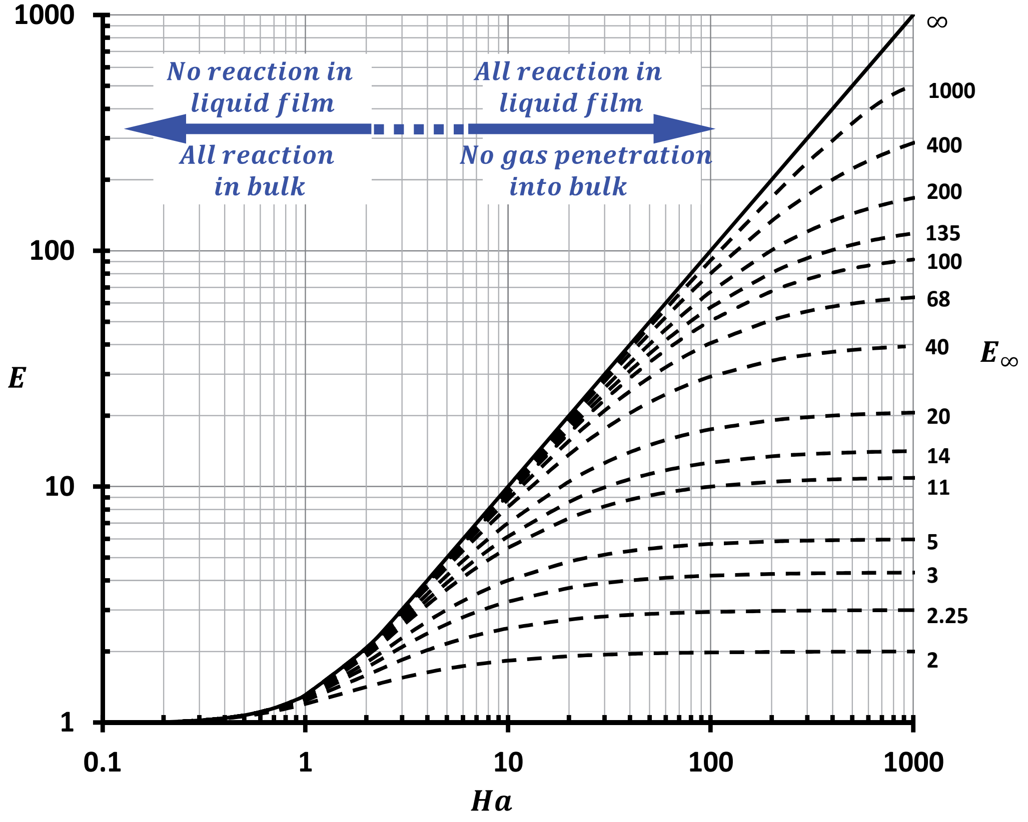

Figure 5. Enhancement factor for a first order gas-liquid reaction based on the numerical solution by van Krevelen and Hoftijzer [11]

3.2. Gas-solid systems

Gas-solid reactions are widely used in industrial applications. There are two main scenarios for gas-solid reactions, either the solid particles remain unchanged in size during reaction or they shrink with time as the reaction proceeds. The former scenario is described using the Continuous Reaction Model (CRM) as shown in Figure 6. This model assumes that the gaseous reactants react inside the solid particle, where its volume remains constant. On the other hand, the Shrinking Core Model (SCM), shown in Figure 7, assumes that the gas-phase reacts with the particle and the reaction front progressively moves inwards, continuously reducing the size of the core of unreacted solids and leaving behind reacted materials. The application of both of models were extensively discussed by Levenspiel [12].

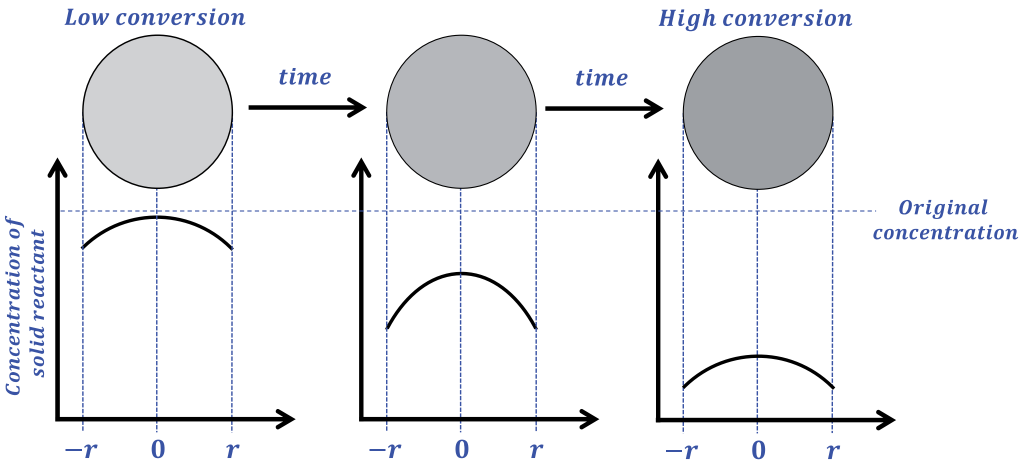

Figure 6. Schematic of the Continuous Reaction Model (CRM)

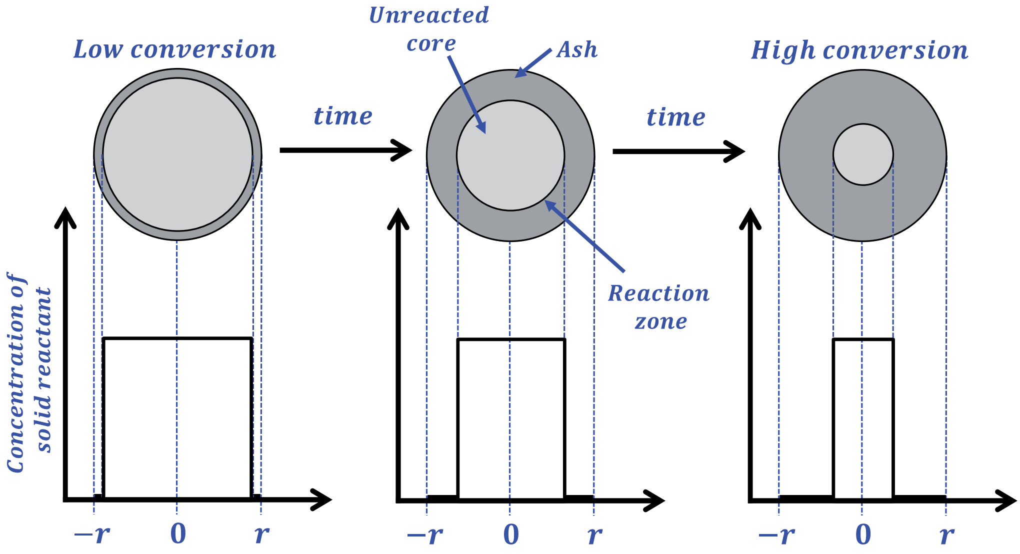

Figure 7. Schematic of the Shrinking Core Model (SCM)

3.3. Gas-liquid-solid systems

Figure 8 depicts a schematic of the concentration profile for mass transfer in three-phase systems, where the reactants in the gas-phase diffuse through the liquid-phase in order to reach the catalyst active sites to react, and then the products have to travel back to the gas-phase or to the liquid-phase. The following steps describe the mass transfer process:

1. Transfer of the reactants from the gas-phase bulk to the gas-side film.
2. Transfer of the reactants through the gas-side film to the gas-liquid interface
3. Transfer of the reactants form the gas-liquid interface through the liquid-side film.
4. Transfer of the reactants through the liquid bulk, then to the liquid film surrounding the catalyst particle.
5. Transfer of the reactants through liquid film surrounding the catalyst particles to the particle surface.
6. Diffusion of the reactants inside the particle pores to the catalyst active sites.
7. Reaction of the reactants to form products.
8. Diffusion of the products through the particle to its external surface.
9. Transfer of the products from the particle external surface through the liquid-film surrounding the particle.
10. Transfer of the products from the liquid-film surrounding the particle through the liquid bulk. Depending of the conditions, products could remain the liquid-phase.
11. Transfer of the gaseous products from the liquid bulk through the liquid-side film.
12. Transfer of the gaseous products from the liquid-side film to gas-liquid interface.
13. Transfer of the gaseous products from the gas-liquid interface to the gas-phase.

An example of processes where the products remain in the liquid phase is the synthesis of cyclohexanol and cyclohexanone by cyclohexane oxidation. These products remain in the liquid phase and their separation is achieved by simple distillation.

Steps 1-4 and 11-13 are evaluated considering the specific gas-liquid interfacial area (a) and the mass transfer coefficients in the gas-side film (k_G) and/or the liquid-side film (k_L). Steps 5 and 10 are accounted for through the particle specific surface area and solid-side mass transfer coefficient (k_S). Steps 6 and 8 are determined by the Knudsen diffusivity (D_κ) and the effective diffusion (D_{eff}) in the catalyst particle, using Equations (10) and (11) as:

$$D_\kappa = 97 r_p \sqrt{\frac{T}{M_L}} \tag{10}$$

$$D_{eff} = \varepsilon_{cat} \frac{D_{AB}}{\tau_{cat}} \tag{11}$$

Where r_p represents the catalyst pore radius; ε_{cat} is the catalyst void fraction; τ_{cat} is the tortuosity in the particle; and M_L is the molecular weight of the liquid phase.

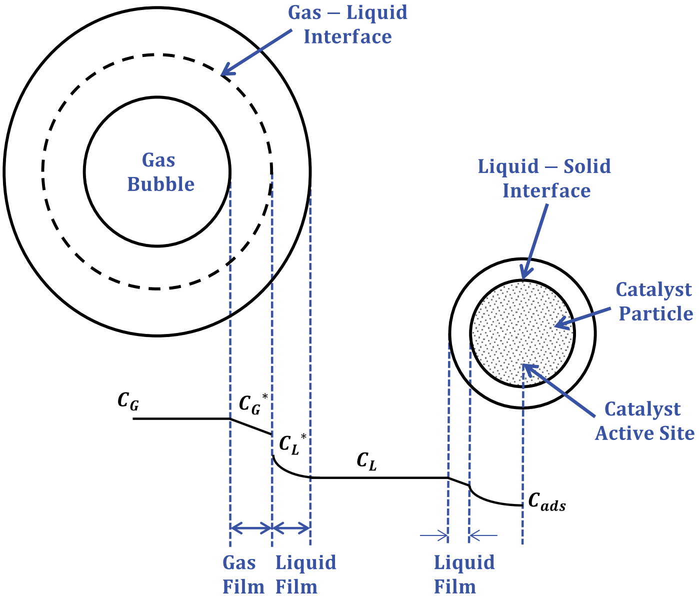

Figure 8. Concentration profiles for mass transfer into a slurry with a catalytic particles [13]

The reactions are quantified for the catalyst by the Thiele modulus (Φ_s), which is valid for first order irreversible reaction, and the effectiveness factor (η), Equations (12) and (13).

$$\Phi_s = R_{cat}\sqrt{\frac{k_{reaction}}{D_{eff}}} \tag{12}$$

$$\eta = \frac{1}{\Phi_s}\left(\frac{1}{tanh\left(3\Phi_s\right)} - \frac{1}{3\Phi_s}\right) \tag{13}$$

Where $k_{reaction}$ is the reaction rate constant for a first order reaction, and *Rcat* is the particle radius. For particles smaller than 200 microns and having a small Thiele modulus, for all practical purposes, the effectiveness factor η is close to unity.

Step 7 represents the chemical reaction of the reactants on the catalyst active sites. A typical first order reaction, which is usually found in hydrogenation processes, is:

$$r_i = A \cdot \eta \cdot exp\left(\frac{-E_{app}}{RT}\right) \cdot C_{L,H_2} \tag{14}$$

The effectiveness factor in this equation is obtained from Equation (13).

4. Measuring gas-liquid mass transfer in multiphase systems

Physical and chemical methods were used to measure the gas-liquid interfacial area (a) and mass transfer coefficients (k_L) in multiphase systems. The gas-liquid interfacial area was measured using different physical and chemical methods. Physical methods, including photography, light reflection and light scattering were used, however, they were restricted to transparent contactors having low gas holdup. Other physical methods, including γ–ray radiography and real time neutron radiography were also used to estimate a. While the aforementioned methods reveal the gas bubble contributions to a, other techniques were devised to determine the impact of gas-liquid interface ripple on a. For instance, Muenz and Marchello [14] measured the wave frequency using a stroboscope and determined the interface amplitude through analysis of the refractive surface properties via a photovolt photometer and densitometer. Moreover, Vazquez-Una et al. [15] used a CDD camera viewing the surface at a 45° angle to calculate through digitized images analysis the wavelength,λ. They determined the surface peak-to-peak amplitude and frequency from the surface displacement recorded using a vertically oriented laser triple-range distance-measuring device.

The chemical methods, on the other hand, were used to measure the gas-liquid interfacial area using a fast chemical reaction, where the reaction kinetics should be known in order to calculate a. Midoux and Charpentier [16] thoroughly reviewed various chemical reactions for measuring the gas-liquid interfacial area a.

Physical and chemical methods were also used to measure the volumetric mass transfer coefficient (k_La) since it was found that the liquid-side mass transfer coefficient (k_L) is strongly dependent on the turbulence induced in the multiphase systems. Among the physical methods is the transient physical gas absorption (TPGA) technique, which appears to be a simple and direct method for measuring k_La. For instance, Chang and Morsi [17] developed a powerful model to describe the transient pressure decline, based on a modified Peng-Robinson equation of state (EOS) and mass balance. In their method, the decline of the total pressure of the system with time was recorded, and in conjunction with total mole and volume balances, k_La values were obtained under high pressures and temperatures for numerous gases (CO, H_2, CH_4, CO_2, N_2, He, etc.), into the liquids (hexane, toluene, cyclohexane, methanol, silicon oil, molten wax, polyalphaolefins, etc.) in the absence and presence of solids (glass beads, alumina, Puralox, iron oxides, etc.). The improvement brought by this model was discussed elsewhere [18]. The chemical methods for measuring k_La were reviewed by Danckwerts et al. [5], Astarita [19] and Charpentier [20]. In these methods, a slow chemical reaction with known kinetics was employed to obtain k_La. The problems encountered in using these methods were due to the difficulty in controlling temperature and the lack of reliable kinetics.

The liquid-side mass transfer coefficient (k_L) could be indirectly calculated, knowing both the gas liquid interfacial area (a) and the volumetric mass transfer coefficient (k_La) determined using any of the physical methods described above. However, one must measure k_La and a simultaneously, i.e., under the same hydrodynamics in order to calculate a meaningful value of k_L. This is because as mentioned above k_L strongly depends on the turbulence induced in the multiphase system. The liquid-side mass transfer coefficient (k_L) was also calculated using a chemical reaction with known kinetics and a contactor with known surface area (gas-liquid interface). The knowledge of the total absorption rate, equilibrium solubility, and reaction kinetics would enable the calculation of k_L [20]. Again, the difficulty in this method resides in the stability of the liquid film on the surface area of the contactor.

5. Literature data on gas-liquid mass transfer in multiphase systems

The effects of mass transfer on three-phase reactor performance have been extensively investigated in the literature. Earlier studies on the mass transfer in F-T systems focused on the significance of hydrogen mass transfer compared to the overall reaction resistance. This was due to the fact that F-T kinetics over iron catalyst were reported to be first order with respect to hydrogen. The principal mass transfer resistance occurs in the slurry-phase and the extent of the effect of gas-liquid mass transfer on the reactor performance has been argued. Satterfield and Huff [21] concluded that the hydrogen mass transfer was the limiting step for reactor productivity, whereas Deckwer [22] showed that the mass transfer resistance was smaller when compared with the kinetics resistance. Inga and Morsi [23] and Sehabiague and Morsi [24] reported that F-T SBCRs operating under a kinetically-controlled regime at low catalyst concentrations could move to a mass transfer-controlled regime at high catalyst concentrations, where the reactor performance quickly declines. Nonetheless, it is generally agreed that the mass transfer strongly depends on the bubble size, where smaller bubbles result in a greater gas-liquid interfacial area, which improves the overall mass transfer.

The volumetric mass transfer coefficients, derived from the inlet and outlet concentrations of absorption experiments, were influenced by the dispersion in both phases [13]. Since the dispersion is strongly dependent on the column size and geometry, the developed equations for the calculating the volumetric mass transfer coefficients appear to include geometric parameters, such as the column diameter and sparger characteristics. Behkish et al. [25, 26] measured the volumetric mass transfer coefficients (k_La) for H_2, CO, N_2, CH_4 and He in Isopar-M (an isoparaffinic liquid mixture of $C_{10} – C_{16}$) in the presence of alumina particles under high pressures (up to 30 bar), temperatures (up to 473 K), gas velocities (up to 0.39 m/s) and solid concentrations (up to 36 vol.%). While the experiments by these authors were conducted under typical F-T operating conditions, they did not use gas mixtures, mimicking the syngas; and the composition of their Isopar-M varies greatly from that of the molten wax produced in the SBCR once a steady-state operation is reached.

More recently, Sehabiague et al. [24] have measured the volumetric mass transfer coefficients for N_2 and He, in C_{12}-C_{13}, paraffins mixture, light F-T cut, heavy F-T cut in a 0.3 m ID SBCR under high pressures (up to 30 bar), temperatures (up to 500 K) in the presence of Alumina, Puralox Alumina and Iron oxide particles (up to 20 vol.%) at various superficial gas velocities (up to 0.27 m/s). Table 2 summarizes the literature studies and correlations for k_La in multi-phase reactors over the past 20 years.

System	Conditions	Correlation	Reference
Air, N_2 – Water, Alcohols, Calcium alginate, Polystyrene	P_{atm} u_g up to $0.15 ms^{-1}$ C_V up to 20 vol% d_C: 0.14, 0.218, 0.3 m h_C: 1.5 m	$k_L\ a = \frac{12.9 Sc^{0.5} \varepsilon_g^{1.3}}{Mo^{0.159} Bo^{0.184}} \cdot \left(\frac{g \rho_l D_{AB}}{(1+0.62C_V) \cdot \sigma_l}\right)$ $\left(0.47 + 0.53\, exp\left(-41.4 \frac{\Pi_\infty k_l}{\mu_l u_p} Re_B^{-0.5}\right)\right)$ $\Pi_\infty = -C_B\left(\frac{d\sigma}{dC_B}\right)$	Salvacion et al [27]
O_2, CO_2 – Glycol, Water, Brine, Aqueous Polyacrylamide	Sieve and Sintered plate	$k_L = \alpha\left(\frac{(\rho_l - \rho_g)\mu_l g}{\rho_l^2}\right)^{\frac{1}{3}}\left(\frac{\mu_l}{\rho_l D_{AB}}\right)^{-\frac{2}{3}}$ $\alpha = \begin{cases} 0.31 \ \ for \ \ d_p < 1.0 \ \ mm \\ 0.0031 \ \ for \ \ 1.0 < d_p < 2.5 \ \ mm \\ 0.0042 \ \ for \ \ d_p > 2.5 \ \ mm \end{cases}$	Calderbank et al. [28]
CO_2 – $NaHCO_3$, Na_2CO_3 surfactants	d_C: 0.113 m , h_C: 1.086 m $u_g < 0.002\ ms^{-1}$	$k_L = K_4 u_g^{0.5} \sigma_l^{1.35}$ *K_4 is a function of the bubble plate size*	Vazquez et al. [29]
He, N_2, SF_6, Air – 0.8 M Na_2SO_4 - Xanthan gum, Diatomite, Alumina suspensions	P: 0.1 – 1 MPa u_G: 0.01–0.08 ms^{-1} C_V: Upto 18% vol d_p: 7, 22 μm d_C: 0.115 m , h_C: 1.37 m	$k_L\ a = u_g^{0.9} \mu_{eff}^{-0.55} \rho_g^{0.46}$ $K = \begin{cases} 0.063 \ \ for \ \ Salt \ \ Solutions \\ 0.042 \ \ for \ \ Salt \ \ free \ \ Systems \end{cases}$ $\mu_{eff} = k(2800 u_g)^{n-1}$ *k is the fluid consistency index = 1.97 ,* *n : empirical constant $1 \geq n \geq 0.18$*	Dewes et al. [30]
N_2/Fe(CN) - NaOH, CMC,$HNaCO_3$-Na_2CO_3/glass, diatomite, silicon carbide, alumina	u_g: 0.007–0.09 ms^{-1} C_V: 1.3–12.4 vol% d_p: 44–105 μm ϱ_s: 2448–3965 kg/m^3 ϱ_l: 1026–1121 kg/m^3 μ_l: 0.99–6.27 mPa · s d_C: 0.05 m , h_C: 0.75 m	$\frac{k_L}{u_g} = 0.103(ReFrSc^2)^{-0.265}$	Neme et al. [31]
Air - Water - Lexan, PS, Glass	u_g: 0.0025–0.05 ms^{-1} ϱ_s: 1170–2460 kg/m^3 C_V: 0.9–2.5 vol% d_p: 2.3–3 mm d_C: 0.06 m , h_C/d_C: 22–30.2	$k_L\ a = 4.49 u_g^{0.338} C_s^{0.595}\left(1 - \frac{\rho_l}{\rho_s}\right)^{0.337}$	Guo et al. [32]
Air - Water - Nickel	u_g: 0.02–0.04 m/s u_l: 0.018–0.037 m/s C_V: 5.7 vol.%	$k_L\ a = 0.4 u_g^{0.625} u_l^{0.26} \times exp[1.477 \cdot 10^{-5} h_C]$	Chen et al. [33]

System	Conditions	Correlation	Reference
	$d_p: 177-210\ \mu m$ $\varrho_s: 8900\ kg/m^3$ $d_C: 0.05\ m$, $h_C: 0.5\ m$		
H_2/CO - Paraffin oil - Silica gel	$T: 293-523\ K$ $P: 1-5\ MPa$ $d_p: 134\ \mu m$ C_v: 5− 20 vol.% $d_C: 0.037\ m$, $h_C: 0.48\ m$	$H_2: \frac{k_L\ d_{32}}{D_{AB}} = 1.546\times10^{-2} Eu^{0.052} Re^{0.076} Sc^{-0.231}$ $CO: \frac{k_L\ d_{32}}{D_{AB}} = 8.748\times10^{-2} Eu^{-0.012} Re^{0.024} Sc^{-0.133}$	Yang et al. [34]
H_2, CO, N_2, CH_4- Isopar-M, Hexanes – Glass beads, Iron Oxide	$u_g: 0.0035-0.574\ m/s$ C_v: 0 −36 vol.% T: 275−538 K P: 0.1−15 MPa $\varrho_s: 700-4000\ kg/m^3$ $d_p: 5-300\ \mu m$ $\varrho_l: 633.4-1583\ kg/m^3$ $\mu_l: 0.189-398.8\ mPa \cdot s$ $\sigma_l: 8.4-75\ mN/m$ d_C: 0.0382−5.5 m	$\frac{k_L}{(1-\varepsilon_g)} = 6.14\times10^4 \cdot$ $\cdot \frac{\rho_l^{026} \mu_l^{0.12} \varepsilon_g^{1.21} D_{AB}^{0.5}}{\sigma_l^{0.52} \rho_g^{0.06} u_g^{0.12} d_p^{0.05} T^{0.68}} \Gamma^{0.11} \left(\frac{d_C}{d_C+1}\right)^{0.4}$	Lemoine et al. [35]
H_2, CO, N_2, CH_4,-Isopar-M, Hexanes – Glass beads, Iron Oxide	Same as Lemoine et al. [35]	$k_L\ a = 0.18 Sc^{0.6} \left(\frac{\rho_l \eta_g}{M w_l}\right)^{-2.84} (\rho_g u_g)^{0.49} \times exp[-2.66 C_V]$	Behkish et al. [36]
He, N_2 – Paraffins mixture, C_{12}-C_{13}, Light F-T Cut, Heavy F-T- Cut – Alumina, Puralox Alumina, Iron oxide	$u_g: 0.14-0.26\ m/s$ C_v: 0 −20 vol.% T: 330−530 K P: 8−30 MPa $\varrho_s: 3218-4000\ kg/m^3$ $d_p: 1.5-140\ \mu m$ $\varrho_l: 631.3-779.5\ kg/m^3$ $\mu_l: 0.27-9.96\ mPa \cdot s$ $\sigma_l: 13-27\ mN/m$ $d_C: 0.3\ m$ m, $h_C: 3\ m$	$k_L\ a = 7.99\times10^{-9} \frac{\rho_l^{1.82} \rho_g^{0.27} u_g^{0.387} \Gamma^{0.173}}{\mu_l^{0.25} \sigma_l^{0.976} M w_g^{0.02}}$ $\left(\frac{P_T}{P_T-P_S}\right)^{0.242} \left(\frac{d_C}{d_C+0.3}\right)^{0.1} \times exp$ $[-1.3C_v + 0.8C_v^2 - C_v^3 - 1675.7 d_p + 0.176 X_W]$	Sehabiague et al. [24]

Table 2. Recently published gas-liquid mass transfer empirical correlations applicable to multiphase reactors

6. Applications to Fischer-Tropsch synthesis

This Chapter focuses on the Fischer-Tropsch (F-T) synthesis process as an example of industrial multiphase systems. In this process, the syngas ($CO + H_2$) react in the presence of a catalyst, conventionally iron or cobalt, to produce synthetic hydrocarbon products, primarily linear alkanes and alkenes. The overall F-T process involves three main steps: syngas generation, F-T catalytic reactions and product upgrading. Syngas generation involves converting the carbonaceous feedstock into a H_2-CO mixture via reactions with steam and optionally oxygen or air. Solid feedstocks, such as coal and biomass, are converted in a gasifier, of which various types have been already in industrial applications [37-40]. Different gasification processes and technologies have also been discussed in the literature [41-52]. Natural gas, on the other hand, is converted to syngas in a reformer using either partial oxidation (POX), steam methane reforming (SMR) or auto-thermal reforming (ATR).

Although many metals have been identified to catalyze F-T reactions, only iron (Fe) and cobalt (Co) have been used in industrial applications [39, 52]. Iron catalyst is cheap and has a high water-gas-shift (WGS) activity, however, it is prone to severe attrition and the water produced during the reaction appeared to decrease its activity [53, 54]. Cobalt-based catalyst, on the other hand, has higher activity than iron catalyst since it is not strongly inhibited by water. It is more resistant to attrition and as such has a longer life in the reactor than iron catalyst. Cobalt-based catalyst, however, is more expensive and has no WGS activity [53, 55]. During Cobalt catalyzed F-T reaction, the oxygen from CO dissociation is converted to H_2O, as shown in Equation (15). Conversely, iron catalyst has a high affinity for the WGS reaction as shown in Equation (16), resulting in the conversion of a significant portion of oxygen from CO dissociation into CO_2.

$$F-T: CO + 2H_2 \rightarrow -CH_2- \; + \; H_2O \tag{15}$$

$$WGS: CO + H_2O \leftrightarrows H_2 + \; CO_2 \tag{16}$$

Thus, the extent of the WGS reaction has to be closely considered as it affects the H_2/CO ratio in the F-T process.

6.1. Multiphase Reactors for F-T synthesis

Depending on the reaction temperature, the F-T process is referred to as low temperature F-T (LTFT) or high temperature F-T (HTFT). The temperature of the LTFT ranges from 180 to 260 ^{o}C and the syncrude produced is wax consisting mostly of long chain hydrocarbons, while the temperature of the HTFT process is between 290 and 360 ^{o}C and the products are mostly short chain hydrocarbons and gases. Therefore, the final products of the LTFT process consist mostly of diesel fuel, while gasoline production has been the focus of the HTFT [56]. The LTFT syncrude product is easy to upgrade by a hydroprocessing step and a fractionation step to obtain naphtha and middle distillate, whereas the HTFT syncrude requires more complex

F-T Plant	Date of Operation	Reactor Technology	Catalysts
German CTL (14 plants active at end of WWII)	1935-1962	LTFT FB	Co/ThO_2/kieselguhr (100:18:100) before 1938 $Co/ThO_2/MgO$/kieselguhr (100:5:8:200) after 1938
Hydrocol GTL	1951-1957	HTFT FFB	Fused $Fe_3O_4/Al_2O_3/K_2O$ (97:2.5:0.5) Later replaced by Magnetite with 0.5% K_2O
Sasol I CTL/GTL	1955-present	HTFT CFB LTFT FB, SBCR	Magnetite with 0.5% K_2O Precipitated $Fe/SiO_2/K_2O/Cu$ (100:25:5:5)
Sasol Synfuels CTL	1980-present	HTFT FFB	Fused Fe (similar to Sasol I HTFT CFB catalyst)
PetroSA GTL	1992-present	HTFT CFB LTFT SBCR	Fused Fe (same as Sasol Synfuels) Co based catalyst
Shell Bintulu	1993-present	LTFT FB	$Co/Zr/SiO_2$
Sasol Oryx GTL	2007-present	LTFT SBCR	$Co/Pt/Al_2O_3$
Shell Pearl GTL	2011-present	LTFT FB	$Co/Zr/SiO_2$

Table 3. F-T Plants: catalysts and reactor technologies [53, 57]

refinery facilities [56]. It should be noted that recent R&D and commercial efforts have been focused on the LTFT due to the current drive for using more diesel engines than gasoline engines, the excellent quality of sulfur-free F-T diesel, and perhaps the mild conditions of the process.

Reactor technologies used for commercial applications of the F-T synthesis are summarized in Table 3. The HTFT reactors include fixed fluidized-bed reactors (FFBRs) and circulating fluidized-bed reactors (CFBRs), whereas multitubular fixed-bed reactors (FBRs) and slurry bubble column reactors (SBCRs) are used for the LTFT process. Also, LTFT micro-channel reactors for small-scale applications have been recently receiving considerable attention, even though no commercial applications are yet available.

In multi-tubular FBRs, the syngas flows through small diameter tubes packed with catalyst at small voidage, resulting in a high pressure drop and an increased operating cost. These reactors have comparatively complex heat transfer characteristics and their maximum production capacity is limited by the amount of heat which can be removed. Hot spots would ultimately result in carbon deposition on the catalyst surfaces and serious plugging of the reactor tubes. These types of reactors, however, have been used to carry out LTFT by Germany during WWII, Sasol since 1950's and Shell at the Bintulu GTL (Malaysia) and more recently at the Pearl GTL (Qatar) [41, 53, 57, 58].

SBCRs, on the other hand, have a simpler design and allow for much higher heat removal efficiencies than multitubular FBRs due to the presence of a large volume of the liquid-phase. Its advantages include a much greater flexibility than FBRs and its capital cost is 20 - 40% lower than that of multitubular FBRs [59]. However, the high mechanical shear on the catalyst, resulting in particles attrition and the lack of a reliable system for the fine particles separation from the liquid products, have delayed commercial deployment of SBCRs until the 1990's.

Conversely, microchannel reactors have a stationary catalyst bed combined with enhanced heat and mass transfer characteristics. Also, they are typically aimed at exploiting a different market than conventional reactors where their small size is an advantage. A schematic of both SBCR and FBR multiphase reactors is shown in Figure 9

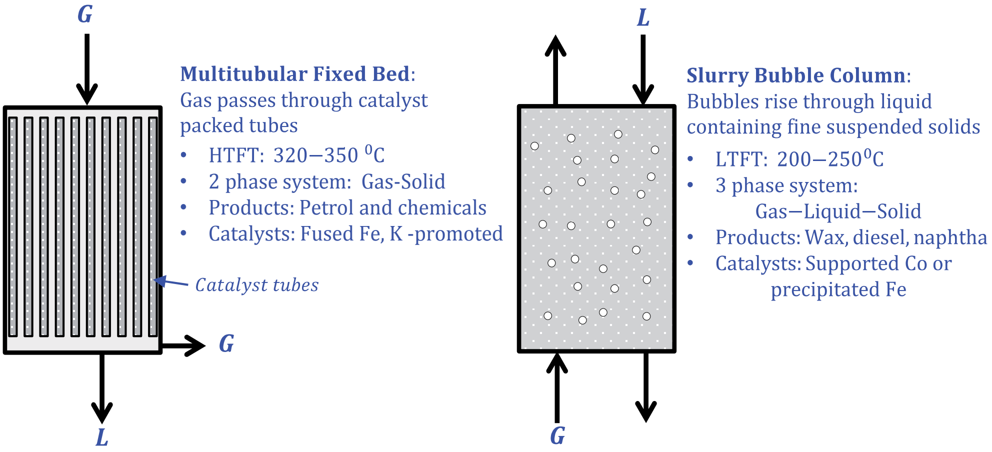

Figure 9. Schematic of SBCR and FBR reactors for F-T

6.2. Mass transfer in SBCRs for F-T synthesis

In general, the longer the molecules stay in the catalyst pores, the heavier the hydrocarbons become, significantly reducing their diffusivities, which could be considered as one of the main reasons for catalyst deactivation, referred to as fouling, in F-T synthesis [53]. In most applications, however, it is often assumed that when the products leave the solid-liquid interface, there is no major effect of their presence on the reaction rate. With these considerations, it can be concluded that the steps that affect the overall reaction rate of the process are the gas-liquid mass transfer step and the reaction on the catalyst active sites. This means that a major impact on the optimization of a gas-liquid or a gas-liquid-solid reactor could be done by increasing the catalyst activity and/or improving the mass transfer rate between the gas and the liquid phases. It should be mentioned, however, that the relative importance of the mass transfer, in certain processes depends on the catalyst activity, operating conditions, and reactor configuration [2].

Figure 8 shows the concentration profiles for mass transfer into a slurry system, and as such, it could be used to explain the mass transfer behavior in SBCRs. In F-T synthesis, since the diameter of catalyst particles used are in the range of 30 to 90 μm [60], the interfacial area between the liquid and the catalyst particles becomes very large and accordingly the resistance to the mass transfer due to steps 4, and 9 can be neglected. Steps 3 and 10 can also be neglected if the reactor is operated in the churn-turbulent flow regime due to the efficient mixing in this flow regime. Also, since the products formed in the F-T reactor are wax and as such the gas-phase consists mainly of the reactants (CO and H_2), one can neglect the resistance associated with steps 1-2 and 13. Thus, the main resistances controlling the behavior of F-T synthesis in SBCRs are (1) the reaction kinetics (step 7), and (2) the gas-liquid mass transfer through the liquid-side film (steps 3 and 12).

7. Factors affecting the hydrodynamics and mass transfer in F-T SBCRs

The hydrodynamics (gas holdup, bubble size/distribution) and mass transfer characteristics (volumetric mass transfer coefficients) in SBCRs for F-T synthesis are affected by numerous factors ranging from the physicochemical properties of the gas-liquid-solid system to the operating conditions and reactor geometry. Unfortunately, the majority the experimental studies found in the literature on the hydrodynamics and mass transfer in SBCRs used air-water-glass beads systems under ambient conditions; and only few data are available under F-T conditions for H_2, CO, N_2 and He in F-T molten wax in the presence and absence of inert solid particles, including iron oxides, alumina and Puralox [24]. None of these studies, however, cover all the conditions encountered in an industrial F-T reactor ($T > 450$ K, $P > 20$ bar, $U_G > 0.15$ m/s, $C_V > 10$ vol%, mixture of hydrocarbons as liquid-phase, H_2 and CO as gas-phase, micron sized Fe or Co-based particles as solid-phase).

7.1. Effect of molecular weight and density of the gas-phase

The density of the gas-phase has been reported to increase the gas holdup [61, 62], and denser gases led to higher gas holdups. It was also reported that an increase of gas density resulted in the shrinkage of the gas bubbles [63]. The impact of the molecular weight of the gas phase is similar to that of the gas density. Indeed, an increase of the molecular weight will translate into an increase of gas density and as such will lead to higher gas holdup and smaller gas bubbles [64]. It is, however, important to note that the increase of gas holdup with density/molecular weight is not true under all conditions. Clark [65] for example reported that at low gas velocities below 0.05 m/s (corresponding to the homogeneous or bubbly flow regime), the gas holdup of N_2 was smaller than that of H_2.

7.2. Effect of density, viscosity and surface tension of the liquid phase

The effect of the liquid density on the gas holdup has been studied by several investigators, but still remains unclear. Some investigators reported an increase [66, 67] of gas holdup with increasing the liquid density, while others reported a decrease [62, 68]. The volumetric mass transfer coefficient was found to decrease with decreasing liquid density [69, 70]. Increasing the liquid viscosity has been found to decrease the gas holdup [61, 67, 68] and increase the gas bubbles size [71]. The volumetric mass transfer coefficient has been reported to decrease with increasing the liquid-phase viscosity [69, 70]. The liquid surface tension was reported to have a similar effect to that of the liquid viscosity on gas holdup, i.e., an increase of liquid surface tension leads to a decrease of gas holdup [61, 68]. Also, an increase of liquid surface tension leads to the formation of larger gas bubbles [71] and smaller volumetric mass transfer coefficients [69].

http://dx.doi.org/10.5772/60516

7.3. Effect of size, density and wettability of solid particles

Slurry suspensions of denser solid particles led to lower the gas holdup [72] than similar suspensions of particles with lower density. Increasing the size of solid particles was found to increase [72] the gas holdup for non-wettable solid particles, however, it was found to decrease [72, 73] the gas holdup for wettable solid particles. The solid particles diameter was reported, in some cases, to have no significant effect [74] on the gas holdup. The wettability of the solid particles has no clear effect on the gas holdup. In some cases, it was found to increase the gas holdup [72] and in others to decrease it [74].

7.4. Effect of operating conditions

Increasing temperature has been found to increase the gas holdup [36] through the decrease of both liquid surface tension and viscosity. Increasing temperature was also reported to increase the volumetric mass transfer coefficient [66] due in part to the increase of the gas diffusivity. On the other hand, the gas holdup was found to increase with pressure [75] which was attributed to the increase of the gas density. The volumetric mass transfer coefficient was also found to increase with pressure [75, 76]. Moreover, numerous experimental studies have shown that increasing the superficial gas velocity led to the increase of the gas holdup [62, 67] and the volumetric mass transfer coefficient [75, 76].

7.5. Effect of liquid and slurry velocity

The effect of liquid superficial velocity on the gas holdup has been investigated by several authors; and increasing liquid velocity was found to decrease the gas holdup in the absence [77] and presence [73, 74] of solid particles.

7.6. Effect of solid loading

The presence of fine micron-size catalyst particles in the liquid-phase greatly affects the properties of the slurry-phase, such as density and viscosity. While a few studies [24, 77] have found an increase of gas holdup with increasing solid concentration, adding more particles has mostly been found to decrease the gas holdup [63, 70, 73] by increasing the slurry viscosity. A decrease of the volumetric mass transfer coefficient and the formation of larger gas bubbles due to the increase of the rate of bubbles coalescence was also reported when increasing the solid loading [70]. It was also observed, particularly at low solid concentrations [78] that the volumetric mass transfer coefficient appeared to increase with increasing solid concentration. It should be noted that these results have to be considered along with the effects of the physical properties of the solids used, such as shape, size and wettability.

7.7. Effect of reactor geometry

The Reactor geometry has a strong influence on the gas holdup. In SBCRs, 3 zones can be identified where the gas holdups are significantly different. The first zone corresponds to the bottom of the reactor in the vicinity of the gas sparger, which is strongly affected by the sparger design. The second zone is the bulk region. The third zone is the top region, where the gas holdup will behave very differently from the bulk region, if foaming occurs. It is important to note that if the reactor is long enough the effect of the first and third regions on the total gas holdup will become negligible [79]. The effect of column diameter on the gas holdup has been found to be strong in the case of small diameter reactors with diameter ≤ 0.15 m [80], however, several investigators have found that this effect would level off or disappear for diameters ≥ 0.15 m [69, 79]. Moreover, the length to diameter (L/D) ratio is frequently used instead of the reactor length when studying the effects of reactor geometry on the hydrodynamics. Several studies found that the gas holdup remained unaffected when the length to diameter ratio was ≥ 6 [24, 79].

7.8. Effect of gas distributor

The design of the gas distributor, the number of openings, their sizes and their orientations play an important role in affecting the hydrodynamics and mass transfer in the SBCRs not only within the bottom region at the vicinity of the gas distributor, but also in the bulk region. The initial bubble size and distribution at the orifice could be controlled by the sparger characteristics, but due to the balance between coalescence and breakup of gas bubbles, the initial bubble size created at the gas sparger would not describe the behavior of gas bubble size distribution in the entire column [71]. Under the same operating conditions, different designs of the gas sparger were found to give different volumetric mass transfer coefficient values [81]. For two different designs of the gas distributor, increasing the size of the openings was found to decrease gas holdup due to the formation of larger gas bubbles [36]. However, several investigators have reported that the gas sparger had a minimal effect on the bubble sizes and gas holdup if the orifice diameters were > 0.001-0.002 m [71, 79]. This suggests that for a certain size of the openings, the gas bubble size and gas holdup reach a maximum and a minimum value, respectively.

7.9. Effect of reactor internals

Since F-T synthesis is an exothermic reaction, cooling tubes are needed in the reactor in order to remove the heat released by the reaction. The presence of those internals will affect the performance of the reactor in terms of hydrodynamics and mass transfer. Saxena et al. [82] have studied 3 different configurations of internals representing 1.9%, 2.7% and 14.3% of the column cross sectional area and could not find any clear effect of the number of internals on the gas holdup. O'Dowd et al. [83] found slightly higher gas holdup value in a column equipped with cylindrical baffles occupying 15% of the cross-sectional area than in an unbaffled column of the same size. However, the difference lies within the range of errors of their experimental measuring technique. Also, another study [84] reported slightly higher gas holdup value when internals representing 5% of the cross section area were present. Yamashita [85] studied the effect of the separation distance between the internals and found out that gas holdup decreased when the separation distance was small (0.006 m) and increased when the separation distance was greater than 0.008 m. He attributed the decrease and increase in gas holdup values to the reduction of the radial mobility of gas bubbles and to the increase in interstitial gas velocity, respectively. Indeed, it is important to note that the slight increase in gas holdup reported in the above mentioned studies might be the result of the increase of interstitial velocity inside the reactor when adding internals.

8. Concluding remarks

The knowledge of hydrodynamic and mass transfer parameters in multiphase systems is critical for the development of numerous industrial processes, and therefore proper understanding, measurement and quantification of these important parameters remains an area of significant interest from research and industrial perspectives. An important example of multiphase systems is the F-T synthesis and although interest in the design and scaleup of SBCRs for low temperature F-T has soared over the past two decades, there still remain significant knowledge gaps, which are yet to be investigated, particularly relating to investigation of the hydrodynamic and mas transfer parameters, such as gas holdup and $k_L a$, under high pressures and temperatures typical to those of F-T industrial process. Such studies at elevated pressures and temperatures remain very limited when compared with the plethora of other studies conducted using air-water systems under ambient conditions. Thus, there is a great need for more studies to further understand the complex and intricate behavior of such multiphase systems and to investigate the effect of various operating parameters on the interphase mass transfer.

Nomenclature

a	Interfacial area	$k_{reaction}$	Reaction rate constant for a first order reaction (1/s)
Bo	Bond number	$k_L\ a$	Volumetric liquid side mass transfer coefficient (1/s)
C*	Equilibrium concentration in the liquid phase ($mol{\cdot}m^{-3}$)	M_L	Liquid average molecular weight ($kg{\bullet}kmol^{-1}$)
C_L	Concentration in the liquid phase ($mol{\cdot}m^{-3}$)	P	Pressure (Pa)
Cv	Concentration of solid particles (vol.%)	r	Reaction rate ($mol{\bullet}kg^{-1}{}_{catalyst}{\bullet}s^{-1}$)
d_c	Column diameter (m)	r_p	Catalyst pore radius (m)
d_p	Solid particle diameter (m)	Re	Reynolds number
D_{AB}	Diffusivity of phase A into B	Mo	Morton number
D_{eff}	Effective diffusivity in catalyst pores ($m^2{\cdot}s^{-1}$)	s	Surface renewal frequency (s^{-1})
D_K	Knudsen diffusion ($m^2{\cdot}s$)	Sc	Schmidt number
E	Enhancement factor	t	Time (s)

Fr	Froude number	T	Temperature (K)
g	Gravitational acceleration, (m/s^2)	u_b	Gas bubble rise velocity (m·s^{-1})
Ha	Hatta number	u_g	Superficial gas velocity (m·s^{-1})
J_i	Molar flux of species i (kmol·s^{-1}·m^{-2})		
Greek Letters			
ε_{cat}	Catalyst void fraction	π	3.14
δ_L	Liquid film thickness (m)	ρ	Density (kg/m^3)
η	Effectiveness factor	σ	Surface tension (N/m)
θ	Contact time	τ_{cat}	Tortuosity of the particle
μ	Viscosity (kg/m•s)	ϕ	Thiele modulus
Subscripts			
cat	Catalyst	l	Liquid
g	Gas	s	Solid

Author details

Badie I. Morsi* and Omar M. Basha

*Address all correspondence to: morsi@pitt.edu

Department of Chemical and Petroleum Engineering, University of Pittsburgh, Pittsburgh, PA, USA

References

[1] A. Shanley, G. Parkinson, and K. Fouhy, "Biotech in the scaleup era," ed: McGraw Hill, 1993.

[2] J. R. Inga and B. I. Morsi, "A Novel Approach for the Assessment of the Rate-Limiting Step in Fischer-Tropsch Slurry Process," *Energy & Fuels,* vol. 10, pp. 566-572, 1996/01/01 1996.

[3] W. K. Lewis and W. G. Whitman, "Principles of Gas Absorption," *Industrial & Engineering Chemistry,* vol. 16, pp. 1215-1220, 1924.

[4] R. Higbie, "The rate of absorption of a pure gas into still liquid during short periods of exposure," *Transaction of the American Institute of Chemical Engineers,* vol. 31, pp. 365-389, 1935.

[5] P. V. Danckwerts, "Gas absorption accompanied by chemical reaction," *AIChE Journal,* vol. 1, pp. 456-463, 1955.

[6] K. Van't Riet, "Review of Measuring Methods and Results in Nonviscous Gas-Liquid Mass Transfer in Stirred Vessels," *Industrial & Engineering Chemistry Process Design and Development,* vol. 18, pp. 357-364, 1979/07/01 1979.

[7] J. T. Davies, A. A. Kilner, and G. A. Ratcliff, "The effect of diffusivities and surface films on rates of gas absorption," *Chemical Engineering Science,* vol. 19, pp. 583-590, 8// 1964.

[8] K. Kuthan and Z. Broz, "Mass transfer in liquid films during absorption Part III. Dependence of the liquid-side mass transfer coefficient on the molecular diffusivity of gases at high values of the schmidt number," *Chemical Engineering and Processing: Process Intensification,* vol. 25, pp. 75-84, 4// 1989.

[9] A. A. Kozinski and C. J. King, "The influence of diffusivity on liquid phase mass transfer to the free interface in a stirred vessel," *AIChE Journal,* vol. 12, pp. 109-116, 1966.

[10] V. Linek, J. Mayrhoferová, and J. Mošnerová, "The influence of diffusivity on liquid phase mass transfer in solutions of electrolytes," *Chemical Engineering Science,* vol. 25, pp. 1033-1045, // 1970.

[11] D. W. van Krevelen and P. J. Hoftijzer, "Kinetics of gas-liquid reactions part I. General theory," *Recueil des Travaux Chimiques des Pays-Bas,* vol. 67, pp. 563-586, 1948.

[12] O. Levenspiel, "Chemical reaction engineering," 1972.

[13] J. R. Inga, "Scaleup and Scaledown of Slurry Reactors: A New Methodology," ed, 1997.

[14] K. Muenz and J. M. Marchello, "Technique for Measuring Amplitudes of Small Surface Waves," *Review of Scientific Instruments,* vol. 35, pp. 953-957, 1964.

[15] G. Vázquez-Uña, F. Chenlo-Romero, M. Sánchez-Barral, and V. Pérez-Muñuzuri, "Mass transfer enhancement due to surface wave formation at a horizontal gas–liquid interface," *Chemical Engineering Science,* vol. 55, pp. 5851-5856, 12// 2000.

[16] J.-C. Charpentier, "Mass-Transfer Rates in Gas-Liquid Absorbers and Reactors," in *Advances in Chemical Engineering*. vol. Volume 11, G. R. C. J. W. H. Thomas B. Drew and V. Theodore, Eds., ed: Academic Press, 1981, pp. 1-133.

[17] M.-y. Chang and M. Badie I, "Mass transfer characteristics of gases in aqueous and organic liquids at elevated pressures and temperatures in agitated reactors," *Chemical Engineering Science,* vol. 46, pp. 2639-2650, // 1991.

[18] A. Behkish, "Hydrodynamic and Mass Transfer Parameters in Large-Scale Slurry Bubble Column Reactors," ed, 2004.

[19] G. Astarita, *Mass transfer with chemical reaction*: Elsevier, 1967.

[20] J. Charpentier, "Advances in chemical engineering," *Vol. II, Academic Press, New York,* 1981.

[21] G. A. Huff and C. N. Satterfield, "Intrinsic kinetics of the Fischer-Tropsch synthesis on a reduced fused-magnetite catalyst," *Industrial & Engineering Chemistry Process Design and Development,* vol. 23, pp. 696-705, 1984.

[22] W.-D. Deckwer, Y. Louisi, A. Zaidi, and M. Ralek, "Hydrodynamic Properties of the Fischer-Tropsch Slurry Process," *Industrial & Engineering Chemistry Process Design and Development,* vol. 19, pp. 699-708, 1980/10/01 1980.

[23] J. R. Inga and B. I. Morsi, "Effect of Operating Variables on the Gas Holdup in a Large-Scale Slurry Bubble Column Reactor Operating with an Organic Liquid Mixture," *Industrial & Engineering Chemistry Research,* vol. 38, pp. 928-937, 1999/03/01 1999.

[24] L. Sehabiague and B. I. Morsi, "Hydrodynamic and Mass Transfer Characteristics in a Large-Scale Slurry Bubble Column Reactor for Gas Mixtures in Actual Fischer–Tropsch Cuts," *International Journal of Chemical Reactor Engineering,* vol. 11, pp. 1-20, 2013.

[25] A. Behkish, R. Lemoine, L. Sehabiague, R. Oukaci, and B. I. Morsi, "Gas holdup and bubble size behavior in a large-scale slurry bubble column reactor operating with an organic liquid under elevated pressures and temperatures," *Chemical Engineering Journal,* vol. 128, pp. 69-84, 2007.

[26] A. Behkish, Z. Men, J. R. Inga, and B. I. Morsi, "Mass transfer characteristics in a large-scale slurry bubble column reactor with organic liquid mixtures," *Chemical Engineering Science,* vol. 57, pp. 3307-3324, 2002.

[27] J. Salvacion and M. Murayama, "Effects of alcohols on gas holdup and volumetric liquid-phase mass transfer coefficient in gel-particle-suspended bubble column.," *Journal of Chemical Engineering of Japan,* vol. 28, pp. 434-442, 1995.

[28] P. H. Calderbank and M. B. Moo-Young, "The continuous phase heat and mass transfer properties of dispersions," *Chemical Engineering Science,* vol. 50, pp. 3921-3934, 1995.

[29] G. Vázquez, E. Alvarez, J. M. Navaza, R. Rendo, and E. Romero, "Surface Tension of Binary Mixtures of Water + Monoethanolamine and Water + 2-Amino-2-methyl-1-propanol and Tertiary Mixtures of These Amines with Water from 25 °C to 50 °C," *Journal of Chemical & Engineering Data,* vol. 42, pp. 57-59, 1997/01/01 1997.

[30] I. Dewes and A. Schumpe, "Gas density effect on mass transfer in the slurry bubble column," *Chemical engineering science,* vol. 52, pp. 4105-4109, 1997.

[31] F. Neme, L. Coppola, and U. Böhm, "Gas holdup and mass transfer in solid suspended bubble columns in presence of structured packings," *Chemical Engineering & Technology,* vol. 20, pp. 297-303, 1997.

[32] Y. X. Guo, M. N. Rathor, and H. C. Ti, "Hydrodynamics and mass transfer studies in a novel external-loop airlift reactor," *Chemical Engineering Journal,* vol. 67, pp. 205-214, 1997.

[33] C.-M. Chen and L.-P. Leu, "Hydrodynamics and mass transfer in three-phase magnetic fluidized beds," *Powder Technology,* vol. 117, pp. 198-206, 2001.

[34] W. Yang, J. Wang, and Y. Jin, "Mass Transfer Characteristics of Syngas Components in Slurry System at Industrial Conditions," *Chemical Engineering & Technology,* vol. 24, pp. 651-657, 2001.

[35] R. Lemoine and B. I. Morsi, "Hydrodynamic and mass transfer parameters in agitated reactors part II: Gas-holdup, sauter mean bubble diameters, volumetric mass transfer coefficients, gas-liquid interfacial areas, and liquid-side mass transfer coefficients," *International Journal of Chemical Reactor Engineering,* vol. 3, p. 1166, 2005.

[36] A. Behkish, R. Lemoine, R. Oukaci, and B. I. Morsi, "Novel correlations for gas holdup in large-scale slurry bubble column reactors operating under elevated pressures and temperatures," *Chemical Engineering Journal,* vol. 115, pp. 157-171, 2006.

[37] K. Ripfel-Nitsche, H. Hofbauer, R. Rauch, M. Goritschnig, R. Koch, P. Lehner, *et al.*, "BTL–Biomass to liquid (Fischer Tropsch process at the biomass gasifier in Güssing)," in *Proceedings of the 15th European Biomass Conference & Exhibition, Berlin, Germany,* 2007.

[38] J. R. Longanbach, G. J. Stiegel, M. D. Rutkowski, T. L. Buchanan, M. G. Klett, and R. L. Schoff, "Capital and Operating Cost of Hydrogen Production from Coal Gasification," Final Report, U.S. DOE Contract No. DE-AM26-99FT40465, Subcontract No. 990700362, PittsburghApril 2003 2003.

[39] F. G. Botes, J. W. Niemantsverdriet, and J. van de Loosdrecht, "A comparison of cobalt and iron based slurry phase Fischer–Tropsch synthesis," *Catalysis Today,* vol. 215, pp. 112-120, 2013.

[40] A.-G. Collot, "Matching gasification technologies to coal properties," *International Journal of Coal Geology,* vol. 65, pp. 191-212, 2006.

[41] R. L. Espinoza, a. P. Steynberg, B. Jager, and a. C. Vosloo, "Low temperature Fischer–Tropsch synthesis from a Sasol perspective," *Applied Catalysis A: General,* vol. 186, pp. 13-26, 1999.

[42] A. Steynberg and M. Dry, *Fischer-Tropsch Technology*: Elsevier Science, 2004.

[43] M. Dry, "The fischer-tropsch process-commercial aspects," *Catalysis today,* vol. 9570, 1990.

[44] J. Xu and G. Froment, "Methane steam reforming, methanation and water-gas shift: I. Intrinsic kinetics," *AIChE Journal,* vol. 35, pp. 88-96, 1989.

[45] W. Mitchell, J. Thijssen, and J. M. Bentley, "Development of a Catalytic Partial Oxidation/Ethanol Reformer for Fuel Cell Applications," *Society of Automotive Engineers,* vol. Paper No.9, 1995.

[46] M. Bradford and M. Vannice, "Catalytic reforming of methane with carbon dioxide over nickel catalysts II. Reaction kinetics," *Applied Catalysis A: General,* vol. 142, pp. 97-122, 1996.

[47] K. Kusakabe, K.-I. Sotowa, T. Eda, and Y. Iwamoto, "Methane steam reforming over Ce–ZrO_2-supported noble metal catalysts at low temperature," *Fuel Processing Technology,* vol. 86, pp. 319-326, 2004.

[48] a. Berman, R. K. Karn, and M. Epstein, "Kinetics of steam reforming of methane on Ru/Al_2O_3 catalyst promoted with Mn oxides," *Applied Catalysis A: General,* vol. 282, pp. 73-83, 2005.

[49] P. Wu, X. Li, S. Ji, B. Lang, F. Habimana, and C. Li, "Steam reforming of methane to hydrogen over Ni-based metal monolith catalysts," *Catalysis Today,* vol. 146, pp. 82-86, 2009.

[50] A. J. de Abreu, A. F. Lucrédio, and E. M. Assaf, "Ni catalyst on mixed support of CeO_2–ZrO_2 and Al_2O_3: Effect of composition of CeO_2–ZrO_2 solid solution on the methane steam reforming reaction," *Fuel Processing Technology,* vol. 102, pp. 140-145, 2012.

[51] H.-S. Roh, I.-H. Eum, and D.-W. Jeong, "Low temperature steam reforming of methane over Ni–$Ce_{(1-x)}Zr_{(x)}O_2$ catalysts under severe conditions," *Renewable Energy,* vol. 42, pp. 212-216, 2012.

[52] D. A. Wood, C. Nwaoha, and B. F. Towler, "Gas-to-liquids (GTL): A review of an industry offering several routes for monetizing natural gas," *Journal of Natural Gas Science and Engineering,* vol. 9, pp. 196-208, 2012.

[53] M. E. Dry, "The Fischer-Tropsch process: 1950-2000," *Catalysis Today,* vol. 71, pp. 227-241, 2002.

[54] H. Schulz, G. Schaub, M. Claeys, and T. Riedel, "Transient initial kinetic regimes of Fischer–Tropsch synthesis," *Applied Catalysis A: General,* vol. 186, pp. 215-227, 1999.

[55] R. Deverell and M. Yu, "Long Run Commodity Prices: Where do we stand?," Credit Suisse27 July, 2011 2011.

[56] D. Leckel, "Diesel Production from Fischer−Tropsch: The Past, the Present, and New Concepts," *Energy & Fuels,* vol. 23, pp. 2342-2358, 2009/05/21 2009.

[57] A. de Klerk, *Fischer-Tropsch Refining*. Weinheim: Wiley-VCH Verlag & Co. KGaA, 2012.

[58] L. Sehabiague, "Modeling, Scaleup and Optimization of Slurry Bubble Column Reactors for Fischer-Tropsch Synthesis," Doctoral Dissertation, Department of Chemical and Petroleum Engineering, University of Pittsburgh, 2012.

[59] D. Gray, A. Elsawy, G. Tomlinson, G. J. Stiegel, and R. D. Srivastava, *Proceedings of the DOE Liquefaction Contractors' Review Meeting,* p. 344, 1991.

[60] A. Raje, J. R. Inga, and B. H. Davis, "Fischer-Tropsch synthesis: Process considerations based on performance of iron-based catalysts," *Fuel,* vol. 76, pp. 273-280, February 1997 1997.

[61] H. Hikita, S. Asai, K. Tanigawa, K. Segawa, and M. Kitao, "Gas hold-up in bubble columns," *The Chemical Engineering Journal,* vol. 20, pp. 59-67, 1980.

[62] I. G. Reilly, D. S. Scott, T. J. W. de Bruijn, and D. MacIntyre, "The Role of Gas Phase Momentum in Determining Gas Holdup and Hydrodynamic Flow Regimes in Bubble Column Operations," *Canadian Journal of Chemical Engineering,* vol. 72, pp. 3-13, 1994.

[63] A. Behkish, R. Lemoine, L. Sehabiague, R. Oukaci, and B. I. Morsi, "Gas holdup and bubble size behavior in a large-scale slurry bubble column reactor operating with an organic liquid under elevated pressures and temperatures," *Chemical Engineering Journal,* vol. 128, pp. 69-84, 1 April 2007 2007.

[64] P. M. Wilkinson and L. L. v. Dierendonck, "Pressure and gas density effects on bubble break-up and gas hold-up in bubble columns," *Chemical Engineering Science,* vol. 45, pp. 2309-2315, 1990.

[65] K. N. Clark, "The effect of high pressure and temperature on phase distributions in a bubble column," *Chemical Engineering Science,* vol. 45, pp. 2301-2307, 1990.

[66] U. Jordan, K. Terasaka, G. Kundu, and A. Schumpe, "Mass transfer in High-Pressure Bubble Columns with Organic Liquids," *Chemical Engineering & Technology,* vol. 25, pp. 262-265, 2002.

[67] T. Sauer and D.-C. Hempel, "Fluid dynamics and mass transfer in a bubble column with suspended particles," *Chemical Engineering & Technology,* vol. 10, pp. 180-189, 1987.

[68] L. S. Fan, G. Q. Yang, D. J. Lee, K. Tsuchiya, and X. Luo, "Some aspects of high-pressure phenomena of bubbles in liquids and liquid–solid suspensions " *Chemical Engineering Science,* vol. 54, pp. 4681-4709, 1999.

[69] K. Akita and F. Yoshida, "Gas Holdup and Volumetric Mass Transfer Coefficient in Bubble Columns. Effects of Liquid Properties," *Industrial & Engineering Chemistry Process Design and Development,* vol. 12, pp. 76-80, 1973/01/01 1973.

[70] K. Koide, A. Takazawa, M. Komura, and H. Matsunaga, "Gas holdup and volumetric liquid-phase mass transfer coefficient in solid-suspended bubble columns," *Journal of Chemical Engineering of Japan,* vol. 17, pp. 459-466, 1984.

[71] K. Akita and F. Yoshida, "Bubble size, Interfacial Area, and Liquid-Phase Mass Transfer Coefficient in Bubble Columns," *Industrial & Engineering Chemistry Process Design and Development,* vol. 13, pp. 84-91, 1974.

[72] M. Jamialahmadi and H. Müller-Steinhagen, "Effect of Solid Particles on Gas Hold-Up in Bubble Columns," *Canadian Journal of Chemical Engineering,* vol. 69, pp. 390-393, 1991.

[73] S. Kara, B. G. Kelkar, Y. T. Shah, and N. L. Carr, "Hydrodynamics and axial mixing in a three-phase bubble column," *Industrial & Engineering Chemistry Process Design and Development,* vol. 21, pp. 584-594, 1982/10/01 1982.

[74] B. G. Kelkar, Y. T. Shah, and N. L. Carr, "Hydrodynamics and axial mixing in a three-phase bubble column. Effects of slurry properties," *Industrial & Engineering Chemistry Process Design and Development,* vol. 23, pp. 308-313, 1984.

[75] H. Kojima, J. Sawai, and H. Suzuki, "Effect of pressure on volumetric mass transfer coefficient and gas holdup in bubble column," *Chemical Engineering Science,* vol. 52, pp. 4111-4116, 1997.

[76] A. Behkish, Z. Men, J. R. Inga, and B. I. Morsi, "Mass transfer characteristics in a large-scale slurry bubble column reactor with organic liquid mixtures," *Chemical Engineering Science,* vol. 57, pp. 3307-3324., 2002.

[77] D. B. Bukur, S. A. Patel, and J. G. Daly, "Gas holdup and solids dispersion in a three-phase slurry bubble column," *AIChE Journal,* vol. 36, pp. 1731-1735, 1990.

[78] A. Schumpe, A. K. Saxena, and L. K. Fang, "Gas/liquid mass transfer in a slurry bubble column," *Chemical Engineering Science,* vol. 42, pp. 1787-1796, 1987.

[79] P. M. Wilkinson, A. P. Spek, and L. L. van Dierendonck, "Design Parameters Estimation for Scale-up of High-Pressure Bubble Columns," *AIChE Journal,* vol. 38, pp. 544-554, 1992.

[80] F. Yoshida and K. Akita, "Performance of Gas Bubble Columns: Volumetric Liquid-Phase Mass Transfer Coefficient and Gas Holdup," *AIChE Journal,* vol. 11, pp. 9-13, 1965.

[81] U. Jordan and A. Schumpe, "The gas density Effect on Mass Transfer in Bubble Columns with Organic Liquids," *Chemical Engineering Science,* vol. 56, pp. 6267-6272, 2001.

[82] S. C. Saxena, N. S. Rao, and P. R. Thimmapuram, "Gas Phase Holdup in Slurry Bubble Column for Two- and Three-Phase Systems," *The Chemical Engineering Journal,* vol. 49, pp. 151-159, 1992.

[83] W. O'Dowd, D. N. Smith, J. A. Ruether, and S. C. Saxena, "Gas and solids behavior in a baffled and unbaffled slurry bubble column," *AIChE Journal,* vol. 33, pp. 1959-1970, 1987.

[84] J. Chen, F. Li, S. Degaleesan, P. Gupta, M. H. Al-Dahhan, M. P. Dudukovic, *et al.*, "Fluid dynamic parameters in bubble columns with internals," *Chemical Engineering Science,* vol. 54, pp. 2187-2197, 1999.

[85] F. Yamashita, "Effects of Vertical Pipe and Rod Internals on Gas Holdup in Bubble Columns," Journal of Chemical Engineering of Japan, vol. 20, pp. 204-206, 1987.

Chapter 10

Ion Exchange Fundamentals and New Challenges

Maria Angélica Simões Dornellas de Barros, Marcelino Luiz Gimenes,
Melissa Gurgel Adeodato Vieira and Meuris Gurgel Carlos da Silva

Additional information is available at the end of the chapter

http://dx.doi.org/10.5772/60864

Abstract

Ion exchange is a stoichiometric phenomenon commonly used in water treatment as an end-of-pipe technique. Such process is highly influenced by mass transfer conditions and may be modeled by adsorption equations. Although widely applied in industries its theory has not been completely understood and depends on the exchanger characteristics. Moreover, competitive systems may add complexity and decrease removal efficiency and exchanger selectivity mainly in dynamic systems. In this chapter some general theory was presented and some detailed examples involving alginate biopolymer, bonechar and zeolite in single and competitive systems were discussed in batch and continuous state.

Keywords: ion exchange, kinetics, equilibrium data, fixed bed, multicomponent systems

1. Introduction

Ion exchange processes are the processes in which a solid phase (ion exchanger) reacts in a double exchange reaction when in contact with a liquid phase with electrolytes. Actually, this should not be considered as a true chemical reaction as it involves the redistribution of ions between two phases by diffusion. Chemical factors are almost negligible with small amount of heat, often less than 2 kcal/mol [1].

In an ion exchange process, the balancing ion (the one previously detected in the solid phase) is replaced by the counter ion (previously in the liquid phase) always when the exchange has a higher affinity to the counter ion. It is important to emphasize that the stoichiometric replacement involves charges. Nevertheless, normality is much more adequate to describe the phenomenon than molarity. Figure 1 presents examples of the monovalent and divalent exchange processes. In this diagram, it is easy to see the importance of charges in the stoichiometric process.

The first citation of an application of ion exchange can be found in Aristotle's, but the ion exchange processes became well known in the nineteenth century. In the 1930s, they were strengthened when organic cation exchangers were discovered. Nowadays, anion exchange resins are also commercially obtained [2].

Ion exchange is considered as an end-of-pipe technique used in wastewater and one of the best available techniques to remove heavy metal ions, which is of a great concern due to the toxic compounds constantly presented in bodies of water.

With such general aspects in mind, this chapter has the main goal to discuss the ion exchange phenomenon through already published results. Theory and fundamental aspects will be briefly revised.

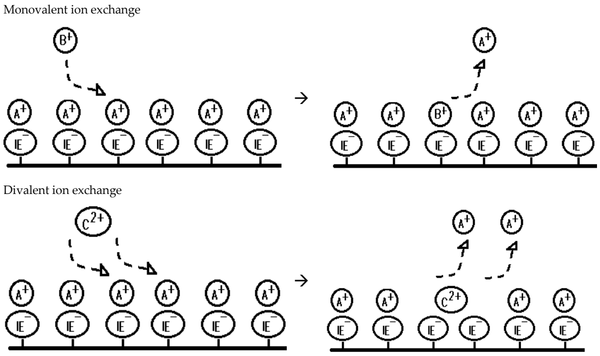

Figure 1. Cationic exchange examples. IE⁻ is the ionic exchanger charge. A is the balancing cation, B is the monovalent counter ion, and C is the divalent counter ion.

2. General theory

Ion exchange is generally controlled by diffusion, a consequence of the material structure. Ion exchange framework, size of the beads, and any other physical chemistry characteristics have important roles in this process. Nevertheless, in all cases, it is accomplished by transfer of ions to and from the interphase boundary, the exchange itself followed by the diffusion of the ion inside the solid phase and the diffusion in the surrounding solution.

Actually, the ion exchange process occurs in the following steps [2]:

1. Dissociation of the electrolytes in the bulk phase, originating the denominated counter ion
2. Diffusion of the counter ion from the bulk phase towards the interphase film
3. Diffusion of the counter ion through the interphase film
4. Diffusion of the counter ion inside the ion exchanger

5. Association between the counter ion and the functional group of the exchanger
6. Dissociation of the balancing ion and functional group of the exchanger
7. Diffusion of the balancing ion inside the exchanger towards the surface
8. Diffusion of the balancing ion through the interphase film
9. Diffusion and random distribution of the balancing ion in the bulk phase
10. Formation of the balancing ion complexes in the solution

Basically, the mechanism of ion exchange processes has some possible rate-controlling steps. The most important ones are related to steps 3 and 8, 4 and 7, 5 and 6. Steps 3 and 8 deal with film resistance and should be minimized through adequate agitation. The mass transfer in this case is defined by the diffusion coefficients. Steps 4 and 7 are related to intraparticle diffusion and depend on the physic-chemical properties of the system. Small particles of the ion exchanger may decrease such resistances. Steps 5 and 6 are the ion exchange processes properly. Almost always, the film and/or intraparticle resistances are considered the most important rate-controlling steps. Many kinetic models take into account these characteristics. More information regarded to kinetics can be seen elsewhere [3, 4]. The regeneration of the saturated ion exchanger may be also modeled [5]. It must be emphasized that many models are used to describe both adsorption and ion exchange mechanisms. Despite of the mathematical similarity, the significant differences related to these mechanisms should be in mind.

Besides kinetic data, ion exchange equilibrium data are also of great value. Isotherms may be classified in five different types [6], as shown in Figure 2.

Isotherm shapes indicate whether or not the ion is solution is preferably exchanged. However, they provide no information on the type of exchange sites or even whether they have similar energies. This is outstanding information as it is directly related to the ion exchange mechanism. The Kielland plot is an interesting thermodynamic tool to understand such process. Ion selectivity and the thermodynamic properties may be obtained from such data.

The Kielland plot may be obtained through log $K\,|_{B}^{A}$ (equilibrium constant through the balancing ion A and the counter ion B) and $x_{A(Z)}$. Linear Kielland plots are a consequence of exchangers with only one kind of exchange site [7]. Nonlinear plots indicate different sites and different cavities where the exchanged cation occupies different positions in the framework [6].

Although batch operations where isotherms may be obtained are rarely used in industries, they are very common when investigating mechanisms such as the ones in equilibrium through isotherms. Continuous systems are almost often well suited for industrial purposes when scale-up process is needed. Continuous ion exchange uses packed beds where the mass transfer is of great importance. As the feed solution passes through the ion exchange packed bed, the outlet solution has different concentrations of the incoming ion as a function of time. Plots of the ratio outlet concentration of the incoming ion/concentration of the incoming ion in the feed solution versus time are well known as breakthrough curve. Mass balances in the column as well as the mass transfer parameters are reported elsewhere [8,9].

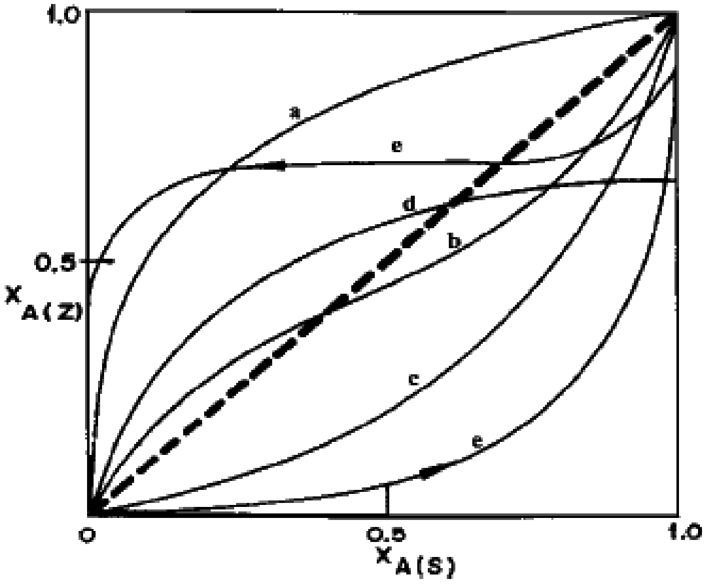

Figure 2. Ion exchange isotherms: $x_{a(z)}$: equivalent fraction of the counter ion in the exchanger; $x_{a(s)}$: equivalent fraction of the counter ion in solution [6]. (a) Favorable isotherm; (b) isotherm with reversal behavior, from favorable to unfavorable; (c) unfavorable isotherm; (d) incomplete favorable isotherm; (e) isotherm with hysteresis.

Besides the use of adsorption models, ion exchange systems may be more correctly represented by the mass action law (MAL). This is the most characteristic property of ion exchange and can be used as one of the possible modeling equations. Actually, it expresses the typical double exchange reaction where the balancing ion in the exchanger is replaced by the in-going ion according to the stoichiometry.

MAL is based on the definition of the chemical equilibrium of the chemical reactions first proposed by Cato Guldberg and Peter Waage in 1864. It was defined as the equilibrium constant *K*, which is the relationship of the activity coefficient of reagents and products in equilibrium at a given temperature.

If the chemical reaction presented in Eq. (1) is considered:

$$bB + cC \rightarrow dD + eE \tag{1}$$

The equilibrium constant may be written as follows:

$$K = \frac{\left[a_D\right]^d \cdot \left[a_E\right]^e}{\left[a_B\right]^b \cdot \left[a_C\right]^c} \tag{2}$$

http://dx.doi.org/10.5772/60864

where *a* stands for the ionic activity of each ion presented in Eq. (1).

It is obvious that monocomponent ion exchange only occurs when the solid in is contact with synthetic solutions. Other solutions, mainly wastewaters, always contain significant amount or other ions that may be also exchanged. That is why selectivity and affinity properties of the ion exchanger in relation to the specific incoming ion should be considered no matter if it is continuous or batch system. Of course, in such a case, modeling is more complex. Some examples of MAL can be seen in reference [10].

3. Ion exchangers

Ion exchangers are porous matrixes from different sources, with positive or negative excess charge, insoluble in aqueous solutions and in many organic solvents. The excess charge of the matrix should be compensated by the balancing ions, which may be replaced by the in-going ion depending on the selectivity and affinity of the exchanger to the ions involved.

Mechanical resistance as well as regeneration capacity is quite important when packed beds are considered. There are acid and basic exchangers being the anionic exchangers that have basic superficial groups and cationic exchangers those containing superficial acid groups. Exchangers may be also classified according to complete or incomplete dissociation based on the pH range where the exchange process is efficient.

Ion exchangers can be natural such as alginate, clay, algae, or even some zeolites. Alginate occurs in seaweeds as calcium alginate and is present in the cells of brown algae. Actually, the term alginate designates salts of alginic acid and its derivatives.

Clays are fine powders constituted by hydrated aluminosilicates that often tend to agglomerate. In clay materials alumina is presented in octahedral form whereas silica is found as tetrahedrons. Such materials are thermally stable and can be greatly improved by pillaring process. Zeolites are also aluminosilicates. Nevertheless, they have an open three-dimensional framework with interconnecting cavities. Both materials can be used as adsorbents, ion exchangers, catalysts, or catalysis support.

Natural exchangers have some disadvantages such as low exchange rate and rather poor mechanical properties and low abrasion resistance, which restrict their application, mainly in packed beds without any previous treatment.

Exchangers obtained specifically from synthetic materials are available commercially being. Zeolites and resins are the most famous representatives of such class. Many zeolites are related to cationic exchange process. Nevertheless, zeolites can act as anionic exchangers if tailored.

Resins are known since 1935. They can be used as ion exchangers or catalysts. Ion exchange resins may be found as in acids and bases, acting, therefore, as anionic or cationic exchangers. Cationic resins generally contain sulfonic acid groups, whereas anionic resins are commonly found in quaternary ammonium groups.

4. Experimental results of ion exchange

4.1. Case study: Metallic ion in calcium alginate biopolymer

4.1.1. Copper kinetics study of calcium alginate particles in a static system

Calcium alginate biopolymer was prepared by dropping sodium alginate into solution of calcium chloride (3% w/w) under continuous agitation. Calcium alginate particles formed (mean diameter, 1083 μm) were washed and dried to be used in adsorption/ion exchange experiments [11].

Kinetic studies were carried out using single nitrate solutions of Cu^{2+}, Cd^{2+}, Pb^{2+}, and Ni^{2+} of 3 mmol/L (Vetec, Brazil) and a bicomponent equimolar solution of $Cu^{2+}$and Cd^{2+} (1 mmol/L for each metal). Values of pH were corrected using NH_4OH and HNO_3.

All runs were conducted in finite baths at 25°C using 1 g of alginate immersed in 0.1 L of metallic solutions. Samples of these solutions were taken at different running times, and after filtration, the concentration of solutions was analyzed through atomic absorption spectrophotometry.

Mathematical modeling of the ion diffusion process in ion exchanger provided relevant information on mass transfer that is essential to the ion exchange/adsorption system design. The diffusion process in a solid matrix was described for the second Fick's law. In the spherical coordinate system, the concentration gradients are negligible in the angular direction, and the second Fick's law is represented by Eq. (3):

$$\frac{\partial q}{\partial t} = D_e \frac{1}{r} \frac{\partial}{\partial} \left(r \frac{\partial q}{\partial r} \right) \tag{3}$$

where q is the ion capacity in ion exchanger (mg/g), D_e is the ion diffusion coefficient in the adsorbent/ion exchanger (cm^2/s), t is time (s), and r is the radial direction (cm).

In this modeling, it was considered that the adsorbent was initially free of metal, the ion diffusivity was constant, the concentration in the fluid phase was homogeneous, and external resistance in the liquid film was negligible due to the agitation. The initial and boundary conditions used are described by Eqs. (4)–(6):

$$\text{at } t = 0 : q = q_0 \tag{4}$$

$$\text{at } r = R \text{ and } t > 0 : q = 0 \tag{5}$$

http://dx.doi.org/10.5772/60864

$$\text{at } r = \; 0 \frac{\partial q}{\partial r} = 0 \tag{6}$$

The average concentration of the metal ion exchanger is given by Eq. (7):

$$\frac{\bar{q}(t) - q_{\text{eq}}}{q_0 - q_{\text{eq}}} = 6 \sum_{j=1}^{\infty} \left(\frac{1}{\gamma_j^2} e^{-\gamma_j Fo_{\text{M}}} \right) \tag{7}$$

where

$$Fo_{_M} = \frac{D_{\text{ef}} t}{R^2}; \gamma_j = j\pi$$

where γ is the j component of the activity coefficient, D_{ef} is the effective diffusivity (m^2/s), and R is the radius of the particle (m).

The metal concentration in the fluid phase is obtained from an overall mass transfer balance, represented by Eq. (8):

$$C(t) = \left(C_0 V - m_s \bar{q}(t) \right) / V \tag{8}$$

where C_0 is the initial concentration of metal in the fluid phase (mg/L), $\bar{q}$ is the metal incoming average capacity in the adsorbent ($\text{mg}_{\text{metal}}/\text{g}_{\text{alginate}}$), m_{s} is the mass of bioadsorbent/ion exchanger (g dry basis), and V is the volume of the solution (dm^3).

The method "golden search" was used to determine the effective diffusion coefficient of ions in bioadsorbent/ion exchanger to minimize the objective function given by Eq. (9):

$$F_{\text{obj}} = \sum_{j=1}^{n} \left(C_j^{\text{MOD}} - C_j^{\text{EXP}} \right)^2 \tag{9}$$

where n is the number of experimental data, C_j^{EXP} is the ion concentration in solution determined experimentally (mEq/L), and C_j^{MOD}: ion concentration in the solution calculated by the model (mg)

Figure 3 shows experimental results of the kinetics of the process and results obtained with the mathematical modeling for different metals in this study. The metal ions nickel, lead, and copper showed adsorption and desorption, indicating the competitiveness of metal ions (with calcium present in alginate) by the occupation of the active sites. The model used does not consider this competitiveness, but only the adsorption of the ions of interest, resulting in slightly different values when compared to the experimental data.

Table 1 shows the quantities of metal ions removed from the single solutions by adsorption/ion exchange process. It appears that nickel was less adsorbed (0.92 mmol Ni/$g_{\text{calcium alginate}}$) in equilibrium. Indeed, alginic acid has a greater affinity for calcium than for nickel [12]. In a study of removal of different metals using calcium alginate, it was obtained the following amounts adsorbed: 0.247 mmol Cu/g, 0.138 mmol Cd/g, and 0.247 mmol Pb/g [13]. Although the conditions used were different from those used in this work, it can be seen that the alginate showed the same order of adsorptive capacity, or $Cu^{2+} > Pb^{2+} > Cd^{2+}$; in the case of this study (Table 1), it was $Cu^{2+} > Pb^{2+} > Cd^{2+} > Ni^{2+}$.

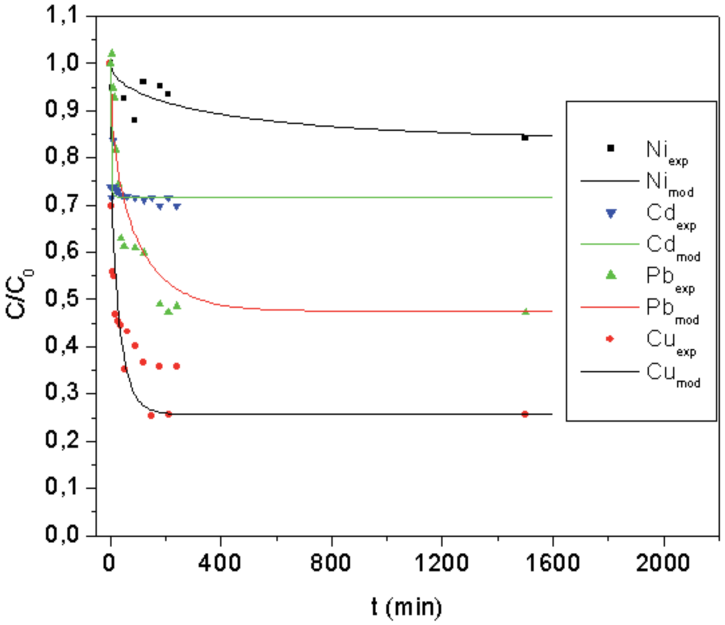

Figure 3. kinetic curves for different metal ions in monocomponent solutions for the adsorption/ion exchange into calcium alginate particles.

Copper	Cadmium	Nickel	Lead
4.658	1.792	0.987	3.106

Table 1. Adsorbed amount ($mmol_{metal}/g_{alginate}$) of different metals in the process of adsorption/ion exchange using single solutions.

The results obtained in finite bath for copper-cadmium binary mixture are shown in Figure 4. It is observed that copper was significantly more removed than cadmium. The adsorbed amount of copper and cadmium was 1.746 mmol Cu/$g_{\text{calcium alginate}}$ and 0.661 mmol Cd/g_{calcium}

$_{alginate}$, respectively. The greater affinity of calcium alginate to copper may be due to the chemical parameters listed in Table 2. The higher the electronegativity and the reduction potential and the lower the ionic radius, the easier the ion exchange/adsorption [14]. In this case, copper is more susceptible to ionic interaction with the alginate than cadmium because it presents all the favorable parameters to the ion exchange.

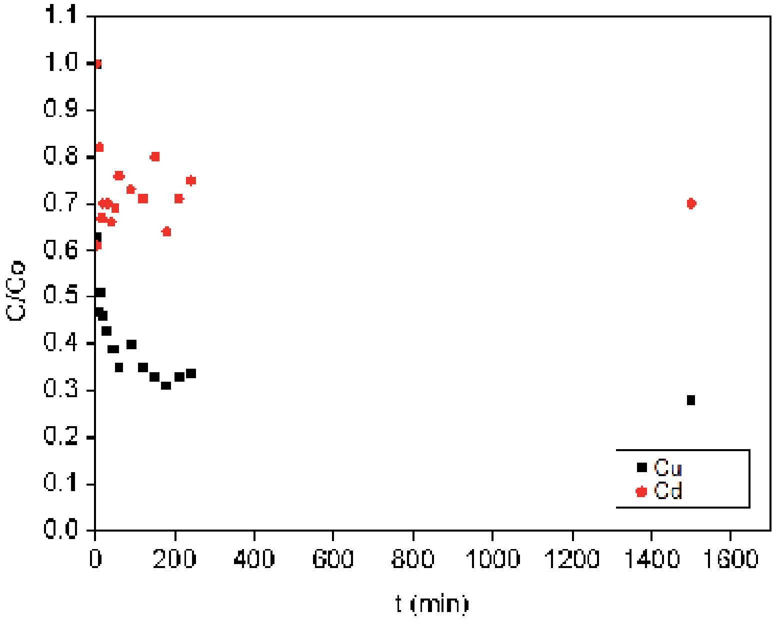

Figure 4. Kinetics of copper and cadmium in binary solution in the adsorption/ion exchange by calcium alginate particles.

	Copper	Cadmium	Lead	Nickel	Calcium
Atomic mass (g/mol)	63.546	112.411	207.200	58.710	40.080
Electronegativity	1.9	1.7	1.8	1.8	1.0
Ionic radius (Å)	0.73	0.97	0.132	0.69	0.99
Chemical reduction potential (V)	0.34	–0.40	–0.13	–0.23	–2.68

Source: reference [11].

Table 2. Chemical properties of divalent cations.

The diffusion capacity of the metal ions in the alginate particles analyzed was evaluated considering the Fick's law, and the respective values are shown in Table 3. It is observed that the cadmium showed higher diffusion capacity, and nickel is the metal resulting in an increased resistance to intraparticle diffusion; thus, the metal adsorption order was $Cd^{2+} > Cu^{2+} > Pb^{2+} > Ni^{2+}$. However, experimental results obtained with single and binary solutions were $Cu^{2+} > Pb^{2+} > Cd^{2+} > Ni^{2+}$ and $Cu^{2+} > Cd^{2+}$, respectively, indicating that this parameter cannot solely describe the metal affinity of alginate. Therefore, it becomes necessary to evaluate other properties of the ion exchanger/adsorbent.

Metal	**Diffusion capacity (cm^2/min)**
Copper	7.44E–06
Cadmium	8.38E–05
Lead	2.19E–06
Nickel	4.57E–07

Table 3. Diffusion capacity of metal ions in calcium alginate.

4.1.2. Copper equilibrium study of calcium alginate particles in a static system

The isotherm of Langmuir model (L) is widely used due to its simplicity and theoretical basis and is expressed by Eq. (10). The parameter b is the ratio between the rate of adsorption and desorption and is directly related to Henry's constant. High values of b indicate high affinity of the ions by the active sites of the material. The parameter $q_{\max}$ indicates the total number of active sites available, and q^* and C^* represent the metal removal capacity at equilibrium in the solid and liquid phases, respectively. Adsorption is very favorable when values of $b.C^* >> 1$; however, if $b.C^* < 1$, the isotherm is almost linear.

$$q^* = \frac{q_{\max} \cdot b \cdot C^*}{1 + b \cdot C^*} \tag{10}$$

The Freundlich isotherm is an empirical adjustment of a model, which considers that the energy of the active sites of the adsorbent material is heterogeneous and that the adsorption process is reversible. It corresponds to the exponential distribution heats of adsorption and is expressed by Eq. (11), where k_d and n are constants in the model. This model does not predict the saturation of the adsorbent, allowing an infinite number of layers covering the ionic adsorbent [15]. When $n < 1$, it is typically a liquid adsorption [16].

$$q^* = k_d \cdot C^{*n} \tag{11}$$

Figure 5 shows the equilibrium data in finite bath by contacting 1 g of hydrated alginate with 100 mL of metal solution with different initial concentrations [11]. The Langmuir isotherm model (Equation 10) and the Freundlich model (Equation 11) were fitted to the experimental equilibrium data as shown in Figure 5, and the respective values of model parameters are presented in Table 4.

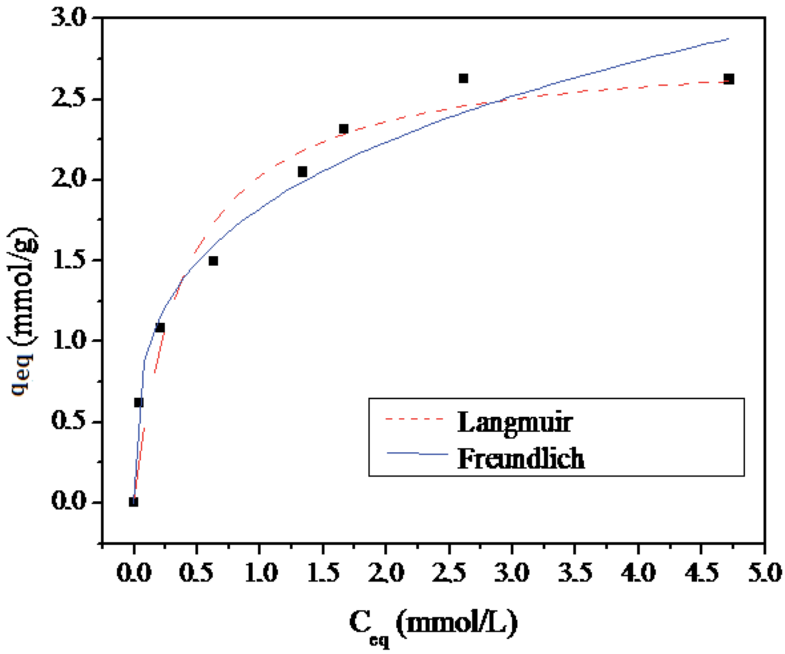

Figure 5. Cu adsorption isotherm in calcium alginate fitted by the Langmuir and Freundlich models.

Langmuir	q_{max} (mg/g)	b (mg/L)	R^2
	2.8323	0.3977	0.9623
Freundlich	k_d	n	R^2
	1.8269	0.2924	0.9739

Table 4. Parameters of Langmuir and Freundlich models.

According to Table 4, both models could satisfactorily adjust the equilibrium experimental data for copper ions. The isotherm obtained in Figure 5 can be classified as type I [17], which is characteristic of the Langmuir isotherm where adsorption occurs only in monolayer. Moreover, these models have also been adequately used to describe the process of removing metal ions using calcium alginate (Ca-Alginate) particles [18,19].

In the ion exchange process involving the binary system of copper and cadmium ions in calcium alginate (systems Cu^{2+}-Ca^{2+}, Cd^{2+}-Ca^{2+}, and Cu^{2+}-Cd^{2+}), it was considered only the presence of the higher affinity ion, or for the Cu^{2+}-Ca^{2+} system, only the presence of Cu^{2+} species, for Cd^{2+}-Ca^{2+}system, the presence of Cd^{2+} species, and for the Cu^{2+}-Cd^{2+} system, the presence of copper [11]. Many single adsorption isotherms were evaluated for the binary systems, as shown in Table 5 and in Figure 6.

Model	**Parameters**	**Equation**
Langmuir	$q_{\max}$, b	$q^* = \dfrac{q_{\max} \cdot b \cdot C^*}{1 + b \cdot C^*}$
Freundlich	$q_{\max}$, n	$q^* = k_d \cdot C^{*n}$
Redlich–Peterson	$q_{\max}$, b, n	$q^* = \dfrac{q_{\max} b C^*}{1 + b C^{*n}}$
Toth	$q_{\max}$, b, n	$q^* = \dfrac{q_{\max} C^* b^{1/n}}{(1 + b C^{*n})^{1/n}}$
Radke–Praunitz	$q_{\max}$, b, n	$q^* = \dfrac{q_{\max} C^* b}{(1 + B C^*)^n}$
Sips	$q_{\max}$, b, n	$q^* = \dfrac{q_{\max} b C^{*n}}{1 + b C^{*n}}$

Table 5. Adsorption isotherm models used for the binary system by considering only the presence of the ion of higher affinity.

Model	**Parameters**	F_{obj}	R^2
Langmuir	$q_{\max}$ (mEq/g) = 14.540 b (L/mEq) = 0.139	0.069	0.990
Freundlich	K (mEq/g) = 2.020 n = 0.658	1.054	0.982
Redlich–Peterson	$q_{\max}$(mEq/g) = 20.7841 b(L/mEq) = 0.091 n = 1.1331	0.56198	0.991
Toth	$q_{\max}$(mEq/g) = 13.207 b(L/mEq) = 0.108 n = 1.1455	0.566	0.990
Radke–Prausnitz	$q_{\max}$(mEq/g) = 40.555 b(L/mEq) = 4.677 n = 2.139	0.549	0.991
Sips	$q_{\max}$(mEq/g) = 25.332 b(L/mEq) = 0.077 n = 0.847	0.592	0.988

Table 6. Parameters obtained for the single component isotherm models for the system Cu^{2+}–Ca^{2+}.

All models resulted in satisfactory determining coefficient values (R^2), indicating proper fit to the experimental data (Table 6).

The Sips model was successfully used to represent the removal of copper and cadmium ions in Ca-Alginate particles, mainly when compared to Langmuir and Freundlich models [19]. It happened due to the heterogeneity of the surface of the adsorbent, especially for metals of lower-affinity with the alginate.

Although in the system involving the Cd^{2+}-Ca^{2+} ions, experimental data have been acceptable adjusted, the interference of calcium on Cd^{2+}-Ca^{2+} system was higher when compared to Cu^{2+}-Ca^{2+}system, indicating that the alginate had a higher affinity for copper than for cadmium [11,20].

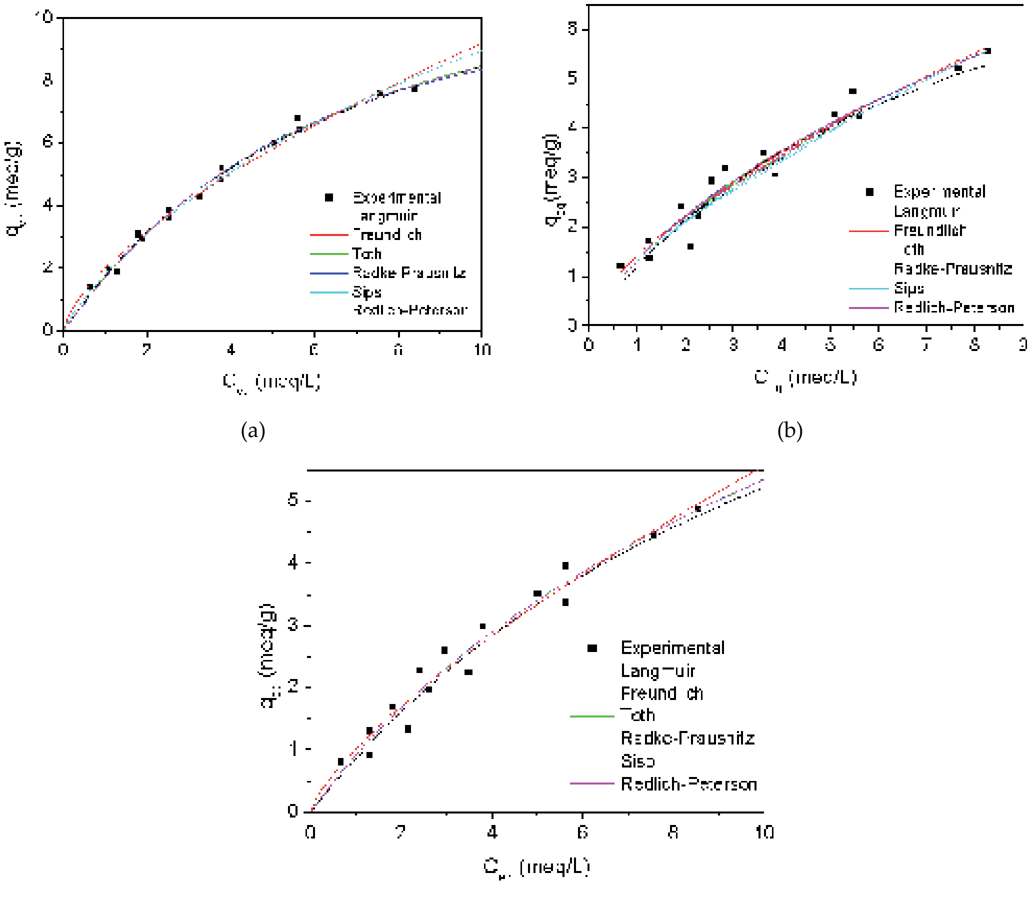

(a)

(b)

(c)

Figure 6. Cu^{2+} adsorption isotherms for Ca-Alginate system (a), Cd-Alginate system (b), and Cd^{2+} adsorption isotherms for Ca-Alginate system (c) in monocomponent system [11,20].

4.1.3. Copper removal in dynamic system: adsorption and desorption cycles

The study of removing copper ions in the calcium alginate particles porous bed column was assessed through adsorption and desorption cycles. The experiments were performed in a glass column (internal diameter, 1.4 cm) filled with 9.80 g of calcium alginate particles to reach a bed height of 13.3 cm. Flow tests were performed with 3 mL/min for adsorption and desorption cycles. The initial concentration of copper used in the adsorption step was 4.72 mmol/L. In the desorption step, calcium chloride solution with a concentration of 18 mmol/L was employed as eluent. The amount of copper removed in the column experiment was calculated by the Eq. (12). The experimental conditions were defined from fluid dynamic preliminary studies.

$$Q = \frac{C_0 F}{1000m} \cdot \int_0^t \left(\frac{C_0 - C}{C_0} \right) \cdot dt \qquad (12)$$

where C_0 is the initial concentration of metal (mmol/L), $C(t)$ is the metal concentration at time t (mmol/L), F is the volumetric flow of the solution (mL/min), m is the mass of alginate (g), Q is the metal removal capacity at time t ($mg_{metal}/g_{bioadsorvente}$), and t is time (min).

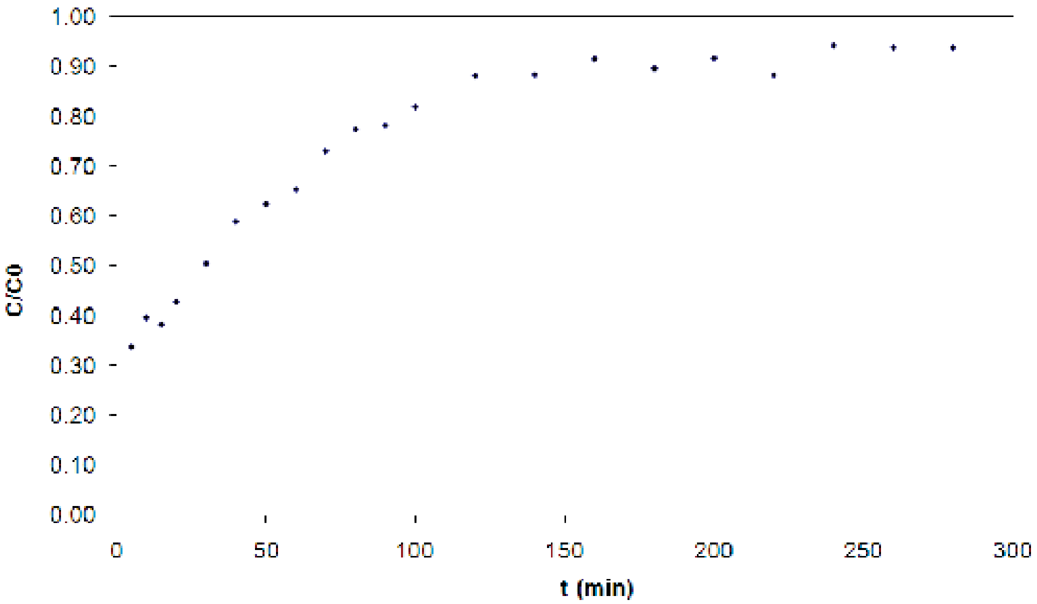

Figure 7. Kinetics of adsorption of copper ions in porous bed (Initial copper concentration 4.72 mmol/L).

Aliquots were withdrawn periodically, and the pH of feed metallic solution was monitored throughout the process, which was maintained between 4 and 4.5. The copper removal kinetics is shown in Figure 7. From the breakthrough curve, the complete saturation of the bed was reached at 140 min of process. The total amount of copper removed given by Eq. (12) was 2.83 mmol/g.

Copper was desorbed from alginate employing calcium chloride solution with a concentration of 18 mmol/L. Initially, it is known that alginate has a greater affinity for copper than the alginate. However, when alginate is saturated with copper ions and comes into contact with a solution containing a high concentration of calcium, copper alginate may desorb ions and adsorb calcium ions to achieve chemical equilibrium. However, in this case, which the ions being adsorbed has a lower affinity, the process occurs only when calcium is present in solution at high concentrations. The kinetics of this process step is in Figure 8. The flow rate used, as well as in adsorption cycle, was 3 mL/min. The calcium alginate recovery was 97%. The equilibrium time of the desorption system was close to 150 min.

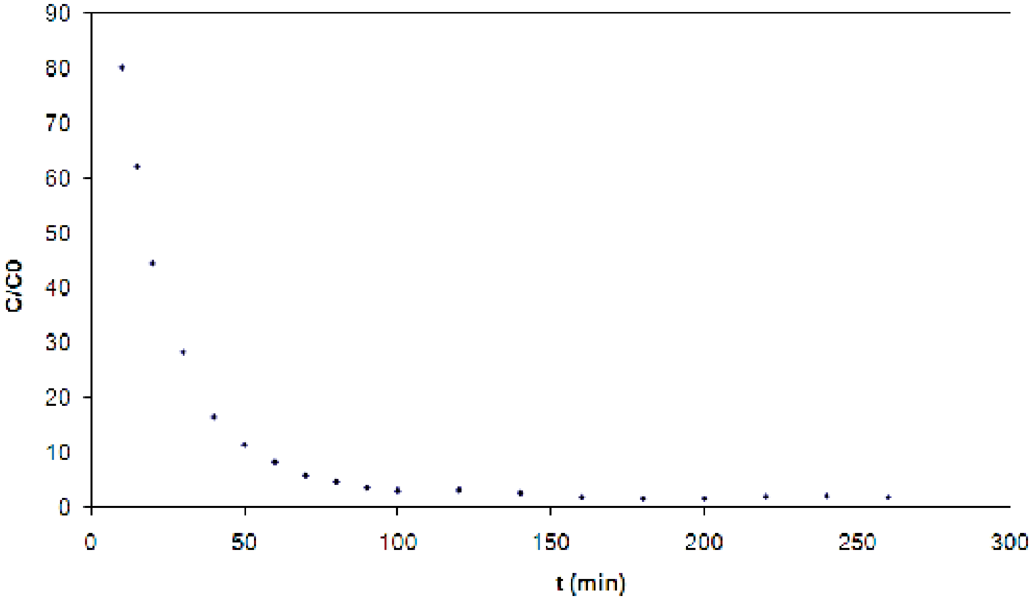

Figure 8. Kinetics of copper desorption in bed of porous calcium alginate particles.

4.2. Case study 2: Equilibrium and dynamic studies of Mn^{2+} and Cr^{3+} in bone char

It is already known that metal ions, like manganese and chromium, when present in wastewaters may contaminate the environment if not adequate treated. In particular, high concentrations of manganese ion in water promote corrosion of pipes, and as this metal is toxic to the brain, it may cause neurological disorders. The hexavalent chromium ion is another highly toxic metal present in wastewater, which is related to cancer diseases. The trivalent chromium specie is less toxic than the hexavalent one, and it can be easily oxidized in wastewater treatment through reduction of manganese ions. The removal of these metals from wastewater can be carried out by adsorption/ion exchange processes using bone char [21].

Bone char is an untypical kind of activated carbon due to its animal origin. It is composed by around 10% carbon and 90% calcium phosphate. Figure 9 illustrates the bone char structure. The calcium phosphate in bone char is present as hydroxyapatite—$Ca_{10}(PO_4)_6(OH)_2$ [22] with a calcium-to-phosphate ratio of 1.67, and unit cell dimensions of $a = b = 9.432$ Å and $c = 6.881$ Å [23].

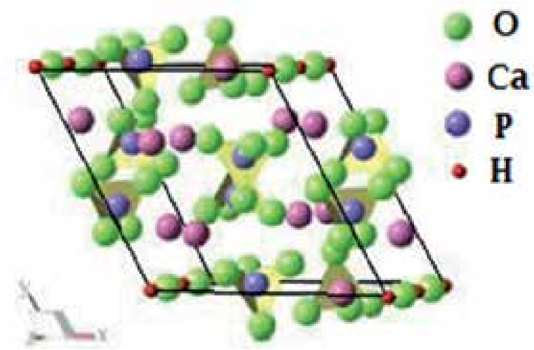

Figure 9. The hydroxyapatite structure viewed along the *c*-axis. The yellow polyhedrons represent the phosphate groups [23].

Cation exchange in bone char may occur preferentially with calcium ions, depending on radius and electronegativity of the incoming ion [24]. Under this consideration, bone char can be quite useful material to be used for removal of both Mn^{2+} and Cr^{3+} through calcium ion exchange.

4.2.1. Materials

The bovine bone char was crushed, sieved (20–28 mesh Tyler, average particle diameter of 0.725 mm), and elutriated with abundant water to remove fine particles and finally dried at 80°C for 24 h. The exchanger particulate material was characterized through N_2 adsorption, scanning electron microscopy (SEM), and infrared spectrophotometry (FTIR). Zero point charge (ZPC) was obtained based on references [25, 26].

Solutions of 15 mEq/L of $CrCl_3.6H_2O$ and $MnCl_2.4H_2O$ were used in single metal removal. Binary solutions containing 7.5 mEq/L of each cation were also used.

4.2.2. Results and discussion

N_2 isotherm showed that the bone char was predominantly mesoporous material with hysteresis and a BET area of 100 $m^2/$ g, which is a typical for this kind of solid material (Figure 10).

Scanning electron microscopy (SEM) of the bone char sample (Figure 11) presented heterogeneity morphology of particles and channels similar to results already reported [27].

FTIR spectrum presented in Figure 12 depicts a characteristic band at 1380 cm^{-1} attributed to $^{v}NO_3$ group, bands at 3450 cm^{-1}, 603 cm^{-1} due to –OH group vibration, band at 1640 cm^{-1} due

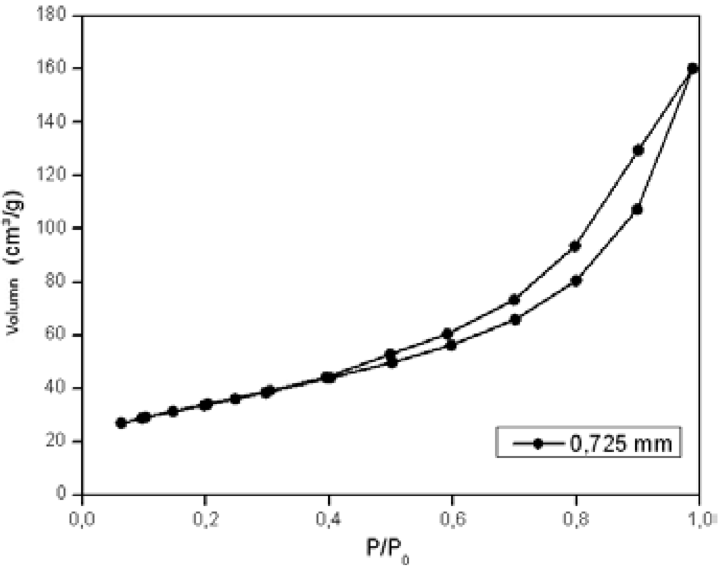

Figure 10. Nitrogen adsorption–desorption isotherm at 77K of bone char.

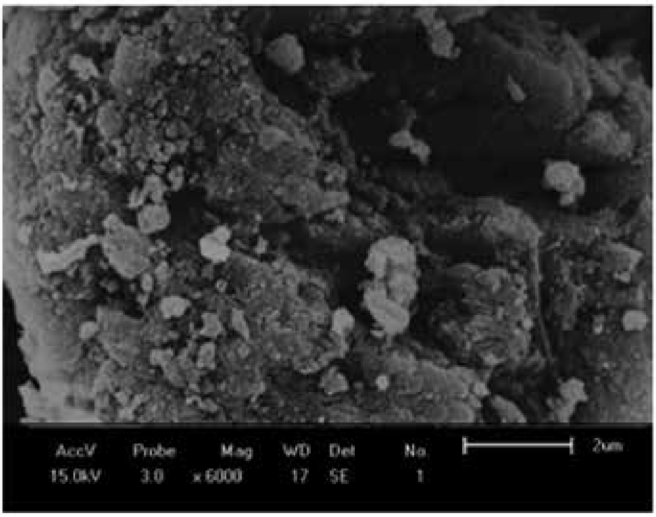

Figure 11. Micrograph obtained by SEM of the bone char.

to $CO_3{}^{2-}$, and a band at 1038 cm^{-1} attributed to the molecular vibration of PO_4^{3-} [22]. The balancing cations of such groups may be exchanged when in contact with electrolyte solutions.

The superficial zero point charge (ZPC) was pH 7.9. As the pH values solutions was 5–6, the surface charge was predominated by positively charged $\equiv CaOH_2^+$ and neutral $\equiv POH^0$ sites. The surface charge was then positive [28].

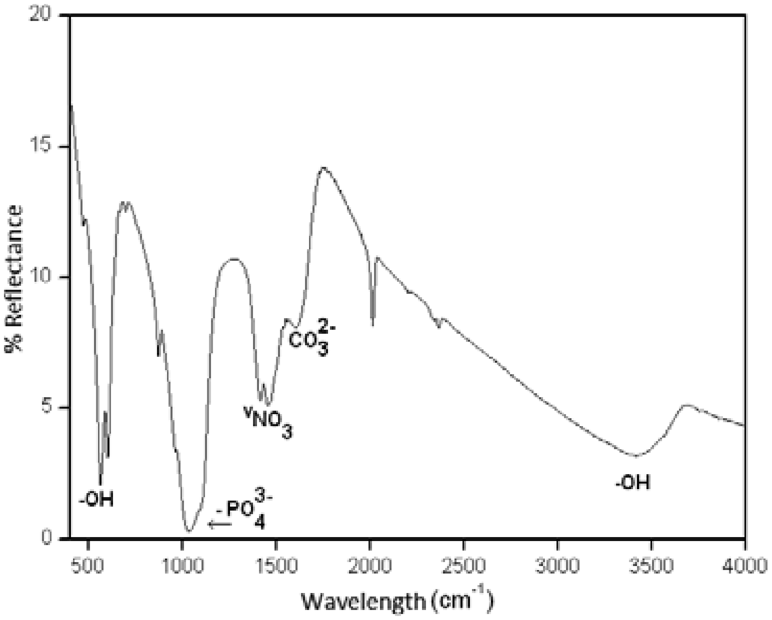

Figure 12. FTIR Spectrum of the bone char samples.

Single and bicomponent isotherms were obtained at 25°C, 30°C, and 40°C. Although bone char is a typical ion exchanger, ions may be also retained by adsorption mechanism. Actually, it is difficult to find out an equation that presents, mathematically, the contribution of all phenomena involved. Classical adsorption equations such as the Langmuir, Freundlich, and Langmuir–Freundlich models are commonly used [2].

Single isotherms are shown in Figure 13. Chromium isotherms are more favorable than the manganese ones. This can be seen through the steeper shape and higher amounts of ion retained, which is a consequence of higher ion charge and electronegativity [24].

Temperature seemed to have a higher influence in chromium removal when temperature was increased to 40°C. Probably, a reduction of the hydration radius occurred exposing the electronegativity and promoting the exchange process. According to the amount retained observed qualitatively in all temperatures, the selectivity order is $Cr^{3+} > Mn^{2+}$.

Cr^{3+} and Mn^{2+} ions may be located in site II, at the edge of the hydroxide channel of the hydroxyapatite. In site II, there would be a shift of the ion. In site I, Cr^{3+} and Mn^{2+} ions would be compressed within the local cluster.

The ion exchange process may be expressed as follows [24]:

$$\mathrm{CaHOAP} + \mathrm{Mn}^{2+} = \mathrm{MnHOAP} + \mathrm{Ca}^{2+}$$

$$3\mathrm{CaHOAP} + 2\mathrm{Cr}^{3+} = \mathrm{Cr}_2\left(\mathrm{HOAP}\right)_3 + 3\mathrm{Ca}^{2+}$$

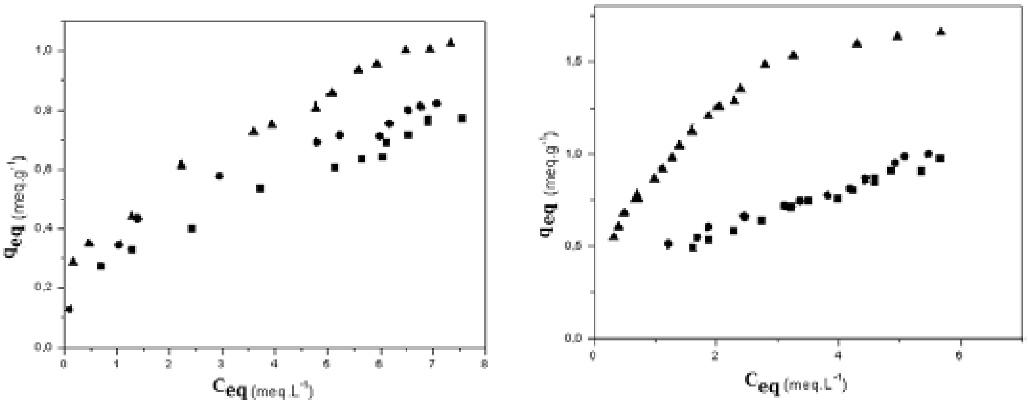

a) b)

Figure 13. (a) Mn^{2+} isotherms; (b) Cr^{3+} isotherms. (■)25°C, (▲) 30°C, (●) 40°C.

Due to pH < ZPC, replacements below may also happen:

$$\equiv POH^0 + Mn^{2+} = \equiv POMn^+ + H^+$$
$$\equiv POH^0 + Cr^{+3} = \equiv POCr^{+2} + H^+$$

Moreover, besides the ion exchange, the multilayer adsorption may occur as the typical plateau of ion exchange monolayer is not seen in the isotherms. In agreement with such phenomena, experimental data may be better represented by the Langmuir–Freundlich isotherms [29]. Tables 7 and 8 show such results.

Parameter	**25°C**	**30°C**	**40°C**
		Langmuir	
q_{max}	0.885 ± 0.073	0.986 ± 0.036	0.962 ± 0.076
B	0.495 ± 0.136	0.539 ± 0.066	1.258 ± 0.523
R^2	0.9136	0.9787	0.8199
	Freundlich		
k_f	0.301 ± 0.017	0.342 ± 0.013	0.472 ± 0.023
N	0.446 ± 0.033	0.446 ± 0.023	0.367 ± 0.029
R^2	0.9736	0.986	0.9698
	Langmuir–Freundlich		
q_{max}	1.341 ± 0.573	1.435 ± 0.395	1.796 ± 0.687
B	0.279 ± 0.144	0.321 ± 0.112	0.281 ± 0.138
$1/n$	0.643 ± 0.159	0.714 ± 0.141	0.700 ± 0.134
R^2	0.996	0.993	0.995

Table 7. Equilibrium parameters for manganese ions.

Parameter	**25°C**	**30°C**	**40°C**
	Langmuir		
$q_{\max}$	1.507 ± 0.082	1.305 ± 0.097	1.836 ± 0.066
B	0.287 ± 0.033	0.450 ± 0.087	1.090 ± 0.121
R^2	0.9772	0.9217	0.9612
	Freundlich		
k_f	0.381 ± 0.011	0.444 ± 0.019	0.897 ± 0.020
N	0.531 ± 0.020	0.452 ± 0.031	0.408 ± 0.019
R^2	0.9886	0.9627	0.9678
	Langmuir–Freundlich		
$q_{\max}$	1.792 ± 0.216	1.263 ± 0.589	3.789 ± 0.013
B	0.261 ± 0.036	0.503 ± 0.029	0.318 ± 0.145
$1/n$	0.779 ± 0.052	0.871 ± 0.049	0.571 ± 0.091
R^2	0.987	0.989	0.983

Table 8. Equilibrium parameters for chromium ions.

The binary isotherms are shown in Figure 14. As expected, chromium is again more retained, although the shape of the isotherms is completely different. This is a consequence of competition of both ions for site II.

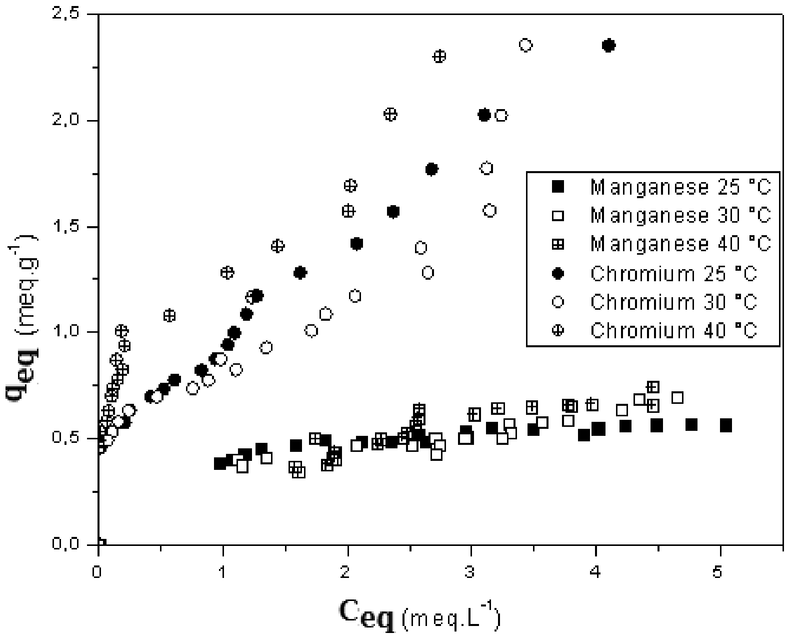

Figure 14. Isotherms for Mn^{2+}/Cr^{3+} binary system in bone char.

Again, the Langmuir–Freundlich model was the one that best represents bicomponent exchange in bone char sample, as seen in Table 9 with the lowest objective function. The parameter b_i for the bicomponent adjustment for the Langmuir–Freundlich model is lower than the ones estimated for the single isotherms due to the competition to site II. Nevertheless, $q_{\max}$ are much higher than the single values, indicating a physisorption process where more ions are retained with weaker energy.

Parameters	**25°C**	**30°C**	**40°C**
		Extended Langmuir [30]	
b_1 (L/mEq)	2.597	0.993	3.000
b_2 (L/mEq)	0.925	0.102	0.007
q_{m1} (mEq/g)	2.914	2.097	2.184
q_{m2} (mEq/g)	0.967	4.121	39.644
Objective function	1.880	1.550	4.287
	Jain and Snowyink [31]		
b_1 (L/mEq)	130.1	11.542	16.16
b_2 (L/mEq)	71.19	0.211	0.047
q_{m1} (mEq/g)	1.222	1.015	1.303
q_{m2} (mEq/g)	0.606	2.304	5.565
Objective function	1.183	0.317	1.658
	Langmuir–Freundlich		
b_1 (L/mEq)	0.296	0.178	0.251
b_2 (L/mEq)	0.394	0.053	0.026
n_1	0.260	0.297	0.203
n_2	0.370	0.550	0.828
q_{m1} (mEq/g)	5.775	6.324	6.045
q_{m2} (mEq/g)	1.592	7.192	10.931
Objective function	0.241	0.148	0.374

Cr^{3+} = subscript 1; Mn^{2+} = subscript 2.

Table 9. Model parameters for Mn^{2+}/Cr^{3+} binary system.

4.3. Case study 3: Dynamic ion exchange in multicomponent solution

Zeolites NaY and NaX are well-known ion exchangers. In this study, these zeolites were used for chromium uptake from bicomponent solutions. As it will be seen, multicomponent ion exchange in dynamic systems may provide some overshooting ($C/C_o > 1$) related to a sequential ion exchange, where a more preferable cation with lower diffusion will be exchanged not by the balancing ion but by the competing ion previously retained [32].

4.3.1. Materials and methods

NaY has the unit cell composition of $Na_{51}(AlO_2)_{51}(SiO_2)_{141}$ on a dry basis, and a cation exchange capacity (CEC) of 3.90 mEq/g NaX zeolite has a unit cell composition of $Na_{81}(AlO_2)_{81}(SiO_2)_{111}$, which corresponds to a higher cation exchange capacity of 5.96 mEq/g.

First, the zeolite samples were added to 1 mol/L solution of NaCl four times at 60°C under stirring. Samples were then washed at the end of each addition with 2 L of hot deionized water and finally oven-dried at 100°C. Such procedure aimed to originate a homoionic sodium zeolite. Samples were pelletized (average diameter size of 0.180 mm).

Reagent-grade $CrCl_3$ $9H_2O$, $MgCl_2$ $6H_2O$, $CaCl_2$ $2H_2O$, and KCl were used to obtain binary solutions, always containing chromium and another cation in an equivalent ratio of 1:1. The concentration of chromium solution was 18 mg/L·.

The dynamic runs were conducted in a packed bed of a clear glass tube 0.9 cm ID and 30 cm long. The zeolite pellets were located in the middle of the column that operated isothermally at 30°C. The packed bed was composed of 1.60 g of NaY or 1.04 g of NaX in order to provide the same cation exchange capacity, whereas the system was fed at 9 mL min^{-1} of ion solution. Although the packed bed heights were different for NaY and NaX zeolites, experiments conducted with the same cation exchange capacity will generate results to compare the performance of the zeolites, mainly when uptake efficiency is aimed.

4.3.2. Results of the dynamic binary runs

Breakthrough curves of metals ions in packed beds of NaY and NaX zeolites are presented in Figures 15 to 17. In all cases, except for the Cr/Mg system in NaX zeolite, some overshooting could be seen as C/C_o reached values higher than 1. In such cases, the incoming ions were first uptaken. As their hydrated radii are smaller than the one for chromium, their diffusion into the zeolitic channels were improved. Rapidly, the incoming ions were exchanged. Chromium ions are much more preferred due to the trivalent charge, and after reaching the exchanging sites, they could replace the ion previously retained.

Besides the sequential ion exchange, it is also important to emphasize the influence of the ion exchanger. NaY and NaX zeolites are isomorph materials, and the only difference between them is the charge density in the packed bed. Denser sites of NaX may promote higher attraction with electrostatic instability due to repulsion of ions closely attracted. As a consequence, the ratio of chromium uptake up to its breakpoint time (tb)/cation exchange capacity (CEC) is less retained than in NaY system, as it can be seen in Table 10.

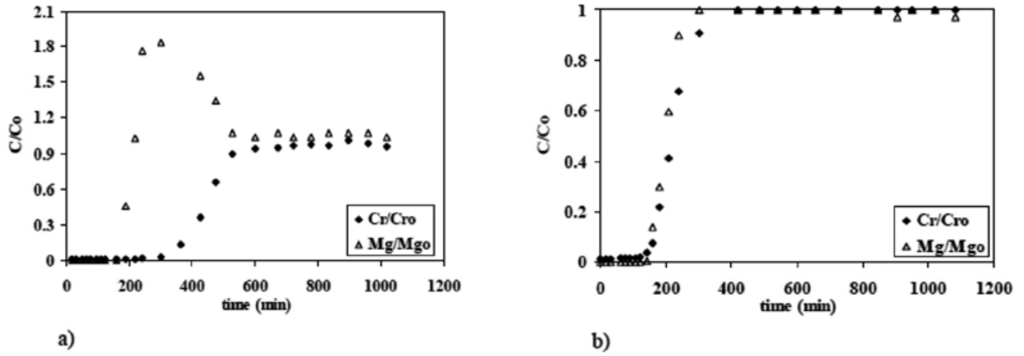

Figure 15. Breakthrough curves for the Cr-Mg competitive system: (a) NaY and (b) NaX.

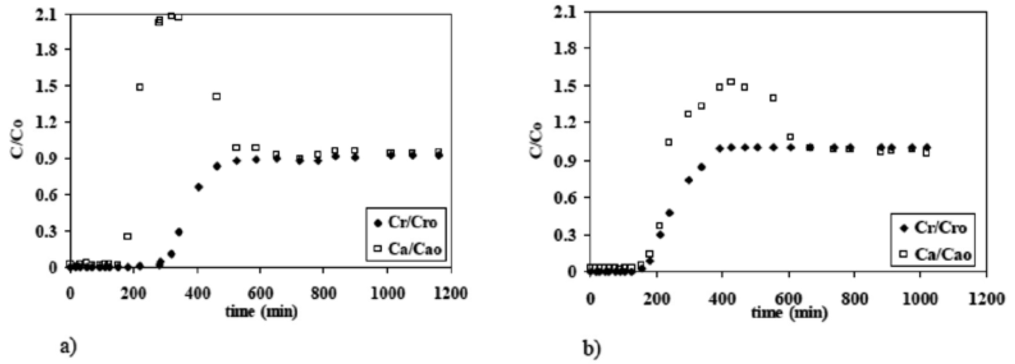

Figure 16. Breakthrough curves for the Cr-Ca competitive system: (a) NaY and (b) NaX.

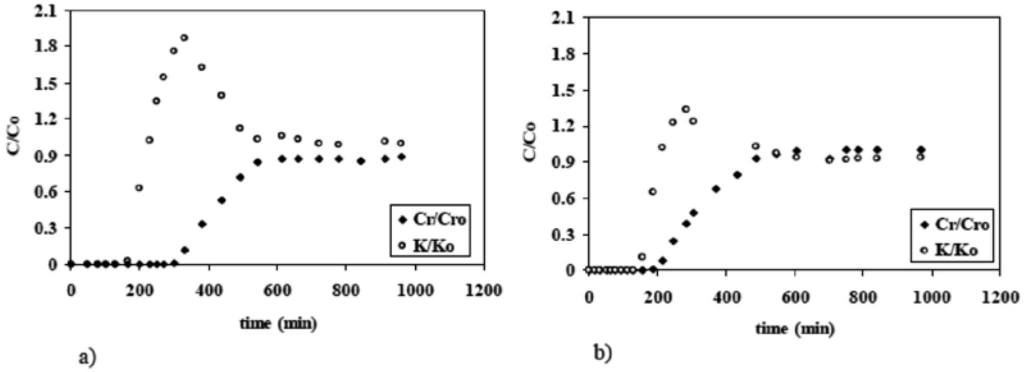

Figure 17. Breakthrough curves for the Cr-K competitive system: (a) NaY and (b) NaX.

System	U_{tb}^{Cr}/CEC	System	U_{tb}^{Cr}/CEC
Cr-NaY	0.69	Cr-NaX	0.71
Cr/Mg-NaY	0.54	Cr/Mg-NaX	0.27
Cr/Ca-NaY	0.51	Cr/Ca-NaX	0.31
Cr/K-NaY	0.66	Cr/K-NaX	0.41

U_{tb}^{Cr}/CEC= ratio of chromium uptake up to chromium breakpoint time (tb) and the cation exchange capacity of the column.

Table 10. Amount of chromium ions retained up to the breakpoint of 5% of the feed concentration.

5. General conclusions

Ion exchange is a much more complex phenomenon than adsorption as many ion exchangers may also act as adsorbents, increasing the difficulty in understanding the sorption removal.

Moreover, electrolytes add complexity in fluid phase and also in the solid phase. Ion charges and hydration energy of the incoming ions as well as charge density of the ion exchanger are undoubtedly factors that deserve detailed investigation, mainly for scaling-up proposals.

Author details

Maria Angélica Simões Dornellas de Barros[1], Marcelino Luiz Gimenes[1],
Melissa Gurgel Adeodato Vieira[2] and Meuris Gurgel Carlos da Silva[2]

1 Chemical Engineering Department, State University of Maringá, Maringá, PR, Brazil

2 School of Chemical Engineering, University of Campinas, Campinas, SP, Brazil

References

[1] Helferich, F., Ion Exchange, EUA, Dover Publications Inc., 1995.

[2] Zagorodni, A.A., Ion Exchange Materials Properties and Applications, Great Britain, Elsevier, 2007.

[3] Febrianto, J., Kosasih, A., N., Sunarco, J., Ju, Y-H., Indraswati, N., Ismadji, S., J. Hazard. Mater., 2009, 162, 2–3, 616.

[4] Qui, H., Lu, L., Pan, B., Zhang, Q., Zhang, W., Zhang, Q., J. Zhejiang Univ. Sci. A, 2009,10, 715.

[5] Tseng, J., Chang, C., Chang, C., Chenc, Y., Chang, C., Ji, D., Chiud, C., Chiang, P., J. Hazard. Mat., 2009, 171, 370.

[6] Breck, D. W., Zeolite Molecular Sieves—Structure, Chemistry and Uses, Robert E. Kriger Publishing Co., USA, 1974.

[7] Barrer, R.M., Bull. Soc. Fr. Minéral. Cristallogr., 1974, 97, 89.

[8] Barros, M. Arroyo, P.A., Silva, E.A., Chap. 14. General aspects of aqueous sorption process in fixed beds, In: Mass Transfer—Advances in Sustainable Energy and Environment Oriented Numerical Modeling, InTech, Croatia, 2013, 361–386.

[9] Ostroski, I. C., Dantas, J. H., Silva, E. A., Arroyo, P. A., Barros, M. A. S. D., Adsoption Sci. Tech., 2012, 30, 4, 275.

[10] Ostroski, I.C., Silva, E.A., Arroyo, P.A., Barros, M.A.S.D., Fluid Phase Equilib., 2014, 372, 76.

[11] Welter, R. A., Estudo do equilíbrio dos sistemas binários e ternário de troca iônica dos íons cobre, cádmio e cálcio pelo biopolímero alginato. Campinas: Universidade Estadual de Campinas, UNICAMP, 2009. 197p. D.Sc. Thesis (in Portuguese).

[12] Davis, T. A., Volesky, B. Mucci, A. Wat. Res., 2003, 37, 4311.

[13] Huang, C., Cheng, Y.C., Liou, M. R., J. Hazard. Mater.,1996, 45, 265.

[14] Sag, Y., Kaya, A., Kutsal, T., Hydrometallurgy, 1998, 50, 297.

[15] Reed, B. E., Matsumoto, M. R., Sep. Sci. Technol., 1993, 28, 13, 2179.

[16] Ciola, R., Fundamentos da Catálise, Ed. Moderna, São Paulo, 1981. Davis, T. A., Volesky, B. Mucci, A., Water Res., 2003, 37, 4311.

[17] Brunauer, S., Deming, L.S., Deming, W. E., Teller, E., Bureau of Agricultural Chemistry and Engineering and George Washington University, 1940, 1723–1732.

[18] Lai, Y.L., Annaduarai, G., Huang, F.C., Lee, J.F., Bioresource Tech., 2008, 99, 6480.

[19] Papageorgiou, S. K., Kouvelos, F. K., Katsaros, F. K., Desalination, 2008, 224, 293.

[20] Vieira, M. G. A., Silva, M. G. C. Adsorção/Bioadsorção de Metais Pesados, Compostos Orgânicos e Corantes em Solução Aquosa In: Aplicações tecnológicas em sistemas particulados. 1 ed.São Carlos: ANIMERIS, 2011, 171–212 (in Portuguese).

[21] Oliveira, C. M., Remoção de Metais Pesados Utilizando Carvão Ativado. Maringá: Universidade Estadual de Maringá, UEM, 2012. 120p. MSc thesis (in Portuguese).

[22] Hassan, S. S. M., Awwad, N. S., Aboterika, A. H. A., J. Hazard. Mater. 2008, 154, 992.

[23] Snyders, R., Music, D., Sigumonrong, D., Schelnberger, B., Jensen, J., Schneider, J. M., Appl. Phys. Letters, 2007, 90, 193902.

[24] Takeuchi, Y., Arai, H. J., Chem. Eng. Jpn., 1990, 23, 75.

[25] Park, J., Regalbuto, J. R., J. Colloid. Interface Sci., 1995, 175, 239.

[26] Babić, B. M. S. K., Milonjic´, B. M. B., Polovina, M. J., Kaludierovi, B. V., Carbon 1999, 37, 477.

[27] Smičklas, I., Dimović, S., Šljivić, M., Plećaš, I., Lončar, B., Mitrić, M., J. Nucl. Mater., 2010, 400, 15.

[28] Pan, X., Wang, J., Zhang, D., Desalination, 2009, 249, 609.

[29] Tóth, J. Adsorption Theory, Modeling, and Analysis, Marcel Dekker, Inc., USA, 2001.

[30] Markhan, E. C., Benton, A. F., J. Am. Chem. Soc., 1931, 53, 497.

[31] Jain, J. S., Snowyink, V. L., J. Water Pollut. Control Fed., 1973, 45, 2463.

[32] Barros, M.A.S.D., Zola A.S., Arroyo, P.A., Sousa-Aguiar, E.F., Tavares, C.R.G., Braz. J. Chem. Eng., 2003, 20, 04, 413.

Application of Mass Transfer Models in Environmental Engineering

Pen-Chi Chiang and Shu-Yuan Pan

Additional information is available at the end of the chapter

http://dx.doi.org/10.5772/60917

Abstract

Generally, unit operation processes that are used in environmental engineering are involved in interfacial reaction where mass transfer is an extremely essential component for system optimization. The purposes of this chapter were intended to provide the information of both theoretical model development and engineering practice for mass transfer of important processes in environmental engineering. Those processes include, but are not limited to, (1) ozonation (gas–liquid process), (2) ion exchange (liquid–solid process), (3) biological activated carbon (liquid–solid process), (4) chlorination (gas–liquid process), and (5) carbonation (gas–liquid–solid process).

Keywords: ozonation, ion exchanger, biological activated carbon, chlorination, carbonaion, rotating packed bed

1. Introduction

1.1. Ozonation process

1.1.1. Model development

1.1.1.1. Process chemistry

Ozone process has been utilized in thousands of water treatment applications such as municipal water (or wastewater) treatment plants, cooling towers, ultrapure water, marine aquaria, beverage industries, industrial process water, swimming pools, bottled-water plants, aquaculture, and food processing. It can oxidize the micro-pollutants and reduce the amount of disinfection by-product (DBP) precursors formed in drinking water [1], such as organic peroxides, aliphatic aldehydes, hydrogen peroxides, mixed functional and saturated carboxylic acids, etc. Some of the DBPs such as aldehydes and/or chlorinated aldehydes would be potential health hazards, leading to the increase of bacterial populations in distribution systems. Three oxygen molecules will combine together to form ozone, as shown in Equation (1); this is an endothermic reaction:

$$2O_3 \leftrightarrow 3O_2,\ \Delta H^0 = +284.5\ \text{kJ/mol}\ \left(\text{at 1 atm}\right) \tag{1}$$

The gaseous ozone (O_3) will decompose to oxygen gas (O_2), as shown in Equation (2). In general, the decomposition rate increases as the temperature increases. The efficiency of ozone production decreases at a higher temperature with a fixed voltage input.

$$O_3 + O_2 \rightarrow O_2 + O_2 + O \tag{2}$$

1.1.2. Reaction kinetics and mass transfer

Ozonation is a gas–liquid process under dynamic conditions; the reaction regime, mass transfer characteristics, and reaction kinetics are critical to system design and operation. As O_3 dissolves in water, it will self-decompose and generate oxygen and hydroxyl-free radicals. In general, the solubility of dissolved O_3 in ozonated water is merely 1 mg/L; higher dissolved O_3 concentration will only happen in the environment with better mass transfer (e.g., mixing). The mass transfer rate is influenced by operating variables such as pH, temperature, agitation speed, and gas flow rate. In general, the ozone concentration generated from ozone generator usually is less than 14 % (v/v) that may restrict the mass transfer between gas and liquid phases. Therefore, residual ozone concentration in water treatment ranges from 0.1 to 1 mg/L. A higher dissolved ozone concentration may happen only if under better mass transfer conditions.

It is noted that the specific interfacial area is of great significance to the gas–liquid mass transfer. In ozonation process, the overall liquid-phase mass transfer coefficient (K_La) and equilibrium dissolved ozone concentration ($[O_3]^*$) can be obtained from the following mass balance equation [2]:

$$\frac{d[O_3]}{dt} + r_{O_3,sd} = K_L a([O_3]^* - [O_3]) \tag{3}$$

where $r_{O3,sd}$ is the self-decomposition rate of ozone, which can be determined by Yang [3] as Equation (4):

$$\begin{aligned} r_{O_3,sd} = {} & 5.117 \times 10^{10} \exp\left(-\frac{8835.25}{T}\right)\left[O_3\right] + 9.207 \\ & \times 10^{16} \exp\left(-\frac{8835.25}{T}\right)[OH^-]^{0.5}[O_3] \end{aligned} \tag{4}$$

where *T* is the temperature (K). With the known $[O_3]$, t, and $r_{O3,sd}$, both the K_La and $[O_3]^*$ can be determined through the use of a linear regression analysis under specific experimental conditions.

1.2. Engineering practice

1.2.1. Determination of overall mass transfer coefficients

Figure 1 presents a typical schematic diagram of ozonation process, where the ozone is produced by an ozone generator and able to reach 10 % or higher.

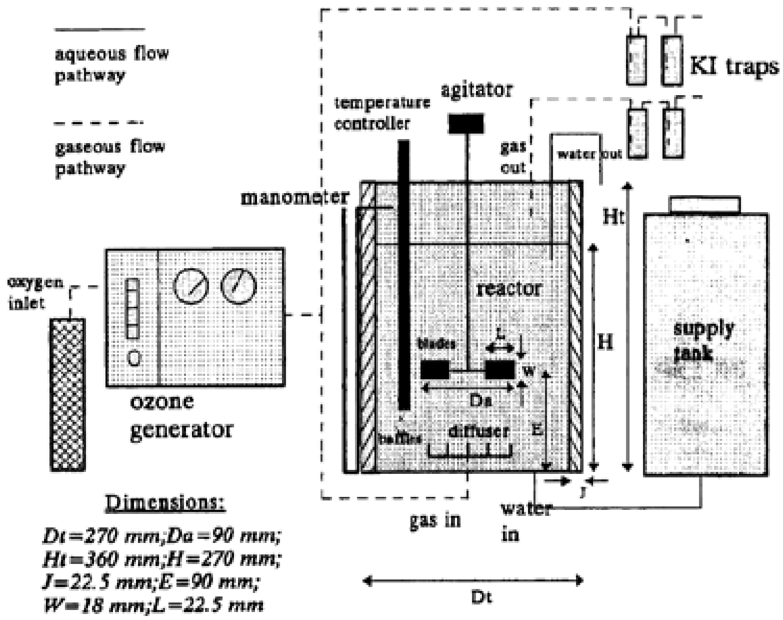

Figure 1. Schematic diagram of ozone experimental system (adapted from Chiang et al. [2])

Ouederni et al. [4] proposed the following equation to determine the ozone transfer in stirred reactors:

$$K_L a = 2.57 \times 10^{-2} \times (nG)^{0.67} \tag{5}$$

where K_La is expressed in s^{-1}, G is the gas flow rate expressed in 10^{-3} m^3/s, and n is the number of rotations per second. According to Sheffer and Esterson [5], the volumetric overall liquid-phase mass transfer coefficient of ozone in tap water (K_La) was around 1.14 min^{-1}. It was also observed that it would reach a higher value at a higher water flow rate (i.e., sufficient agitation). For instance, there was a large decrease in K_La to 0.25 min^{-1} without agitation.

In addition, combining the empirical relationship reported by Stankovic [6], the following equation can be derived:

$$K_L a = h \cdot D_v^{0.5} \cdot n^{0.5} \cdot G^x \tag{6}$$

where h and x are constants, a is the specific interfacial area (cm^{-1}), and G is the influent gas flow rate (L min^{-1}).

1.2.2. Determination of Fractional Ozone Absorption (FOA)

To determine the optimal operation conditions for semi-batch ozonation process, the "fractional ozone absorption (FOA)," defined as the ratio of the ozone transferred to water to the ozone applied to the reactor [7], should be applied. The FOA value in semi-batch operation can be expressed as [2]

$$FOA(\%) = \frac{V \times K_L a \times ([O_3]^* - [O_3])}{G \times P_{O_3} \times 1.98 \times 10^5} \times 10 \tag{7}$$

where P_{O3} is the ozone partial pressure (kPa). The value of 1.98×10^5 is the factor which will transfer the term of denominator into the unit of mg/min.

An increase in temperature will increase the ozone diffusivity in water and enhance the liquid-phase mass transfer, because the K_L value is directly proportional to $Dv^{0.5}$ based on Higbie's penetration theory [8].

Figure 2 shows the relationships between the agitation speeds and influent gas flow rates under the specific conditions of K_La and FOA_0. The results indicate that the FOA_0 is mainly controlled by n (not by G). Both the values of K_La and FOA_0 (i.e., initial FOA) increase as the agitation speeds increase due to the breakdown of liquid film resistance and the enhancement of surface renewal rates. Therefore, the K_La increased with the increase of the influent gas flow rate since the specific interfacial surface area between gas and liquid phases increases. In addition, Figure 2 provides the baseline information of engineering to obtain the best achievable alternative among the various scenarios of n, G, and K_La values, in terms of the same level of FOA_0. Furthermore, the desired FOA_0 in the water treatment plants can be determined by the agitation speed, if the value of G is given.

The power consumption (P_g) should be taken into consideration for the most efficient design and operating conditions in practice. P_g can be calculated as follows [9]:

$$P_g = \alpha \times N_p \times n^3 \times d_i^5 \times \rho \tag{8}$$

where P_g is the power consumption with gas dispersion (watt) and α is the ratio of P_g over P_0, where P_0 is the power consumption in un-gassed liquid. Moreover, α is a function of superficial gas velocity so it is directly proportional to G.

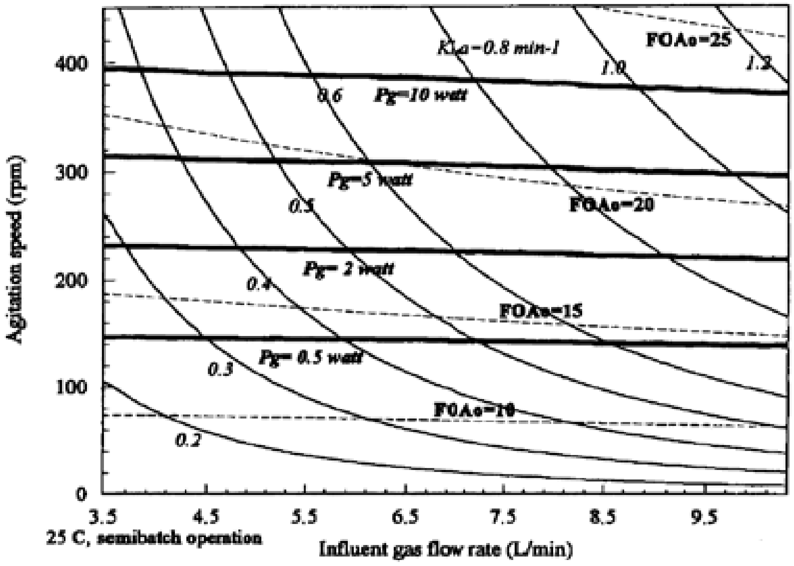

Figure 2. Effect of agitation speeds and influent gas flow rates on K_La, initial fractional ozone absorption (FOA_0), and power consumption. (Adapted from Chiang et al. [2])

N_p is the power number:

$$N_p = \frac{P_0}{n^3 \times d_i^5 \times \rho} \tag{9}$$

Figure 2 can be used to determine G and n for given requirements of FOA_0 and P_g, since the P_g value is influenced by both n and G. Under a constant value of G, the optimum operation conditions for semi-batch operation can be determined. For a standard six-bladed turbine with an N_p value of 5.2 [9], the desired value of α can be determined corresponding to various G values.

1.2.3. Integration of mass transfer and reaction kinetics

Two important factors for determining the kinetic regime of ozonation are the enhancement factor (E) and Hatta number (Ha). The E factor is defined as the ratio between the apparent reaction and the maximum physical absorption rates:

$$E = \frac{N_t}{K_L a [O_3]^*} \tag{10}$$

where Nt is the actual ozone absorption rate (M s^{-1}) and K_La is the overall mass transfer coefficient (s^{-1}). The $[O_3]^*$ values can be determined from Henry's constant and the ozone partial pressure at the reactor outlet. On the other hand, the Ha number for O_3 reaction is defined as

$$Ha = \sqrt{\frac{k_1[O_3]^* D_{O_3,L}}{k_L^{\,2}}} \tag{11}$$

DeCoursey [10] proposed a correlation between E and Ha for irreversible second-order reactions based on the Danckwerts penetration model, which takes the form as follows:

$$E = -\frac{Ha^2}{2\left(E_\infty - 1\right)} + \sqrt{\frac{Ha^4}{4\left(E_\infty - 1\right)^2} + \frac{E_\infty \cdot Ha^2}{\left(E_\infty - 1\right)} + 1} \tag{12}$$

where E_∞ is the infinite mass transfer enhancement factor. It is also noted that the expression is particularly accurate as the diffusivity coefficients of the reactants in the liquid are of the same order of magnitude.

Since the prediction model of K_La is applicable only to the deionized water, it is necessary to introduce the enhancement factor (E) to account for the effect of organic compounds in the real water sample on K_La. The n value (rps) for the fixed level of water quality parameters, applied ozone concentration [O_3], and influent gas flow rate (Q) can be developed as

$$n = \left(\frac{Q\left[O_3\right] + Vr_{O_3}}{1.20 \times EV\left(\frac{P_{O_3}}{0.38} - \left[O_3\right]\right)} - 0.0225 \right)^2 D_v^{-1} G^{-236} \tag{13}$$

Therefore, the marginal level of ozone partial pressure (P_{O3}) to achieve the highest removal of TOC can be determined through Equation (13). It is also noted that the mass transfer is successfully incorporated with reaction kinetics characterizations in Equation (13) for predicting the optimal n value (i.e., the most efficient agitation) to control the formation potential of organic compounds in the ozonation process.

Figure 3 gives the relationship between the agitation speed and applied ozone concentration under various retention times. For example, the TOC removal efficiency of 15 % and enhancement factor (E = 1) were held constant under the temperature of 25 °C, a pH value of 7, and an influent gas flow rate of 10 L/min. The higher the ozone partial pressure, the lower the agitation speed needed to achieve the same level of performance. In other words, it suggests that the ozone partial pressure (P_{O3}) should slightly increase, instead of greatly enhancing the agitation power consumption, to obtain the same level of removal efficiency of TOC.

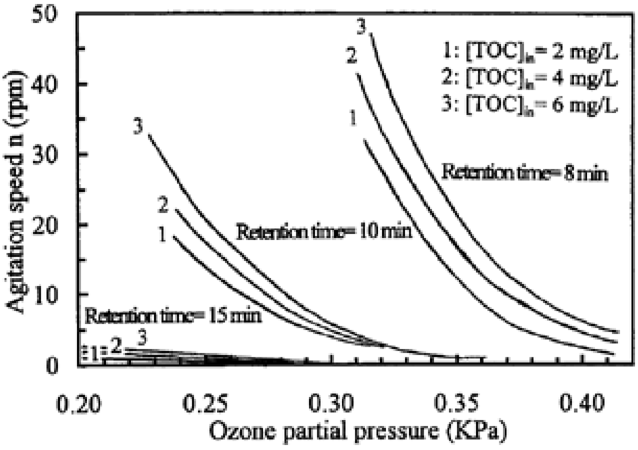

Figure 3. Simulation results of the relationship between agitation speed and ozone partial pressure in view of controlling the formation of TOC. (Chiang et al. [2])

2. Ion Exchange (IE)

Deionization is the process of removing the alts of electrolytes from water by ion exchange. "Deionization" is generally considered synonymous with "demineralization," by various authors, but since some of the ions exchanged are not necessarily of mineral origin, the term "deionization" appears more inclusive.

2.1. Model development

2.1.1. Rate-determining step

According to the Nernst static diffusion film theory, three mechanisms might be the rate-determining step under appropriate conditions:

1. Film diffusion (F-mechanism): transport of ions from the bulk liquid to the liquid solid interface
2. Particle diffusion (P-mechanism): transport of ions into the resin particle
3. Chemical reaction (C-mechanism): the chemical process of exchange

Recently, the principle of ion exchange kinetics has been investigated by applying either empirical rate equations or theoretical equations derived from fundamental diffusional mechanisms. In the latter approach, the rate-determining step could have been film diffusion, surface chemical reaction, or particle diffusion.

According to the kinetics of anion exchange on various resins, diffusion was the rate-controlling process in all cases. Turse and Rieman III [11] reported that the rate of exchange was controlled by the chemical reaction if chelates were formed by cations and resins. Without formation of chelates, at low concentration, the rate was controlled by "film" diffusion and, on the other hand, at high concentration by "particle" diffusion. In other words, the rate-determining step of the ion exchange process is always a combination of these two limiting steps of film diffusion and particle diffusion, except for the case of large organic ions (quaternary ammonium ions) which are controlled by particle diffusion.

2.1.2. Crank model

The derivation of the Crank model is given below. For particle-diffusion controlled, the rate of exchange could be expressed as Fick's second law as follows:

$$\mathrm{D}\frac{\partial^2}{\partial r^2}(rc)=\frac{\partial}{\partial t}(rc) \tag{14}$$

With the initial condition:

$$\mathrm{C{=}0,0 \le r \le a, t \le 0} \tag{15}$$

and the boundary condition:

$$\left(\frac{\partial r}{\partial t}\right)_{r=0}=0,\ t>0 \tag{16}$$

Equation (14) can be easily solved by the Laplace transform. The *F (t)*, fraction of the electrolyte uptake by the resin, is expressed as [12]

$$F(t)=1-\sum_{m=1}^{\infty}\frac{6\sigma(\sigma+1)}{9+9\sigma+\sigma^2{q_n}^2}\exp\left[-\left(D_p{q_n}^2+\frac{1}{\sigma^2}\right)\right] \tag{17}$$

where D_p^2 is the diffusion coefficient. q_ns are the nonzero roots of Equation (17) as follows:

$$\tan(q_n)=\frac{3q_n}{3+\sigma{q_n}^2} \tag{18}$$

In addition, $\sigma$is the ratio of the solute in the external solution to that in the resin particles at equilibrium, which can be determined by Equation (19):

$$\sigma = \frac{3V}{4a^3K} \tag{19}$$

where *K* is the partition factor. Therefore, the diffusion coefficient can be determined with the aid of F (t) vs. D_pt/a^2, which is given by Crank (1957).

Huang and Tsai [13] have developed a more appropriate and general equation which combined film diffusion, particle diffusion, and chemical surface reaction on the exchange rate for a finite bath. Under a specified case, the rate equation (Table 1) using only isotopic exchange with particle resistance is consistent with the Crank model [12].

Models	**Particle diffusion** **(P-mechanism)**	**Film diffusion** **(F-mechanism)**	**Chemical reaction** **(C-mechanism)**
Kressman and Kitchener (Limited bath)	$\frac{Q^\tau}{Q_\infty} = \frac{6}{r}\frac{Q}{Q_0 - Q_\infty}\frac{Dpt}{\pi}$	$\frac{Q_\infty}{Q^0}\text{In}\left(1 - \frac{Q^\tau}{Q_\infty}\right)K_f t$	$\text{In } Z = \frac{2KQ^0\left(Q^0 - Q_\infty\right)t}{Q_\infty}$ where $Z = \frac{t\left(Q^0 - 2Q_\infty\right) + Q^0Q_\infty}{Q^0\left(Q_\infty - Q_t\right)}$
Yagi and Kunii (Shell progressive)	$t = \frac{Q \cdot r^2}{6Dpc}[3 - 3(1 - X)^{2/3} - 2X]$	$t = \frac{Qr}{3K_fC}X$	$t = \frac{Q}{K_sC}[1 - (1 - X)^{1/3}]$
Boyd (Shallow bed)	$F = 1 - \frac{6}{\pi^2}\sum_{n=1}^{\infty}\frac{1}{n^2}\exp\left(-n^2\pi^2t\right)$	$\text{In}(1 - F) = -3t$	$\text{In}(1 - F) = -t$
Crank (Finite bath)	$F = 1 - \sum_{n=1}^{\infty}\frac{6\sigma(\sigma + 1)\exp\left(-Dpq_n^2t / a^2\right)}{9 + 9\sigma + q_n^2\sigma^2}$	$\text{In}(1 - F) = -3\left(1 + \frac{1}{\sigma}\right)t$	$\text{In}(1 - F) = -\left(1 + \frac{1}{\sigma}\right)t$

Table 1. Rate equation of isotopic ion exchange reaction with particle diffusion (P-mechanism), film diffusion (F-mechanism), and chemical reaction (C-mechanism) for various mathematical models

2.2. Engineering practice

2.2.1. Determination of rate-determining steps

In this chapter, the HPC and BHDAC are demonstrated as the representative quaternary ammonium ions because they are easy to prepare, highly soluble in water, and can be rapidly analyzed by use of UV. In addition, Dow-50-X8 was utilized as the resin for illustration. By plotting the θ_t / θ_∞ for HPC and BHDAC on each Dow-50-X8 resin (i.e., 20–50, 50–100, and 100–200 mesh), one can observe three straight lines with slopes of K (the parabolic rate constant). Subsequently, a liner correlation can be found between K and 1/D (the reciprocal of resin diameter), as shown in Figure 4. It suggests that the rate-determining step of these quaternary ammonium ions on the strong acid cation exchanger was particle-diffusion controlled.

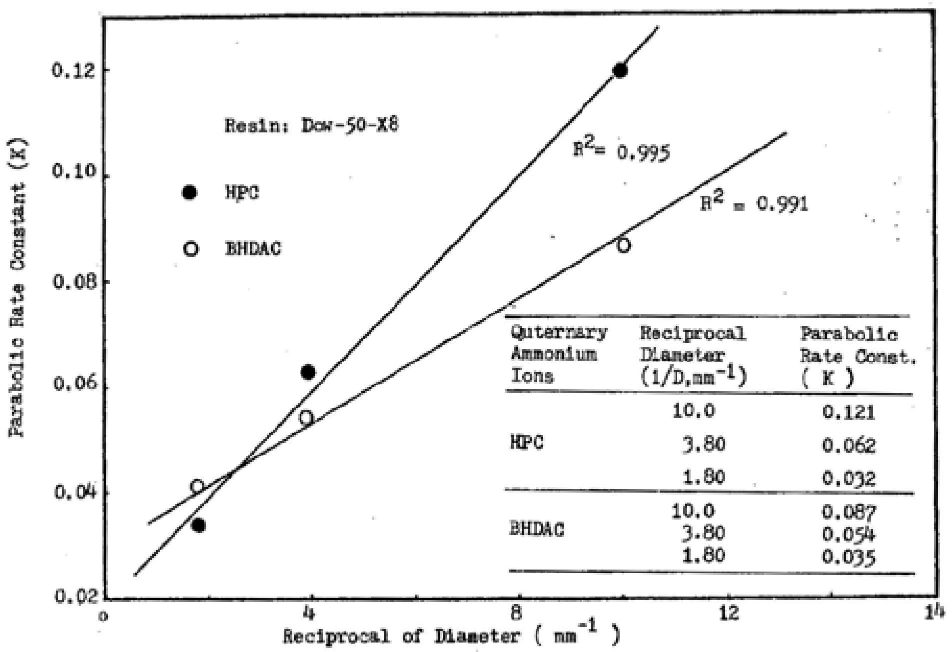

Figure 4. Effect of particle size on parabolic rate constant (resin: Dow-50-X8)

2.2.2. Determination of particle-diffusion coefficient

The particle-diffusion coefficients of LPC, HPC, and BHDAC through the Amb-200, Amb-DPI, and Dow-50-X8 resins were determined and summarized in Table 2. As previously cited, the rate of exchange of HPC and BHDAC on various particle sizes on Dow-50-x8 resins was shown in Figure 4. It was observed that the Dow-50-X8 resin possessed the lowest particle-diffusion coefficient in comparison with the Amb-200 and Amb-DPI resins. This evidence strongly suggested that the macroporous resin had an advantage over the gel-structure resins for exchange of organic ions.

Quaternary ammonium ions	**Amb-200** (**10^9 cm^2/sec**)	**Amb-DPI** (**10^9 cm^2/sec**)	**Dow-50-X8** (**10^9 cm^2/sec**)
LPC	3.03	2.35	-
HPC	2.43	2.12	0.85
BHDAC	0.90	1.70	0.57

Table 2. Particle-diffusion coefficient of LPC, HPC, and BHDAC through the Amb-200, Amb-DPI, and Dow-50-X8 resins (20–50 mesh)

It was thus concluded that the Amb-200 (strong acid cation exchanger), Amb-DPI (weak acid cation exchanger), and XE-318 (chelating cation exchanger) resins were the ones to be selected as the representative cation exchangers for the resin selectivity test as described later.

3. Biological Activated Carbon (BAC)

3.1. Model development

3.1.1. Representative models of BAC

The biological activated carbon (BAC) process contains adsorption and biodegradation mechanisms. The BAC process also exhibits lower regeneration cost and prolongs the life of granular activated carbon (GAC) beds. Therefore, it has been widely used in water and wastewater treatments.

A well-validated mathematical model can provide valuable information to evaluate and predict the performance of BAC process. Table 3 presents several representative models for BAC process. Chang and Rittmann [14] developed a model that the mass transfer of substrates diffusing through the biofilm, metabolized by microbes, and finally reaching the surface of GAC was illustrated and quantified. However, the limitation of the model is that it cannot be used under unsteady or plug flow conditions. Sakoda et al. (1996) developed a theoretical model for a BAC column considering the mechanisms including dispersion, convection, biodegradation, and adsorption. The assumption included that the substrate concentration on the interface between the biofilm and the GAC is identical to that in the bulk solution. Furthermore, Liang and Chiang [15] developed a non-steady-state numerical model to differentiate the adsorption and biodegradation quantities of a continuous BAC column including the mechanisms of adsorption, biodegradation, convection, and diffusion.

Reactor type	**Mechanisms**[a]	**Consideration of kinetics**				**Mass transport description**[b]	**Solution method**	**Reference**
		Substrate in bulk phase	**Substrate in biofilm**	**Biofilm amount**	**Substrate in GAC**			
Complex mixing	A, B	Nonsteady Monod	Monod	Nonsteady	Non-equilibrium	1, 2, 3, 4, 5	Analytical	Chang and Rittmann [14]
Column	A, B, C, D	Nonsteady, no biodegradation, uniform Monod	n.a.[c]	Steady	Equilibrium	1	Analytical	Sakoda, Wang and Suzuki [17]

Reactor type	Mechanisms[a]	Consideration of kinetics				Mass transport description[b]	Solution method	Reference
		Substrate in bulk phase	Substrate in biofilm	Biofilm amount	Substrate in GAC			
Column	A, B	Uniform	Monod	Nonsteady	n.a.[c]	1	Analytical	Walker and Weatherley [18]
Column	A, B, C	Nonsteady, no biodegradation	Monod	Steady	Non-equilibrium	1, 5	Analytical	Abumaizar, Smith and Kocher [19]
Column	B, C, D	Nonsteady Monod	Monod	Nonsteady	n.a.[c]	1, 2, 3	Numerical	Hozalski and Bouwer [20]
Column	A, B, C, D	Nonsteady, no biodegradation	Monod	Nonsteady	Non-equilibrium	1, 2, 3, 4, 5	Numerical	Badriyha, Ravindran, Den and Pirbazari [21]
Column	A, B, C, D	Nonsteady, no biodegradation, uniform Monod	Monod	Steady	Non-equilibrium	1, 2, 3, 4, 5	Numerical	Liang and Chiang [15]

[a] A, adsorption; B, biodegradation; C, convection; D, dispersion.

[b] 1, bulk phase; 2, interface between bulk phase and biofilm; 3, biofilm; 4, interface between biofilm and GAC; 5, GAC.

[c] Not analyzed in the article.

Table 3. Several representative models for biological activated carbon (BAC) process (modified from Liang et al. [16])

3.1.2. Non-steady-state models for adsorption and biodegradation of BAC

A numerical model can be developed to simulate both adsorption and biodegradation quantities of a BAC column under a non-steady-state condition. The governing equation based on mass balance of the substrate concentration in the liquid phase of the BAC column can be expressed as follows [16]:

$$\varepsilon \frac{\partial S_b}{\partial t} = D_b \frac{\partial^2 S_b}{\partial x^2} - v \frac{\partial S_b}{\partial x} - \frac{\left(1-\varepsilon\right)}{V_g} \int_0^{L_f} \frac{k_f X_f S_f}{K_f + S_f} 4\pi \left(r_f + r_g\right)^2 dr_f - \left(1-\varepsilon\right) \rho_g \frac{\partial q_a}{\partial t} - \varepsilon \left(\frac{k_b X_b S_b}{K_b + S_b} \right) \tag{20}$$

Table 4 presents the parameter details of Equation (20):

Abbreviations	Units	Descriptions
ε	-	Bed porosity of the BAC column
S_b	M/L^3	Substrate concentration in the liquid phase
D_b	L^2/T	Dispersion coefficient in the liquid phase
x	L	Distance along the BAC column
V_g	L^3	Volume of a GAC granule
L_f	L	Length of the biofilm
k_f	M/T-cell	Maximum utilization rate in the biofilm
k_b	M/T-cell	Maximum utilization rate in the liquid phase
X_f	$cell/L^3$	Cell density of the biofilm
X_b	$cell/L^3$	Cell density in the liquid phase
S_f	M/L^3	Substrate concentration in the biofilm
K_f	M/L^3	Monod half-velocity coefficient in the biofilm
K_b	M/L^3	Monod half-velocity coefficient in the liquid phase
r_f	L	Radius of the biofilm
r_g	L	Radius of the GAC granule
ϱ_g	M/L^3	GAC granule apparent density
q_a	M/M	Adsorption capacity

Table 4. Parameter details of non-steady-state models for adsorption and biodegradation of BAC

Two boundary conditions (BC) for the equation of dispersion advection reaction can be described as follows:

$$\mathrm{BC1}: S_b = S_0 \ \ , \ \ x = 0, \ \text{and} \ \ t \geq 0 \tag{21}$$

$$\mathrm{BC2}: \frac{\partial S_b}{\partial x} = 0 \bigg|_{x=L_c} \tag{22}$$

where Lc is the length of the BAC column (L). If the diffusion and reaction simultaneously occurred under a non-steady-state biofilm condition, the non-steady-state form of mass transfer and biodegradation reaction within biofilm, based on Fick's law and Monod equation, can be expressed as

$$\frac{\partial S_f}{\partial t} = D_f \frac{\partial^2 S_f}{\partial r_f^2} - \frac{k_f S_f}{K_s + S_f} X_f \qquad 0 \le r_f \le L_f \tag{23}$$

where D_f (L^2/T) is the diffusivity within the biofilm. A diffusion layer exists between the bulk solution and the biofilm, and the substrate concentration profile can be solved according to Rittmann and McCarty [22]. Therefore, the boundary condition can be simplified as

$$S_f\Big|_{r_f=0} = k_{bf} S_b \tag{24}$$

where k_{bf} is a factor to estimate the concentration reduction within the diffusion layer. Langmuir isotherm was used for the calculation of the boundary concentration of the biofilm near the GAC side, which was derived from the solid-phase concentration of the adsorbates. For single-component adsorbate, the surface concentration (q_s, M/M) can be expressed as follows:

$$q_s = \frac{q_0 K_L C_a}{1 + K_L C_a} \tag{25}$$

where q_0 (M/M) is the unit layer adsorption capacity, K_L (L^3/M) is the Langmuir coefficient, and C_a (M/L^3) is the concentration on the boundary of the biofilm. It is assumed that the concentration flux from the biofilm should be identical to the substrate absorbed on a GAC granule, as Equation (26):

$$4\pi r_g^2 \cdot D_f \frac{\partial S_f}{\partial r_f}\Bigg|_{r_f=L_f} = \frac{\partial q_a}{\partial t} m_g \tag{26}$$

where m_g (M) is the mass of a GAC granule. In a control volume, the average biodegradation rate can be derived by integrating the Monod reaction expression and the amount of biofilm volume:

$$\left[\int_0^{L_f} \frac{k_f S_f}{K_f + S_f} X_f 4\pi \left(r_g + r_f\right)^2 dr_f\right] \times N_g \qquad 0 \le r_f \le L_f \tag{27}$$

$$N_g = \frac{\Delta V \left(1 - \varepsilon\right)}{V_g} \tag{28}$$

where ΔV is a control volume unit of the BAC bed (L^3) and Ng is the number of BAC granules in a control volume.

3.1.3. *Estimation of biofilm thickness*

On the other hand, the thickness of biofilm will increase due to growth and decrease by the shear of water and the self-decay of bacteria. As a result, the biofilm thickness can be described as

$$\frac{\partial L_f}{\partial t} = \frac{Y\int_0^{L_f} \frac{kS_f}{K_s + S_f} X_f 4\pi\left(r_g + r_f\right)^2 dr_f}{A_f X_f} - b_{tot} L_f, \quad 0 \le r_f \le L_f \tag{29}$$

where Y is the yield coefficient of biomass (CFU/M) and A_f is the surface area of a BAC granule (L^2).

In addition, the governing equation for the bacterial density in bulk solution can be simplified as an advection–reaction form:

$$\frac{\partial X_b}{\partial t} = -v\frac{\partial X_s}{\partial x} + \frac{Yk_b S_b X_b}{K_b + S_b} \tag{30}$$

In this situation, the BCs of Equation (30) can be expressed as follows:

$$\mathrm{BC1}: X_b = S_0 \quad x = 0,\ t \ge 0 \tag{31}$$

$$\mathrm{BC2}: \left.\frac{\partial S_b}{\partial x} = 0\right|_{x=L_c} \tag{32}$$

The governing equation is a second-order partial-differential equation, which can be approximately solved by the Crank–Nicolson finite differential and Crout factorization methods. Therefore, the developed model can quantify the amounts of adsorption and biodegradation. In addition, the significances of each parameter can be determined throughout the results of sensitivity analysis.

3.2. Engineering practice

3.2.1. *Dimensionless analysis*

The mass transfer coefficient can be determined by the dimensionless groups of Reynolds (Re), Sherwood (Sh), and Schmidt (Sc) numbers. Since these dimensionless groups are developed for process scale-up, different reactors can be compared to each other through the dimensionless analysis. The Reynolds number represents the ratio between inertial force and viscous force, and the Sherwood number represents the ratio between liquid-film transfer and biofilm diffusive transfer. The N_{Sh} can be correlated with the dimensionless groups as follows (Wakao and Funazkri, 1978):

$$N_{Sh} = 2 + 1.1 \times N_{Re}^{\ 1/2} N_{Sc}^{\ 1/3} \tag{33}$$

Several key operational parameters reasonably dominating the performance of a BAC column include the superficial influent velocity and the particle size of packing. As a result, the effects of particle size on adsorption and biodegradation can be simulated by the dimensional analysis.

3.2.2. Liquid-film mass transfer

Figure 5 shows the relationship between the Stanton number (N_{St}) and the liquid-phase mass transfer coefficient (k_bf) reported in the literature. It is observed that the Stanton number (i.e., the ratio of the liquid-film transfer to the bulk transfer) exhibits an inverse proportion to the particle size (d_p) and the superficial velocity (v_s). In other words, both larger particle sizes and higher superficial velocities will lead to a relatively lower performance in liquid-film mass transfer (N_{St}). Therefore, the mass transfer from bulk solution into the biofilm can be enhanced with the increase of the Stanton number.

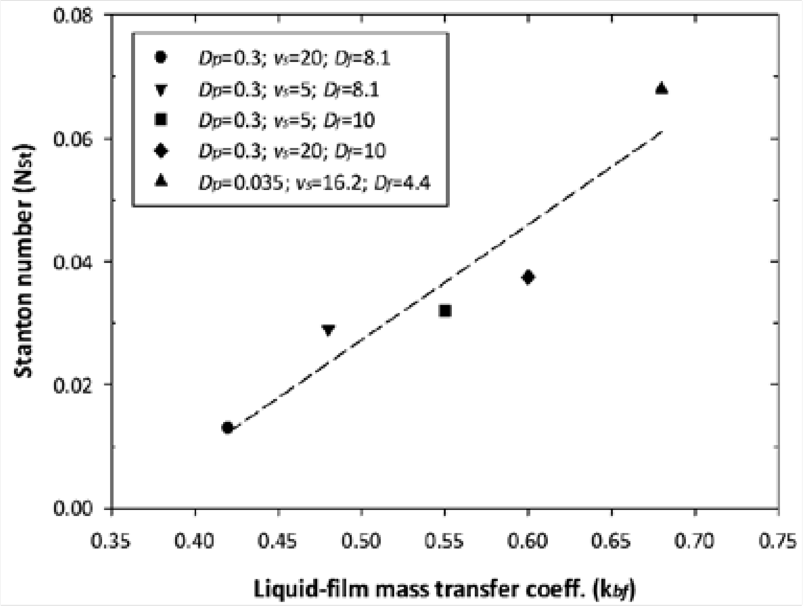

Figure 5. Correlation between the Stanton number (N_{St}) and the liquid-film mass transfer coefficient (k_{bf}). D_p (cm) is the particle size, v_s (cm/min) is the superficial velocity, and D_f (10^{-6} cm^2/s) is the diffusivity. Available data was from Liang et al. [16]) and Badriyha et al. [21])

4. Chlorination process

4.1. Model development

Chlorination (using chlorine as disinfectant) is the common process used in daily water disinfection because of its high efficiency with a relatively low cost. However, as aforementioned in the Ozonation chapter, the disinfection by-products (DBP), specifically trihalomethane (THM) including chloroform, bromodichloromethane, dibromochloromethane, and bromoform, will also be formed during the chlorination process. Control of the formation potential of THM during chlorination is thus an important target for the supply of drinking water. THMs can be formed in the presence of specific precursors such as humic substances and methyl ketones [23]. Several good engineering practices to prevent THM formation include (1) decrease of chlorine dose, (2) change of the point of chlorination, (3) substitution with an alternative disinfectant, and (4) reduction of precursors in solution by GAC or enhanced coagulation. In addition, several factors including precursor concentration (as represented by total organic carbon concentration), chlorine dose, bromide concentration, reaction temperature, pH of solution, contact time, and reactor configuration (length-to-width ratio and mixing conditions) will affect the formation of THMs. To predict the performance of disinfection efficiency and kinetics, and/or THM formation potential, numerous models such as dispersion model have been applied in chlorine process, as illustrated in the following context.

4.1.1. Dispersion model

In general, the chlorination process is applied in either a rectangular basin with baffles (rectangular-long and narrow channel) or a circular basin (circular-annular ring surrounding). The hydrology in a rectangular basin with baffles is the most advantageous because of a plug-flow-like reactor. It can be examined by the exit age distribution (E_θ) curve (Equation (34)) of the basin reactor, assuming the independence of fluid element and agitation with respect to radial position [24]:

$$E_\theta = \frac{1}{\sqrt{4\pi\theta d}} exp \frac{-(1-\theta)^2}{4\theta d} \tag{34}$$

where d is the dimensionless diffusion coefficient representing the degree of axial mixing. The d value approaching zero represents the reactor behaving as an ideal plug-flow type, otherwise (approaches infinity) representing a mixed-flow type. The E_θ in Equation (34) is a function of θ which follows a Gaussian distribution.

For a baffled rectangular basin with a total flow length of L and a channel width of W, the dimensionless diffusion coefficient (d) in open-channel flow, taking the nonideal nature of the reactor into consideration, could be expressed by Equation (35) [25]:

$$d = \frac{0.14k}{L/W} \tag{35}$$

where k is a nonideality coefficient of the reactor.

4.1.2. Disinfection kinetics

According to Collins and Selleck [26], the die-off of microorganisms in a batch reactor due to disinfection can be expressed by Equations (36) and (37):

$$\left[\frac{N}{N_0}\right]_{\text{batch}} = 1, \quad \text{for } \theta < \frac{b}{CT} \tag{36}$$

$$\left[\frac{N}{N_0}\right]_{\text{batch}} = \left(\frac{b}{Ct}\right)^n, \text{ for } \theta < \frac{b}{CT} \tag{37}$$

where *t* is the exit residence time representing the actual traveling time of the component of the fluid. The value of *b* for the combined chlorine was about 4 and 2.8 for total coliform and fecal coliform, respectively, and the value of *n* was about 3 for both total and fecal coliform [26]. *T* is the theoretical residence time (i.e., hydraulic retention time (HRT)), measured as the volume divided by the flow rate.

The overall survival fraction of bacteria can be determined by integrating the survival fraction of a series of batch reactors over the E_θ function, if the reaction in a continuous flow reactor. In this case, the average disinfection efficiency (i.e., 1 – (N/No)) is expressed as follows [25]:

$$1 - \frac{N}{N_0} = 1 - \int_0^\infty \left[\frac{N}{N_0}\right]_{\text{batch}} E_\theta d\theta \tag{38}$$

Therefore, the average disinfection efficiency can be calculated by the given chlorine dose (*C*), dimensionless diffusion coefficient (*d*), disinfection coefficients (*b* and *n*), and residence time distribution function (E_θ and $d\theta$) using Equation (39) [25]:

$$\begin{aligned} 1 - \int_0^\infty \left[\frac{N}{N_0}\right]_{\text{batch}} E_\theta d\theta = 1 - \int_0^{b/CT} \frac{1}{\sqrt{4\pi\theta d}} \exp\left(\frac{-(1-\theta)^2}{4\theta d}\right) d\theta \\ + \int_{b/CT}^\infty \left(\frac{b}{CT}\right)^n \frac{1}{\sqrt{4\pi\theta d}} \exp\left(\frac{-(1-\theta)^2}{4\theta d}\right) d\theta \end{aligned} \tag{39}$$

4.1.3. Formation kinetics of THMs

The reaction chemistry between chlorine and aquatic humic precursors to form THMs can be expressed by the following short-hand way [25]:

$$\mathrm{Cl}_2 + m''\mathrm{TOC}\left(\mathrm{precursors}\right) \rightarrow \mathrm{THMs} + \mathrm{other\ products} \tag{40}$$

Based on the above process chemistry, the kinetics of chlorine decay and the THMs formation can be expressed by Equations (41) and (42), respectively:

$$-\frac{d\left[\mathrm{Cl}_2\right]}{dt} = k_1\left[\mathrm{Cl}_2\right]\left[\mathrm{TOC}\right]^{m'} \tag{41}$$

$$\frac{d\left[\mathrm{THMs}\right]}{dt} = k_2\left[\mathrm{Cl}_2\right]\left[\mathrm{TOC}\right]^{m} \tag{42}$$

When reactions take place in a continuous flow reactor, the overall change of free chlorine and THMs can be obtained by integration of the batch concentration over the entire exit time distribution (E_θ) as follows:

$$\begin{aligned}\left(\frac{\left[\mathrm{Cl}_2\right]}{\left[\mathrm{Cl}_2\right]_0}\right) &= \int_0^\infty \left(\frac{\left[\mathrm{Cl}_2\right]}{\left[\mathrm{Cl}_2\right]_0}\right)_{\mathrm{batch}} E_\theta d\theta = \\ &= \int_0^\infty \frac{1}{\sqrt{4\pi\theta d}} \exp\left(\frac{-\left(1-\theta\right)^2}{4\theta d}\right) \exp\left(-k_1 T\theta\left[\mathrm{TOC}\right]\right) d\theta\end{aligned} \tag{43}$$

$$\begin{aligned}[\mathrm{THMs}] &= \int_0^\infty [\mathrm{THMs}]_{\mathrm{batch}} E_\theta d\theta = \\ &= \int_0^\infty k_2 T\left[TOC\right]^m \left[\mathrm{Cl}_2\right]_0 \exp(-k_1 T\theta[\mathrm{TOC}]) \frac{1}{\sqrt{4\pi\theta d}} \exp\left(\frac{-\left(1-\theta\right)^2}{4\theta d}\right) d\theta\end{aligned} \tag{44}$$

4.2. Engineering practice

4.2.1. Determination of coefficients in disinfection kinetic model

In practice, the total coliform and total bacteria count can be measured by the membrane filter method and heterotrophic plate count method, respectively. The effect of chlorine doses and contact time on the survival of total coliform and total bacteria can be determined, as shown in Figures 6 (a) and (b), respectively.

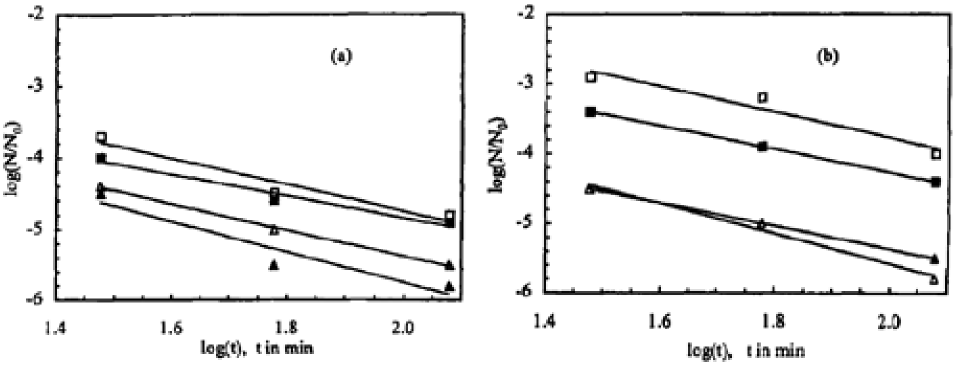

Figure 6. Effect of applied chlorine and contact time on survival of (a) total coliform and (b) total count. □ Cl_2, 1.2 mg/L; ■ Cl_2, 2.0 mg/L; △Cl_2, 1.8 mg/L; ▲Cl_2, 0.9 mg/L. (Adapted from Chiang et al. [25])

4.2.2. *Prediction of THMs Formation*

As shown in Figure 7, the effect of the contact time (i.e., 0–70 min) and the chlorine dose (i.e., 0.5–8.0 mg/L) on the THM formation was presented at a TOC of 3 mg/L with an L/W ratio of 20. The THM concentrations increase linearly with the contact time over the range of 0 to 70 min. By knowing the water quality parameters and experimental conditions, it is possible to predict the THM formation in the effluent of the chlorine contact chamber. To keep the THM formation below 100 μg/L at the water treatment plant, it is necessary to maintain the chlorine dose below 2 mg/L for a contact basin with an L/W ratio of 20.

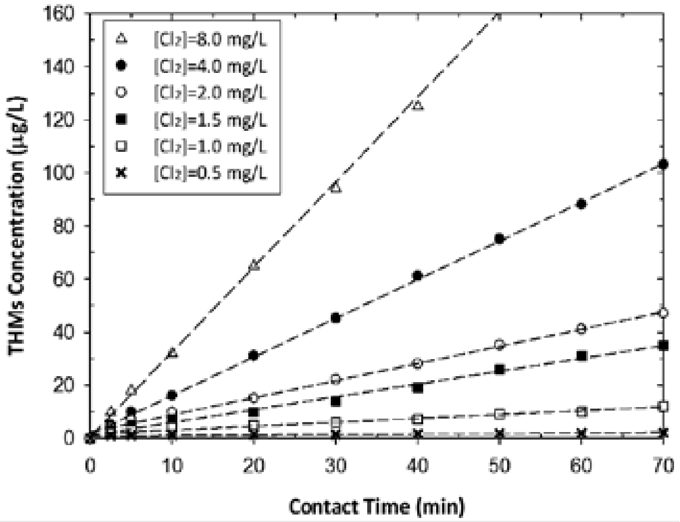

Figure 7. Effect of applied chlorine dose ad contact time on THM formation at inlet TOC concentration of 3.0 mg/L and an L/W ratio of 20. (Modified from Chiang et al. [25])

4.2.3. Balancing disinfection efficiency and THM formation

As the aforementioned, balancing the disinfection efficiency (in Section 2.1) and THM formation (in Section 2.2) is an important task in chlorination process. Table 5 provides the engineering practice (exemplified by Case A wastewater treatment plant) to balance the disinfection efficiencies and THM formation, in terms of contact time, L/W ratio, and applied chlorine doses. It can be used to determine the applied chlorine dose needed to meet a specified degree of inactivation (e.g., 99.99 % kill) and level of THM formation. In general, the THM formation increases rapidly with the increases of contact time. Conversely, the disinfection efficiency of chlorine increases gradually as both contact time and chlorine dosage increase.

It is noted that the applied chlorine dose at about 1.0 mg/L exhibits the most economically feasible way to control the THM formation and to maintain the disinfection efficiency at the Case A water treatment plant. Under these conditions, the Case A plant is able to achieve an acceptable level of residual chlorine (i.e., 0.5 mg/L) at the THM formation below 100 μg/L.

Items		**Unit**	**Category I**			**Category II**			**Category III**		
Applied chlorine		mg/L	0.5	0.5	0.5	1.0	1.0	1.0	1.25	1.25	1.25
L/W		–	2	10	20	2	10	20	2	10	20
Disinfection efficiency	20 min	%	99.40	99.59	99.62	99.96	99.97	99.98	99.98	99.98	99.99
	30 min	%	99.94	99.96	99.96	99.98	99.99	99.99	99.99	99.99	99.99
	40 min	%	99.97	99.98	99.98	99.99	99.99	99.99	99.99	99.99	99.99
	50 min	%	99.98	99.99	99.99	99.99	99.99	99.99	99.99	99.99	99.99
THM formation	20 min	μg/L	3.54	3.99	4.00	7.08	7.97	7.99	8.85	9.97	9.99
	30 min	μg/L	5.22	5.90	5.91	10.45	11.79	11.83	13.06	14.74	14.79
	40 min	μg/L	6.85	7.75	7.78	13.70	15.50	15.56	17.13	19.37	19.45
	50 min	μg/L	8.42	9.55	9.60	16.85	19.10	19.20	21.06	23.88	23.99

Table 5. Disinfection efficiency and THM formation during chlorination at TOC = 3 mg/L in a real water treatment plant (Case A) (modified from Chiang et al. [25])

In addition, the THM concentration and disinfection efficiency associated with a given contact time, L/W ratio, and applied chlorine dose are also presented in Table 5. Prior to chlorine input to the solution, reducing the TOC concentration is definitely the best engineering practice (BEP) for controlling the THM formation, rather than improving the hydraulics through the geometric design of the reactor. On the other hand, the results imply that the geometry of a chlorine contactor can effectively control the disinfection efficiency (not on the formation of THMs), especially for large chlorine doses and a high L/W ratio.

Furthermore, in order to reduce the formation of THM, the ozonation process is sometimes utilized in disinfection for the purpose of eliminating bacteria, viruses, cysts, as well as organic compounds, especially, the precursors of disinfection DBPs [27]. The performance of the ozone disinfection processes is evaluated by the residual ozone and contact time. Therefore, factors such as the efficiency of gas–liquid contact, chemical reactivity of the raw water toward ozone, susceptibility of microorganisms, and hydrodynamic characteristics of the contactor can influence the disinfection performance of an ozonation process. Several researchers have shown that ozonation prior to chlorination can lower the formation potential of THM (trihalomethanes) and HAA (haloacetic acid) [28, 29].

5. Carbonation process

5.1. Model development

5.1.1. Process chemistry

Carbonation is generally classified as a heterogeneous reaction containing gas, liquid, and solid phases. CO_2 fixation by accelerated carbonation has been regarded as mass transfer limited reaction (i.e., film-diffusion controlled) according to the findings reported in the literature [30-32]. Therefore, different types of approaches such as physical intensification [33] and biological or chemical activation [34, 35] were recently carried out to improve the mass transfer and reaction kinetics. Based on this idea, a rotating packed bed (RPB) reactor has been introduced to improve the mass transfer rate among phases due to its high centrifugal forces and great micro-mixing ability. RPB, the so-called high-gravity (sometimes called the "HI-GEE") process, is able to generate high acceleration via centrifugal force so the mass transfer between gas and liquid and even between liquid and solid can be enhanced. Since RPB can provide a mean acceleration of hundreds, and even thousands, of times greater than the force of gravity, it can effectively lead to the formation of thin liquid films and micro- or nano-droplets [36-38]. Therefore, the volumetric gas–liquid mass transfer coefficients (K_Ga) are an order of magnitude higher than those in a conventional packed bed, leading to dramatic reductions in equipment size over that required for equivalent mass transfer in a gravity-flow packed bed [36, 38, 39].

According to the findings in the literature [40], the CO_2 consumption in bulk solution was mainly attributed (over 98 % contribution) to carbonation reaction with calcium ions in solution leached from the steel slag to form calcium carbonate precipitates, where the stoichiometric formula was briefly presented as Equation (45). In this case, the stoichiometric coefficient (*b*) is assigned a value of one.

$$\mathrm{CO}_{2(\mathrm{fluid})} + \mathrm{b\ CaO}_{(\mathrm{solid})} \rightarrow \mathrm{CaCO}_{3(\mathrm{s})} \tag{45}$$

From the gas-phase point of view, the CO_2 removal efficiency (η) for a carbonation process can be calculated as Equation (46):

$$\eta(\%) = \left[1 - \frac{\left(\rho_{CO_2,o} Q_{G,o}\ C_{G,o}\right)}{\rho_{CO_2,i} Q_{G,i}\ C_{G,i}}\right] \times \% \tag{46}$$

where the $\rho_{CO_2,i}$ and $\rho_{CO_2,o}$ are the densities of inflow and outflow streams of CO_2, respectively. $Q_{G,i}$ and $Q_{G,o}$ are the flow rates of inflow and outflow streams, respectively. $C_{G,i}$ and $C_{G,o}$ are the CO_2 concentration in inflow and outflow streams, respectively.

From the solid-phase point of view, the carbonation conversion (X_B, %) of the solid can be defined as the ratio of reacted CaO fraction with CO_2 to the original total available CaO content in solid before carbonation., as expressed in Equation (47):

$$X_B(\%) = \left[\frac{\Delta m_{CO_2}}{MW_{CO_2}} \times \frac{MW_{Cao}}{CaO_{total}} \right] \times \% \tag{47}$$

where Δm_{CO2} is the weight gain due to CO_2 carbonation per dry weight of the solid sample. MW_{CaO} and MW_{CO2} are the molecular weight of CaO and CO_2, respectively. CaO_{total} is the total available CaO content in the solid before carbonation.

5.1.2. Rate-determining steps

The shrinking core model (SCM) has been utilized to determine the rate-limiting steps in a heterogeneous reaction because of its conceptual and mathematical simplicity [41]. In the SCM, it is assumed that the reaction occurs at the outer skin of solid particle and then proceeds at a narrow front [24]. The narrow front moves into the particle and leaves behind completely reacted product layer and/or reactive-species-depleted rims (i.e., ash layer). An unreacted core of material exists at any time, which shrinks in size during the reaction. Based on the above assumption, three factors might affect the reaction (i.e., rate-limiting steps) including (1) fluid-film diffusion, (2) ash-layer (or product layer) diffusion, and (3) chemical reaction at the unreacted-core surface, as illustrated in Figure 8.

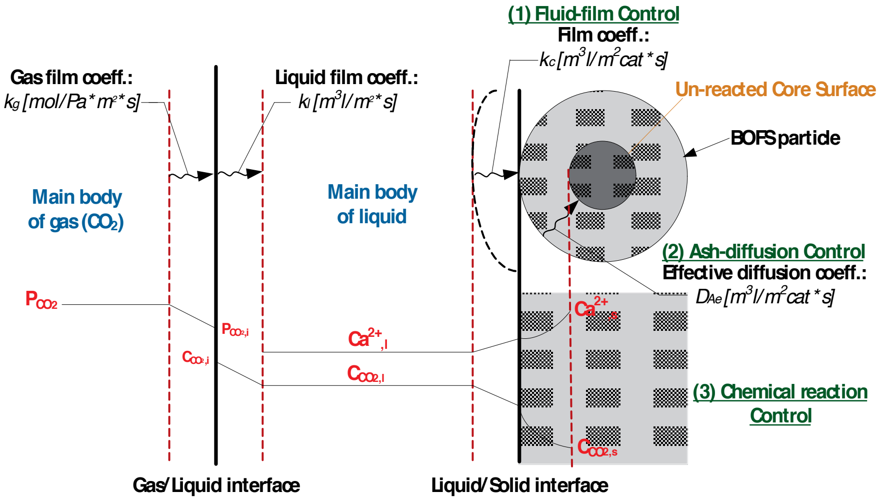

Figure 8. Schematic diagram of mass transfer among gas, liquid, and solid phases in the case of basic oxygen furnace slag (BOFS) carbonation.

When the reactant transfer through the boundary layer of the liquid–solid interface is the rate-limiting step of a reaction, the relationship between the conversion (X_B, %) and reaction time (t, s) can be correlated with Equation (48):

$$t = \frac{\rho_B R}{3bk_e C_{Ag}} X_B = \tau\ X_B \tag{48}$$

where ρ_B (mole cm^{-3}) and R (cm) are the molar density and the radius of the particle, respectively, C_{Ag} (mole cm^{-3}) is the CO_2 concentration in the liquid phase, k_e (mole m^{-2} Pa^{-1} s^{-1}) is the mass transfer coefficient between the fluid and particle, and τ (s) is the time for complete conversion to a product particle.

When the reactant transfer through the ash layer is the rate-limiting step, the dependence of the reaction time on the conversion and the effective diffusivity of the reactant in the ash layer (D_e, cm^2 s^{-1}) can be described by Equation (49):

$$t = \frac{\rho_B R^2}{6bD_e C_{Ag}} \left[1 - 3\left(1 - X_B\right)^{2/3} + 2\left(1 - X_B\right)\right] = \tau\left[1 - 3\left(1 - X_B\right)^{2/3} + 2\left(1 - X_B\right)\right] \tag{49}$$

For simplicity, the particle radius (R) is generally assumed to remain constant in the literature. However, in reality, the R value is not a constant because the thickness of ash layer changes with the reaction, also affecting the diffusivity of the gaseous reactant in the ash layer. Sohn and Szekely [42] have introduced this phenomenon into SCM to make it more general to the fluid–solid reaction. In their recent report [43], a "Z" factor was incorporated with the governing equation of SCM for pore diffusion control, as shown in Equation (50). Z is defined as the volume of product solid formed from a unit volume of reactant solid, where both volumes include those of pores. In this case, the volume of the solid product is different from that of the solid reactant, which means R changes with time:

$$t = \frac{\rho_B R^2}{2bD_e C_{Ag}} \left[\frac{Z - \left(Z - \left(Z - 1\right)\left(1 - X_B\right)\right)^{2/3}}{Z - 1} - \left(1 - X_B\right)^{2/3} \right] \tag{50}$$

If the R value is assumed to remain constant, the Z, herein, should be assigned a value of 1, i.e., the total volume of solid product is the same as that of solid reactant. Thus, Equation (50) will be simplified to Equation (49) by applying L'Hospital's rule.

When the chemical reaction between reactants is the rate-limiting step, the relationship between the conversion and reaction time can be determined by Equation (51):

$$t = \frac{\rho_B R}{bk^{''} C_{Ag}} \left[1 - \left(1 - X_B\right)^{1/3}\right] = \tau\left[1 - \left(1 - X_B\right)^{1/3}\right] \tag{51}$$

where k" (s^{-1}) is the first-order rate constant for the surface reaction.

5.1.3. Mass transfer coefficients

For determining the $K_G a$ value in a heterogeneous system containing the gas, liquid, and solid phases, the following assumptions are generally made for simplicity: (1) the effect of an inclined gas–liquid interface is neglected, (2) solid distribution throughout the bed is uniform, (3) the concentration of the liquid at the particle surface is equal to the saturation concentration of the solution (i.e., the mass transfer between the liquid and the solid is neglected), and (4) the changes in particle size and particle surface area are neglected. In this case, the $K_G a$ in a packed bed can be determined by the two-film theory as Equation (52):

$$\frac{1}{K_G a_e} = \frac{1}{k_G a_e} + \frac{H}{I(k_L a_e)} \tag{52}$$

where k_G is the gas-side mass transfer coefficient (m s^{-1}), k_L is the liquid-side mass transfer coefficient (m s^{-1}), H is the Henry's law constant, and I is the enhancement factor.

On the other hand, the driving force between the saturated CO_2 concentration in the bulk gas and the CO_2 concentration on the surface of liquid film can be determined by shell mass balance over a thin film of fluid with the RPB as shown in Equations (53) and (54):

$$\frac{1}{\rho_{CO_2}} \frac{\mathrm{d}M_G}{\mathrm{d}V} = K_G a_e \ (C_G^* - C_G^{'}) \tag{53}$$

$$\mathrm{d}V = 2\pi r h \cdot \mathrm{d}r \tag{54}$$

where ρ_{co2} is the CO_2 mass density at the temperature of gas streams, M_G is the gas mass flow rate (kg s^{-1}), C_G^* is the saturation concentration of CO_2 in solution (mg/L), $C_G^{'}$ is the concentration of CO_2 in solution (mg/L), V is the volume of packed bed (m^3), h is the height of packing bed (m), and r is the radius of packed bed (m).

In this case, by substitution of Equation (54) into Equation (53), the $K_G a$ can be determined as Equation (55):

$$K_G a_e = \frac{M_G}{\rho_G h\pi (r_o^2 - r_i^2)} \left(NTU_G\right) = \frac{Q_G}{h\pi (r_o^2 - r_i^2)} ln\left(\frac{C_{G,i}}{C_{G,o}}\right) \tag{55}$$

Furthermore, Kelleher and Fair (1996) have obtained an overall volumetric mass transfer coefficient in terms of the area of transfer unit (ATU) for the gas side from the literature [44]. The height of transfer unit (HTU) and ATU can be calculated from the experimental data using Equations (56) and (57), respectively [45]:

$$\mathrm{HTU} = \frac{r_o - r_i}{\mathrm{NTU}} = \frac{r_o - r_i}{\ln(C_{G,i} / C_{G,o})} \tag{56}$$

$$\mathrm{ATU} = \frac{\pi (r_o^2 - r_i^2)}{\mathrm{NTU}} = \frac{\pi (r_o^2 - r_i^2)}{\ln(C_{G,i} / C_{G,o})} \tag{57}$$

It is noted that the K_Ga value in an RPB are an order of magnitude greater than those in a conventional packed bed. In other words, the HTU value of an RPB is smaller than that of conventional packed bed. Therefore, the volume of the RPB reactor for achieving a certain degree of performance is much smaller than that of a conventional reactor such as autoclave and slurry reactors [38, 39]. Several operating factors will affect the performance of RPB reactor. In general, K_Ga increases with the increases of the gas flow rate, the liquid flow rate, and mainly the rotor speed [46].

5.2. Engineering practice

5.2.1. Determination of diffusion coefficients

According to the findings reported by Changet al. [47], the accelerated carbonation of the basic oxygen furnace slag (BOFS) in an RPB is controlled by the ash-layer diffusion mechanism because the experimental data exhibit a good correlation with Equation (51). Similar findings were observed in the literature [48], which suggests that the carbonation reaction should be ash-layer diffusion controlled. The particles exhibited an ash layer of calcium carbonate ($CaCO_3$) product after carbonation, which could be classified as a shrinking core. As shown in Figure 9, the D_e values of CO_2 gas through the ash layer are in the range of 5.47×10^{-7} to 1.49×10^{-6} cm^2 s^{-1}, increasing with the increase of reaction temperature.

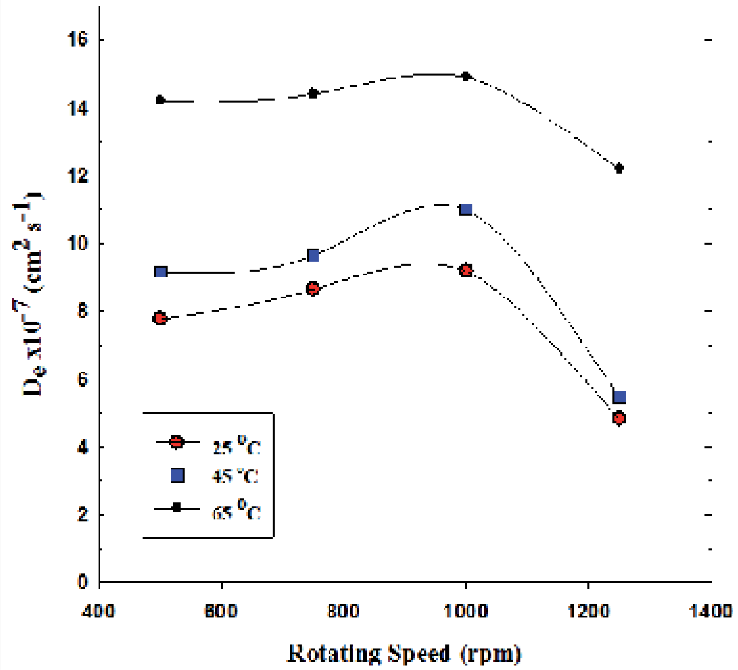

Figure 9. Variation of D_e with reaction temperature for BOFS carbonation based on the SCM (operating conditions: P_{CO2}, 1 bar; flow rate, 1.2 L min^{-1}; D_p, ~ 62 μm; L/S, 20 mL/g^{-1}) (adapted from Chang et al. [47])

In addition, Changet al. [41]) reported an effective diffusivity of steelmaking slag in a slurry reactor of 2.9×10^{-7} to 7.3×10^{-7} $cm^2\ s^{-1}$ according to the results of the SCM. It was found that the rate of CO_2 molecular diffusion was not significantly enhanced by the RPB because the very similar temperatures were operated in the two reactors. Therefore, the D_e values measured in a slurry reactor exhibit the same magnitude of 10^{-6} $cm^2\ s^{-1}$ to that in an RPB. Equation (58) shows the relationship between D_e value ($L^2\ T^{-1}$) and K_Ga ($L\ T^{-1}$) value:

$$K_G = \frac{D_e}{\delta} \tag{58}$$

where δ (L) is the thickness of fluid film. Only a slight discrepancy in *De* values between an RPB and a slurry reactor was found; however, the RPB reactor can generate a thinner liquid film (δ), thereby resulting in a higher mass transfer rate.

5.2.2. Determination of overall gas-phase mass transfer coefficients

Based on the above illustration, the K_Ga value in an RPB can be estimated by the key operating parameters including gas diffusivity, gas superficial velocity, gas density, gas viscosity, liquid superficial velocity, liquid density, liquid viscosity, centrifugal acceleration, total specific surface area of packings, and effective diameter of packings. Therefore, the mass transfer characteristics of RPB (such as K_Ga value and HTU) can be obtained by the nonlinear regression of experimental data [49]:

$$K_G a_e = 0.01 \left(\frac{a_t D_G}{d_p} \right) Re_G^{-1.16}\ Gr_G^{0.33}\ Re_L^{2.12} \tag{59}$$

$$HTU = 0.0003 \left(\frac{a_t D_G}{d_p} \right) Re_G^{2.16}\ Gr_G^{-0.33}\ Re_L^{-2.12} \tag{60}$$

where the ranges of the dimensionless groups in this correlation should be as follows:

$$7.8 < Re_G < 15.9 \tag{61}$$

$$1.3 < Re_L < 2.2 \tag{62}$$

$$2.3 < Gr_G < 26.8 \tag{63}$$

Table 6 presents the K_Ga value for high-gravity carbonation of BOFS-CRW, respectively. The rotation speed varied from 150 to 550 rpm, offering a centrifugal acceleration variation from

60 m/s^2 to 770 m/s^2. The $K_G a$ values moderately increase with an increase of rotation speed (i.e., up to 300–500 rpm), indicating that the mass transfer resistance was reduced by an increasing rotation speed within this range. However, a reduction in $K_G a$ was observed if the rotation speed further increased beyond this range. This might be attributed to the fact that the extent of reduction in mass transfer resistances at higher rotation speed was compensated for by a reduction of the retention time, which was unfavorable to reaction.

No	**ω'a (rpm)**	**Q_G ^{a} (m^3/min)**	**Q_{sl} ^{a} (L/min)**	**G/L ratio (-)**	**L/S ratio (mL/g)**	**K_Ga value (s^{-1})**
1	462.1	0.33	9.33	35.4	10.12	0.672
2	462.7	0.34	9.33	36.4	10.61	0.650
3	505.1	0.82	6.50	126.2	12.35	0.715
4	487.3	0.44	9.17	48.0	11.21	0.680
5	534.4	0.72	6.33	113.7	12.77	0.632
6	360.2	0.42	9.00	46.7	10.06	0.699

^{a}ω', rotation speed (rpm); Q_G, gas flow rate (m^3/min); Q_{sl}, slurry flow rate (L/min)

Table 6. Candidates of optimal K_Ga solutions under different operating conditions and verified with theoretical model

On the other hand, several studies have utilized different kinetic models to determine the rate-limiting step of mineral carbonation [31, 41]. In fact, solid–liquid mass transfer is particularly important in mineral carbonation and, in many cases, the rate limiting factor [50, 51] because minerals in solid matrix dissolve partly and passive layers are formed, gradually increasing resistance to mass transfer and eventually leading to incomplete conversion. In general, the solid–liquid mass transfer coefficient is occasionally correlated as itself, where such correlations are specific to the system under consideration and are not generally applicable [50].

In spite of the significant differences between RPB and traditional packed column, penetration theory was still capable of describing the liquid-side mass transfer behavior fairly well in RPB [52]. These correlations are most often expressed in terms of dimensionless numbers in the form of a power series. For instance, penetration theory can be applied to RPB to yield as Equation (64):

$$k_L = 0.92 \left(\frac{D_L}{d_p} \right) Sc_L^{1/2} \ Re_L^{1/3} Gr_L^{1/6} \tag{64}$$

where the Grashof number which represents the ratio of gravitational to viscous forces can be determined by Equation (65) and the g value can be replaced by the centrifugal acceleration term as shown in Equation (66):

$$Gr_L = gd_p^3\left(\frac{\rho_L}{\mu_L}\right)^2 \tag{65}$$

$$g = a_m = \left(\frac{r_o^2 + r_i^2}{2}\right)^{1/2}\omega^2 \tag{66}$$

The Grashof (*Gr*) number is generally determined by the mean radius of the packed bed. Another commonly used prediction for liquid-side (k_L) and gas-side (k_G) mass transfer coefficient in a conventional packed column is that of Onda et al. (1968), as shown in Equations (67) and (68), respectively. Onda et al. suggested the constant 5.23 of Equation (68) should be best correlated by changing the constant into 2.00 for smaller packings (i.e., diameter is less than 1.5 cm) since the K_Ga data for packings smaller than 1.5 cm tend to decrease in the literatures [53].

$$k_L = 0.0051\left(\frac{a_t}{a_w}\right)^{2/3} Re_L^{2/3}Sc_L^{-1/2}\left(\frac{\rho_L}{\mu_L g}\right)^{-1/3}(a_pd_p)^{0.4} \tag{67}$$

and

$$k_G = 5.23\left(a_pD_G\right)Re_G^{0.7}Sc_G^{1/3}\left(a_pd_p\right)^{-2} \tag{68}$$

It is usually difficult to obtain mass transfer coefficients separated from volumetric mass transfer coefficients k_La_e and k_Ga_e since the effective interfacial area between the liquid and vapor phase is usually not known [38]. Several correlations have been reported to estimate the wetted surface area (a_w), among which Tung and Mah [52] found that the a_w/a_t predicted value by Perry and Chilton [54] is "reliable" under high-gravity RPB process as shown in Equation (69).

$$\frac{a_w}{a_t} = \frac{a_e}{a_t} = 1 - \exp[-1.45\left(\frac{\sigma_c}{\sigma_L}\right)^{0.75} Re_L^{0.1}\ We_L^{0.2}\ Fr_L^{-0.05}] \tag{69}$$

The assumption of the above equality is that for packing materials with small static holdup (i.e., large packing size), the wetted area (a_w) may equal the interfacial area (a_e). In addition, Basic (1992) has correlated the wetted surface area of packing by combining experimental data of liquid holdup and estimation of mean liquid film thickness, as shown in Equation (70):

$$\frac{a_w}{a_t} = 584\ Re_L^{-1.03}\ We_L^{0.576}\ Fr_L^{0.123} \tag{70}$$

5.2.3. Balancing mass transfer performance and energy consumption

Balancing the gas-phase mass transfer rate for the high-gravity carbonation process with a relatively lower energy consumption is also an important task for carbonation process. As shown in Figure 10, the favorable operating conditions can be determined via graphical presentation, where the energy consumptions including rotation, blowers, air compressors, and pumps were measured during operation in terms of kWh per ton CO_2 capture by the RPB. It suggests that a centrifugal acceleration should be maintained at 475 m/s^2 for a relatively lower energy consumption (L1 → L2) and higher K_Ga value (L3 → L4). Moreover, the favorable G/L ratio should range between 40 and 55 for high-gravity carbonation process (by both L5 → L6 and R1 → R2 → R3). A further increase in G/L ratio up to 80 will lead to a low mass transfer performance (i.e., K_Ga value) with high energy consumption for rotation and pumps, thereby exhibiting a poor CO_2 removal efficiency and capacity.

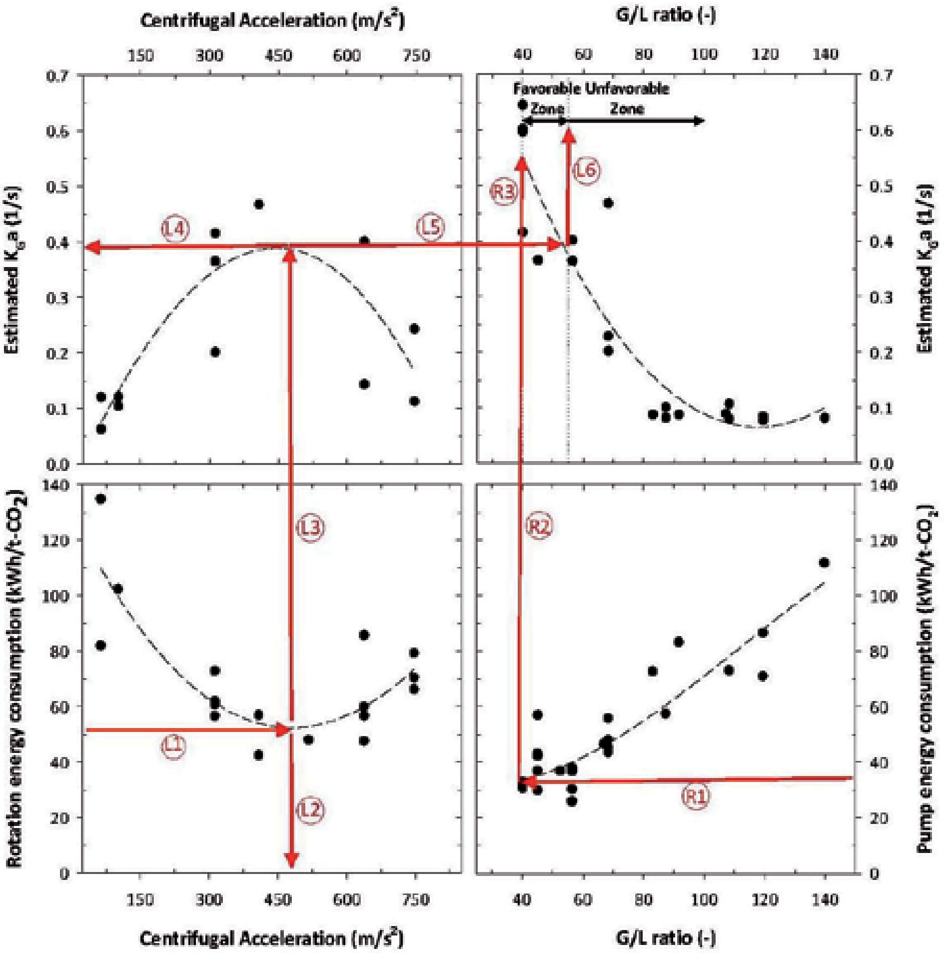

Figure 10. Graphical presentation for determining the optimal K_Ga value with favorable centrifugal acceleration (i.e., rotation speed) and G/L ratio for high-gravity carbonation process (as indicated by red line) (courtesy of Pan et al. [49])

6. Summary

A clear understanding in process chemistry, reaction kinetics, and mass transfer is the essential requirement to achieve the best achievable technology. Many industrial and/or waste treatment processes are involved in diffusion-controlled mechanism. To increase process efficiency and reaction rate, the mass transfer of those processes should be improved, which can be approached by development of prediction model using theoretical theory such as Fick's law or penetration theory. For those heterogeneous processes, especially the system containing gas, liquid, and solid phase, assumptions should be appropriately made to simplify the complex governing equation. Lastly, from the viewpoint of engineering practice, the energy consumption of a process is also an important factor to optimize the overall process, thereby reducing the operation costs.

Author details

Pen-Chi Chiang* and Shu-Yuan Pan

*Address all correspondence to: pcchiang@ntu.edu.tw

Graduate Institute of Environmental Engineering, National Taiwan University, Taiwan

References

[1] Y.-W. Ko, P.-C. Chiang, C.L. Chuang, E.E. Chang, Kinetics of the Reaction Between Ozone and p-Hydroxybenzoic Acid in a Semi-batch Reactor, Ind. Eng. Chem. Res., 39 (2000) 635-641.

[2] P.-C. Chiang, Y.-W. Ko, Y.-M. Yang, Applying Mass Transfer Models for Controlling Organic Compounds in Ozonation Process, Environ Int, 23 (1997) 819-828.

[3] Y.M. Yang, Effects of ozone mass transfer on the formation and control of volatile organic compounds in drinking water, in: Graduate Institute of Environmental Engineering, National Taiwan University, Taipei, 1991.

[4] A. Ouedemi, J.C. Mora, R.S. Bes, Ozone absorption in water: Mass transfer and solubility, Ozone Sci. Eng., 9 (1987) 1-12.

[5] S. Sheffer, G.L. Esterson, Mass transfer and reaction kinetics in the ozone/tap water system, Water Res., 10 (1982) 383-389.

[6] I. Stankovic, Comparison of ozone and oxygen mass transfer in a laboratory and pilot plant operation, Ozone Sci. Eng., 10 (1988) 321-338.

[7] M.D. Gurol, Factors controlling the removal of organic pollutants in ozone reactors, J. Am. Water Wks. Assoc., 77 (1985) 55-60.

[8] P.V. Danckwerts, Gas Liquid Reactions, McGraw-Hill, New York, 1970.

[9] W.L. McCabe, J.C. Smith, P. Harriott, Unit operations of chemical engineering, 4 ed., McGraw-Hill, New York, 1985.

[10] W.J. DeCoursey, Absorption with chemical reaction: development of a new relation for the Danckwerts model, Chem. Eng. Sci., 29 (1974) 1867-1872.

[11] R. Turse, W. Rieman III, J. Phys. Chem., 65 (1961) 1821.

[12] J. Crank, The mathematics of Diffusion, Oxford Univ. Press, London, 1956.

[13] T.C. Huang, F.N. Tsai, The Canadian Journal of Chemical Engineering, 55 (1977) 302.

[14] H.T. Chang, B.E. Rittmann, Mathematical modeling of biofilm on activated carbon, Environ. Sci. Technol., 21 (1987) 273-280.

[15] C.H. Liang, P.C. Chiang, Mathematical model of the non-steady-state adsorption and biodegradation capacities of BAC filters, J Hazard Mater, 139 (2007) 316-322.

[16] C.H. Liang, P.C. Chiang, E.E. Chang, Modeling the behaviors of adsorption and biodegradation in biological activated carbon filters, Water research, 41 (2007) 3241-3250.

[17] A. Sakoda, J. Wang, M. Suzuki, Microbial activity in biological activated carbon bed by pulse responses., Water Sci. Technol., 34 (1996) 222-231.

[18] G.M. Walker, L.R. Weatherley, A simplified predictive model for biologically activated carbon fixed beds., Process. Biochem., 32 (1997) 327-335.

[19] R.J. Abumaizar, E.H. Smith, W. Kocher, Analytical model of dual-media biofilter for removal of organic air pollutants, J. Environ. Eng. ASCE, 123 (1997) 606-614.

[20] R.M. Hozalski, E.J. Bouwer, Non-steady state simulation of BOM removal in drinking water biofilters: model development., Water Res., 35 (2001) 198-210.

[21] B.N. Badriyha, V. Ravindran, W. Den, M. Pirbazari, Bioadsorber efficiency, design, and performance forecasting for alachlor removal, Water Res., 37 (2003) 4051-4072.

[22] B.E. Rittmann, P.L. McCarty, Substrate flux into biofilms of any thickness, J. Environ. Eng., ASCE, 107 (1981) 831-849.

[23] B.G. Oliver, J. Lawrence, Haloforms in Drinking Water: A Study of Precursors and Precursor Removal,, J. Amer. Water Works Assoc., 71 (1979) 161-163.

[24] O. Levenspiel, Chemical Reaction Engineering, third edition ed., John Wiley and Sons, 1999.

[25] P.-C. Chiang, E.E. Chang, Y.-W. Ko, J.-C. Lou, Balancing Disinfection Efficiency and THM Formation During Chlorination Theoretical Considerations, The Canadian Journal of Chemical Engineering, 75 (1997) 892-898.

[26] H. Collins, R. Selleck, Process Kinetics of Wastewater Chlorination, in, University of California, Berkeley, 1972.

[27] P.-C. Chiang, Y.-W. Ko, C.H. Liang, E.E. Chang, Modeling An Ozone Bubble Column for Predicting its Disinfection Efficiency and Control of Disinfection By-Products Formation, Chemosphere, 39 (1999) 55-70.

[28] J.G. Jacangelo, N.L. Patania, K.M. Reagau, E.M. Aieta, S.W. Krasner, M.J. McGuire, Ozonation: assessing its role in the formation and control of disinfection by-products, J. Amer. Water Works Assoc., 81 (1989).

[29] G.L. Amy, L. Tan, M.K. Davis, The effects of ozonation and activated carbon adsorption on trihalomethane speciation, War. Res., 25 (1991) 191-202.

[30] E.E. Chang, Y.-C. Wang, S.-Y. Pan, Y.-H. Chen, P.-C. Chiang, CO_2 Capture by Using Blended Hydraulic Slag Cement via a Slurry Reactor, Aerosol and Air Quality Research, 12 (2012) 1433-1443.

[31] S.N. Lekakh, C.H. Rawlins, D.G.C. Robertson, V.L. Richards, K.D. Peaslee, Kinetics of Aqueous Leaching and Carbonization of Steelmaking Slag, Metallurgical and Materials Transactions B, 39 (2008) 125-134.

[32] S.-Y. Pan, E.E. Chang, P.-C. Chiang, CO_2 Capture by Accelerated Carbonation of Alkaline Wastes: A Review on Its Principles and Applications, Aerosol and Air Quality Research, 12 (2012) 770-791.

[33] R.M. Santos, D. François, G. Mertens, J. Elsen, T. Van Gerven, Ultrasound-intensified mineral carbonation, Applied Thermal Engineering, 57 (2013) 154-163.

[34] S. Teir, S. Eloneva, C. Fogelholm, R. Zevenhoven, Fixation of carbon dioxide by producing hydromagnesite from serpentinite, Applied Energy, 86 (2009) 214-218.

[35] G. Costa, R. Baciocchi, A. Polettini, R. Pomi, C.D. Hills, P.J. Carey, Current status and perspectives of accelerated carbonation processes on municipal waste combustion residues, Environ Monit Assess, 135 (2007) 55-75.

[36] C. Lin, B. Chen, Characteristics of cross-flow rotating packed beds, Journal of Industrial and Engineering Chemistry, 14 (2008) 322-327.

[37] M. Wang, Controlling factors and mechanism of preparing needlelike CaCO3 under high-gravity environment, Powder Technology, 142 (2004) 166-174.

[38] T. Kelleher, J.R. Fair, Distillation studies in a high-gravity contactor, Ind Eng Chem Res, 35 (1996) 4646-4655.

[39] C. Tan, J. Chen, Absorption of carbon dioxide with piperazine and its mixtures in a rotating packed bed, Separation and Purification Technology, 49 (2006) 174-180.

[40] S.Y. Pan, P.C. Chiang, Y.H. Chen, C.S. Tan, E.E. Chang, Ex Situ CO_2 capture by carbonation of steelmaking slag coupled with metalworking wastewater in a rotating packed bed, Environ Sci Technol, 47 (2013) 3308-3315.

[41] E.E. Chang, C.H. Chen, Y.H. Chen, S.Y. Pan, P.C. Chiang, Performance evaluation for carbonation of steel-making slags in a slurry reactor, J Hazard Mater, 186 (2011) 558-564.

[42] H.Y. Sohn, J. Szekely, Reactions between solids through gaseous intermediates- I Reactions controlled by chemical kinetics, Chemical Engineering Science, 28 (1973) 1789-1801.

[43] H.Y. Sohn, The effects of reactant starvation and mass transfer in the rate measurement of fluid–solid reactions with small equilibrium constants, Chemical Engineering Science, 59 (2004) 4361-4368.

[44] P. Sandilya, D.P. Rao, A. Sharma, Gas-phase mass transfer in a centrifugal contactor, Ind Eng Chem Res, 40 (2001) 384-392.

[45] H.-H. Cheng, J.-F. Shen, C.-S. Tan, CO2 capture from hot stove gas in steel making process, International Journal of Greenhouse Gas Control, 4 (2010) 525-531.

[46] H. Liu, C. Kuo, Quantitative multiphase determination using the Rietveld method with high accuracy, Materials Letters, 26 (1996) 171-175.

[47] E.E. Chang, S.Y. Pan, Y.H. Chen, C.S. Tan, P.C. Chiang, Accelerated carbonation of steelmaking slags in a high-gravity rotating packed bed, J Hazard Mater, 227-228 (2012) 97-106.

[48] S.N. Lekakh, D.G.C. Robertson, C.H. Rawlins, V.L. Richards, K.D. Peaslee, Investigation of a Two-Stage Aqueous Reactor Design for Carbon Dioxide Sequestration Using Steelmaking Slag, Metallurgical and Materials Transactions B, 39 (2008) 484-492.

[49] S.-Y. Pan, E.G. Eleazar, E.-E. Chang, Y.-P. Lin, H. Kim, P.-C. Chiang, Systematic Approach to Determination of Optimum Gas-phase Mass Transfer Rate for High-gravity Carbonation Process of Steelmaking Slags in a Rotating Packed Bed, Applied energy, 148 (2015) 23-31.

[50] D.C. Arters, L.-S. Fan, Experimental methods and correlation of solid liquid mass transfer in fluidized beds, Chemical Engineering Science, 41 (1986) 107-115.

[51] S. Munjal, M.P. Dudukovic, P. Ramachandran, Mass-transfer in Rotating Packed Beds - I. Development of Gas-Liquid and Liquid-Solid Mass Transfer Correlations Chemical Engineering Science, 44 (1989) 2245-2256.

[52] H.H. Tung, R.S.H. Mah, Modeling liquid mass transfer in HIGEE separation process, Chemical Engineering Communication, 39 (1985) 147-153.

[53] K. Onda, H. Takeuchi, Y. Okumoto, Mass transfer coefficients between gas and liquid phases in packed columns, Journal of Chemical Engineering of Japan, 1 (1968) 56-62.

[54] R.H. Perry, C.H. Chilton, Chemical engineers' handbook, McGraw-Hill, New York, 1973.

Edited by Marek Solecki

This book covers a wide variety of topics related to advancements in different stages of mass transfer modelling processes. Its purpose is to create a platform for the exchange of recent observations, experiences, and achievements. It is recommended for those in the chemical, biotechnological, pharmaceutical, and nanotechnology industries as well as for students of natural sciences, technical, environmental and employees in companies which manufacture machines for the above-mentioned industries. This work can also be a useful source for researchers and engineers dealing with mass transfer and related issues.

Photo by inarik / iStock

IntechOpen

ISBN 978-953-51-6394-7